Ph.D. Thesis

Compressive Sensing Based Candidate Detector and its Applications to Spectrum Sensing and Through-the-Wall Radar Imaging

By

Eva Lagunas Targarona
e-mail: eva.lagunas@upc.edu

Advisor: Prof. Dr. Montserrat Nájar Martón
Universitat Politècnica de Catalunya (UPC)
montse.najar@upc.edu

Co-Advisor: Prof. Dr. Moeness G. Amin
Center for Advanced Communications (CAC)
Villanova University, PA, USA
moeness.amin@villanova.edu

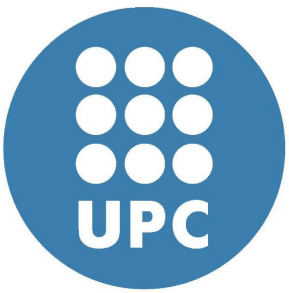

Barcelona, March 2014

A dissertation submitted to the department of signal theory and communications of
Universitat Politècnica de Catalunya (UPC)

Except where acknowledged in the customary manner, the material presented in this thesis is, to the best of my knowledge, original and has not been submitted in whole or part for a degree in any university.

Eva Lagunas Targarona

UNIVERSITAT POLITÈCNICA DE CATALUNYA
BARCELONATECH
Escola de Doctorat

Curs acadèmic: 2013 / 2014

Acta de qualificació de tesi doctoral

Nom i cognoms
Eva Lagunas Targarona

Programa de doctorat
Teoria del Senyal i Comunicacions

Unitat estructural responsable del programa
Departament de Teoria del Senyal i Comunicacions

Resolució del Tribunal

Reunit el Tribunal designat a l'efecte, el doctorand / la doctoranda exposa el tema de la seva tesi doctoral titulada Compressive Sensing based Candidate Detector and its Applications to Spectrum Sensing and Through-the-Wall Radar Imaging.

Acabada la lectura i després de donar resposta a les qüestions formulades pels membres titulars del tribunal, aquest atorga la qualificació:

☐ NO APTE ☐ APROVAT ☐ NOTABLE ☐ EXCEL·LENT

(Nom, cognoms i signatura)	(Nom, cognoms i signatura)	
President/a	Secretari/ària	
(Nom, cognoms i signatura)	(Nom, cognoms i signatura)	(Nom, cognoms i signatura)
Vocal	Vocal	Vocal

_____, _____ d'/de _____ de _____

El resultat de l'escrutini dels vots emesos pels membres titulars del tribunal, efectuat per l'Escola de Doctorat, a instància de la Comissió de Doctorat de la UPC, atorga la MENCIÓ CUM LAUDE:

☐ SÍ ☐ NO

(Nom, cognoms i signatura)	(Nom, cognoms i signatura)
Presidenta de la Comissió de Doctorat	Secretària de la Comissió de Doctorat

Barcelona, _____ d'/de _____ de _____

Talent means nothing, while experience,
acquired in humility and with hard work,
means everything.

Patrick Süskind
Perfume: The Story of a Murderer

Abstract

Signal acquisition is a main topic in signal processing. The well-known Shannon-Nyquist theorem lies at the heart of any conventional analog to digital converters stating that any signal has to be sampled with a constant frequency which must be at least twice the highest frequency present in the signal in order to perfectly recover the signal. However, the Shannon-Nyquist theorem provides a worst-case rate bound for any bandlimited data. In this context, Compressive Sensing (CS) is a new framework in which data acquisition and data processing are merged. CS allows to compress the data while is sampled by exploiting the sparsity present in many common signals. In so doing, it provides an efficient way to reduce the number of measurements needed for perfect recovery of the signal. CS has exploded in recent years with thousands of technical publications and applications being developed in areas such as channel coding, medical imaging, computational biology and many more.

Unlike majority of CS literature, the proposed Ph.D. thesis surveys the CS theory applied to signal detection, estimation and classification, which not necessary requires perfect signal reconstruction or approximation. In particular, a novel CS-based detection technique which exploits prior information about some features of the signal is presented. The basic idea is to scan the domain where the signal is expected to lie with a candidate signal estimated from the known features. The proposed detector is called candidate detector because its main goal is to react only when the candidate signal is present.

The CS-based candidate detector is applied to two topical detection problems. First, the powerful CS theory is used to deal with the sampling bottleneck in wideband spectrum sensing for open spectrum scenarios. The radio spectrum is a natural resource which is recently becoming scarce due to the current spectrum assignment policy and the increasing number of licensed wireless systems. To deal with the overcrowded spectrum problem, a new spectrum management philosophy is required. In this context, the revolutionary Cognitive Radio (CR) emerges as a solution for the dynamic radio spectrum access. CRs benefits from the poor usage of the spectrum by allowing the use of temporarily unused licensed spectrum to secondary users who have no spectrum licenses. To protect the primary (licensed) systems from the opportunistic secondary users' interference, the primary user activity should be reliably monitored. The identification procedure of available spectrum is commonly known as spectrum sensing. Spectrum sensing involves making observations of the radio frequency spectrum and reporting on the availability of unused spectrum for use by the CR users. However, one of the most important problems that spectrum sensing techniques must face is the scanning of wide band of frequencies, which implies high sampling rates. The proposed CS-based candidate detector exploits some prior knowledge of primary users, not only to relax the sampling bottleneck, but also to provide an estimation of the candidate signals'

frequency, power and angle of arrival without reconstructing the whole spectrum.

The second application is Through-the-Wall Radar Imaging (TWRI). Sensing through obstacles such as walls, doors, and other visually opaque materials, using microwave signals is emerging as a powerful tool supporting a range of civilian and military applications. High resolution imaging is achieved if large bandwidth signals and long antenna arrays are used. However, this implies acquisition and processing of large amounts of data volume. Decreasing the number of acquired samples can also be helpful in TWRI from a logistic point of view, as some of the data measurements in space and frequency can be difficult, or impossible to attain. In this thesis, we addressed the problem of imaging building interior structures using a reduced number of measurements. The proposed technique is based on prior knowledge about common construction practices. In particular, dominant scatterers, such as corners and walls, are used as candidates in the proposed detector. The interior building scenes are composed of a small number of dominant scatterers allowing the application of CS. Real data collection experiments in a laboratory environment, using Radar Imaging Lab (RIL) facility at the Center for Advanced Communications (CAC), Villanova University, PA, USA, are conducted to validate the proposed approach.

Resumen

La adquisición de datos es un tema fundamental en el procesamiento de señales. Hasta ahora, el teorema de Shannon-Nyquist ha sido el núcleo de los métodos convencionales de conversión analógico-digital. El teorema dice que para recuperar perfectamente la información, cualquier señal debe ser muestreada a una frecuencia constante igual al doble de la máxima frecuencia presente en la señal. Sin embargo, este teorema asume el peor de los casos: cuando las señales ocupan todo el espectro. En este contexto aparece la teoría del muestreo compresivo (conocido en inglés como *Compressed Sensing* (CS)). CS ha supuesto una auténtica revolución en lo que se refiere a la adquisición y muestreo de datos analógicos en un esfuerzo hacia resolver la problemática de recuperar un proceso continuo comprimible con un nivel suficiente de similitud si únicamente se realiza un número muy reducido de medidas o muestras del mismo. El requerimiento para el éxito de dicha técnica es que la señal debe poder expresarse de forma dispersa en algún dominio. Esto es, que la mayoría de sus componentes sean cero o puedan considerarse despreciables. La aplicación de este tipo de muestreo compresivo supone una línea de investigación de gran auge e interés investigador en áreas como la transmisión de datos, procesamiento de imágenes médicas, biología computacional, entre otras.

A diferencia de la mayoría de publicaciones relacionadas con CS, en esta tesis se estudiará CS aplicado a detección, estimación y clasificación de señales, que no necesariamente requiere la recuperación perfecta ni completa de la señal. En concreto, se propone un nuevo detector basado en cierto conocimiento a priori sobre la señal a detectar. La idea básica es escanear el dominio de la señal con una señal llamada Candidata, que se obtiene a partir de la información a priori de la señal a detectar. Por lo tanto, el detector únicamente reaccionará cuando la señal candidata esté presente.

El detector es aplicado a dos problemas particulares de detección. En primer lugar, la novedosa teoría de CS es aplicada al sensado de espectro o spectrum sensing, en el contexto de Radio Cognitiva (CR). El principal problema radica en que las políticas actuales de asignación de bandas frecuenciales son demasiado estrictas y no permiten un uso óptimo del espectro radioeléctrico disponible. El uso del espectro radioeléctrico puede ser mejorado significativamente si se posibilita que un usuario secundario (sin licencia) pueda acceder a un canal desocupado por un usuario primario en ciertas localizaciones y momentos temporales. La tecnología CR se ha identificado recientemente como una solución prometedora al denominado problema de escasez de espectro, es decir, la creciente demanda de espectro y su actual infrautilización. Un requerimiento esencial de los dispositivos cognitivos es la capacidad de detectar la presencia de usuarios primarios (para no causarles interferencia). Uno de los problemas que se afronta en este contexto es la necesidad de escanear grandes

anchos de banda que requieren frecuencias de muestreo extremadamente elevadas. El detector propuesto basado en CS aprovecha los huecos libres de espectro no sólo para relajar los requerimientos de muestreo, sino también para proporcionar una estimación precisa de la frecuencia, potencia y ángulo de llegada de los usuarios primarios, todo ello sin necesidad de reconstruir el espectro.

La segunda aplicación es en radar con visión a través de paredes (*Through-the-Wall Radar Imaging* - TWRI). Hace ya tiempo que la capacidad de ver a través de las paredes ya no es un asunto de ciencia ficción. Esto es posible mediante el envío de ondas de radio, capaces de atravesar objetos opacos, que rebotan en los objetivos y retornan a los receptores. Este es un tipo de radar con gran variedad de aplicaciones, tanto civiles como militares. La resolución de las imágenes proporcionadas por dichos radares mejora cuando se usan grandes anchos de banda y mayor número de antenas, lo que directamente implica la necesidad de adquirir un mayor número de muestras y un mayor volumen de datos que procesar. A veces, reducir el número de muestras es interesante en TWRI desde un punto de vista logístico, ya que puede que algunas muestras frecuenciales o espaciales sean difíciles o imposibles de obtener. En esta tesis focalizaremos el trabajo en la detección de estructuras internas como paredes internas para reconstruir la estructura del edificio. Las paredes y/o diedros formados por la intersección de dos paredes internas formaran nuestras señales candidatas para el detector propuesto. En general, las escenas de interiores de edificios están formadas por pocas estructuras internas dando paso a la aplicación de CS. La validación de la propuesta se llevará a cabo con experimentos realizados en el Radar Imaging Lab (RIL) del Center for Advanced Communications (CAC), Villanova University, PA, USA.

Resum

L'adquisició de dades és un tema fonamental en el processament de senyals. Fins ara, el teorema de Shannon-Nyquist ha sigut la base dels mètodes convencionals de conversió analògic-digital. El teorema diu que per recuperar perfectament la informació, qualsevol senyal ha de ser mostrejada a una freqüència constant igual al doble de la màxima freqüència present a la senyal. No obstant, aquest teorema assumeix el pitjor dels casos: quan les senyals ocupen tot l'espectre. En aquest context apareix la teoria del mostreig compressiu (conegut en anglès amb el nom de *Compressed Sensing* (CS)). CS ha suposat una autèntica revolució pel que fa a l'adquisició i mostreig de dades analògiques en un esforç cap a resoldre la problemàtica de recuperar un procés continu comprimible amb un nivell suficient de similitud si únicament es realitza un número molt reduït de mesures o mostres del mateix. El requisit para l'èxit d'aquesta tècnica és que la senyal ha de poder ser expressada de forma dispersa en algun domini. Això és, que la majoria dels seus components siguin zero o puguin considerar-se despreciables. L'aplicació d'aquest tipus de mostreig compressiu suposa una línia de investigació de gran interès en àrees com la transmissió de dades, el processament d'imatges mèdiques, biologia computacional, entre altres.

A diferència de la majoria de publicacions relacionades amb CS, en aquesta tesi s'estudiarà CS aplicat a detecció, estimació i classificació de senyals, que no necessàriament requereix la recuperació perfecta ni completa de la senyal. En concret, es proposa un nou detector basat en cert coneixement a priori sobre la senyal a detectar. La idea bàsica és escanejar el domini de la senyal amb una senyal anomenada Candidata, que s'obté a partir de la informació a priori de la senyal a detectar. Per tant, el detector únicament reaccionarà quan la senyal candidata estigui present.

El detector és aplicat a dos problemes particulars de detecció. En primer lloc, la teoria de CS és aplicada al sensat d'espectre o *spectrum sensing*, en el context de Radio Cognitiva (CR). El principal problema radica en que les polítiques actuals d'assignació de bandes freqüencials són massa estrictes i no permeten l'ús òptim de l'espectre radioelèctric disponible. L'ús de l'espectre radioelèctric pot ser significativament millorat si es possibilita que un usuari secundari (sense llicència) pugui accedir a un canal desocupat per un usuari primari en certes localitzacions i moments temporals. La tecnologia CR s'ha identificat recentment com una solució prometedora al problema d'escassetat d'espectre, és a dir, la creixent demanda d'espectre i la seva actual infrautilització. Un requeriment essencial dels dispositius cognitius és la capacitat de detectar la presència d'usuaris primaris (per no causar interferència). Un dels problemes que s'afronta en aquest context és la necessitat d'escanejar grans amples de banda que requereixen freqüències de mostreig extremadament elevades. El detector proposat basat en CS aprofita els espais buits lliures d'espectre no només per relaxar els requeriments

de mostreig, sinó també per proporcionar una estimació precisa de la freqüència, potència i angle d'arribada dels usuaris primaris, tot això sense necessitat de reconstruir l'espectre.

La segona aplicació és en radars amb visió a través de parets (*Through-the-Wall Radar Imaging* - TWRI). Ja fa un temps que la capacitat de veure a través de les parets no és un assumpte de ciència ficció. Això és possible mitjançant l'enviament d'ones de radio, capaços de travessar objectes opacs, que reboten en els objectius i retornen als receptors. Aquest és un tipus de radar amb una gran varietat d'aplicacions, tant civils como militars. La resolució de las imatges proporcionades per aquests radars millora quan s'usen grans amples de banda i més nombre d'antenes, cosa que directament implica la necessitat d'adquirir un major nombre de mostres i un major volum de dades que processar. A vegades, reduir el nombre mostres és interessant en TWRI des de un punt de vista logístic, ja que pot ser que algunes mostres freqüencials o espacials siguin difícils o impossibles d'obtenir. En aquesta tesis focalitzarem el treball en la detecció d'estructures internes com per exemple parets internes per reconstruir l'estructura de l'edifici. Les parets i/o díedres formats per la intersecció de dos parets internes formaran les nostres senyals candidates per al detector proposat. En general, les escenes d'interiors d'edificis estan formades per poques estructures internes donant pas a l'aplicació de CS. La validació de la proposta es durà a terme amb experiments realitzats en el Radar Imaging Lab (RIL) del Center for Advanced Communications (CAC), Villanova University, PA, USA.

Acknowledgements

I would like to thank many people who have helped me through the completion of this dissertation.

First and foremost, I would like to begin by thanking my supervisors. Thank to my thesis advisor Prof. Montse Nájar for his guidance and support throughout my Ph.D. at Universitat Politècnica de Catalunya (UPC). It is a great pleasure and privilege for me to have worked together with her over the past four years. Montse has been very supportive and has given me the freedom to pursue various projects without objection. Part of this thesis was written during a 6-month stay at the Center for Advanced Communications, at Villanova University, PA, USA. It has been a privilege to have worked with Prof. Moeness G. Amin and Prof. Fauzia Ahmad, who have taught me so much and have been endlessly patient with my countless questions. I would especially like to thank Prof. Amin and his wife for their hospitality throughout our visit to Villanova. Also, thank to Janice Moughan for all her kindness.

I would also like to thank all of the members of my Ph.D. evaluation committee, Prof. Abdelhak M. Zoubir, Prof. Aawatif Hayar, and Prof. Ana I. Pérez Neira for accepting this task and for their generous and professional commitment to the review.

I would like to express my gratitude to the staff of the International Student Office at Villanova University. Thanks to Hubert WhanTong, who was very helpful and answered all of our questions regarding VISA issues quickly and easily. A warm thank you to Debra Hoover for welcoming my husband Iñaki into her english class with open arms.

I would very much like to thank some of the good friends we made during our time in USA. Special thanks to Sergio and Paulina for introducing us to their wonderful group of friends. Many thanks also to Allan for opening the doors of his home to us and for his generous friendship.

I would like to thank all my office collegues at UPC, Barcelona, for making this a wonderful working place, specially Josep Font-Segura, Màrius Caus, Miriam León, Adriano Pastore, Javi Rubio, Sandra Lagén and Adrián Agustín.

Many thanks to all the administrative staff of the Escola Tècnica Superior de Telecomunicació de Barcelona (ETSETB), UPC, especially Asunción Salvat and Ana Benedicto, for their indispensable help in solving administrative formalities during my graduate and undergraduate studies.

I would also like to thank my colleagues during my undergraduate studies at UPC for the good times we shared over the past years: Joana Maria Frontera, Marc Maceira, Albert Mazarico, Ricard Sauch, Jesús Campos, Jordi Marín, Marc Suñé, Ferran Anglada and Gerard Amposta. I was also involved in activities outside UPC, where I met amazing people. I am lucky to have a wonderful group of friends. Sincere thanks to Sílvia Pons, Maria Cortés,

Clara Segués, Cristina Pàmies, Blanca Beltran and Àuria Artigas, and all their respective boyfriends and husbands, for every moment we enjoy together. I can not forget to mention the girls (former and current players) of my two football teams: CF Can Colapi and 'Les Antonies'. We had a lot of fun playing football together (despite the subfreezing temperatures of the winter season). Thanks for the friendship and memories and thanks for making me forget my tensions at work.

Last but not the least, to those who mean the most to me, my family. My parents deserve special mention for their unconditional support. My father, Miguel Angel, has been helpful in providing advice many times during my graduate and ungraduate school career. He was and remains my best role model for a scientist, professor and father. I will forever be indebted to my mother, Montse, for always being there for me. Thanks for letting me borrow your car, thanks for making my lunch every day and thanks for driving me to work. But thank you, most of all, for never letting me believe there was anything I couldn't do. I would also like to thank my sister Anna. At the beginning, we were humoring about putting her name in the 'Unacknowledgements' section for being late every morning. However, I must say that I really enjoyed the interesting discussions during our commute to Barcelona every morning (at least the ones I did not fall asleep). I am really going to miss those mornings with you and mom. Also, thanks to Oriol, Jac, my grandparents and my family from Madrid, thanks to all of you for always being there for me.

I would like to express my sincere gratitude to my in-laws, Eugenia and Adolf, who have warmly taken care of my child when I was at work or traveling. Thank you for all of the sacrifices that you've made on my behalf.

I will forever be thankful to my husband, Iñaki, for his support, understanding and patience which are undeniably the bedrock upon which this work has been built. Thank you for leaving everything behind and coming with me to the United States. Thank you for taking care of our child when I was traveling. I know it was not easy being married to a PhD student, so thank you for coping with every excruciating step and mood change with me.

Finally, thanks to my little son Roc. Thank you for the happiness you brought into my life: You really gave me the reason to continue.

The generous financial help of the Generalitat de Catalunya (scholarship FI-DGR) is gratefully acknowledged.

Eva Lagunas Targarona

Notation

π	Pi $\pi = 3.1416$.
j	Imaginary unit $j = \sqrt{-1}$.
$\delta(t)$	Dirac delta function.
$\log(x)$	Natural logarithm function of x.
e^x	Exponential function of x.
$O(\cdot)$	$f(x) \in O(g(x))$ iif $\lim_{x\to\infty} f(x)/g(x)$ equals a constant.
$\mathbb{E}\{\cdot\}$	Expected value.
$\mathbb{R}\mathbf{e}\{\cdot\}$	Real part.
$\mathbb{I}\mathbf{m}\{\cdot\}$	Imaginary part.
a**,a,A**	A scalar, a column vector and a matrix.
$\mathbf{a}(i)$	The i-th entry of vector $\mathbf{a}$.
$\mathbf{A}_{ij}$	The entry of the i-th row and j-th column of matrix $\mathbf{A}$.
$\mathbf{a}^*$**,** $\mathbf{A}^*$	Complex conjugate of vector $\mathbf{a}$, complex conjugate of matrix $\mathbf{A}$.
$\mathbf{a}^T$**,** $\mathbf{A}^T$	Transpose of vector $\mathbf{a}$, transpose of matrix $\mathbf{A}$.
$\mathbf{a}^H$**,** $\mathbf{A}^H$	Complex conjugate and transpose (hermitian) of vector $\mathbf{a}$, complex conjugate and transpose (hermitian) of matrix $\mathbf{A}$.
$\mathbf{A}^{-1}$	Inverse of square matrix $\mathbf{A}$.
$\mathbf{A} \succ 0$	Matrix $\mathbf{A}$ positive definite.
$\mathbf{A} \succeq 0$	Matrix $\mathbf{A}$ positive semidefinite.
$\mathbf{A} \odot \mathbf{B}$	Hadamard product between matrices $\mathbf{A}$ and $\mathbf{B}$, i.e., the element-wise multiplication of their elements.
$\mathbf{A} \otimes \mathbf{B}$	Kronecker product between matrices $\mathbf{A}$ and $\mathbf{B}$.

$\mathbf{Tr}(\mathbf{A})$	Trace of matrix $\mathbf{A}$.
$\mathbf{diag}(\mathbf{a})$	Diagonal matrix whose entries are the elements of vector $\mathbf{a}$.
$\mathbb{R}$	The set of real numbers.
$\mathbb{C}$	The set of complex numbers.
$\mathbb{R}^{n\times m}$	The set of $n \times m$ matrices with real-valued entries.
$\mathbb{C}^{n\times m}$	The set of $n \times m$ matrices with complex-valued entries.
$\mathbf{I}_Q$	Identity matrix of dimension Q.
H_0	Null hypothesis.
H_1	Alternative hypothesis.
arg	Argument.
max	Maximum.
min	Minimum.
$\mathcal{N}(\mu, \sigma^2)$	Gaussian or Normal distribution with mean μ and variance σ^2.
$\lvert a\rvert$	Modulus of scalar a.
$\lVert\mathbf{A}\rVert_F$	Frobenius norm of matrix $\mathbf{A}$ defined as $\sqrt{\mathrm{Tr}(\mathbf{A}^H\mathbf{A})}$
$\lVert\mathbf{a}\rVert_{l_p}$	l_p-norm of vector $\mathbf{a}$: $\lVert\mathbf{a}\rVert_{l_p} = (\sum_{i=1}^{n} \lvert a_i\rvert^p)^{1/p}$.

List of Tables

List of Figures

Contents

Preface

This Ph.D. Thesis has been carried out from July, 2009 to December, 2013, in part at the Department of Signal Theory and Communications, Universitat Politècnica de Catalunya (UPC), Barcelona, Spain, under supervision of Prof. Montserrat Nájar Martón from UPC and in part at the Radar Imaging Lab, Center for Advanced Communications (CAC), Villanova University, PA, USA, under supervision of Prof. Moeness G. Amin, director of CAC.

Contents

This Ph.D. Thesis entitled *Compressive Sensing Based Candidate Detector and its Applications to Spectrum Sensing and Through-the-Wall Radar Imaging* is divided into six chapters. In Chapter 1, the objectives and contributions of this thesis are described. Chapter 2 provides a literature review of the three topics tackled in this thesis: compressive sensing, cognitive radio and through-the-wall radar imaging. The mathematic formulation of the CS-based candidate detector is presented in Chapters 3. The two next chapters examine two applications where the proposed detector proves useful. The detector is applied to spectrum sensing for cognitive radio in Chapter 4, and to Through-Wall Radar Imaging in Chapter 5. Finally, Chapter 6 provides concluding remarks and future work.

Collaborations

Chapter 5 presents work performed during the stay as a Visiting Research Associate at the Center for Advanced Communications (CAC), Villanova University, PA, USA, from November 2011 to April 2012.

Support of the Thesis

This Ph.D. Thesis has been partially supported by the Catalan Government under grant FI-DGR 2010/2011/2012. It has received further support from the Catalan Government under grant 2009 SGR 891, from the European Commission under project FP7 Network of Excellence in Wireless COMmunications NEWCOM++ (ICT-FP7-216715) and NEWCOM# (Grant agreement no. 318306), from the Spanish Ministry of Science and Innovation (Ministerio de Ciencia e Innovación) under projects TEC2008-06327-C03 (MULTI-ADAPTIVE) and TEC2011-29006-C03-02 (GRE3N-LINK-MAC), and from the European Cooperation in Science and Technology under project COST Action IC0902.

The 6-months stay as Visiting Research Associate at the Center for Advanced Communications (CAC), Villanova University, PA, USA, was partially funded by the Spanish Ministry of Education (Ministerio de Educación) under ARGO GLOBAL program.

Papers

Below is a list of original publications that have been produced during the period of Ph.D. candidacy, which are referred to in the text by roman numbers.

Book Chapters

[I] P. Closas, A. Conti, D. Dardari, N. Decarli, E. Falletti, C. Fernández-Prades, M. Reza Gholami, M. Nájar, E. Lagunas, M. Pini, M. Rydström, F. Sottile, E. G. Ström, *Casting Signal Processing to Real-World Data*, Chapter in *Satellite and Terrestrial Radio Positioning Techniques: A Signal Processing Perspective*, edited by D. Dardari, E. Falletti, M. Luise, Oxford, UK: Elsevier Academic Press, 2011. ISBN: 9780123820846.

[II] D. Dardari, M. Di Dio, A. Emmanuele, D. Fontanemma, S. Gezici, M. Reza, M. Kieffer, E. Lagunas, J. Louveaux, A. Mallat, M. Nájar, M. Navarro, M. Nicoli, L. Reggiani, M. Rydström, E. Ström, L. Vanderdorpe, F. Zanier, *Innovative Signal Processing Techniques for Wireless Positioning*, Chapter in *Satellite and Terrestrial Radio Positioning Techniques: A Signal Processing Perspective*, edited by D. Dardari, E. Falletti, M. Luise, Oxford, UK: Elsevier Academic Press, 2011. ISBN: 9780123820846.

Journal Papers

[III] E. Lagunas, M.G.Amin, F.Ahmad, M. Nájar, *Determining Building Interior Structures Using Compressive Sensing*, SPIE Journal of Electronic Imaging, vol. 22, no. 2, Jan 2013.

[IV] E. Lagunas, M.G.Amin, F.Ahmad, M. Nájar, *Joint Wall Mitigation and CS for Indoor Image Reconstruction*, IEEE Trans. on Geoscience and Remote Sensing, vol. 50, no. 12, Dec 2012.

[V] E. Lagunas, M. Nájar, *Sparse Correlation Matching-Based Spectrum Sensing for Open Spectrum Communications*, EURASIP Journal on Advances in Signal Processing, Feb 2012, 2012:31.

Letters

[VI] E. Lagunas, M.G.Amin, F.Ahmad, M. Nájar, *Pattern Matching for Building Feature Extraction*, submitted to IEEE Geoscience and Remote Sensing Letters, Dec 2013.

Conference/Workshop Papers

[**VII**] E. Lagunas, M. Nájar, *Robust Primary User Identification using Compressive Sampling for Cognitive Radios*, submitted to IEEE Int. Conf. Acoustics, Speech and Signal Processing (ICASSP), Nov 2013.

[**VIII**] E. Lagunas, M. Nájar, *Sparsity-Based Primary User Detection for Cognitive Radio*, 4th COST Action IC0902 Workshop: Cognitive Radio and Networking for Cooperative Coexistence of Heterogeneous Wireless Networks, Rome, Italy, Oct 9-11, 2013.

[**IX**] E. Lagunas, M.G.Amin, F.Ahmad, M. Nájar, *Correlation Matching Approach for Through-Wall Corner Detection*, Int. Workshop on Compressive Sensing Applied to Radar (CoSeRa), Bonn, Germany, Sep 2013.

[**X**] E. Lagunas and M. Nájar, *Compressive Spectrum Sensing Based on Spectral Feature Detection*, Cognitive Radio Advances, Applications and Future Emerging Technologies (CRAFT) Workshop, International Symposium on Wireless Communication Systems (ISWCS), Ilmenau, Germany, Aug 2013.

[**XI**] E. Lagunas, M.G.Amin, F.Ahmad, M. Nájar, *Improved Interior Wall Detection Using Designated Dictionaries in Compressive Urban Sensing Problems*, SPIE Symposium on Defense, Security, and Sensing, Compressive Sensing Conference, Baltimore, MD, Apr 2013.

[**XII**] E. Lagunas and M. Nájar, *Spectral Feature Detection for Spectrum Sensing*, in Proceedings of Barcelona Forum on Ph.D. Research in Information and Communication Technologies, Barcelona, Spain, Oct 2012.

[**XIII**] E. Lagunas, M.G.Amin, F.Ahmad, M. Nájar, *Sparsity-Based Radar Imaging of Building Structures*, European Signal Processing Conference (EUSIPCO), Bucharest, Romania, Aug 27-31, 2012.

[**XIV**] E. Lagunas, M.G.Amin, F.Ahmad, M. Nájar, *Wall Clutter Mitigation based on L1 Norm Range Reconstruction for Through the Wall Radar Imaging Application*, International Conference On Information Science, Signal Processing and their Applications (ISSPA), Montreal, Canada, Jul 3-5, 2012.

[**XV**][1]E. Lagunas, M.G.Amin, F.Ahmad, M. Nájar, *Wall Mitigation Techniques for Indoor Sensing within the Compressive Sensing Framework*, IEEE Sensor Array and Multichannel Signal Processing Workshop (SAM), New York, USA, Jun 17-20, 2012.

[**XVI**] E. Lagunas, M. Nájar, *New Sparse Spectral Estimation based on Correlation Matching for Spectrum Sensing*, 2nd COST Action IC0902 Workshop: Cognitive Radio and Networking for Cooperative Coexistence of Heterogeneous Wireless Networks, Castelldefels, Spain, Oct 5-7, 2011.

[**XVII**] E. Lagunas and M. Nájar, *Sparse Channel Estimation based on Compressed Sensing for Ultra WideBand Systems*, in IEEE Int. Conference on Ultra WideBand (ICUWB), Bologna, Italy, Sep 14-16, 2011.

[1]The paper won the $1000 Cash Award at the 2012 IEEE Sensor Array and Multichannel Signal Processing Workshop. A total of 136 papers were presented at the Conference.

[**XVIII**] E. Lagunas, M. Nájar and M.A. Lagunas, *Space-Time-Frequency candidate Methods for Spectrum Sensing*, European Signal Processing Conference (EUSIPCO), Barcelona, Spain, Aug 29 - Sep 2, 2011.

[**XIX**] E. Lagunas, M. Nájar, *Spectrum Sensing based on Correlation Matching: 2D Candidate Methods*, 1st Int. Summer School on Cognitive Wireless Communications, Florence, Italy, Jul 12-15, 2011.

[**XX**] E. Lagunas, M. Nájar and M. Navarro, *Joint TOA and DOA Estimation Compliant with IEEE 802.15.4a Standard*, in IEEE International Symposium on Wireless Pervasive Computing (ISWPC), Modena, Italy, May 5-7, 2010.

[**XXI**] E. Lagunas, L. Taponecco, M. Nájar and A. D'Amico, *TOA Estimation in UWB: Comparison between Time and Frequency Domain Processing*, in 2nd International ICST Conference on Mobile Lightweight Wireless Systems (MOBILIGHT), Barcelona, Spain, May 10-12, 2010.

[**XXII**] A. Dhital, P. Closas, C. Fernández, J. Arribas, F. Sotille, M.A. Spirito, Z. Xiong, E. Lagunas and M. Nájar, *Evaluation of Tracking Algorithms using the NEWCOM++ WPRB Database Measurements*, in Future Network and Mobile Summit (FUNEMS) within the NewCom++ Dissemination Day, Florence, Italy, Jun 16-18, 2010.

[**XXIII**] F. Sottile, M.A. Spirito, P. Closas, J. Arribas, C. Fernández, M. Nájar, E. Lagunas, D. Dardari, N. Decarli, A. Conti and M. Guerra, *Evaluation of Tracking Algorithms using Heterogeneous Technologies*, in IEEE GLOBECOM 2010, Miami, Florida, Dec 6-10, 2010.

[**XXIV**] E. Lagunas, M. Nájar and M. Navarro, *UWB Joint TOA and DOA estimation*, in IEEE International Conference on UWB, Vancouver, Canada, Sep 9-11, 2009.

Project Deliverables

[**XXV**] T. Pedersen, G. Steinböck (AAU); S. Gezici (BILKENT); E. G. Ström, M. Rydstrom, M. Gholami (CHALMERS); D. Dardari (CNIT-BO); M. Nicoli, D. Fontanella, L. Reggiani (CNIT-MI); U. Mengali, A. D'Amico, G. Tiberi, A. Monorchio (CNIT-PI); J. Arribas, P. Closas, C. Fernández (CTTC); E. Falletti, F. Sottile, M. Caceres (ISMB); A. Mallat, P. Gérard, J. Louveaux, F. Keshmiri, C. Craeye, L. Vandendorpe (UCL); M. Nájar, E. Lagunas (UPC), *NewCom++ Deliver number 3 (DB.3): Progress Report II on Advanced Localization and Positioning Techinques: Data Fusion and Applications.*, Dec, 2010. Online in: http://www.newcom-project.eu/public-deliverables.

[**XXVI**] T. Pedersen, G. Steinböck (AAU); S. Gezici (BILKENT); E. G. Ström, M. Rydstrom, M. Gholami (CHALMERS); D. Dardari (CNIT-BO); M. Nicoli, D. Fontanella, L. Reggiani (CNIT-MI); F. Montorsi, S. Sergi (CNIT-MORE); G. Bacci, M. Di Dio, A. Emmanuele, M. Luise (CNIT-PI); P. Closas, C. Fernández-Prades, J. Arribas (CTTC); E. Falletti, F. Sottile, M. Caceres (ISMB); A. Mallat, P. Gérard, J. Louveaux, F. Keshmiri, C. Craeye, L. Vandendorpe (UCL); M. Nájar, E. Lagunas, A. Dhital (UPC), *NewCom++ Deliverable number 4 (DB.4): Final Report: Seamless Positioning Techniques inWireless Communications.*, Nov, 2009. Online in: http://www.newcom-project.eu/public-deliverables.

Ms.C. Thesis

[**XXVII**] E. Lagunas, *Sparse Channel Estimation based on Compressive Sensing for UWB Systems*, MSc Thesis, Universitat Politècnica de Catalunya (UPC), Barcelona, Spain, Jul, 2009.

Chapter 1

Introduction

Compressed Sensing (CS) is a signal processing technique for efficiently acquiring and reconstructing a signal which takes advantage of the signal's sparseness or compressibility in some domain, allowing the entire signal to be determined from relatively few measurements. The present thesis surveys the CS theory applied to signal detection, estimation and classification, which not necessary requires perfect signal reconstruction or approximation. In particular, a novel CS-based detection technique which exploits prior information about some features of the signal is presented. The basic idea is to scan the domain where the signal is expected to lie with a candidate signal estimated from the known features. The proposed detector is called candidate detector because their main goal is to react only when the candidate signal is present. We examine two applications where the CS-based candidate detector proves useful: spectrum sensing for Cognitive Radio and Through-the-Wall Radar Imaging (TWRI). First, we address the problem of monitoring the licensed holder activity in open spectrum communications. CS has been successfully applied to alleviate the sampling bottleneck in wideband spectrum sensing leveraging the sparsity described by the low spectral occupancy of the licensed radios. The sparsity can also be used to increase the accuracy of the detections by using sparsity-based recovery methods. The second application focuses on the desire to see inside walls and urban structures such as buildings. TWRI is an emerging technology which provides vision into optically obscured areas for situation awareness. High resolution imaging is associated with large bandwidth signals and long array apertures. However, this demands acquisition and processing of large amounts of data. When the target scene can be considered sparse, i.e., the number of targets is small compared to the scene dimensions, CS can be a very effective approach to compress while sampling. Besides expediting data acquisition and alleviating processing bottlenecks, using few measurements to generate a high-resolution image in TWRI is important logistically, as some of the data observations in time, space and frequency can be difficult or impossible to attain. Such difficulty may be attributed to interference within a frequency band or at specific frequencies, and also due to the inability of the EM waves to reach the behind-the-wall scene from certain aspect angles.

1.1 Objectives and contributions

The main objectives and contributions of this thesis are summarized below.

- **General formulation:** The main goal of this thesis is to provide a complete and general mathematical formulation of the CS-based candidate detector. The detector

will be firstly presented in the raw data domain and, secondly, it will be applied in a second order statistic domain, such as the correlation domain. In both cases, the basic idea is to match a candidate or reference signal/correlation with the collected data.

- **Two possible matching strategies:** We define two different strategies to do the matching between the candidate and the received data. The conventional approach to resolve the matching problem is to perform a matched filter reconstruction for every possible locations of the scanning grid. A detection occurs then at the locations of maxima in the scanning grid. Generally, potential targets cover a small part of the total scanning grid. The detection problem can then be linearized over a set of possible hypothesis by construction of an overcomplete dictionary of candidates and solved using CS-based recovery techniques. In contrast to the matched filtering approach, the overcomplete dictionary of candidates allow all possible hypothesis to be evaluated jointly in a global unified optimization framework.

- **Interference rejection:** The main contribution of this thesis is the interference rejection capabilities of the proposed detector when presented in the correlation domain. The proposed detector is called candidate detector because their main goal is to react only when the candidate signal is present. CS-based detection literature has thus far assumed that the observable data can be represented as a linear combination of candidate signals corrupted by noise. In this thesis, we face a more general problem where the compressive measurements capture the entire signal space, including possible undesired interference. The presence of interference in the CS model has been shown to significantly affect the performance of conventional CS-based detection techniques. In this thesis, the intereference problem is solved in the matching stage through appropriate choices of the matching error function in the matched filtering approach and through weighted sparsity constraint when solving the CS optimization problem.

- **Applications:** The CS-based candidate detector will be applied to two topical detection problems in order to prove its effectiveness. First, the candidate detector is applied to primary user detection in spectrum sensing for open spectrum scenarios. The second application is Through-the-Wall Radar Imaging.

  - **Spectrum sensing:** CS is a powerful technique for accurately detect the existence of primary users from a reduced number of measurements by exploiting the sparsity described by active primary users. In practical settings, primary signals must be detected even with the presence of low-regulated transmissions from secondary systems. Capitalizing on the sparsity described by licensed users, we successfully apply the proposed detector for primary user's spectrum identification, providing an accurate estimation of the frequency support and other characteristics of the primary users. Supporting MATLAB®-based simulation results that assert the effectiveness in primary user detection and proved the interference rejection capabilities are presented.
  - **Through-the-wall radar imaging:**
    - **Wall mitigation:** Wall mitigation in conjunction with CS has never been considered in the literature. That is, CS was applied to TWRI, already assuming prior and complete removal of the front wall EM returns. Without this assumption, strong wall clutter, which extends along the range dimension, reduces the sparsity of the scene and, as such, impedes the application of CS.

In this section, we examine the performance of conventional wall mitigation techniques in conjunction with sparse image reconstruction. Using real data, collected in a laboratory environment with a stepped-frequency radar, we show that these methods maintain proper performance when acting on reduced data measurements. In applying CS reconstruction, we use prior knowledge of the standoff distance from the wall to speed up the convergence of the CS-based reconstruction algorithms.

* **Imaging of building interior structure:** We address imaging of the interior structure of a building using a reduced number of measurements. The objective is to exploit prior information of construction practices together with either the sparsity described by the features or by the sparsity of the scene, to use the proposed detector to determine building layouts. We make use of prior information about building construction practices to form an appropriate sparse representation of the building interior layout. In a first approach, a sparsifying dictionary based on the expected wall alignment relative to the radar's scan direction was designed and used to detect interior walls parallel to the front wall. A follow-on step consists on employing a sparsifying dictionary based on the possible corner reflector locations to detect the wall-wall junctions along the detected parallel walls, in order to determine the wall extents and detect walls perpendicular to the front wall. Results based on computer simulations will be presented, which show that the proposed method provides reliable determination of building layouts, while achieving substantial reduction in data volume.
  Assuming flexibility in radar operation, which allows proper angular radar illuminations, thereby avoiding the front wall returns and preserving the corner features created by the junction of walls, we propose an image pattern matching strategy, which is based on a novel type of image descriptor, namely, the correlogram. The known correlogram of the scattering response of an isolated canonical corner reflector will be used as candidate in the detector. Simulation results demonstrated that the proposed method effectively detects the corner reflectors.

Chapter 2

Background

In this Ph.D. thesis we consider two different detection scenarios where CS proves useful: The problem of spectrum sensing for cognitive radio applications and the problem of through-the-wall radar imaging. The purpose of this chapter is to introduce the basics of CS together with the fundamental ideas of the two mentioned applications.

2.1 Compressive sensing

2.1.1 Conventional sensing: The Nyquist sampling theorem

Signal acquisition is a main topic in signal processing. Sampling theorems provide the bridge between the continuous and the discrete-time worlds. The most famous theorem is often attributed to Shannon [4, 5] (but usually called Nyquist theorem) and states that the sampling rate must be twice the maximum frequency present in the signal in order to perfectly recover the signal. In the field of data conversion, standard analog-to-digital converter (ADC) technology implements the usual quantized Shannon representation: the signal is uniformly sampled at or above the Nyquist rate. For many signals the Nyquist rate can be very high, thus, very large number of samples need to be acquired, leading to impractical and costly designs. However, sampling at the Nyquist rate is shown to be inefficient when the signals of interest contain only a small number of significant frequencies relative to the bandlimit [6]. To alleviate the strong hardware requirements of the ADCs as well as the subsequent storage and processing bottlenecks, a promising alternative for this type of sparse signals is the use of sub-Nyquist sampling techniques.

In this context, in 2004 appeared the Compressed Sensing (CS) concept [7, 8], a novel sampling paradigm that goes further than Shannon-Nyquist's theorem. CS allows to compress signals with sparse or compressible representation while they are sampled. It originates from the idea that it is not necessary to invest a lot of power into observing the entries of a sparse signal because most of them will be zero. Considering a sparse signal, it should be possible to collect only a small number of measurements that still allow for reconstruction.

As it is explained in [7], most of the data acquired by modern systems and technologies can be thrown away with almost no perceptual lost. This phenomenon raises very natural questions: why to acquire all the data when most of that will be thrown away? why don't we try to just directly mesure the part that will not be thrown away?

2.1.2 Fundamentals of compressive sensing

A tutorial overview of some of the foundational developments in CS can be found in [9–11], and a large collection of the vastly growing research literature on the subject is available on the web page **http://www.compressedsensing.com**.

CS theory states that a sparsely representable signal can be reconstructed using very few number of measurements compared to the signal dimension [7–9]. In order to briefly review the main ideas of CS, consider the following finite length, discrete time signal $\mathbf{x} \in \mathbb{C}^L$. Representing a signal involves the choice of a *dictionary*, which is the set of elementary waveforms used to decompose the signal. Sparsity of a signal is defined as the number of non-zero elements in signal under some representation. A signal is said to have a sparse representation over a known dictionary $\boldsymbol{\Psi} = \begin{bmatrix}\boldsymbol{\psi}_0 & \boldsymbol{\psi}_1 & \cdots & \boldsymbol{\psi}_{M-1}\end{bmatrix}$, with $\boldsymbol{\psi}_m \in \mathbb{C}^{L\times 1}$, if there exists a sparse vector $\boldsymbol{\theta} = \begin{bmatrix}\theta_0 & \theta_1 & \cdots & \theta_{M-1}\end{bmatrix}^T$ such that,

$$\mathbf{x} = \sum_{m=1}^{M-1} \boldsymbol{\psi}_m \theta_m \tag{2.1}$$

Or using matrix notation,

$$\mathbf{x} = \boldsymbol{\Psi}\boldsymbol{\theta} \tag{2.2}$$

with $\|\boldsymbol{\theta}\|_{l_0} = K << M$. The l_0-norm used here simply counts the number of non-zero components in $\boldsymbol{\theta}$[1]. A dictionary that leads to sparse representations can either be chosen as a prespecified set of functions or designed by adapting its content to fit a given set of signal examples [12]. Choosing a prespecified transform matrix is appealing because it is simpler. In this thesis we will only consider prespecified dictionaries.

The framework of CS aims at recovering the unknown vector $\mathbf{x}$ from an underdetermined system of linear equations,

$$\mathbf{y} = \boldsymbol{\Phi}\mathbf{x} \tag{2.3}$$

where $\boldsymbol{y} \in \mathbb{C}^{\kappa\times 1}$ is the received data vector and matrix $\boldsymbol{\Phi} \in \mathbb{C}^{\kappa\times L}$ with $K < \kappa < L$ is the sub-sampling matrix or *sensing* matrix since the number of rows is less than the number of columns. Since $\kappa < L$, this system has more unknowns than equations, and thus the system is not invertible. In particular, equation (2.3) has infinitely many solutions. Among the infinitely many solutions of (2.3), we are only interested in the sparsest one. If we know a priori that our original signal $\boldsymbol{\theta}$ is sparse, then the most natural choice will be to find a vector with least non-zero entries,

$$\min_{\boldsymbol{\theta}} \|\boldsymbol{\theta}\|_{l_0} \quad \text{subject to} \quad \mathbf{y} \approx \boldsymbol{\Phi}\boldsymbol{\Psi}\boldsymbol{\theta} \tag{2.4}$$

This is an NP-complete problem, which basically means that it requires an exhaustive search and, in general, it is not a feasible problem.

Special cases of interest for convexity are all the l_p-norms for $p \geq 1$. Among them, l_1-norm is very interesting and popular due to its tendency to sparsify the solution. Chen et al. [13] stated that the sparse signal $\boldsymbol{\theta}$ can be recovered from only $\kappa = O(K\log(L/K))$ linear non-adaptive measurements by solving the following relaxation of (2.4),

$$\min_{\boldsymbol{\theta}} \|\boldsymbol{\theta}\|_{l_1} \quad \text{subject to} \quad \mathbf{y} \approx \boldsymbol{\Phi}\boldsymbol{\Psi}\boldsymbol{\theta} \tag{2.5}$$

[1] l_p-norms are no longer formal norms for $p < 1$. Nevertheless, in this thesis the term $\|\cdot\|_{l_0}$ is used as a norm keeping in mind this reservation

where $\|\boldsymbol{\theta}\|_{l_1} = \sum_i |\theta_i|$. Several methods are available in the literature to solve the optimization problem in (2.5). The l_1-minimization is a convex problem and can be recast as a linear program (LP) [14]. This is the foundation for the Basis Pursuit (BP) techniques [8, 10, 13]. Alternatively, greedy methods, known as Matching Pursuit (MP), can be used to solve (2.5) iteratively [15,16]. The design of reconstruction algorithms to efficiently and accurately solve (2.5) is an open problem which is currently very topical in the scientific community.

Another problem in CS consist of designing a convenient measurement matrix $\boldsymbol{\Phi}$ such that salient information in any compressible signal is not damaged by the dimensionality reduction. Work on CS thus far assumed that $\boldsymbol{\Phi}$ is drawn at random, which simplifies its theoretical analysis, and also facilitates a simple implementation [17]. The CS reconstruction performance can be substantially improved by optimizing the choice of $\boldsymbol{\Phi}$ [18]. In general, the relationship between the sensing matrix ($\boldsymbol{\Phi}$) and signal model ($\boldsymbol{\Psi}$) affects the number of measurements required to reconstruct a sparse signal. Almost all theory of CS is based on the assumption that $\mathbf{D} = \boldsymbol{\Phi}\boldsymbol{\Psi}$ is the concatenation of two orthogonal matrices. These theories follow the uncertainty principle which says that a signal cannot be sparsely represented both in $\boldsymbol{\Phi}$ and $\boldsymbol{\Psi}$ [19]. This claim depends on the similarity between $\boldsymbol{\Phi}$ and $\boldsymbol{\Psi}$. A rough characterization of the degree of similarity between the sparsity and measurement systems is given by the *mutual coherence*, which is given by,

$$\mu(\boldsymbol{\Phi}, \boldsymbol{\Psi}) = \max_{\substack{i,j \\ i \neq j}} \frac{\left|\boldsymbol{\phi}_i^H \boldsymbol{\psi}_j\right|}{\|\boldsymbol{\phi}_i\|_{l_2} \cdot \left\|\boldsymbol{\psi}_j\right\|_{l_2}} \tag{2.6}$$

In other words, $\mathbf{D}$ is desired to have columns $\mathbf{d}_i, i = 1, \ldots, N$ with small correlations. A explicit example of matrices which have small coherence is the concatenation of the Identity and Fourier matrices.

Another suitable way to describe μ is to compute the Gram matrix $\mathbf{G} = \tilde{\boldsymbol{D}}^T \tilde{\boldsymbol{D}}$, using the matrix $\mathbf{D}$ after normalizing each of its columns ($\tilde{\boldsymbol{D}}$). The *mutual coherence* is given in this case by the off-diagonal entry of $\mathbf{G}$ with largest magnitude.

On the other hand, another criterion for evaluating the quality of a CS matrices that are nearly orthonormal, is the restricted isometry property (RIP) introduced in [10] by Candés, Romberg and Tao (which they initially called the uniform uncertainty principle). RIP is a sufficient condition on $\tilde{\boldsymbol{D}}$ for exact recovery of a K-sparse $\boldsymbol{\theta}$.

The matrix $\tilde{\boldsymbol{D}}$ satisfies RIP of order $s \in \mathbb{N}$, $s < L$, if there exist an isometry constant $0 < \delta_s < 1$ such that,

$$(1 - \delta_s) \|\boldsymbol{\theta}\|_{l_2}^2 \leq \left\|\tilde{\boldsymbol{D}}\boldsymbol{\theta}\right\|_{l_2}^2 \leq (1 + \delta_s) \|\boldsymbol{\theta}\|_{l_2}^2 \tag{2.7}$$

holds for all s-sparse vectors. δ_s is the smallest number satisfying (2.7). However, working with the RIP condition is much more complex compared to the simple coherence concept since for a given matrix checking the validity of RIP condition is an NP-complete problem itself.

Current CS theory only applies when the dictionary is an orthonormal basis, or when the columns of $\boldsymbol{D}$ are extremely uncorrelated. However, there are numerous practical examples in which there exist coherence between the sparsifying basis and sensing matrix. Sparsity is sometimes expressed in terms of an overcomplete dictionary, i.e., $\boldsymbol{\Psi}$ has many more columns than rows ($L < M$) [20], which inevitably generates coherence between dictionary's waveforms. Recent publications [21] showed that CS and recovery via l_1-norm minimization is also viable in the context of overcomplete and coherent dictionaries. Through this thesis,

we will face sparsifying basis that are redundant and have correlation between its columns $\mathbf{d}_i, i = 1, \ldots, N$.

2.1.3 CS-based reconstruction methods

The RIP provides the theoretical basis to not damage the compressed samples, but it does not tell us how to recover the sparse vector. We now focus on solving the CS recovery problem presented in (2.5).

As previously noted, the l_1-norm minimization approach proposed in (2.5) can be solved with LP methods, which are often not optimally fast. An alternative approach is the use of greedy algorithms or MP, which calculate the support of the signal iteratively. These greedy algorithms are computationally fast but have lacked both stability and uniform guarantees.

A summary of reconstruction algorithms for CS is listed below.

1. **Greedy Pursuit:** They are composed of two steps per iteration: the selection of an atom and the update of the solution from the selected atoms. Many different methods appear as a result of different selection/updating step. In general, a more sophisticated selection/updating step often performs better, but at the price of a higher computational cost. This section presents an overview of the existing algorithms.

    - **Matching Pursuit (MP):** Introduced in 1993 [15], at each iteration of the algorithm, it chooses dictionary elements in a greedy fashion that best aproximates the signal.
    - **Orthogonal Matching Pursuit (OMP):** First introduced in [22], it is an improvement on conventional MP which instead of taking the inner product of the residual and the selected atom to get the coefficient weight (as conventional MP does), it fits the original signal to all the already selected dictionary elements.
    - **Stagewise Orthogonal Matching Pursuit (StOMP):** Introduced in [23] in 2007, is an improvement of OMP that allows multiple coefficients to be added in a single iteration.
    - **Gradient Pursuit (GP):** Introduced in [24] in 2008, instead of selecting the atom which has largest inner product with the residual, it takes a particular direction to update the model.
    - **COmpressive SAmpling Matching Pursuit (CoSaMP):** Introduced in [25] in 2008, is an extension of OMP. It was shown to have tighter bounds on its convergence and performance.
    - **Iterative (Hard/Soft) Thresholding:** At each iteration, they perform some thresholding function that acts on the output of the previous iterate.

2. **Denoising Methods:** When noise is present, i.e., $\mathbf{y} = \mathbf{D}\boldsymbol{\theta} + \mathbf{w}$ where $\mathbf{w}$ is bounded or Gaussian noise, there are two well-known l_1-norm minimization methods. Both are controlled by the regularization parameter λ, which is a threshold parameter that essentially controls the trade-off between the sparsity of the solution and its fidelity to the measurements.

    - **Basis Pursuit Denoising (BPDN) or Least Absolute Shrinkage and Selection Operator (LASSO):** Proposed by Tibshirani in 1996 [26], it refers to

the solution of

$$\min_{\boldsymbol{\theta}} \frac{1}{2} \|\mathbf{y} - \mathbf{D}\boldsymbol{\theta}\|_{l_2}^2 + \lambda \|\boldsymbol{\theta}\|_{l_1} \tag{2.8}$$

where the term $\|\cdot\|_{l_2}$ keeps the solution close to the measurements. The solution to (2.8) yields good numerical results and has strong theoretical guarantees [27].

- **Dantzig Selector (DS):** Introduced in [28], it solves the following optimization problem,

$$\min_{\boldsymbol{\theta}} \|\boldsymbol{\theta}\|_{l_1} \quad \text{subject to} \quad \left\|\mathbf{D}^H(\mathbf{D}\boldsymbol{\theta} - \mathbf{y})\right\|_{l_\infty} \leq \lambda\sigma_w \tag{2.9}$$

where $\lambda > 0$, σ_w is the standard deviation of the noise and $\|\cdot\|_{l_\infty}$ is the supremum norm defined as $\|\boldsymbol{\theta}\|_{l_\infty} = \max_i |\boldsymbol{\theta}_i|$. It is a convex problem and can be recast as LP.

The value of $\|\boldsymbol{\theta}\|_{l_0}$, i.e., the sparsity level K, is commonly assumed to be known in some of the recovery algorithms. For example, the OMP is typically run for K iterations or the regularization parameter of LASSO is examined over a limited range of values which is a function of K. Moreover, the value of $\|\boldsymbol{\theta}\|_{l_0}$ is sometimes used to estimate the minimum number of measurements required to perfectly recover the original signal. For instance, for very specific models such as the Gaussian sensing matrices, it is known that on the order of $\kappa = C \cdot 2K \log(L/2K))$ samples are sufficient for stable recovery, where C refers to a positive, universal constant [25]. Anyhow, is clear that $\|\boldsymbol{\theta}\|_{l_0}$ plays an important theoretical role in many aspects of CS. However, it is typically unknown in practice.

Current reconstruction algorithms such as the DS generally assume a prior knowledge of the error variance and/or the signal sparsity. These information about the noise magnitude and the sparsity is also used to establish a stopping criterion in greedy pursuit methods. If these parameters are set incorrectly, the quality of the reconstructed signal significantly decreases. There exist some works that try to overcome the mentioned drawbacks. In [29], an estimate of these parameters is obtained by dividing the data set into a training/estimation set. In [30], an algorithm is proposed to estimate an approaximation of sparsity level. In the present thesis, we do not assume any prior information about the sparsity and neither about the noise/interference level.

2.1.4 Incomplete dictionaries: Interference

This section focuses on the construction of appropriate prespecified dictionaries. As stated before, in this thesis we consider an overcomplete dictionary matrix $\boldsymbol{\Psi} \in \mathbb{C}^{L \times M}$, $L < M$, which contains M prototype signal atoms for columns $\left\{\boldsymbol{\psi}_j\right\}_{j=0}^{M-1}$. In other words, the overcomplete dictionary $\boldsymbol{\Psi}$ incorporate multiple patterns or candidates. Increasing the value of M improves the sparseness of $\boldsymbol{\theta}$, but it also increases the mutual coherence and the computational complexity of the reconstruction process. On the other hand, making the value of M too small might introduce substantial bias into the estimate of $\boldsymbol{\theta}$.

In general, it is assumed that the signal of interest $\mathbf{x}$ can be represented as a linear combination of these atoms, either exact ($\mathbf{x} = \boldsymbol{\Psi}\boldsymbol{\theta}$) or corrupted by AWGN or bounded noise ($\mathbf{x} = \boldsymbol{\Psi}\boldsymbol{\theta} + \boldsymbol{\eta}$). However, there are some cases where the overcomplete dictionary do not well represent the observed signal. The compressive measurements capture the entire signal space, which often includes undesired interference. Very little has been done to investigate alternative CS-based reconstruction algorithms dealing with models contaminated with interference. Moreover, the presence of interference in the CS has been shown to significantly affect the

performance of algorithms such as those described in the previous section [31]. There are two main strategies for dealing with interference, namely avoiding and canceling methods. One solution would be to simply ignore the corrupted measurements. Having access to the exact location of the corrupted measurements, however, is not always possible in practical applications. There are few approaches which successfully mitigate the interference contribution assuming some prior information about the interference. Assuming that the interfering signals lie in a known subspace, [32] proposed to remove the unwanted signal components from the compressive measurements before further processing. The same prior information is assumed in [33, 34], where a compressive sampling strategy and an algorithm are derived, respectively, to effectively null out the interference. To the best of our knowledge, interference mitigation in conjunction with CS assuming no prior information about the interference has never been considered in the literature.

2.1.5 Weighted l_1-norm minimization

In 2008, Candes and Wakin noted in [35] that the use of the l_1-norm heavily penalizes the large coeffients than the smaller coefficients, unlike the more democratic penalization of the l_0-norm. To address this magnitude dependence, they proposed an alternative weighted formulation of l_1-norm minimization. The weighted l_1-norm is defined as,

$$\sum_{m=0}^{M-1} w_m \left|\theta_m\right| \tag{2.10}$$

where $w_0, w_1, \ldots, w_{M-1}$ are positive weights. In the sequel, we will sometimes denote the weighted l_1-norm by $\mathbf{W}\boldsymbol{\theta}$, where $\mathbf{W}$ is the diagonal matrix with $w_0, w_1, \ldots, w_{M-1}$ on the diagonal and zeros elsewhere. In general, the weights must be large for encourging near-zero entries and small for discouraging nonzero entries. In other words, the weights should relate inversely to the true signal magnitudes. Since information about the true location and magnitude of the nonzero entries is not available a priori, common approaches select the weights iteratively [35, 36].

2.1.6 Analog-to-information conversion: Implementation issues

By leveraging the CS theory, an analog-to-information converter (AIC) can be designed to acquire samples at a lower rate while successfully recovering the compressible signal of interest. CS seems clear with the matrix notation, but as in many others signal processing techniques, the implementation in real systems involves certain difficulties. Three methods will be discussed below:

- **Random Demodulator:** A practical AIC architecture was presented in [1] in 2006. The input signal is multiplied by a pseudo random sequence which spreads the information across the entire spectrum. A low pass filter is then applied to capture a smaller part of the signal which is later sampled at a lower rate. The actual implementation is shown in Fig. 2.1.

- **Multi-Coset sampling (MC):** MC sampling implements sub-Nyquist periodic nonuniform sampling strategy [37, 38]. Instead of implementing a single ADC at a high-rate R, interleaved ADCs use L devices at rate R/L with appropiate time shifts. A possible implementation of the MC sampler is depicted in Fig. 2.2.

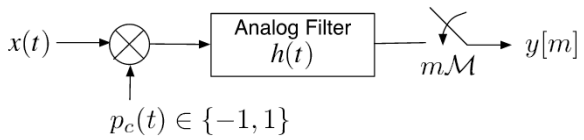

FIGURE 2.1: Block diagram of Random Demodulator extracted from [1]

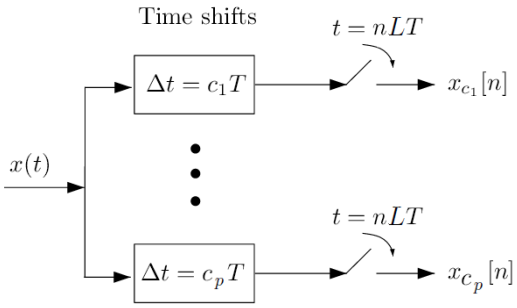

FIGURE 2.2: Block diagram of MC sampling extracted from [2]

- **Modulated Wideband Converter (MWC):** Mishali et al. proposed an alternative to MC sampling in 2010 [2], which follows the principles of Xsampling [39]. It first multiplies the analog signal by a bank of periodic waveforms. The output is lowpass filtered and sampled uniformly at low rate, which is orders of magnitude smaller than Nyquist. The resulting system is shown in Fig. 2.3.

2.1.7 Applications of compressive sensing

CS can be potentially used in all applications where the task is the reconstruction of a signal or an image from a small set of linear measurements.

The field of compressive sensing has had a great impact on radar/sonar applications [40]. Many radar processing tasks can be posed as finding sparse solutions to underdetermined linear equations. The resolution in radar, sonar and similar imaging systems is limited by classical time-frequency uncertainty principles. The suppression of image sidelobes by l_1-norm or greedy recovery algorithms provide better resolution over classical radar. However, super-resolution usually implies large mutual coherence. One interesting applications of CS is in Magnetic Resonance Imaging (MRI). MRI is a medical imaging technique used in radiology to visualize internal structures of the body in detail. However, it is burdened by an inherently slow data acquistion process. CS aims to reduce the time of acquisition by reducing the number of acquired samples. For more information on CS-based MRI refer to [41] and the references therein.

In communications, the wireless channel can often be modeled as a sparse channel in which the delay spread could be very large, but the number of significant paths is normally very small. The prior knowledge of the channel sparseness can be effectively use to improve the channel estimation using the CS theory. In previous author's publication **[XVII]**-**[XXVII]**, the use of CS was examined in the estimation of highly sparse channel by means of a new sparse channel estimation approach based on the frequency domain model of the UWB signal. UWB is a leading technology for freeing people from wires, enabling wireless connection

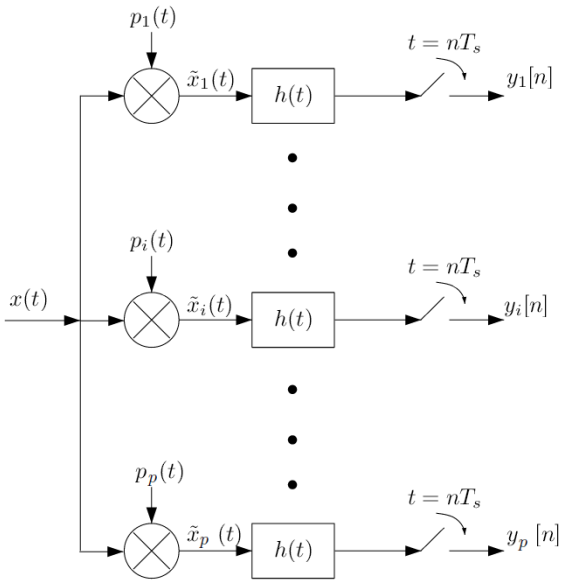

FIGURE 2.3: Block diagram of MWC sampling extracted from [2]

of multiple devices for transmission of video, audio and other high-bandwidth data. The transmision of ultrashort pulses in UWB leads to several desirable characteristics such as the rich multipath diversity introduced by the large number of propagation paths existing in a UWB channel. The rich multipath coupled with the fine time resolution of UWB create a challenging channel estimation problem. Fortunately, multipath wireless channels tend to exhibit impulse responses dominated by a relatively small number of clusters of significant paths, especially when operating at large bandwidths. It was shown that conventional channel estimation methods provide higher errors because they ignore the prior knowledge of the sparseness UWB channel.

Seismic data collection is another expensive and time consuming process where CS has been shown to be usefull by making the whole process faster and cheaper [42].

Summarizing, CS is a very general concept reported to be adaptable to a tremendous amount of applications covering astronomy, radars, seismology, satellite telemetry, etc. In this thesis we restrict our attention to only two of them, namely sparse spectrum sensing and compressive urban sensing.

2.2 Cognitive Radio: the intelligent spectrum management

2.2.1 Spectrum scarcity

Current spectrum division among users in wireless communication systems is assigned by regulatory and licensing bodies like the Federal Communication Commission[2] (FCC) in the US or the European Telecommunications Standard Institute[3] (ETSI) in Europe. In the usual spectrum management approach, the radio spectrum is divided into fixed and non-overlapping blocks, which are assigned to different services and wireless technologies. Thus,

[2]http://www.fcc.gov/
[3]http://www.etsi.org/

the assigned spectrum is completely controlled by the regulatory body that owns this portion of spectrum and therefore it can unilaterally manage interference between its users and hence their Quality of Service (QoS).

On the other hand, the recent proliferation of wireless communications systems has made the problem of spectrum utilization more critical than ever. The rapid growth of wireless systems together with the inflexible spectrum regulations have resulted in a crowded radio frequency (RF) spectrum. As a consequence, the availability of wireless spectrum has become severally limited to the extent that almost all frequency bands have been assigned. The spectrum scarcity is evident by a glance at the National Telecommunications and Information Administration's frequency allocation chart, which is shown in Fig. 2.4. The spectrum chart seems to indicate a high degree of spectrum utilization but we will soon see that what really happens is completely the opposite.

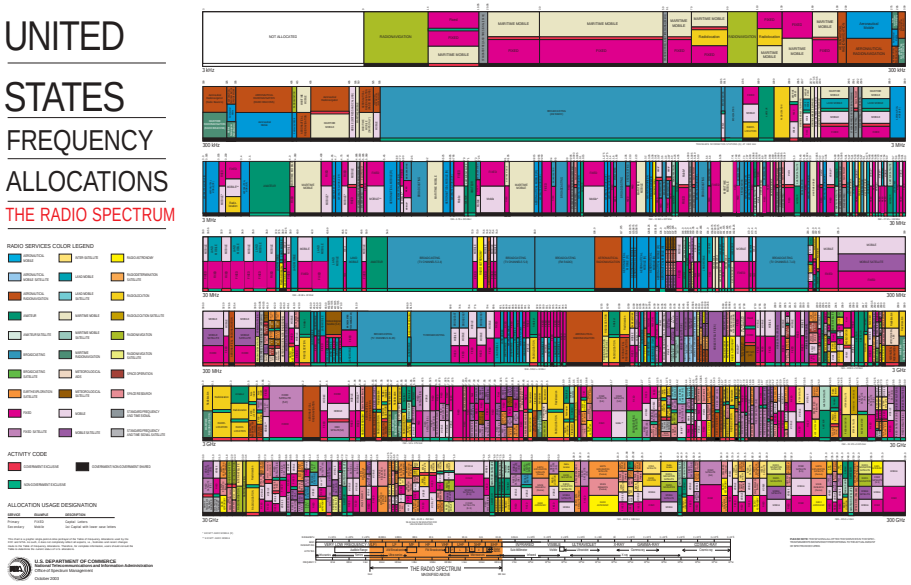

FIGURE 2.4: United States frequency allocation chart

Another consequence of the scarsity of the spectrum is the exorbitant prices currently paid at auction for desirable frequency bands. The radio spectrum is among the most expensive resources around the world. Just as an example, Fig. 2.5 shows how the European 3G spectrum auction yielded multibillion dollars for a merely 20MHz of band.

The scarcity of electromagnetic spectrum is obvious, but the real problem is not a dearth of radio spectrum; it's the way that spectrum is used. The radio spectrum is actually poorly utilized in many bands in the sense that large portion of the assigned bands are not used most of the time [43]. This discrepancy between allocation and use provides the motivation for opportunistic use of the spectrum. A solution to combat the inefficiency is to make spectra available to unlicensed users. The key enabling technology of dynamic spectrum access techniques is Cognitive Radio (CR) technology [44, 45], which provides the capability to share the wireless channel with licensed users in an opportunistic manner.

FIGURE 2.5: A new that appeared in www.lightreading.com (Aug 1st, 2011) about spectrum auction in Spain

2.2.2 The cognitive radio alternative

Formally, a CR is defined as an smart wireless communication system that is aware of its surrounding environment. The basic idea of CR is spectral reusing or spectrum sharing, which allows the unlicensed users to communicate over spectrum licensed to primary systems when they are not fully utilizing it, as shown in Fig. 2.6.

There are three main cognitive radio network paradigms: underlay, overlay and interweave. The underlay paradigm allows cognitive users to operate if the interference caused to primary users is below a given threshold. In overlay systems, the cognitive radios use sophisticated signal processing and coding to maintain or improve communication of noncognitive radios while also obtaining some additional bandwidth for their own communications. In interweave systems, the cognitive radios opportunistically exploit spectral holes to communicate without disrupting other transmissions. It is clear that each cognitive radio approach require different amount of side information: underlay systems require knowledge of the interference caused by the cognitive transmitter to the primary users; interweave systems require considerable side information about the primary users activity; and overlay systems require a large amount of side information (noncausal knowledge of noncognitive user's codebook and possibly its message). In general, any approach described previously requires knowledge of the primary (licensed) user spectrum activity in order to avoid causing interference. Protecting the non-cognitive users is mandatory since they have the priority of service. The task of accurately detecting the presence of licensed user is encompassed in spectrum sensing.

2.2.3 Spectrum sensing

At this point is clear that there is no way to avoid properly monitoring of the spectrum of the primary users in CR. In fact, one of the most important components of the CR concept is the ability to measure, sense, learn and be aware of the parameters related to the radio channel characteristics. Spectrum sensing in CR involves deciding whether the primary user is present or not from the observed signals. Thus, spectrum sensing is a binary decision problem: Is it empty the particular frequency that we would like to use or it is not? It can be formulated as the following detection problem:

$$y(t) = \begin{cases} w(t) & H_0 \\ x(t) + \eta(t) & H_1 \end{cases} \tag{2.11}$$

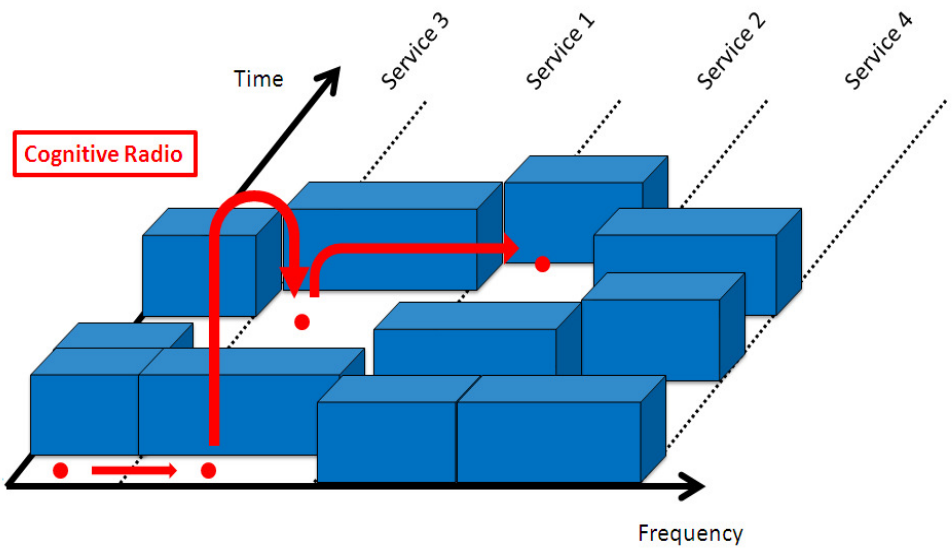

FIGURE 2.6: Example of primary services' spectrum occupancy over time and frequency and possible opportunistic access (in red) by CR.

where $y(t)$ is the received signal at the CR user, $x(t)$ is the primary signal and $\eta(t)$ is the additive white Gaussian noise (AWGN). The CR user has to decide if the primary signal is present (H_1) or not (H_0) from the observation $y(t)$.

There are a number of ways in which cognitive radios are able to perform spectrum sensing. When a cognitive radio configures itself according to the signals it can detect we talk about non-cooperative spectrum sensing. On the other hand, when sensing is undertaken by a number of different radios within a cognitive radio network we talk about cooperative spectrum sensing [46]. While cooperative spectrum sensing provides a better picture of the spectrum usage over the area where the cognitive radios are located, it is obviously more complicated than a single non-cooperative system. In any case, the information about the frequencies that can and cannot be used is required in both cooperative and non-cooperative.

The identification procedure of available spectrum is quite a difficult task due to the strict requirements imposed to guarantee no harmful interference to the licensed users. In general, the minimum signal-to-noise ratio (SNR) at which the primary signal may still be accurately detected required by the sensing procedure is very low. Thus, low SNR levels must be sensed which translates into a high detection sensitivity. A second constraint is the required detection time [47]. The longer the time that we sense, the better the signal processing gain. However, the spectrum behaves dynamically, changing all the time, and cognitive users need to be aware of these fast changes. Another desirable feature is that the primary user detector has to provide an accurate power level for the primary user. The estimated power level can be used to obtain information about the distance at which the primary user is located and that can give us an idea of the level of interference that unlicensed users represent. The performance of a spectrum sensor depends crucially on the transmission channel. Indeed, due to fading of the channels and shadowing effects, the sensing performances will be degraded. Several authors have proposed collaboration among users to overcome the channel variations. Other authors directly assume the availability of accurate channel models at the receiver. Finally, the noise/interference time dependence introduce what is called noise uncertainty [48, 49], which may further deteriorate the detection performance.

According to the a priori information required to detect the primary user and the resulting complexity and accuracy, spectrum sensing techniques can be categorized in the following types.

- **Matched Filter Sensing.** It is well known that if the whole structure of the primary signal is completely known, the optimal detector in stationary Gaussian noise is a matched filter [50] since it maximizes the received SNR. Although it requires a priori knowledge of the primary signal, the main advantage of the matched filter is that it achieves high processing gain due to the coherency in quick time. The main drawback is that if the prior information is not accurate, then the matched filter performs poorly. Fortunately, most wireless systems have pilots, preambles, synchronization word or spreading codes that can be used for the coherent detection.

- **Energy Detector.** The energy detector is the most common way of spectrum sensing because of its low complexity (computational and implementation). It is the simplest spectrum sensing technique because it is a blind technique, i.e., do not rely on any signal feature. It simply treats the primary signal as noise and decides on the present or absence of the primary signal based on the energy of the observed signal [51]. If the energy of the observed signal is higher than a given threshold (which depends on the noise floor) than the CR user considers that the primary signal is present. The main drawback of the energy detector is its inability to discriminate between sources of received energy (the primary signal and noise) making it susceptible to uncertainties in background noise power, specially at a low SNR.

- **Cyclostationary Detection Sensing.** If some features of the primary signal such as its carrier frequency or modulation type are known a priori, more sophisticated feature detectors may be employed to address this issue at the cost of increased complexity. Cyclostationary detection [52, 53] is particularly appealing because its ability to distinguished the primary signal from the interference and noise. It can work in a very low SNR region due to its noise rejection capability which is a result of the fact that noise is wide-sense stationary with no correlation while modulated signals are cyclostationary. However, it is computationally complex and requires significantly long observation time.

- **Covariance-Based Algorithms:**

  Completely blind spectrum sensing techniques suffer from challenges in the low signal to noise range. Information theoretic criteria for spectrum sensing has recently been proposed to overcome this problem. The most prominent work on this area was presented in [54–56]. Model selection tools like Akaike information criterion (AIC) [57] and the Minimum Description Length (MDL) criterion were suggested in [54] to conclude on the nature of the sensed band. In [55], these tools were used as detection rules for the Dimension Estimation Detector (DED). Closed-form expressions of false alarm probabilities for a given threshold for DED and MDL were presented in [56]. Another recent proposed blind method comparable with the energy detector is the covariance absolute method (CAV) proposed in [58], where the uncorrelated nature of the noise and the correlated nature of the signal is exploited by means of the covariance matrix eigenvalues. However, the model selection was not considered in [58].

An excellent survey of the most common spectrum sensing techniques, both non-feature and feature-based detectors, has been published in [3]. A basic comparison of the sensing

methods given in this section is presented in Fig. 2.7. The amount of information available a priori about the characteristic of the primary users are the main factor in selecting a spectrum sensing method. Other factors include required accuracy, sensing duration requirements, computational complexity and network requirements. This thesis will focus on radio identification based sensing, where the spectrum characteristics of the primary users are used as features.

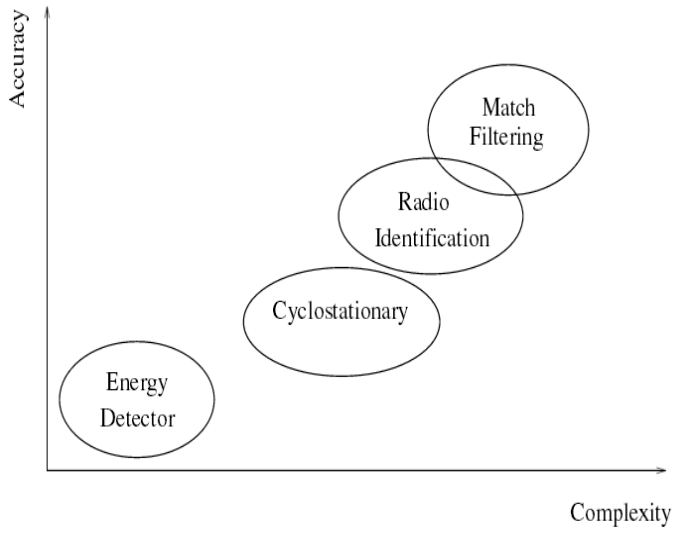

FIGURE 2.7: Main sensing methods in terms of their sensing accuracies and complexities. Figure extracted and modified from [3].

2.2.4 Spatial diversity

The problem of estimating the angle of arrival (AoA) of sources impinging on a passive array of sensors has been an active area of research for a long time, being MUSIC [59] and ML [60] the most popular high-resolution techniques used to distinguish two closely separated sources. More recently, AoA estimation has become important in Cognitive Radio. The conventional spectrum sensing algorithms usually exploit two dimensions of the spectrum space: frequency and time. In other words, they look for bands of frequencies that are not being used at a particular time. Fortunately, there are other dimensions that need to be explored further for spectrum opportunity. With the recent developments of beamforming technology, a new dimension emerges: the angle dimension. If a primary user is transmitting in a specific direction, the secondary user can transmit in other directions without interfering on the primary user. Thus, the spatial diversity brings extra spectrum opportunities [61].

2.2.5 Implementation challenges

The design of the analog front-end is critical in the case of CR [50, 62]. The worst problem is the high sampling rate required to process very wide bandwidth. The traditional way for detecting holes in a wide-band spectrum is channel-by-channel scanning. In order to implement this, an RF front-end with a bank of tunable and narrow bandpass filters is needed. Sampling at the Nyquist rate is shown to be inefficient when the signals of interest contain only a small number of significant frequencies relative to the bandlimit [6]. To alleviate

the sampling bottleneck, a promising alternative for this type of sparse signals is the use of sub-Nyquist sampling techniques.

2.2.6 Compressive spectrum sensing

CS is a powerful technique for accurately detect the existence of primary users from a reduced number of measurements by exploiting the sparsity described by active primary users. In the spectrum sensing problem, the spectral support of the signals of interest is significantly smaller compared to the bandwidth under scrutiny. Furthermore, the sparsity can also be leveraged to increase the accuracy of the detections by using sparsity-based recovery methods. Several publications have used the fact that wireless signals in open spectrum networks are typically sparse in the frequency domain. In [47, 63], sub-Nyquist rate samples are utilized to detect and classify frequency bands via a wavelet-based edge detector. Authors in [64] proposed a two-step compressed spectrum sensing method which first quickly estimates the actual sparsity order of the wide spectrum of interest, and adjusts the total number of samples collected according to the estimated signal sparsity order. Many research works such as Viberg [65] or Lexa [66] use the sub-Nyquist methods to obtain information of the unknown power spectrum from the compressed samples avoiding the signal reconstruction. The MC sampling or periodic non-uniform sampling is used in both publications [65,66] at a rate lower than the Nyquist rate, that captures enough information to enable perfect reconstruction of the spectrum. Mishali et al. solved the spectrum hole detection problem in [2] using the MWC by estimating the sparse wideband signal from the acquired samples.

In practical settings, primary signals must be detected even with the presence of low-regulated transmissions from secondary systems. As mentioned in section (2.1.4), the existance of interferences emanating from low-regulated transmissions, which cannot be taken into account in the CS model because of their non-regulated nature, greatly degrade the identification of licensed activity. Capitalizing on the sparsity described by licensed users, this thesis introduces a feature-based technique for primary user's spectrum identification with interference immunity which works with a reduced amount of data.

2.3 Through-the-wall radar imaging

2.3.1 Seeing through walls

Sensing through building walls using RF signals to gain vision into concealed scenes is the aim of Through-the-Wall Radar Imaging (TWRI) [67–70]. The objectives of seeing through walls include the determination of the building layouts, discerning the intent of activities inside the building, or detecting, locating, tracking, and imaging of targets inside enclosed structures. This type of technology is highly desirable for a range of civil and military applications, examples being search-and-rescue missions, behind-wall target detection, and surveillance and reconnaissance in urban environments [68, 69, 71, 72] (see Fig. 2.8). TWRI combines electromagnetic waves transmitted and received at several different antenna locations along an array aperture, either real or synthesized, to obtain 2D or 3D images of the region of interest located behind the front wall.

In order to achieve all these objectives, however, much attention should be paid to the front wall and its effects on the imaged scene accuracy and fidelity. Free-space propagation does not apply in TWRI, where transmission through opaque material is encountered. Although radio frequency is the modality of choice for TWRI applications, it is well known

that electromagnetic waves passing through a medium are subject to amplitude and phase distortion, rendering sensing through walls a complex and difficult problem. There are many challenges facing TWRI system development, namely, the system should be reliable and portable, with both short set-up time and acquisition time. System performance should be robust to ambiguities in wall characterization and should properly function under non-uniform wall, multiple walls, and operator motion. The system should have high range and cross-range resolutions that are application specific. Finally, it must be able to detect and classify motions in the presence of heavy clutter, which may include interior back and side walls, water pipes, and various types of furniture items.

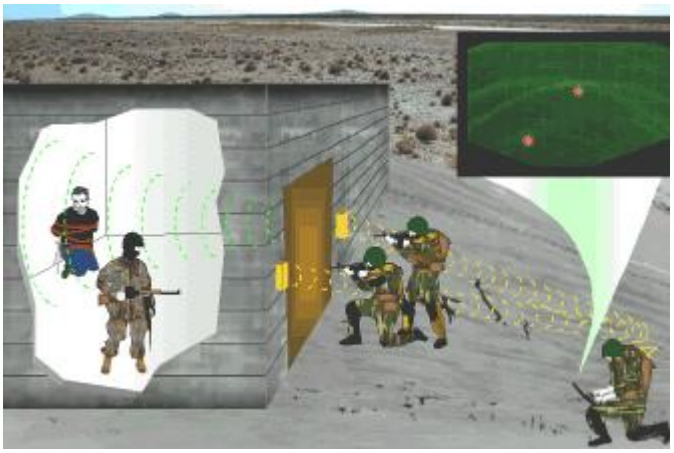

FIGURE 2.8: Soldiers scanning the room with terrorists and hostage. © Lawrence Livermore National Laboratory

2.3.2 Front wall mitigation

Radar imaging through building walls and ceilings is a challenging problem due to the anisotropic and periodic scattering response of many types of walls, the significant attenuation loss of building walls and ceilings, and the high clutter and multipath effects of complex building and interior structure [73]. Front walls cause strong EM reflections back in the directions of the radar which obscure the behind-the-wall target returns. The latter are relatively weak compared to wall reflections and cannot be generally detected without an effective removal of the wall clutter. For moving targets, subtraction of data acquired at different times alleviates this problem and leads to removal of cross talk and wall EM reflections as well as suppression of stationary clutter inside the room [74–76]. However, in stationary scenes, removing the wall reflections from the received data by change detection cannot be performed. This is because the subtraction of consecutive imaging results would eliminate both target and clutter. In this case, techniques to remove the front wall returns without affecting the target RCS can prove useful.

Whithout any knowledge of the wall in front of the radar, one has to assume free space propagation from the transmitter to the target and back to the transmitter. If an image is formed based on this assumption, the strong glint from the front wall reflection can bleed into the entire image domain, creating significant clutter that limits the target detection.

In this context, there are three main approaches to mitigate the wall contribution. In [77], a method to extract the dielectric constant and thickness of the non-frequency dependent wall from the time-domain scattered field is presented. Then, the time-domain response of

the wall is analytically modeled and removed from the measured wall response to mitigate the shadowing effect of the wall on targets of interest within a building structure. The same authors proposed in [78] a similar method based on the frequency domain scattered field for frequency-dependent walls. The other two methods rely on the strong similarity between wall response viewed by different antenna locations along the entire synthesized array aperture. In [79], a spatial filtering method is applied to remove the dc component corresponding to the constant-type return, typically associated with the front wall. The last method, presented in [80], is based not only on the invariance along the antenna locations but also on the wall returns are relatively stronger than target reflections. As a result, the wall eigen-subspace is usually captured in the most dominant singular values. By applying singular value decomposition (SVD) to the measured data matrix, the wall contribution can be removed by orthogonal subspace projection.

2.3.3 Detection and classification in TWRI

Automatic detection of humans and objects of interest is of high practical interest which is fundamental to follow-on tasks of target classification and tracking, image interpretation and understanding. The detection of targets behind the wall is only possible with radars working at lower frequencies, usually below 4GHz. Even so, radar imaging through building walls and ceilings is a challenging problem due to the anisotropic and periodic scattering response of many types of walls, the significant attenuation loss of building walls and ceilings, and the high clutter and multipath effects of complex building and interior structure [73]. As a result, the image resolution is significantly degraded difficulting the task of detection. Furthermore, the challenge usually consists (depending on the scenario) to distinguish between desired and undesired objects.

Detection of moving objects can resort to Doppler discrimination of movement from background clutter [81]. Detection of living objects, e.g. people, can be achieved exploiting its breathing, which causes minor variations (micro-doppler) in the body's shape that can be determined by radar [82,83]. The application of Doppler and micro-Doppler filters for indoor target surveillance may not be a viable option in particular cases where the Doppler signal becomes complex and difficult to interpret, especially when dealing with non-homogeneous walls. Instead, detection of moving targets can proceed based on subtraction of data frames acquired over successive probing of the scene. The subtraction operation is referred to as change detection [74–76]. However, the recognition of static objects is more challenging since decisions must be based on the radar image. Feature detection of through-the-wall objects is usually developed in the image-domain because it has been shown to handle multiple targets without prior assumptions on target radar cross section (RCS) [84]. Omitting the image formation step is the most attractive advantage of data-domain based detection approaches, which, however, involve transmit waveform design incorporating some prior knowledge of the target RCS [76].

Detection of building interior structures

The research developed in this thesis would be concentrated on signal processing techniques for imaging the interior structure of a building scanned from the outside.

Detection of building interior structures assuming availability of full data measurements was presented in [73,85–89]. In [85], the problem of building structure estimation was solved using microwave ray tomography. The authors developed a Bayesian formulation and used

Markov chain Monte Carlo procedure to sample the posterior distribution. In [86], an iterative procedure based on the jump-diffusion algorithm was proposed to estimate the building layout for moving sensor systems. The building layout mapping technique discussed in [87] relates the measurements to a list of floor-plan topologies through a graph-theoretical approach. Direct interpretation of the radar image was proposed in [88], where an image of the full building layout and the interior targets was obtained by combining images obtained from two sides of the building. Building construction practices suggest the exterior and interior walls to be parallel or perpendicular to each other. Consistent with this fact is the works presented in [90]. In [90], an improvement to the conventional the Hough Transform (HT) was proposed assuming knowledge of the orientation of walls and by applying sharp windowing to the resulting HT. With proper angular radar illuminations, which certainly avoid the front wall returns, the corner features created by the junction of walls of a room are preserved. This can be achieved using squint beamforming or broadside beams with tilted aperture [91]. Estimating dominant scatterers such as corners allows the inference of building interior structure. This idea was exploited in [73,89], where a building feature based approach was applied to estimate the type and location of different canonical scattering mechanisms. However, the corner-based detection aggravates the data acquisition time problem, since it requires data measured from different scanning positions. Corners will only be revealed if the scanning path is on the concave side of the corner. Moreover, the oblique scan images must be clear so that all corners can be identified by a simple search of local maxima, which is not a straightforward assumption when a reduced number of data samples is considered.

2.3.4 Implementation issues

Current ground-based TWRI systems utilize the strip-map geometry [92], i.e., a radar is mounted on a moving platform (such as a vehicle) looking sideways with respect to the moving direction, which in general is assumed parallel to one side of the building. The scene of interest may also be accessible by two or more vantage points, either along one wall or using neighboring walls, as shown in Fig. 2.9. An alternative multi-look approach combines images processed with different squint angles from one side of the building. The benefits of multi-look fusion approach for both interior room mapping and concealed target detection were demonstrated in [91, 93].

For a high-resolution TWRI system, it is desirable to operate over a wide frequency band or radiate a short-duration pulse for better down-range resolution. On the other hand, the cross-range resolution is determined by the antenna aperture size, necessitating a large radar array to improve the quality of the image. Thus, high resolution in TWRI both in cross-range and down-range demands wideband signals and large array apertures. However, this considerably increases the percentage of the acquisition time and processing. Therefore, to have a practical system, there is a need to develop fast and efficient image formation techniques. If few measurements are used in lieu of the entire data collection, significant savings in acquisition time can be achieved. Additionally, reducing the number of spatial and frequency observations can be logistically attractive, as some of these specific measurements can be difficult, or impossible to attain. For instance, EM emission at some antenna locations in a SAR system can be blocked by natural or manmade surrounding obstacles. On the other hand, some individual frequencies or frequency subbands may be unavailable due to competing wireless services or intentional interferences (jammers).

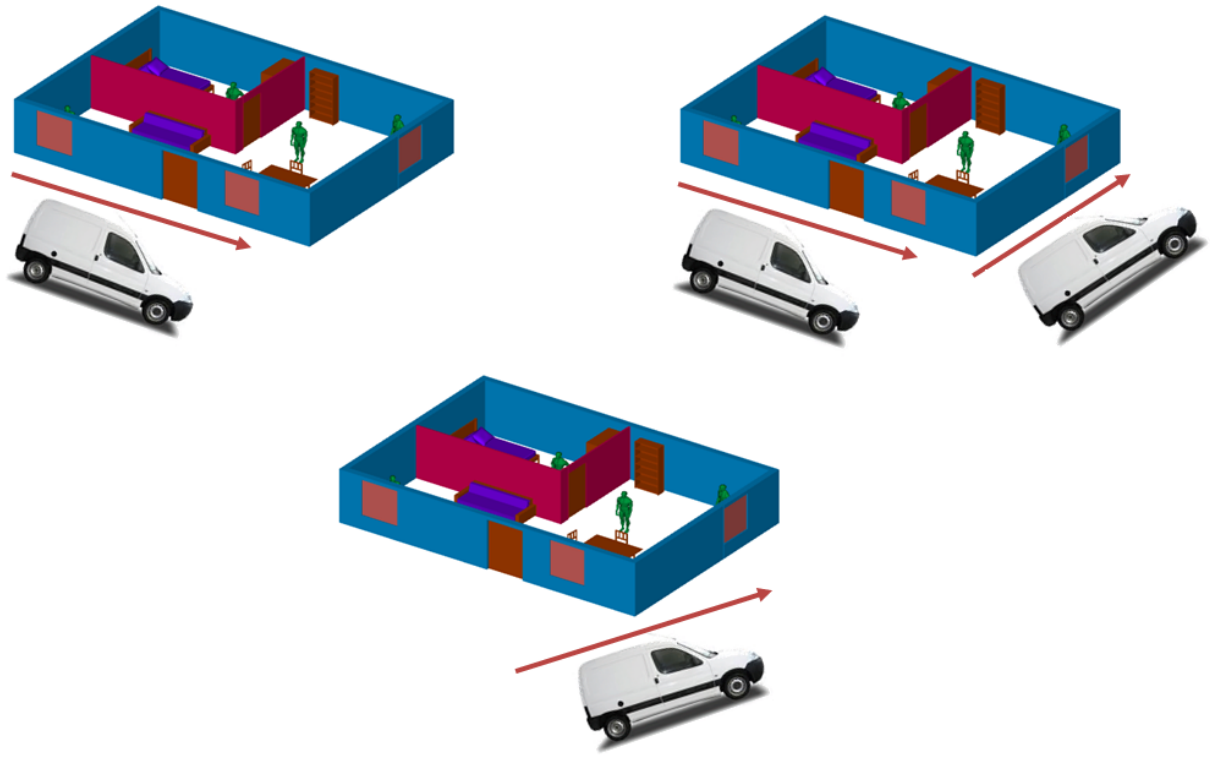

FIGURE 2.9: Imaging a scene of interest from multiple vantage points

2.3.5 Compressive urban sensing

The most desirable goal of through-wall radar systems is to provide situational awareness in a fast and reliable manner. Towards the objective of providing timely actionable intelligence in urban environments, it has been recently shown that CS is a very effective technique for indoor scene reconstruction from a relatively small number of data samples without compromising the image quality [94]. In so doing, significant savings in acquisition time can be achieved. Further, as already stated, producing an image of the indoor scene using few observations can be logistically important, as some of the data measurements in space and frequency can be difficult, or impossible to attain.

Front wall mitigation using CS

CS techniques have been shown to yield reduced cost and efficient sensing operations that allow super-resolution imaging of sparse behind-the-wall scenes. The application of CS for TWRI was first reported in [95] and further developed in [96–98]. However, wall mitigation in conjunction with CS has never been considered in these references. That is, CS was applied to TWRI, already assuming prior and complete removal of the front wall EM returns. Without this assumption, strong wall clutter, which extends along the range dimension, reduces the sparsity of the scene and, as such, impedes the application of CS. If the reference scene is known, then background subtraction can be performed to remove wall clutter, thereby improve sparsity. Having access to the background scene or reference data, however, is not always possible in practical applications.

Imaging of building interior structures using CS

Consistent with the fact that interior walls are typically parallel or perpendicular to the front wall, in [99], the Hough Transform (HT) domain for continuous infinite-length line detection was strictly discretized for tunnel detection in Ground Penetrating Radar (GPR) using a reduced set of observations and applying CS techniques.

Building interiors may have structures that have recognizable signatures, such as dihedral reflectors caused by intersections between perpendicular walls. Locating wall-wall junctions may be useful in determining the true wall extents and detecting walls perpendicular to the scan direction that are not visible. Recently, the use of overcomplete dictionaries for sparse representation of corners have been proposed [100,101], whose atom coefficient directly indicate the presence of a building feature at a given position. However, the discrimination of corners with respect to other scattering objects present in the scene is not perfectly achieved using an overcomplete dictionary of canonical dihedral scattering responses because, although corners are assumed to have different response than that of other scatterers, they might not be orthogonal.

Chapter 3

Compressive Sensing based Candidate Detector

This chapter presents the mathematic formulation of the compressive sensing based candidate detector. The detector will be firstly presented in the raw data domain. Secondly, the candidate detector is applied in a second order statistic domain, such as the correlation domain. In both cases, the basic idea is to match a candidate or reference signal/correlation with the collected data. We define two different strategies to do the matching. The conventional approach to resolve the matching problem is to perform a matched filter reconstruction for every possible locations of the scanning grid. A detection occurs then at the locations of maxima in the scanning grid. The alternative strategy is to utilize an inverse problem formulation by taking advantage of insights from sparse signal representation. The detection problem is linearized over a set of possible hypothesis by construction of an overcomplete dictionary of candidates. In contrast to the matched filtering approach, the overcomplete dictionary of candidates allow all possible hypothesis to be evaluated jointly in a global unified optimization framework.

The main contribution of this thesis is the interference rejection capabilities of the proposed detector, which is solved in the matching problem through appropriate choices of the matching error function in the matched filtering approach and through weighted sparsity constraint when solving the CS optimization problem.

3.1 Problem Statement

Our goal is to decide whether given signals are present or not based on the observation of sub-Nyquist samples of the received signal. Let us denote $x(t)$ the signal representing the superposition of different desired signals,

$$x(t) = \sum_{k=1}^{K} x(t, \theta_k) \tag{3.1}$$

where $x(t, \theta_k)$, $k = 1, \ldots, K$, are the signals that we would like to detect. These signals are of the same nature but they may differ on some characteristics θ_k, for instance, the carrier frequency, the angle of arrival, position, etc. The received signals are usually corrupted by noise and interference, which can come from nearby transmission systems, unintentionally or

intentionally. Thus, the received signal can be expressed as,

$$y(t) = x(t) + i(t) + \eta(t) \tag{3.2}$$

where $i(t)$ and $\eta(t)$ are the interferent signal and the additive Gaussian noise (AGWN) $\mathcal{N}(0, \sigma_\eta^2)$, respectively. Unlike previous works present in the literature, here we consider the general case where no information about the interference is available. Thus, it is impossible to filter out this unwanted signal component as prior to any processing.

The problem of determining weather a given type of signals $x(t)$ is present or not can be modeled into a binary hypothesis test,

$$y(t) = \begin{cases} i(t) + \eta(t) & (H_0) \\ x(t) + i(t) + \eta(t) & (H_1) \end{cases} \tag{3.3}$$

where (H_0) stands for the absence of desired signal and (H_1) stands for the presence of a desired signal. Note the difference between the problem stated in (3.3) and the simplified spectrum sensing problem stated in (2.11). The presence of unknown interfering signal adds additional challenges to the detection problem.

3.2 Candidate matching approach

This section is divided into two parts. In the first one, the candidate matching approach is applied directly in the raw data domain. In this case, the candidate detector becomes the conventional matched filtering approach: it matches the received signal with a reference or candidate signal. Although it is computationally simple, sometimes, however, the amount of prior information about the desired signal is not enough to obtain an accurate candidate signal to be applied in the raw data domain. In this case, we need to define the candidate matching in a second order statistic domain, such as the correlation domain. Even in cases where full candidate information is provided, there are specific cases where working in the correlation domain may be useful. For instance, if the channel causes nonlinear distortions on the transmitted signal, as the candidate will not be optimal anymore, the raw data based detector is expected to yield suboptimal signal detection and false alarm performance. The second part of this section focuses on the definition of the candidate correlation matching strategy.

3.2.1 Raw data domain

For the purpose of the present work, let us define the candidate signal $x_c(t)$ which is obtained using some prior knowledge of the nature of the desired signals $x(t, \theta_k)$, $k = 1, \ldots, K$. The proposed detector follows the basis of a matched filter detector, where the candidate signal $x_c(t)$ is tuned to different values of θ and matched with the received signal. To do so, the parameter space θ must be discretized. Discretization generates a finite set of M parameters $\{\theta_0, \theta_1, \ldots, \theta_{M-1}\}$. The value of M determines the grid density of the parameter to be scanned. Increasing M makes the grid finer, but it also increases the computational complexity. On the other hand, making the grid too rough might introduce substantial bias into the estimates. For the sake of clarity we assume a fix and appropriate value of M in the sequel. It is worth mentioning, however, that the proposed method is suitable for grid refinement: initially a coarse grid may be used to obtain approximate estimations and then the grid can be refined in regions where better accuracy is required.

Let us define a modulated candidate signal $x_{cm}(t, \theta_m)$ as follows,

$$x_{cm}(t, \theta_m) = x_c(t) \cdot e(t, \theta_m) \tag{3.4}$$

where $e(t, \theta_m)$ is a function that modulates the candidate signal to a specific parameter θ_m. According to this notation, the corresponding model for the received signal $y(t)$ defined in (3.2) is given by,

$$y(t) = \sum_{k=1}^{K} \gamma(\theta_k) x_{cm}(t, \theta_k) + i(t) + \eta(t) \tag{3.5}$$

where $\gamma(\theta_k)$, $k = 1, \ldots, K$, denote the amplitudes of each candidate signal $x_{cm}(t, \theta_k)$.

Based on this assumption, a simple detector is given by,

$$\min_{\beta(\theta_m)} \quad \mathbf{\Omega}\left[y(t), \beta(\theta_m) x_{cm}(t, \theta_m)\right] \tag{3.6}$$

where $\mathbf{\Omega}[\cdot, \cdot]$ is an error function between the two signals. Ideally, $\beta(\theta_m) = \gamma(\theta_k)$ when $\theta_m = \theta_k$ and $\beta(\theta_m) = 0$ elsewhere. Note that the solution to (3.6) will be clearly a function of the steering parameters θ_m. Thus, the proposed candidate-based detector is based on a particular candidate-scan which reacts only when the desired signal is present. Summarizing, the problem to solve consists in finding the parameters θ_m that the candidate signal $x_c(t)$ has to be tuned and the scalars $\beta(\theta_m)$ to best fit the collected data $y(t)$.

3.2.2 Correlation domain

A digital communication signal is a non-stationary stochastic process. Nevertheless, the second order statistics of communications signals show periodicity. This kind of process are called cyclostationary process and its power density spectrum is computed by averaging over a cyclic period. In the case of digital linearly I/Q modulated signals, the associated mean spectral shape depends mainly on the energy spectrum of the modulation pulse. For such a case, when the modulation symbols are not known, it is more appropriate to define a second-order based detector. Moreover, as mentioned above, there are specific cases where working in the correlation domain is better than working in the raw data domain, even with the complete knowledge of the desired signal structure. In this section, the candidate-based detector under a correlation-matching perspective is addressed. Let $r_y(t, \tau)$ denote the autocorrelation of the second-order cyclostationary process $y(t)$, where τ indicate the time lag, which is defined as,

$$r_y(t, \tau) = \mathbb{E}\left\{y(t) \cdot y^*(t + \tau)\right\} = r_y(t, \tau + T_0) \tag{3.7}$$

where T_0 indicates the cyclic period. The conventional autocorrelation function (CAF), $r_y(\tau)$, is obtained averaging over a cyclic period as follows,

$$r_y(\tau) = \frac{1}{T_0} \int_{-T_0/2}^{T_0/2} r_y(t, \tau) dt \tag{3.8}$$

For the purpose of the present work, let us define $r_c(\tau)$ as the autocorrelation of the candidate signal $x_c(t)$. The corresponding model for the autocorrelation of the received signal $r_y(\tau)$ is given by,

$$r_y(\tau) = \sum_{k=1}^{K} \sigma^2(\theta_k) r_{cm}(\tau, \theta_k) + r_i(\tau) + r_\eta(\tau) \tag{3.9}$$

where $r_i(\tau)$ and $r_\eta(\tau)$ denote the autocorrelation of the interference and the noise, respectively, $\sigma^2(\theta_k)$, $k = 1, \ldots, K$, denote the transmitted power of $x_k(t)$ defined as $\sigma^2(\theta_k) = \mathbb{E}\left\{|\gamma(\theta_k)|^2\right\}$, and $r_{cm}(\tau, \theta_k)$ is defined as,

$$r_{cm}(\tau, \theta_k) = r_c(\tau) \cdot f_e(\theta_k) \tag{3.10}$$

where $f_e(\theta_k)$ is a function that particularizes the candidate autocorrelation for a specific parameter θ_k.

The candidate detector based on second order statistics is formulated as follows,

$$\min_{p(\theta_m)} \quad \mathbf{\Omega}\left[r_y(\tau), p(\theta_m) r_{cm}(\tau, \theta_m)\right] \tag{3.11}$$

As happened in the raw data domain, different detectors result from the proper choice of the aforementioned error function $\mathbf{\Omega}[\cdot, \cdot]$. The solution to (3.11), as the solution to (3.6), is a function of the steering parameter θ_m. The only difference between (3.11) and (3.6) is that the outputs are estimates of powers $\sigma^2(\theta_k)$ and estimates of amplitudes $\gamma(\theta_k)$, respectively. Therefore, ideally, $p(t, \theta_m) = \sigma^2(\theta_k)$ when $\theta_m = \theta_k$ and $p(\theta_m) = 0$ elsewhere. As we move forward in this chapter, we will present the advantages of working in the correlation domain.

3.3 Overcomplete dictionary of candidates

Note that the candidate matching approach described either in section (3.2.1) or section (3.2.2) implicitly assume the use of overcomplete dictionary of candidate signals/autocorrelations.

Working on the raw data domain, the received signal is assumed to be a linear combination of candidate signals, i.e.,

$$y(t) = \sum_{m=0}^{M-1} \beta(\theta_m) x_{cm}(t, \theta_m) + \epsilon(t) \tag{3.12}$$

where $\epsilon(t)$ models the imperfections of this formulation, including $i(t)$ and $\eta(t)$.

The same happens in the second order statistic domain, where the autocorrelation of the received signal is modeled as a summation of candidate correlations as follows,

$$r_y(\tau) = \sum_{m=0}^{M-1} p(\theta_m) r_{cm}(\tau, \theta_m) + r_\epsilon(\tau) \tag{3.13}$$

where $r_\epsilon(\tau)$ encompasses the imperfections of this formulation, including autocorrelation of the interference and noise.

Indeed, in both cases, when $K < M$, they both become overcomplete dictionaries [20], i.e., each dictionary contains M prototype signal/correlations. As the value of M increases with respect to K, the signal is more and more sparsely represented.

The sparse vectors,

$$\boldsymbol{\beta} = \begin{bmatrix} \beta(\theta_0) & \beta(\theta_1) & \cdots & \beta(\theta_{M-1}) \end{bmatrix}^T \tag{3.14}$$

and

$$\mathbf{p} = \begin{bmatrix} p(\theta_0) & p(\theta_1) & \cdots & p(\theta_{M-1}) \end{bmatrix}^T \tag{3.15}$$

can be viewed as the output of two indicator functions, whose elements different from zero correspond to the values of the parameter θ where the reference is present. Moreover, the

values different from zero give us an idea of the *amount* of that particular type of candidate signal being present in the received signal.

$$\beta(\theta_m) = \begin{cases} \gamma(\theta_k) & \text{if } \theta_m = \theta_k \quad (H_1) \\ 0 & \text{otherwise} \quad (H_0) \end{cases} \tag{3.16}$$

$$p(\theta_m) = \begin{cases} \sigma^2(\theta_k) & \text{if } \theta_m = \theta_k \quad (H_1) \\ 0 & \text{otherwise} \quad (H_0) \end{cases} \tag{3.17}$$

This is, $\beta(\theta_m)$ provides an estimate of the amplitude of the desired signal while $p(\theta_m)$ provides an estimate of the power, i.e., $p(\theta_m) \approx \mathbb{E}\left\{|\beta(\theta_m)|^2\right\}$.

The sparse nature of these vectors $\boldsymbol{\beta}$ and $\mathbf{p}$ motivates the design of novel detection strategies based on the compressive sensing theory.

3.4 Signal digitalizing: Compressive sampling

In this section, the relation between the Nyquist samples and the sub-Nyquist samples given in (2.3) is particularized for three different sub-Nyquist sampling strategies.

3.4.1 Uniform sub-Nyquist sampling

One possible way to reduce samples is uniform sub-Nyquist sampling. It is generally accepted that the uniform sampling interval and the upper limit of the recoverable signal are inexorably linked. When the Nyquist limit is exceeded, the phenomenon of aliasing occurs. Gurbuz et Al. showed in [102] that CS reconstruction methods remains stable using either uniform or random sample selection when the uniform sub-sampling does not exceed the aliasing limit. It is generally assumed that uniform sampling cannot exploit the presence of sparse structure of the signals to be sampled. However, the overlap of aliases in the reconstruction process can be allowed if and only if the aliased part of the signal is sparse. In other words, some type of sparse signals allow uniform sub-Nyquist sampling when the non-sparse part of the signal is not damaged by the aliasing phenomenon. The advantage of uniform sampling versus random sampling is its simple implementation. In this case, the relation between the Nyquist samples and the sub-Nyquist samples defined in (2.3) is given by $\boldsymbol{\Phi}$, which is constructed by uniformly selecting κ rows of an $L \times L$ identity matrix $\mathbf{I}_L$.

3.4.2 Non-uniform sub-Nyquist sampling

Random sub-Nyquist sampling

The ambiguity with uniform sub-sampling is overcomed with the random selection of samples. An important result in sampling theory is the Landau lower bound [103]. Landau's bound is given by the total length of support of the Fourier transform of the signal, which is often much lower than the corresponding Nyquist rate. Landau's bound is the bedrock upon which the random sub-Nyquist sampling was built. The only restriction imposed on the minimum number of random samples is given by the conventional CS theory (see section 2.1.2). It was shown that random matrices, e.g., Gaussian or ± 1 random matrices, are largely incoherent with any fixed sparsifying basis with overwhelming probability. Recent results on theoretical limits of CS strongly rely on random sensing matrices, since they provide universally incoherence and are well conditioned for reconstruction [104]. In this

case, matrix $\mathbf{\Phi}$ in (2.3) can be constructed either from a random distribution (Gaussian, Bernoulli,...) or by randomly selecting κ rows of an $L \times L$ identity matrix $\mathbf{I}_L$.

Periodic non-uniform sampling: Multi-coset sampling

In parts of this thesis we consider a particular case of non-uniform sub-Nyquist sampling, which is the periodic non-uniform sub-Nyquist sampling strategy known as multi-coset (MC) sampling [105].

In MC sampling, we first pick a suitable sampling period T. The inverse of this period $(1/T)$ will determine the base frequency of the system, being $1/T$ at least equal to the Nyquist rate so that sampling at $1/T$ ensures no aliasing. Assuming that $y(t)$ is bandlimited to $F = [0, f_{max}]$, the Nyquist sampling period is given by $T = 1/f_{max}$.

Given the received signal $y(t)$, the periodic non-uniform samples are obtained at the time instants,

$$t_i(n) = (nL + c_i)T \tag{3.18}$$

where $L > 0$ is a suitable integer, $i = 1, 2, \ldots, \kappa$ and $n \in \mathbb{Z}$. The set $\{c_i\}$ contains κ distinct integers chosen from $\{0, 1, \ldots, L-1\}$. The reader can notice that the MC sampling process can be viewed as a classical Nyquist sampling followed by a block that discards all but κ samples in every block of L samples periodically. The samples which are not thrown away are specified by the set $\{c_i\}$. Thus, a sequence (or coset, hence the name of the method) of equally-spaced samples is obtained for each c_i. The period of each one of these sequences is equal to LT. Therefore, one possible implementation consists of κ parallel ADCs, each working uniformly with period LT.

Another widely-used notation for the MC sampling is to express each $i-th$ sampling scheme as follows,

$$y^i[n] = \begin{cases} y(nT), & n = mL + c_i,\ m \in \mathbb{Z} \\ 0, & \textit{Otherwise} \end{cases} \tag{3.19}$$

The set $\{c_i\}$ is referred to as an (L, κ) sampling pattern and the integer L as the period of the pattern. Fig. 3.1 shows a scheme of how the κ cosets are obtained.

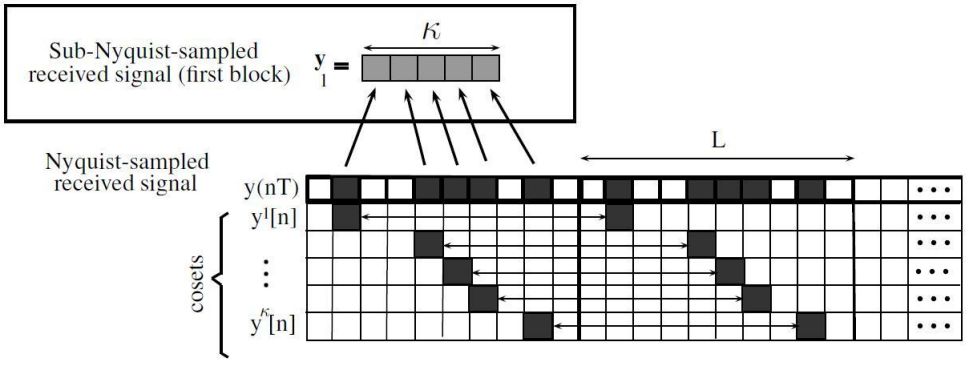

FIGURE 3.1: Scheme of the multi-coset generation (L=10 and κ=5).

The complete observation consists of a data record of N_f blocks of κ non-uniform samples notated as $\mathbf{y}_f$. Thus, the notation can be compacted in $\mathbf{Y}$ as follows,

$$\mathbf{Y} = \begin{bmatrix} \mathbf{y}_1 & \cdots & \mathbf{y}_{N_f} \end{bmatrix} \tag{3.20}$$

In order to relate the acquired samples with the original Nyquist-sampled signal, let us consider $\mathbf{z}_f$ as the f-th block of L uniform Nyquist samples of $y(t)$,

$$\mathbf{z}_f = \begin{bmatrix} y(t_1^f) & \dots & y(t_L^f) \end{bmatrix}^T \tag{3.21}$$

where $t_n^f = (fL+n)T$. Thus, the relation between the Nyquist samples and the sub-Nyquist samples is given by,

$$\mathbf{y}_f = \mathbf{\Phi}_f \mathbf{z}_f \tag{3.22}$$

where $\mathbf{\Phi}_f$ is a matrix that non-uniformly selects κ samples of $\mathbf{z}_f$ ($\kappa < L$). This matrix $\mathbf{\Phi}_f$ is known as sampling matrix and is given by randomly selecting κ rows of the identity matrix $\mathbf{I}_L$ as the random conventional sub-sampling did. Note, however, that matrix $\mathbf{\Phi}_f$ is the same for all values of f, preserving a random sub-Nyquist pattern in each fth block. Henceforth, we remove the subindex f and we simply denote it as $\mathbf{\Phi}$.

3.5 CS-based candidate matching approach

This section is divided into two parts. Firstly, the compressed version of the candidate detector applied in the raw data domain presented in section (3.2.1) is addressed. If the candidate signal is completely known, it is easy to show that the optimal design would be the compressive matched filter [106]. In cases where the availability of complete candidate signal information is limited, we have seen that working with second order statistics seems more appropriate. In the last part of this section, the CS-based candidate correlation matching approach is introduced and its advantages are highlighted.

3.5.1 Compressed raw data domain

In this section we face the compressed-sampling version of section (3.2.1). Let us assume that the desired part of the received signal $y(t)$ has a sparse representation in a suitable overcomplete dictionary. Thus, according to CS theory, there is no need to acquire the whole set of Nyquist samples.

The CS extension of the candidate based detector is straightforward. The candidate signal $x_c(t)$ needs to be compressed in the same way as the received data $y(t)$ did. Considering $\mathbf{\Phi}$ the sub-Nyquist sensing matrix used to compress $y(t)$, the modulated CS candidate signal $\{\breve{x}_{cm}(n,\theta_m)\}$ can be obtained as follows,

$$\breve{\mathbf{x}}_{cm}(\theta_m) = \mathbf{\Phi}\left(\mathbf{x}_c \odot \mathbf{e}(\theta_m)\right) \tag{3.23}$$

where vector $\mathbf{x}_c$ and $\mathbf{e}(\theta_m)$ contain the Nyquist sampled versions of $x_c(t)$ and $e(t,\theta_m)$, respectively, and $\odot$ denotes the elementwise product of two vectors. In this formulation and all subsequent formulas in this thesis, the digital-time dependency n was removed to clarify notation. Therefore, based on this assumption, the candidate-based detector working with compressive samples is given by,

$$\min_{\beta(\theta_m)} \quad \mathbf{\Omega}\left[\breve{\mathbf{y}}, \beta(\theta_m)\breve{\mathbf{x}}_{cm}(\theta_m)\right] \tag{3.24}$$

That is, the detector should be tuned to the compressed version of the candidate signal $\breve{\mathbf{x}}_{cm}(\theta_m)$ and compare it with the compressed received signal $\breve{\mathbf{y}}$. Along this thesis we will use the most natural error function $\mathbf{\Omega}[\cdot,\cdot]$ for the raw data domain case which is given by the Euclidean norm.

- **Euclidean distance:** A simple matching approach can be developed in the raw data domain with the most natural matching function: the Euclidean distance. The detection problem in the raw data domain can be written as,

$$\min_{\beta(\theta_m)} \|\breve{\mathbf{y}} - \beta(\theta_m)\breve{\mathbf{x}}_{cm}(\theta_m)\|_{l_2}^2 \tag{3.25}$$

  Thus, the solution to (3.25) is given by,

$$\beta_E(\theta_m) = \frac{\breve{\mathbf{x}}_{cm}^H(\theta_m)\breve{\mathbf{y}}}{\breve{\mathbf{x}}_{cm}^H(\theta_m)\breve{\mathbf{x}}_{cm}(\theta_m)} \tag{3.26}$$

The comparison or candidate matching defined in (3.24) must be performed independently for all candidate hypothesis $\breve{\mathbf{x}}_{cm}(\theta_m)$, $m = 0, \ldots, M-1$. The multiple hypothesis can be incorporated into an overcomplete dictionary, which highlights the sparseness of the vector $\boldsymbol{\beta}$. This fact motivates the design of matching detection strategies based on the CS reconstruction techniques.

Detection with CS-based reconstruction

As mentioned before, the desired part of the received signal is assumed to be a linear combination of candidate signals (see section (3.3)). Thus, the signal model can be rewrited into conventional CS notation as follows,

$$\breve{\mathbf{y}} = \boldsymbol{\Phi}\mathbf{C}\boldsymbol{\beta} + \breve{\boldsymbol{\epsilon}} \tag{3.27}$$

where $\mathbf{C}$ denotes the overcomplete dictionary of Nyquist-sampled candidate signals defined as,

$$\mathbf{C} = \begin{bmatrix} \mathbf{x}_{cm}(\theta_0) & \mathbf{x}_{cm}(\theta_1) & \cdots & \mathbf{x}_{cm}(\theta_{M-1}) \end{bmatrix} \tag{3.28}$$

Vector $\breve{\boldsymbol{\epsilon}}$ encompasses imperfections of the proposed model, together with noise and interference. Vector $\boldsymbol{\beta}$ works as an indicator function as described in (3.16) and is assumed to be time invariant, i.e., $\boldsymbol{\beta} = \begin{bmatrix} \beta(\theta_0) & \beta(\theta_1) & \cdots & \beta(\theta_{M-1}) \end{bmatrix}^T$.

Since $\kappa < L$, there are many solutions to the following problem,

$$\min_{\boldsymbol{\beta} \geq 0} \|\breve{\mathbf{y}} - \boldsymbol{\Phi}\mathbf{C}\boldsymbol{\beta}\|_{l_2} \tag{3.29}$$

Among all the solutions of (3.29), we are interested in finding the sparsest one. The sparsity restriction is usually imposed by adding a l_1-norm constraint to the optimization problem [107]. The l_1-norm promotes sparse solution because it prevents diffusing the energy of the signal over a lot of coefficients. Although the natural choice would be to count the non-zero entries using the l_0-norm, as mentioned in the previous chapter, it is discarded due to its computational complexity. Thus, a common restriction to impose sparsity in $\boldsymbol{\beta}$ is given by,

$$\|\boldsymbol{\beta}\|_{l_1} \leq Q \tag{3.30}$$

where $\|\boldsymbol{\beta}\|_{l_1} = \sum_{m=0}^{M-1} |\beta(\theta_m)|$ and Q a given constant.

As seen previously, when the CS model is only corrupted by noise, there are two well-established recovery methods. One is l_1-norm minimization under a a l_2 constraint on the

residual. In the former, the l_2-norm of the residual is upperbounded by a constant χ derived from the noise power.

$$\min_{\boldsymbol{\beta}\geq 0} \|\boldsymbol{\beta}\|_{l_1} \quad \text{s.t.} \quad \|\check{\mathbf{y}} - \boldsymbol{\Phi}\mathbf{C}\boldsymbol{\beta}\|_{l_2} < \chi \tag{3.31}$$

The optimization problem stated in (3.31) can be solve using the denoising methods techniques introduced in section (2.1.3). The second alternative relaxes the constraint on the reconstruction error with a regularization or threshold parameter which is establish using information about the noise magnitude [13, 28, 108]. A family of iterative algorithms [15] were shown to provide the same reconstruction accuracy, generally with less computational complexity. Consequently, iterative algorithms become more preferable than directly solving the l_1-norm optimization problem and those will be the methods used throughout this thesis. Finding robust stopping criteria in iterative algorithms is a long standing problem. Some relevant stopping criteria are [16]:

- Stop the algorithm after a fixed number of iterations.
- Wait until the l_2-norm of the residual declines to a certain level.
- Halt the algorithm when the maximum total correlation between an atom or column of $\boldsymbol{\Phi}\mathbf{C}$ and the residual drops below a threshold.

In general, the methods for deciding when to halt the iteration depend on information available at each particular scenario. To the best of our knowledge, stopping criteria for models corrupted by interference have never been considered in the literature. One important drawback of the raw data domain is the difficulty on rejecting interference when solving (3.31). The interference immunity is not achieved only using a dictionary of candidate signal because, although the desired signals are assumed to be of different nature than that of the interference, they might not be orthogonal. The problem formulated in correlation domain brings more tools to face the interference problem.

3.5.2 Compressed correlation domain

In this section we face the compressed-sampling version of section (3.2.2). Let $\{R_y(k)\}$ denotes the correlations of the Nyquist-sampled signal $\{y(n)\}$ and $\mathbf{R}_y$ be the $L\times L$ correlation matrix (i.e. $[\mathbf{R}_y]_{ij} = R_y(j-i)$). For the purpose of the present work, let us define $\{R_c(k)\}$ as the correlations of the Nyquist-sampled candidate signal $\{x_c(n)\}$.

The correlation-matching perspective of the CS-based candidate detector is not straightforward. To build correlation matrices we need some kind of sampling pattern to allow us comparison between samples with the same time lag. The sampling strategy that has no aliasing problems and preserves a periodic pattern is the MC sampling (see section (3.4.2)). Following the notation of (3.22), the estimated autocorrelation matrix of the compressed samples $\hat{\mathbf{R}}_y \in \mathbb{C}^{\kappa\times\kappa}$ can be obtained as,

$$\hat{\mathbf{R}}_y = \frac{1}{N_f}\sum_{f=1}^{N_f} \mathbf{y}_f\mathbf{y}_f^H = \sum_{k=1}^{K} \boldsymbol{\Phi}\mathbf{R}_{x_k}\boldsymbol{\Phi}^H + \hat{\mathbf{R}}_{\boldsymbol{\epsilon}} \tag{3.32}$$

with $\mathbf{R}_{x_k} \in \mathbb{C}^{L\times L}$ being the sample autocorrelation matrix of the k-th Nyquist-sampled desired signal and $\hat{\mathbf{R}}_{\boldsymbol{\epsilon}}$ encompassing interference and noise compressed contributions.

Following the same idea as (3.11), a simple detector is given by,

$$\min_{p(\theta_m)} \mathbf{\Omega}\left[\hat{\mathbf{R}}_y, p(\theta_m)\mathbf{\Phi}\mathbf{R}_{cm}(\theta_m)\mathbf{\Phi}^H\right] \tag{3.33}$$

where,

$$\mathbf{R}_{cm}(\theta_m) = \mathbf{R}_c \odot \mathbf{F}(\theta_m) \tag{3.34}$$

In (3.34), $\mathbf{F}(\theta_m)$ indicates the matrix obtained from $f(\theta_m)$ that particularizes the candidate autocorrelation for a specific parameter θ_m.

The novelty of this second order statistics is that further restrictions can be imposed to better reject the interference. As mentioned before, the interference immunity is not achieved only with the candidate (signal/correlation) matching because, although the desired signals are assumed to be of different nature than that of the interference, they might not be orthogonal. The interference rejection capabilities of the detector are linked to the proper choice of the error function $\mathbf{\Omega}[\cdot,\cdot]$. Along this thesis we evaluate two types of error functions applied to correlation matrices: (1) error functions based on the Frobenius distance between the two matrices and (2) error functions based on the positive semi-definite character of the difference $(\hat{\mathbf{R}}_y - p(\theta_m)\mathbf{\Phi}\mathbf{R}_{cm}(\theta_m)\mathbf{\Phi}^H)$:

- **Frobenius Norm**: The first attempt is to define a detector based on the traditional Frobenius norm, which is the natural extension of the Euclidean norm for vectors to matrices. Thus, our problem can be written as,

$$\min_{p(\theta_m)\geq 0} \left\| \hat{\mathbf{R}}_y - p(\theta_m)\mathbf{\Phi}\mathbf{R}_{cm}(\theta_m)\mathbf{\Phi}^H \right\|_F^2 \tag{3.35}$$

  Developing (3.35) we get,

$$\min_{p(\theta_m)} \mathrm{Tr}\left[\left(\hat{\mathbf{R}}_y - p(\theta_m)\mathbf{\Phi}\mathbf{R}_{cm}(\theta_m)\mathbf{\Phi}^H\right)^H \left(\hat{\mathbf{R}}_y - p(\theta_m)\mathbf{\Phi}\mathbf{R}_{cm}(\theta_m)\mathbf{\Phi}^H\right)\right] \tag{3.36}$$

  Taking the derivative with respect to $p(\theta_m)$ and setting equal to zero we obtain,

$$\begin{aligned}\nabla_{p(\theta_m)} = &-2\mathrm{Tr}\left[(\mathbf{\Phi}\mathbf{R}_{cm}(\theta_m)\mathbf{\Phi}^H)^H\hat{\mathbf{R}}_y\right] \\ &+ 2p(\theta_m)\mathrm{Tr}\left[(\mathbf{\Phi}\mathbf{R}_{cm}(\theta_m)\mathbf{\Phi}^H)^H(\mathbf{\Phi}\mathbf{R}_{cm}(\theta_m)\mathbf{\Phi}^H)\right] = 0\end{aligned} \tag{3.37}$$

  The solution to (3.35), denoted as $p_F(\theta_m)$, is thus given by,

$$p_F(\theta_m) = \frac{\mathrm{Tr}\left[(\mathbf{\Phi}\mathbf{R}_{cm}(\theta_m)\mathbf{\Phi}^H)^H\hat{\mathbf{R}}_y\right]}{\mathrm{Tr}\left[\left(\mathbf{\Phi}\mathbf{R}_{cm}(\theta_m)\mathbf{\Phi}^H\right)^2\right]} \tag{3.38}$$

  The linear space considered by the Frobenius norm does not guarantee that the residual matrix, $\hat{\mathbf{R}}_y - p(\theta_m)\mathbf{\Phi}\mathbf{R}_{cm}(\theta_m)\mathbf{\Phi}^H$, belongs to the space generated by the autocorrelation matrices. A more proper distance is based on the geodesic distance, which is introduced below.

- **Geodesic Norm**: The second alternative is a detector based on the geodesic distance that best suits the space generated by hermitian matrices. The set of autocorrelation matrices is a convex cone because they are hermitian and positive semi-definite matrices.

Therefore, a more proper distance for the space generated by the semi-definite positive matrices is the geodesic distance. The geodesic distance [109] between $\mathbf{R}_1$ and $\mathbf{R}_2$ is the length of the geodesic line or segment described as,

$$\check{\mathbf{R}}(t) = \mathbf{R}_1^{1/2} e^{t(\mathbf{R}_1^{-1/2} \ln(\mathbf{R}_2) \mathbf{R}_1^{-1/2})} \mathbf{R}_1^{1/2} \tag{3.39}$$

In Fig. 3.2, the cone depicts the surface where all autocorrelation matrices are present. The points on the cone are connected by exponential paths and only locally looks like a flat Euclidean pace.

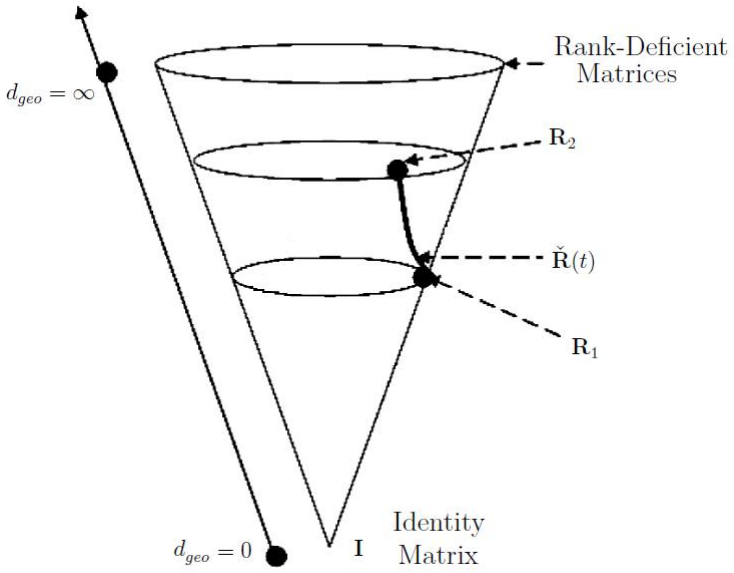

FIGURE 3.2: Illustration of geodesic distance in the cone of positive definite autocorrelation matrices.

The geodesic distance between $\mathbf{R}_1$ and $\mathbf{R}_2$ is given by (3.40), which is the l_2-norm of the vector formed by the natural logarithm of the generalized eigenvalues of the two matrices.

$$d_{geo}^2(\mathbf{R}_2, \mathbf{R}_1) = \sum_{i=1}^{\kappa} |Ln(\lambda_i)|^2 \tag{3.40}$$

where

$$\mathbf{R}_1^{-1} \mathbf{R}_2 \mathbf{e}_i = \lambda_i \mathbf{e}_i \quad \text{for} \quad i = 1, \ldots, \kappa \tag{3.41}$$

Identifying $\mathbf{R}_1 = p(\theta_m) \mathbf{\Phi} \mathbf{R}_{cm}(\theta_m) \mathbf{\Phi}^H$ and $\mathbf{R}_2 = \hat{\mathbf{R}}_y$ and minimizing (3.40), the power level estimate and the resulting minimum geodesic distance can be derived (3.42).

$$p_G(\theta_m) = \left(\prod_{i=1}^{\kappa} l_i \right)^{\frac{1}{\kappa}} \tag{3.42a}$$

$$d_{geo,min}^2 = \sum_{i=1}^{\kappa} |\ln (l_i / p_G(\theta_m))|^2 \tag{3.42b}$$

where l_i, $i = 1, \ldots, \kappa$, are defined as,

$$(\mathbf{\Phi} \mathbf{R}_{cm}(\theta_m) \mathbf{\Phi}^H)^{-1} \hat{\mathbf{R}}_y \mathbf{e}_i = l_i \mathbf{e}_i \quad \text{for} \quad i = 1, \ldots, \kappa \tag{3.43}$$

which are the generalized eigenvalues of the matrix $((\mathbf{\Phi R}_{cm}(\theta_m)\mathbf{\Phi}^H)^{-1}\hat{\mathbf{R}}_y)$.

- **Eigenvalue-based Method**: As stated before, correlation matrices are hermitian positive semi-definite matrices by definition and they lie in a convex cone. Thus, the difference between $\hat{\mathbf{R}}_y$ and the compressed reference matrix $p(\theta_m)\mathbf{\Phi R}_{cm}(\theta_m)\mathbf{\Phi}^H$ must lie in the surface of the cone too. In other words, the residual matrix must be positive semi-definite. This is,

$$\hat{\mathbf{R}}_y - p(\theta_m)\mathbf{\Phi R}_{cm}(\theta_m)\mathbf{\Phi}^H \succeq 0 \tag{3.44}$$

Therefore, the problem can be formulated as follows,

$$\begin{aligned} \max_{p(\theta_m)\geq 0} \quad & p(\theta_m) \\ \text{s.t.} \quad & \hat{\mathbf{R}}_y - p(\theta_m)\mathbf{\Phi R}_{cm}(\theta_m)\mathbf{\Phi}^H \succeq 0 \end{aligned} \tag{3.45}$$

This is, the maximum $p(\theta_m)$ that guarantees the difference between the data autocorrelation matrix and the candidate autocorrelation matrix remains positive semi-definite. If $\hat{\mathbf{R}}_y - p(\theta_m)\mathbf{\Phi R}_{cm}(\theta_m)\mathbf{\Phi}^H$ is positive semi-definite, $\mathbf{I} - p(\theta_m)\hat{\mathbf{R}}_y^{-1}(\mathbf{\Phi R}_{cm}(\theta_m)\mathbf{\Phi}^H)$ must be too. Thus, using the Eigen-Decomposition of $\hat{\mathbf{R}}_y^{-1}(\mathbf{\Phi R}_{cm}(\theta_m)\mathbf{\Phi}^H)$ defined by $\mathbf{U}(\theta_m)\mathbf{\Lambda}(\theta_m)\mathbf{U}^H(\theta_m)$,

$$\mathbf{I} - p(\theta_m)\mathbf{U}(\theta_m)\mathbf{\Lambda}(\theta_m)\mathbf{U}^H(\theta_m) \succeq 0 \;\Rightarrow\; \mathbf{I} - p(\theta_m)\mathbf{\Lambda}(\theta_m) \succeq 0 \tag{3.46}$$

Eqn. (3.46) defines κ different constraints,

$$1 - p(\theta_m)\lambda_q(\theta_m) \geq 0 \qquad q = 1, \ldots, \kappa \tag{3.47}$$

where $\lambda_1(\theta_m) \geq \lambda_2(\theta_m) \geq \ldots \geq \lambda_\kappa(\theta_m)$ are the eigenvalues contained in the diagonal of matrix $\mathbf{\Lambda}(\theta_m)$. Note that if (3.47) is satisfied for $q = 1$, it is satisfied $\forall q$. Thus, the restriction that always ensures positive semi-definite residual correlation at each scanned parameter θ_m is given by,

$$p_M(\theta_m) \leq \lambda_1^{-1}(\theta_m) \qquad m = 0, \ldots, M-1 \tag{3.48}$$

Note that the values $\lambda_1^{-1}(\theta_m)$, $m = 0, \ldots, M-1$, work as upperbounds on the estimated power of the desired signal. The meaning of eqn. (3.48) is that if the values of $p(\theta_m)$ are chosen lower than $\lambda_1^{-1}(\theta_m)$, the residual matrix will be positive semi-definite.

Again, solving (3.33) implies M comparisons or matchings to be performed independently. In contrast, CS-based reconstruction techniques can be used to jointly evaluate all possible hypothesis by defining an overcomplete dictionary of candidates.

Detection with CS-based reconstruction

As mentioned before, the autocorrelation of the received signal is assumed to be a summation of candidate autocorrelations (see section (3.3)). Therefore, the model in (3.9) can be conveniently rewrited into a sparse notation as follows,

$$\hat{\mathbf{r}}_y = \mathbf{kron}(\mathbf{\Phi}, \mathbf{\Phi})\mathbf{BSp} + \hat{\mathbf{r}}_{\boldsymbol{\epsilon}} = \mathbf{Ap} + \hat{\mathbf{r}}_{\boldsymbol{\epsilon}} \tag{3.49}$$

where $\hat{\mathbf{r}}_y \in \mathbb{C}^{\kappa^2 \times 1}$ vector formed by the concatenation of the columns of $\hat{\mathbf{R}}_y$. From now on, to clarify notation, the concatenation of columns will be denoted with the operator $\mathbf{vec}(\cdot)$.

Therefore, $\hat{\mathbf{r}}_y = \mathbf{vec}(\hat{\mathbf{R}}_y)$. $\mathbf{B} \in \mathbb{C}^{\kappa^2 \times \kappa^2}$ contains the correlation information of the desired signal and is defined as $\text{diag}(\mathbf{r}_c)$ where $\mathbf{r}_c = \mathbf{vec}(\mathbf{R}_c)$. Matrix $\mathbf{S}$ defines the scanning grid of the parameter θ,

$$\mathbf{S} = \begin{bmatrix} \mathbf{s}(\theta_0) & \mathbf{s}(\theta_1) & \cdots & \mathbf{s}(\theta_{M-1}) \end{bmatrix} \tag{3.50}$$

where $\mathbf{s}(\theta_m) \in \mathbb{C}^{\kappa^2 \times 1}$ is defined as $\mathbf{vec}(\mathbf{F}(\theta_m))$. The variable $\hat{\mathbf{r}}_{\boldsymbol{\epsilon}}$ encompasses interference and noise contribution. Vector $\mathbf{p} = \begin{bmatrix} p(\theta_0) & p(\theta_1) & \cdots & p(\theta_{M-1}) \end{bmatrix}^T$ can be viewed as the output of an indicator function, whose elements different from zero provide estimates of the power of the desired signal (see (3.17)).

Again, since $\kappa < M$, there are infinitely many solutions to the following problem,

$$\min_{\mathbf{p} \geq 0} \|\hat{\mathbf{r}}_y - \mathbf{A}\mathbf{p}\|_{l_2}^2 \tag{3.51}$$

Among all the solutions of (3.51), we are interested in the solution that meets the following requirements: (1) $\mathbf{p}$ must be sparse, and (2) the solution must not include interference. In the previous section, we mentioned that the interference immunity is not achieved only with the overcomplete dictionary $\mathbf{A}$ and we presented alternative second-order based strategies to enhance the interference rejection capabilities of the detector. The goal of the remainder of this section is to impose sparsity and interference rejection at once.

The sparsity restriction is usually imposed by adding a l_1-norm constraint. However, as seen before, the l_1-norm tends to penalize large coefficients to the detriment of smaller coefficients [8]. Weighted l_1-norm have been proposed to democratelly penalize nonzero entries. Let us consider the following weighted l_1-norm,

$$\sum_{m=0}^{M-1} w_m \cdot p(\omega_m) \leq \alpha \tag{3.52}$$

where $w_0, \ldots, w_{M-1}$ are positive weights. Note that the values of $p(\omega_m)$ must be greater than or equal to zero and, thus, the absolute value is removed for simplicity. The value of α depends on the chosen weights. One way to rectify the dependence on magnitude of the l_1-norm is to enforce each product $w_m \cdot p(\omega_m)$ be equal to 1. Thus, the weights must be estimates of the inverse power corresponding to the primary users present in the band under scrutiny. Ideally,

$$w(\omega_m) = \begin{cases} \frac{1}{\sigma^2(\theta_k)} & \text{if } \omega_m = \omega_k \quad (H_1) \\ 0 & \text{otherwise} \quad (H_0) \end{cases} \tag{3.53}$$

Interestingly, initial estimates of the powers can be obtained from the upperbound defined in eqn. (3.48),

$$w_m = \lambda_1(\omega_m) \qquad m = 0, \ldots, M-1 \tag{3.54}$$

With the weights defined in eqn. (3.54), the value of α in eqn. (3.52) is approximately equal to the number of primary users present in the band under scrutiny, K, which determines the sparsity level of vector $\mathbf{p}$. However, the value of K is unknown. The level of sparsity is typically unknown in CS problems even though it plays a fundamental role in solving the sparse vector recovery problem.

In this thesis, sparse reconstruction is performed using the iterative greedy algorithm known as Weighted Orthogonal Matching Pursuit (WOMP) [110] which provides fast l_1 solutions with low computational complexity and is appropriate to the problem at hand. As mentioned before, conventional CS assumes sparse signals corrupted by noise. As a

consequence, robust stopping criteria for iterative reconstruction algorithms are usually based on information about the noise magnitude. Our model considers noise and interference (both unknown) and, as such, impedes the application of conventional stopping criteria.

The weights defined in eqn. (3.54) impose that the licensed-holder users are selected by WOMP before the interference. This is because the value of w_m^{-1} is expected to be ideally zero at the frequency bands that are not occupied by the licensed users. Interestingly, if a licensed-holder user is selected, the weighted l_1-norm will increse one point with respect to the weighted l_1-norm of the previous iteration. Consequently, after K iterations, the weighted l_1-norm is expected to be equal to K and the residual is expected to contain noise plus interference. We would like the algorithm to stop here. If we keep running the algorithm, the next selected atom will probably correspond to an interferent signal. Therefore, the increase of the weighted l_1-norm at the $(K+1)$-th iteration with respect to the weighted l_1-norm at the (K)-th iteration will be different than one (ideally infinity). So, we propose to stop the WOMP when the difference between the present weighted l_1-norm and the weighted l_1-norm of the previous iteration does not fall into the following interval,

$$1 - \xi_{down} \leq \Delta_{l_1}^{(t)} \leq 1 + \xi_{up} \tag{3.55}$$

where $\Delta_{l_1}^{(t)} = \sum_{m=0}^{M-1} w_m \cdot p^{(t)}(\omega_m) - \sum_{m=0}^{M-1} w_m \cdot p^{(t-1)}(\omega_m)$, with $\mathbf{p}^{(t)}$ being the estimated sparse vector at iteration t. The values of $\xi_{down} \in [0, 1)$ and $\xi_{up} \in [0, \infty)$ determine the detector performance and their value should be chosen based on the particular characteristics of the scenario at hand.

Chapter 4

Application I: Spectrum Sensing for Cognitive Radio

The material presented in this chapter was partially published by the author in [**V**], [**VII**], [**VIII**], [**X**], [**XII**], [**XV**], [**XVIII**] and [**XIX**].

In this section, the candidate detector based on compressive sampling is applied to wideband spectrum sensing for open spectrum scenarios. Capitalizing on the sparsity described by licensed users, we apply the proposed detector for primary user's spectrum identification, providing an accurate estimation of the frequency support, transmitted power and Angle of Arrival (AoA) of the primary systems. We evaluate the resulting spectrum sensing technique with MATLAB-based simulation results that show the effectiveness in primary user detection and prove its interference rejection capabilities. This section extends previous results presented in [111–114] by researchers from the UPC and the Centre Tecnològic de Comunicacions de Catalunya (CTTC), Castelldefels, Spain, where only the frequency and power of the primary user were identified without tackling the sampling bottleneck. There are two main reasons why CS is particularly appealing in the spectrum monitoring problem: (1) due to the timing requirements for rapid sensing, which seriously limits the number of measurements that can be acquired from the received signal; and (2) the implementation quickly becomes untenable for wideband spectrum sensing. Here, we sense and compress in a single stage, thus alleviating the sampling burden and allowing fast spectrum sensing.

4.1 Problem statement

Our goal is to decide whether a given frequency band is occupied by a primary user or not using a sub-Nyquist sampling alternative suitable for sparse signals. Let us denote $x(t)$ the wideband signal representing the superposition of different primary services in a CR network. Signal $x(t)$ is assumed to be sparse multiband signal, i.e, a bandlimited, continuous-time, squared integrable signal that has all of its energy concentrated in a small number of disjoint frequency bands. In other words, its spectral support has Lebesgue measure small relative to the overall signal bandwidth [37]. Denoting the spectral density of $x(t)$ as $S_x(f)$, the spectral support $\mathcal{F} \subset [0, f_{max}]$ of the multiband signal $x(t)$, namely $S_x(f) = 0$, $f \notin \mathcal{F}$, is the union of

the frequency intervals that contain the signal's energy:

$$\mathcal{F} = \bigcup_{i=1}^{N_b} [a_i, b_i) \tag{4.1}$$

The spectral occupancy Ω is defined as,

$$\Omega = \frac{\lambda(\mathcal{F})}{f_{max}} \quad 0 \leq \Omega \leq 1 \tag{4.2}$$

where $\lambda(\mathcal{F})$ is the Lebesgue measure of the frequency set $\mathcal{F}$ which, in this particular case, is equal to $\sum_{i=1}^{N_b} (b_i - a_i)$. For the set of sparse multiband signals, Ω ranges from 0 to 0.5 (see Fig. 4.1). In the spectrum sensing framework, the spectral support F is unknown but the total bandwidth under study is assumed to be sparse.

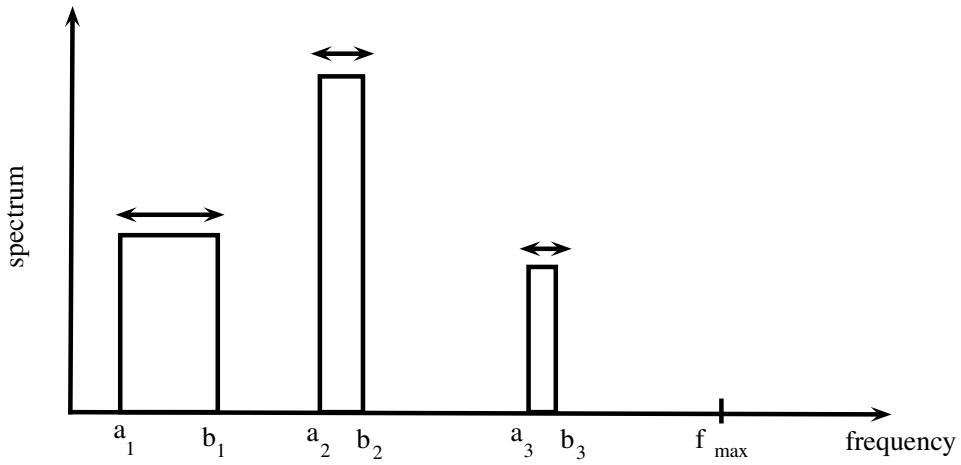

FIGURE 4.1: Spectrum of a sparse multiband signal, with N_b=3 and spectral occupancy $\Omega < 0.5$.

The Nyquist rate corresponding to $x(t)$ is $T = 1/f_{max}$. According to Landau's lower bound [103], the minimum average sampling rate for most signals is given by the Nyquist rate multiplied by the spectral occupancy, which is often much lower than the corresponding Nyquist rate.

Some of the channels left idle by primary users may be already occupied by low-regulated transmissions generated by the unlicensed radios. The goal of this part of the thesis is to obtain the frequency locations and extract as much information as possible about the primary users using a correlation matching spectrum sensing strategy based on the compressed samples. The non-regulated activity of the spectrum will be denoted as $i(t)$ and henceforth is considered interference. The problem of determining weather a given frequency is occupied or not by a licensed radio can be modeled into a binary hypothesis test,

$$y(t) = \begin{cases} i(t) + \eta(t) & (H_0) \\ x(t) + i(t) + \eta(t) & (H_1) \end{cases} \tag{4.3}$$

where (H_0) stands for the absence of primary signal and (H_1) represents the presence of a primary signal in the frequency channel under study. $\eta(t)$ is AWGN, $\mathcal{N}(0, \sigma_\eta^2)$. The interference $i(t)$ is independent of the noise and primary signal, and we assume that its spectral

shape is different from that of the primary. In practice, the secondary user is rarely going to use the same modulation as the primary. Moreover, the secondary user generally transmits at a lower rate than the primary in order to not disturb the quality of service of the primary user. Therefore, and as a baseline, it is assumed throughout this section that the interference has bandwidth smaller than that of the primary. The presence of unknown interference, which has not been addressed in conventional spectrum sensing publications, adds additional challenges.

4.2 Spectral matching detection

This part of the thesis assumes that the primary signal $x(t)$ is unknown, i.e., the transmitted symbols are not known a priori. For such a case, it is more appropriate to define a second-order based detector. Here, the spectrum characteristics of the primary signals, which can be obtained by identifying its transmission technologies, are used as features. The basic strategy of the proposed detector is to compare the a priori known spectral shape of the primary user with the power spectral density of the received signal. To save us from computing the power spectral density of the received signal, the comparison is made in terms of autocorrelation by means of a correlation matching. The diagram of the CR receiver is sketched in Fig. 4.2. Firstly, taking advantage of the sparsity of the primary user's signal spectrum, a sub-Nyquist sampling is used to overcome the problem of high sampling rate. Then, the compressed samples are processed in the autocorrelation estimation stage and finally, the correlation-matching based spectrum sensing is performed using a predetermined spectral shape, which has to be known a priori.

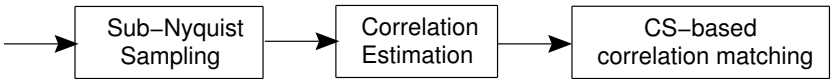

FIGURE 4.2: Block diagram of the cognitive receiver

4.2.1 Signal model

Single antenna receiver

The basic idea of Cognitive Radio is spectral reusing or spectrum sharing, which allows the unlicensed users to communicate over licensed spectrum when the licensed holders are not fully utilizing it. Thus, the received signal $y(t)$ consists on the superposition of multiple primary and secondary (interference) services as shown in (4.3). Let us rewrite the received signal as,

$$y(t) = \sum_{k=1}^{K} x(t, \omega_k) + i(t) + \eta(t) \tag{4.4}$$

where K denotes the number of primary users. The analytic representation of the k-th primary user is denoted as $x(t, \omega_k)$, which is given by,

$$x(t, \omega_k) = a_k(t) e^{j(\omega_0 + \omega_k)t} \tag{4.5}$$

where $a_k(t)$ indicates the complex envelope of the source and ω_k denotes the baseband frequency of the source with respect to the center frequency of the band under scrutiny ω_0. For the sake of simple notation, we are assuming linear propagation channel with no distortion. However, the robustness in front of a frequency selective channel, instead of flat fading, have also been studied using computer simulations.

Multiple antenna receiver

In this section, we introduce the notation for multiple antenna receivers used when dealing with the primary users' angle of arrival estimation.

An array antenna is a configuration of multiple antenna elements arranged and interconnected in space [115]. Arrays can be constructed in various types of geometries. Here, we focus on uniform linear arrays (ULA) of omni-directional isotropic sensors, in which the elements are aligned and equispaced along a straight line. Fig. 4.3 shows the general configuration for an ULA having N elements with a distance d between sensor elements. As observed from Fig. 4.3, the far-field approximation is considerer in this thesis.

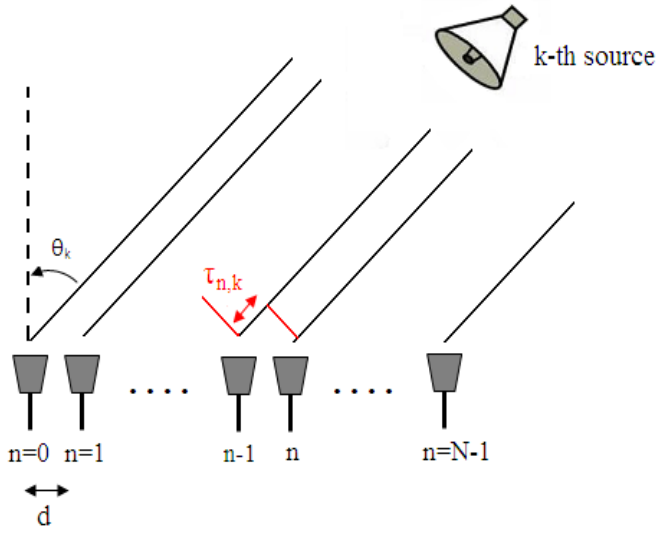

FIGURE 4.3: Geometry on Uniform Linear Array (ULA)

The signal received at the nth sensor, denoted as $y(t,n)$, will be a superposition of delayed versions of the original sources. That is,

$$y(t,n) = y(t - t_0 - \tau_n) = \sum_{k=1}^{K} x(t - t_0 - \tau_{n,k}, \omega_k, \theta_k) + i(t,n) + \eta(t,n) \tag{4.6}$$

where t_0 is the propagation delay up to the phase center, τ_n and $\tau_{n,k}$ are the propagation delays, with respect to the phase center, of the nth sensor and of the kth source arriving to the nth sensor, respectively. The angle of arrival of the kth primary source is denoted as θ_k. The array outputs are corrupted by interference $i(t,n)$ and AWGN $\eta(t,n)$, $n = 0, \ldots, N-1$, which are uncorrelated with the primary sources. Taking $t_0 = 0$ and without loss of generality, the kth primary signal received at the nth sensor is given by,

$$x(t - \tau_{n,k}, \omega_k, \theta_k) = a_k(t - \tau_{n,k}) e^{j(\omega_0 + \omega_k)(t - \tau_{n,k})} \approx a_k(t) e^{j(\omega_0 + \omega_k)(t - \tau_{n,k})} \tag{4.7}$$

Note that (4.7) assumes the narrowband model, i.e, negligible group delay. Since $\omega_k << \omega_0$, the expression (4.7) can be approximated as,

$$x(t-\tau_{n,k},\omega_k,\theta_k) \approx a_k(t)e^{j\omega_0 t}e^{j\omega_k t}e^{-j\omega_0\tau_{n,k}} \tag{4.8}$$

The phase load is determined by the relative delay $\tau_{n,k}$, which can be extracted from the geometry of the scenario (see Fig. 4.3). The relative delay $\tau_{n,k}$ depends only on the distance from the sensor to the phase center, its location and the angle of arrival of the source. Dividing this distance by the velocity of propagation, c, we obtain the following expression of $\tau_{n,k}$,

$$\tau_{n,k} = n\frac{d}{c}\sin(\theta_k) \tag{4.9}$$

where c is the speed of the light. $0°$ denotes the broadside direction while $90°$ denote the end-fire directions in this thesis.

Summarizing, the kth primary signal received at the nth sensor can be written as,

$$x(t-\tau_{n,k},\omega_k,\theta_k) \approx a_k(t)e^{j\omega_0 t}e^{j\omega_k t}e^{-j\omega_0 n\frac{d}{c}\sin(\theta_k)} \tag{4.10}$$

A general vector form of the array output model is stated as,

$$\mathbf{y}(t) = \sum_{k=1}^{K} a_k(t)e^{j\omega_0 t}e^{j\omega_k t}\mathbf{s}(\theta_k) + \mathbf{i}(t) + \boldsymbol{\eta}(t) \tag{4.11}$$

where vector $\mathbf{s}(\theta_k)$, known as steering vector, is defined as,

$$\mathbf{s}(\theta_k) = \begin{bmatrix} 1 & e^{-j\omega_0\frac{d}{c}\sin(\theta_k)} & \dots & e^{-j\omega_0(N-1)\frac{d}{c}\sin(\theta_k)} \end{bmatrix}^T \tag{4.12}$$

which is a Vandermonde vector. The snapshot expression corresponding to all N antennas given in (4.11) can be rewritten into a more compact matrix form as follows,

$$\mathbf{y}(t) = \mathbf{S}\mathbf{a}(t) + \mathbf{i}(t) + \boldsymbol{\eta}(t) \tag{4.13}$$

where

$$\mathbf{S} = \begin{bmatrix} \mathbf{s}(\theta_1) & \mathbf{s}(\theta_2) & \cdots & \mathbf{s}(\theta_K) \end{bmatrix} \tag{4.14a}$$

$$\mathbf{a}(t) = \begin{bmatrix} a_1(t)e^{j\omega_0 t} & a_2(t)e^{j\omega_0 t} & \cdots & a_K(t)e^{j\omega_0 t} \end{bmatrix}^T \tag{4.14b}$$

$$\mathbf{y}(t) = \begin{bmatrix} y(t,0) & y(t,1) & \cdots & y(t,N-1) \end{bmatrix}^T \tag{4.14c}$$

$$\mathbf{i}(t) = \begin{bmatrix} i(t,0) & i(t,1) & \cdots & i(t,N-1) \end{bmatrix}^T \tag{4.14d}$$

$$\boldsymbol{\eta}(t) = \begin{bmatrix} \eta(t,0) & \eta(t,1) & \cdots & \eta(t,N-1) \end{bmatrix}^T \tag{4.14e}$$

4.2.2 Sub-Nyquist sampling

Periodic non-uniform sub-Nyquist sampling is a popular approach among compressive sampling techniques. In this part of the thesis we consider the multi-coset (MC) sampling [105] described in section 3.4.2.

Assuming a Nyquist-rate sampling T, let us consider $\mathbf{z}_f(n)$ as the f-th block of L uniform Nyquist samples of the received signal $y(t,n)$,

$$\mathbf{z}_f(n) = \begin{bmatrix} y(t_1^f, n) & \dots & y(t_L^f, n) \end{bmatrix}^T \tag{4.15}$$

where $t_q^f = (fL+q)T$. The sub-Nyquist observation consists of a data record of N_f blocks of κ non-uniform samples denoted as $\mathbf{y}_f(n)$, whose relation with the Nyquist sampled block $\mathbf{z}_f(n)$ is given by,

$$\mathbf{y}_f(n) = \mathbf{\Phi}\mathbf{z}_f(n) \tag{4.16}$$

where $\mathbf{\Phi}$ is the sampling matrix that non-uniformly selects κ samples of $\mathbf{z}_f(n)$ with $\kappa < L$.

4.2.3 Sub-Nyquist autocorrelation estimation

Single antenna receiver

Following the notation of (4.16) and removing the sub-index n corresponding to the antenna sensor being used, the correlation matrix $\hat{\mathbf{R}}_y \in \mathbb{C}^{\kappa\times\kappa}$ can be obtained as,

$$\hat{\mathbf{R}}_y = \frac{1}{N_f}\sum_{f=1}^{N_f} \mathbf{y}_f\mathbf{y}_f^H = \Phi\left[\frac{1}{N_f}\sum_{f=1}^{N_f}\mathbf{z}_f\mathbf{z}_f^H\right]\Phi^H = \sum_{k=1}^{K}\mathbf{\Phi}\mathbf{R}_{x_k}\mathbf{\Phi}^H + \hat{\mathbf{R}}_{\boldsymbol{\epsilon}} \tag{4.17}$$

where $\mathbf{R}_{x_k} \in \mathbb{C}^{L\times L}$ indicates the estimated autocorrelation matrix of the kth Nyquist-sampled primary user, and $\hat{\mathbf{R}}_{\boldsymbol{\epsilon}}$ encompassing interference and noise compressed contributions. Concerning the order κ or dimension of correlation matrices, it is expected that accurate results are obtained when the order selected is above the number of samples per symbol pulse.

Multiple antenna receiver

Following the notation of (4.16), let us arrange the κ consecutive compressive snapshots in a matrix $\mathbf{Y}_f \in \mathbb{C}^{\kappa\times\kappa N}$ as follows,

$$\mathbf{Y}_f = \begin{bmatrix} \mathbf{y}_f(0) & \cdots & \mathbf{y}_f(n) & \cdots & \mathbf{y}_f(N-1) \end{bmatrix} \tag{4.18}$$

Thus, the estimated data autocorrelation matrix can be obtained as follows,

$$\hat{\mathbf{R}}_y = \frac{1}{N_f}\sum_{f=1}^{N_f}\text{vec}(\mathbf{Y}_f)\text{vec}^H(\mathbf{Y}_f) \tag{4.19}$$

where $\text{vec}(\mathbf{Y}_f)$ is $\mathbb{C}^{\kappa N\times 1}$ and denotes the concatenation of the κ snapshots contained in $\mathbf{Y}_f$. In general, when the number of snapshots being averaged N_f is greater than ten times the number of sensors N, the estimated correlation matrix $\hat{\mathbf{R}}_y$ stabilizes on the true value of the autocorrelation $\mathbf{R}_y$.

4.2.4 Candidate correlation matrix

In order to obtain the frequency location of each primary user, the baseband reference autocorrelation $\mathbf{R}_b \in \mathbb{R}^{L\times L}$ (extracted from spectral features of the primary user) is modulated

by a rank-one matrix formed by the steering frequency vector at the sensed frequency ω_m as follows,

$$\mathbf{R}_{cm}(\omega_m) = \left[\mathbf{R}_b \odot \mathbf{e}(\omega_m)\mathbf{e}^H(\omega_m)\right] \tag{4.20}$$

where $\odot$ denotes the elementwise product of two matrices and $\mathbf{e}(\omega_m) \in \mathbb{C}^{L\times 1}$ is the steering vector defined as,

$$\mathbf{e}(\omega_m) = \begin{bmatrix}1 & e^{j\omega_m} & \dots & e^{j(L-1)\omega_m}\end{bmatrix}^T \tag{4.21}$$

The resulting modulated candidate correlation $\mathbf{R}_{cm}(\omega_m) \in \mathbb{C}^{L\times L}$ must be compressed in the same way we did for the data, i.e., using the same sampling matrix $\mathbf{\Phi}$, as follows,

$$\hat{\mathbf{R}}_{cm}(\omega_m) = \mathbf{\Phi}\mathbf{R}_{cm}(\omega_m)\mathbf{\Phi}^H \tag{4.22}$$

An extended compressed candidate correlation matrix must be built to cope with the angle of arrival dependency, if a multiple antenna receiver is being considered. The angle-dependent candidate correlation matrix can be obtained as follows,

$$\hat{\mathbf{R}}_{cm}(\omega_m, \theta_i) = \mathbf{S}(\theta_i)\hat{\mathbf{R}}_{cm}(\omega_m)\mathbf{S}^H(\theta_i) \tag{4.23}$$

where matrix $\mathbf{S}(\theta_i) \in \mathbb{C}^{\kappa N\times\kappa}$ is defined as $\mathbf{S}(\theta_i) = \mathbf{I}_\kappa \otimes \mathbf{s}_d(\theta_i)$, with $\mathbf{I}_\kappa$ being the identity matrix of dimension κ, $\mathbf{s}_d(\theta_i) = \begin{bmatrix}1 & e^{-j\omega_0\frac{d}{c}\sin(\theta_i)} & \dots & e^{-j\omega_(N-1)\frac{d}{c}\sin(\theta_i)}\end{bmatrix}^T$ and $\otimes$ denoting the Kronecker product. The dimensions of the general candidate correlation matrix are $\hat{\mathbf{R}}_{cm}(\omega_m, \theta_i) \in \mathbb{C}^{\kappa N\times\kappa N}$.

According to this notation, the corresponding model for the data autocorrelation matrix defined in (4.17) is given by,

$$\hat{\mathbf{R}}_y = \sum_{k=1}^{K} \sigma^2(\omega_k, \theta_k)\hat{\mathbf{R}}_{cm}(\omega_k, \theta_k) + \hat{\mathbf{R}}_{\boldsymbol{\epsilon}} \tag{4.24}$$

4.2.5 Correlation matching

Summarizing, the problem to solve consists in finding the frequency and the angle that the candidate correlation has to be modulated to best fit the received data autocorrelation matrix $\hat{\mathbf{R}}_y$ and to find the contribution of this modulated candidate autocorrelation contained in $\hat{\mathbf{R}}_y$. Thus, the procedure not only provides the frequency location and angle of arrival of the desired user but also an estimation of its transmitted power.

The two possible candidate correlation matching procedures were explained in detail in section (3.5.2). Following the expressions of section (3.5.2), we can briefly review the two different ways to solve the matching:

- **Direct correlation matching:** Solving

$$\min_{p(\omega_m,\theta_i)\geq 0} \mathbf{\Omega}\left[\hat{\mathbf{R}}_y, p(\omega_m, \theta_i)\hat{\mathbf{R}}_{cm}(\omega_m, \theta_i)\right] \tag{4.25}$$

  which can be solve considering the Frobenius norm, the Geodesic norm or the Eigenvalue-based method. Eqn. (4.25) implies all the comparisons or matchings defined by the grid (ω_m, θ_i), $m = 0, \dots, M-1$, $i = 0, \dots, Q-1$, to be performed independently.

- **CS-based reconstruction:** Thus far, in this thesis, the CS-based reconstruction has been applied to the frequency sensing problem only, leaving the angle of arrival search as a future research point. Focusing on the frequency scanning, the problem consist in solving,

$$\min_{\mathbf{p}\geq 0} \quad \|\mathbf{W}\mathbf{p}\|_{l_1} \quad \text{s.t.} \quad \hat{\mathbf{r}}_y \approx \mathbf{A}\mathbf{p} \tag{4.26}$$

where $\hat{\mathbf{r}}_y = \mathbf{vec}(\hat{\mathbf{R}}_y)$, $\mathbf{A} = \mathbf{kron}(\mathbf{\Phi}, \mathbf{\Phi})\mathbf{BS}$ with $\mathbf{B} = \text{diag}(\mathbf{r}_c)$ where $\mathbf{r}_c = \mathbf{vec}(\mathbf{R}_c)$. Matrix $\mathbf{S} \in \mathbb{C}^{L^2 \times M}$ defines the scanning grid of the frequency parameter ω_m, $m = 0, \ldots, M-1$,

$$\mathbf{S} = \begin{bmatrix} \mathbf{s}(\omega_0) & \mathbf{s}(\omega_1) & \cdots & \mathbf{s}(\omega_{M-1}) \end{bmatrix} \tag{4.27}$$

where $\mathbf{s}(\omega_m)$ is defined as $\mathbf{vec}(\mathbf{e}(\omega_m)\mathbf{e}^H(\omega_m))$. Matrix $\mathbf{W} \in \mathbb{R}^{M \times M}$ is defined as $\mathbf{W} = \text{diag}(\mathbf{w})$, being $\mathbf{w} = \begin{bmatrix} w_0 & \cdots & w_{M-1} \end{bmatrix}^T$ the weights of the l_1 norm (see section (3.5.2) for more details). The sparse reconstruction presented in (4.26) is performed using the iterative greedy algorithm known as Weighted Orthogonal Matching Pursuit (WOMP) [110] which provides fast l_1 solutions with low computational complexity and is appropriate to the problem at hand.

4.3 Simulation results

4.3.1 Direct matching

Frequency scanning

To test the ability of the proposed sparse correlation matching-based spectrum sensing technique to properly label a desired user, we first consider a scenario with one desired user in the presence of noise. The desired user is assumed to be a Binary Phase Shift Keying (BPSK) signal with a rectangular pulse shape, and 4 samples per symbol. The SNR of the desired user is 10 dB and the normalized carrier frequency is $\omega = 0.2$ (the bandwidth under scrutiny is 10MHz). The size of the observation $\mathbf{z}_f$ in $L = 33$ samples. The sampling rates of $\mathbf{y}_f$ and $\mathbf{z}_f$ are related through the compression rate $\rho = \frac{\kappa}{L}$. To strictly focus on the performance behavior due to compression and remove the effect of insufficient data records, the size of the compressed observations is forced to be the same for any compression rate. Therefore, we set $N_f = 2L\epsilon\rho^{-1}$ where ϵ is a constant (in the following results $\epsilon = 10$). Thus, for a high compression rate, the estimator takes samples for a larger period of time. The spectral occupancy (set of frequencies where the Fourier transform does not vanish) Ω for this particular example is about 0.25. According to [38], the signal admits perfect reconstruction from periodic nonuniform sampling at rates approaching Landau's lower bound [103] equal to the measure of the spectral occupancy. Thus, if the spectral occupancy is 0.25, we can discard three of every fourth Nyquist samples. The simulation parameters are summarized in Table 4.1. The frequency grid considers $M = 200$ points equispaced over the desired bandwidth under scrutiny $B_\omega = \omega_{M-1} - \omega_0$,

$$\omega_m = \omega_0 + m\Delta_\omega \quad m = 0, \ldots, M-1 \tag{4.28}$$

where ω_0 and Δ_ω are the lowest frequency in the band under scrutiny and the frequency step size, respectively. In this case, the frequency resolution is given by Δ_ω, which is equal to 50 KHz.

TABLE 4.1: Simulation Parameters

$\rho = \frac{\kappa}{L}$	**1**	**0.76**	**0.52**	**0.24**
κ	33	25	17	8
N_f	660	871	1281	2723
Acquisition Time (ms)	2.2	2.9	4.2	9.0

Fig. 4.4 shows the performance for different compression rates of the three different choices of the error function $\mathbf{\Omega}[\cdot,\cdot]$ in eqn. (4.25): the Frobenius norm ($p_F(\omega_m)$), the Geodesic norm ($p_G(\omega_m)$ and $d^{-1}_{geo,min}(\omega_m)$) and the eigenvalue-based method ($p_M(\omega_m)$). The $p_F(\omega_m)$ estimate, which is shown in Fig. 4.4(a), presents lower resolution and higher leakage compared with $p_M(\omega_m)$ and $d^{-1}_{geo,min}(\omega_m)$, which are plotted in Fig. 4.4(b) and in Fig. 4.4(c1), respectively. From Fig. 4.4 it can be concluded that the best power estimate in terms of resolution is given by $p_M(\omega_m)$. Moreover, the range of $d^{-1}_{geo,min}(\omega_m)$ is smaller than the range of $p_M(\omega_m)$, which is longer than 15 dB when there is no compression and decreases when the compression rate decreases. This robustness makes us think that eigenvalue-based method may still work in scenarios with low SNR, where the geodesic norm probably fails (it is confirmed in next results). On the other hand, it is noted the independence of $p_G(\omega_m)$ with respect to the frequency ω_m, which may be observed in Fig.4.4(c2).

Fig. 4.5 depicts the same as Fig. 4.4 but with 2 BPSK desired signals: one located at normalized frequency $\omega_1 = 0.2$ and one located at normalized frequency $\omega_2 = 0.7$, both with the same SNR level equal to 10 dB. While all three methods successfully detect the 2 primary users, $p_G(\omega_m)$ is not able to provide two power level estimates because the non-dependency on the frequency of p_G.

Fig. 4.6 considers the same primary user considered in Fig. 4.4 but with the presence of a narrow band interference (pure tone) with SNR=10 dB at normalized frequency $\omega_I = 0.7$. While $p_M(\omega_m)$ remains practically unfazed, the geodesic norm based detector performance has suffered a slight degradation. The method using the Frobenius norm, shown in Fig. 4.4(a), clearly works as an energy detector. This sensitivity to interference suggests to discard the Frobenius norm in favor of the two other methods. Although both figures (Fig. 4.4 and Fig. 4.6) make evident the degradation of the correlation-matching based spectrum sensing techniques in terms of detection capability due to the effect of the compression, it is interesting to note that the frequency and power level estimation do not suffer from the compression.

If a deterministic pattern (e.g., pilot, preamble, or training sequence) of primary signals is known, then the optimal detection performance is given by the candidate detector applied in the raw data domain. Therefore, if a complete prior knowledge about the structure of the primary signal is available, there is no need to compute higher-order statistics such as correlation. However, the available knowledge of the primary users signaling features is not usually precise, so the performances of matched filter degrade quickly. In such cases, using second order statistics, such correlation, in lieu of the data, may lead to important performance improvements.

This concept is easily illustrated with the following simulation example. Let us consider a scenario with a single primary user (BPSK, rectangular pulse, 4 samples per symbol, SNR=10 dB, and frequency $\omega = 0.2$). Known pilot symbols are transmitted. To investigate the impact of candidate imperfections we introduce phase distortion on the received symbols. In particular, we add a random phase following a normal distribution with zero mean and

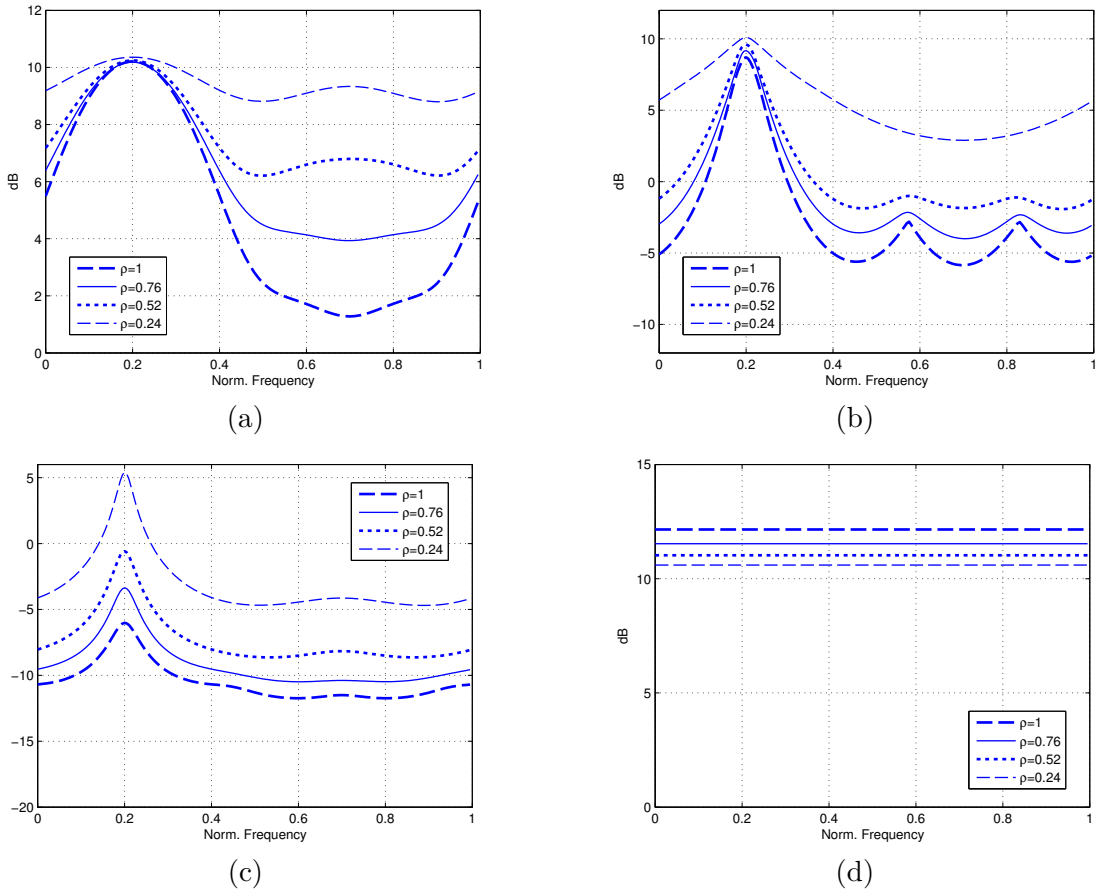

FIGURE 4.4: Performance of candidate detector solving direct correlation matching. The scenario considers a single primary user with the following parameters: BPSK signal with rectangular pulse and 4 samples per symbol, SNR=10 dB at frequency $\omega = 0.2$. (a) $p_F(\omega_m)$, (b) $p_M(\omega_m)$, (c) $d^{-1}_{geo,min}(\omega_m)$, and (d) $p_G(\omega_m)$.

standard deviation of π to each symbol. The performance of the candidate detector applied in the raw data domain by using the matched filtering $\beta^2_M(\omega_m)$ defined in (3.26), shown in Fig. 4.7(a), is compared with the performance of the candidate detector applied in the correlation domain $p_M(\omega_m)$, shown in Fig. 4.7(b). For the sake of comparison, Fig. 4.7(c) and Fig. 4.7(d) show the corresponding results for ideal signal transmission, respectively. We observe that the raw data based detector is unable to detect the primary user when phase distortion occurs, while the correlation based detector mantains the desired detection performance.

For the evaluation of the frequency and power estimation accuracy, the same simple scenario with one active primary user (BPSK with rectangular pulse shape and 4 samples per symbol) plus noise is considered. The normalized carrier frequency is again $\omega = 0.2$. Fig. 4.8 and Fig. 4.9 show the normalized Root Mean Squared Error (RMSE) of the estimated power level (this is the RMSE divided by the SNR) and the RMSE of the estimated normalized frequency location of the resulting simulation, respectively, for different compression rates and after a total of 1000 Monte Carlo runs. From Fig. 4.8 and Fig. 4.9 it can be conclude that both the power level estimation accuracy and the frequency estimation accuracy remain almost constant whatever the compression rate is considered.

On the other hand, Fig. 4.10 shows the comparison between the eigenvalue-based method

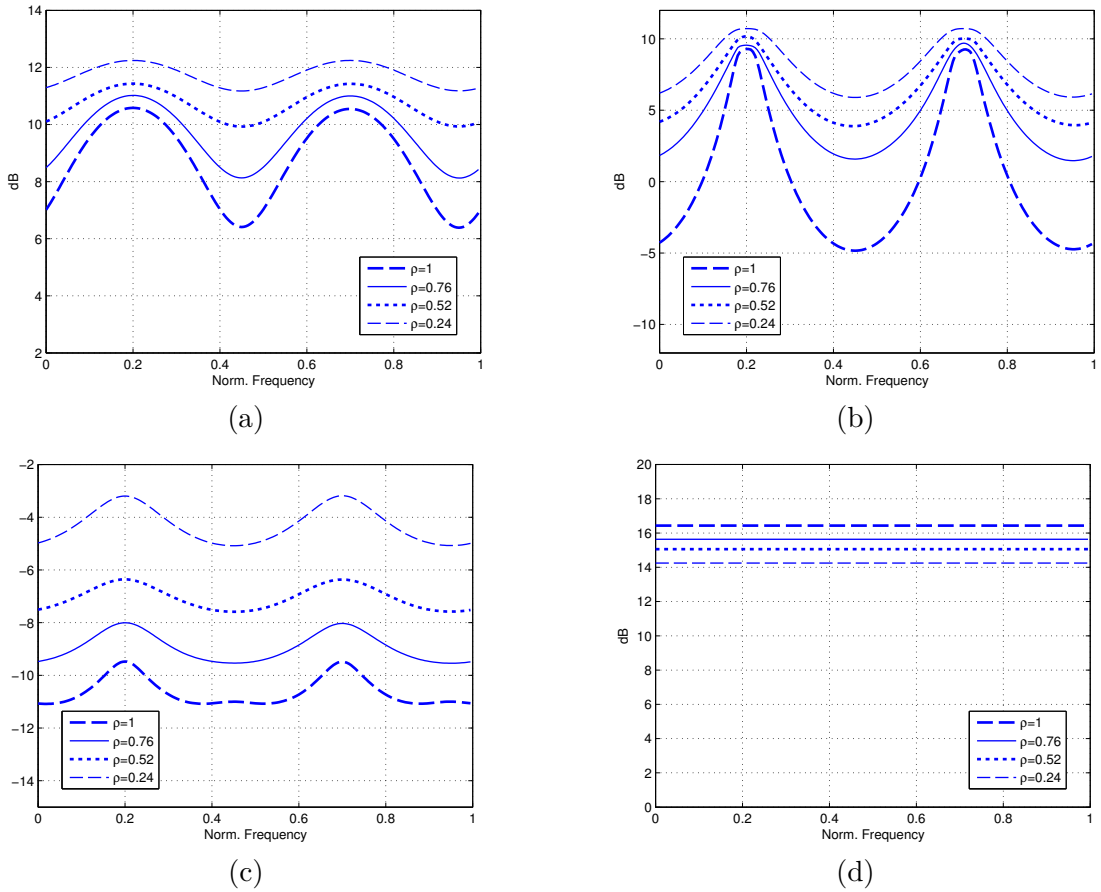

FIGURE 4.5: Performance of candidate detector solving direct correlation matching. The scenario considers two primary user with the following parameters: BPSK signals with rectangular pulse and 4 samples per symbol, both with SNR=10 dB and at frequencies $\omega_1 = 0.2$ and $\omega_1 = 0.7$. (a) $p_F(\omega_m)$, (b) $p_M(\omega_m)$, (c) $d^{-1}_{geo,min}(\omega_m)$, and (d) $p_G(\omega_m)$.

and the geodesic norm based method for a particular compression rate in terms of RMSE. Fig. 4.10(a) reflects that the eigenvalue-based method provides more accurate power estimations than the geodesic norm based method, while Fig. 4.10(b) makes evident that the geodesic norm based method is the one that provides better results for the frequency location estimation. However, it is interesting to remember that $p_G(\omega_m)$ does not depend on the frequency and therefore it only works properly when only one desired user is present. In conclusion, the eigenvalue-based method seems to be the most complete technique of the three proposed methods because it provides good frequency and power estimations and it works in scenarios where more than one desired user is present.

The results obtained in Fig. 4.6 can be compared with the performance of the current most prominent spectral estimation procedures applied in the scenario under consideration. To this end, Fig. 4.11 shows two major filter-bank spectral estimates (Periodogram and Normalized Capon) and Thompson's multitaper method (MTM) [116] for an scenario consisting of a desired signal (BPSK signal, rectangular pulse shape with 4 samples per symbol) with SNR=10 dB at frequency $\omega = 0.2$, plus a pure tone interference signal located at frequency $\omega_I = 0.7$ and with SNR=10dB. Besides presenting low resolution, note also that they are not robust to the strong interference. In contrast, the candidate detector proposed in this

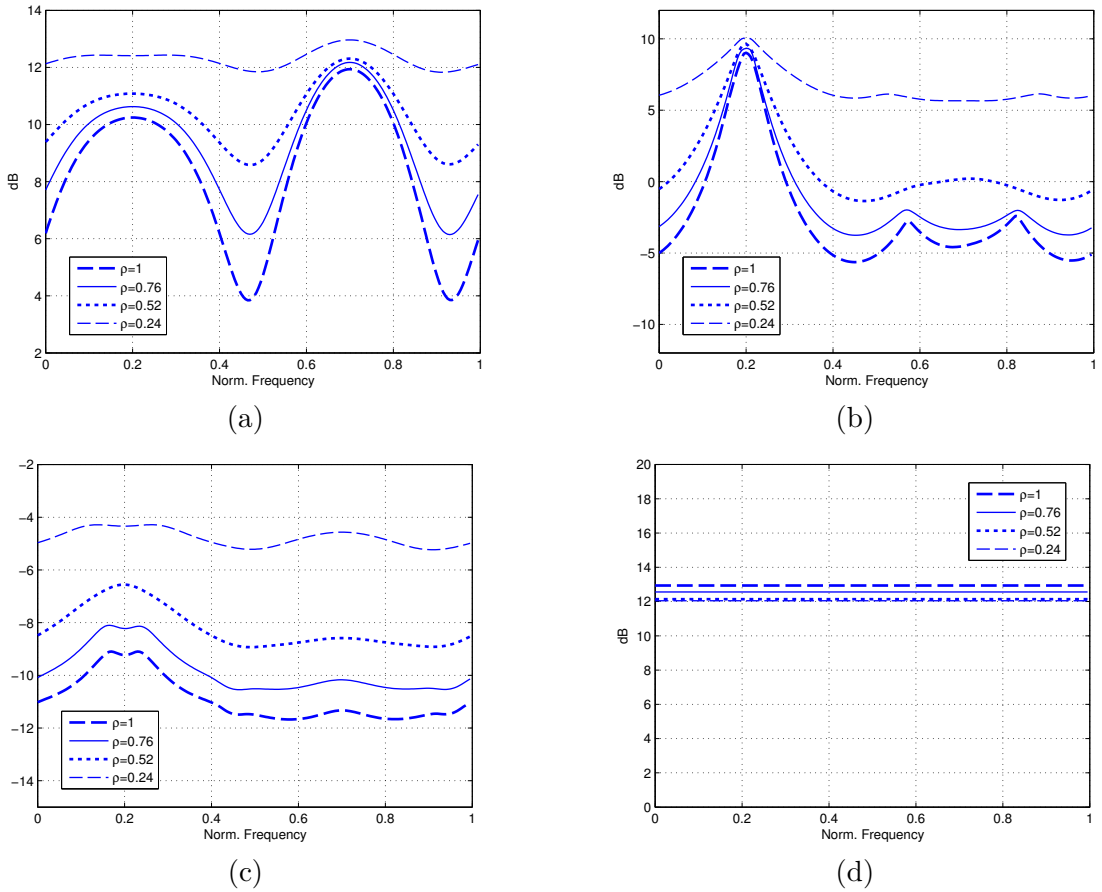

FIGURE 4.6: Performance of candidate detector solving direct correlation matching. The scenario considers a primary user (BPSK with rectangular pulse and 4 samples per symbol) with SNR=10 dB and at frequency $\omega = 0.2$ plus a narrow band interference (pure tone) with SNR=10 dB at frequency $\omega_I = 0.7$. (a) $p_F(\omega_m)$, (b) $p_M(\omega_m)$, (c) $d^{-1}_{geo,min}(\omega_m)$, and (d) $p_G(\omega_m)$.

thesis provides a clear frequency and power estimation and make the interference disappear because of their feature-based nature.

Because the method proposed here is a correlation matching-based method, a question regarding its robustness in front of a frequency selective channel, instead of flat fading, arises. We consider here the scenario of a BPSK primary signal located at frequency $\omega = 0.2$ and a pure tone interference located at $\omega_I = 0.7$, both with SNR=10 dB, but both propagating through a 20-tap Rice channel (a channel with a LOS and some random late arrivals). The LOS presents a gain of one, and the late random arrivals altogether also have energy equal to one. The impulse response of a particular channel is depicted in Fig. 4.12. The performance of $p_M(\omega_m)$ is shown in Fig. 4.13 for different compression rates. The ideal channel performance is shown in Fig. 4.13 for comparison purposes. It can be observed that the multipath causes significant losses regarding detection capabilities and also a deterioration in the frequency estimation due to the appearance of a bias into the frequency location. In any case, if these losses imply serious problem, it is reasonable to assume channel equalization at the sensing station.

Next, the performance in low SNR scenarios is evaluated by means of the ROC curves (Receiver Operating Characteristic) in order to illustrate the proposed candidate spectrum

sensing methods robustness against noise. To evaluate the probability of false alarm versus the probability of detection, a threshold for $p_M(\omega_m)$ and $d^{-1}_{geo,min}(\omega_m)$ should be derived. However, theoretical derivation of the threshold requires the statistical distribution of $p_M(\omega_m)$ and $d^{-1}_{geo,min}(\omega_m)$ for H1 and H0, which is a difficult task, especially when eigenvalues appear on the test statistic function. To find an approximate distribution of $p_M(\omega_m)$ and $d^{-1}_{geo,min}(\omega_m)$, we recorded 2.000 Monte Carlo simulations, each in the presence of a BPSK primary user located at $\omega = 0.5$ (H1), and 2.000 records of the same length without the primary user (H0), for a particular sub-Nyquist sensing matrix.

$$\hat{\mathbf{R}}_y = \begin{cases} \mathbf{R}_\eta & H_0 \\ \gamma^2(\omega_m)\hat{\mathbf{R}}_{cm}(\omega_m) + \mathbf{R}_\eta & H_1 \end{cases} \tag{4.29}$$

Fig. 4.14(a) and Fig. 4.14(b) show the obtained distributions of the function $p_M(\omega_m)$ and $d^{-1}_{geo,min}(\omega_m)$, respectively, for H0 and H1 for a particular example with SNR=-18 dB and $\rho = 0.52$. In Fig. 4.14 it is seen that both distributions closely match the Gaussian approximation (also shown in the figure with black solid line). In view of the results we have obtained, we decided to adopt Gaussian models for computing ROC figures. Therefore, from the 2.000 Monte Carlos runs we extract mean and variance of each hypothesis to build the corresponding probability density function (PDF) in the following way,

$$\text{pdf}(x) = \frac{1}{\sqrt{2\pi\sigma_x^2}} e^{-\frac{(x-\mu_x)^2}{2\sigma_x^2}} \tag{4.30}$$

where μ_x and σ_x^2 denote the mean and the variance, respectively.

As an example, Fig. 4.15 shows the perfect agreement between the ROC curves obtained with the Gaussian approaximation and the ROC curves obtained with Monte Carlo runs for a BPSK primary signal at $\omega = 0.5$ and SNR$=-18$dB. The compression rate is $\rho = 0.52$. The latter are obtained by averaging 2.000 simulation runs each in H1, and 2.000 in H0, recording the value of $p_M(\omega_m)$ and $d^{-1}_{geo,min}(\omega_m)$ at the true frequency location of the primary user and comparing it with an heuristic threshold.

In order to show the effect of the compression rate on both eigenvalue-based and geodesic-based detectors, the ROC curves of the scenario described above are compared in Fig. 4.16 for $p_M(\omega_m)$ and Fig. 4.17 for $d^{-1}_{geo,min}(\omega_m)$, for different compression rates and for SNR ranging from -16 dB to -22 dB. In agreement with the Landau's lower bound [103], the performance of both detectors remains stable until the compression rate exceeds the limit given by the spectral occupancy, which in this particular case is 0.5. Both detectors show similar curves for ρ ranging from 1 to 0.5, however, the superiority of $p_M(\omega_m)$ is clear comparing the curves of $p_M(\omega_m)$ and $d^{-1}_{geo,min}(\omega_m)$ for $\rho = 0.24$, shown in Fig. 4.16(d) and Fig. 4.17(d), respectively.

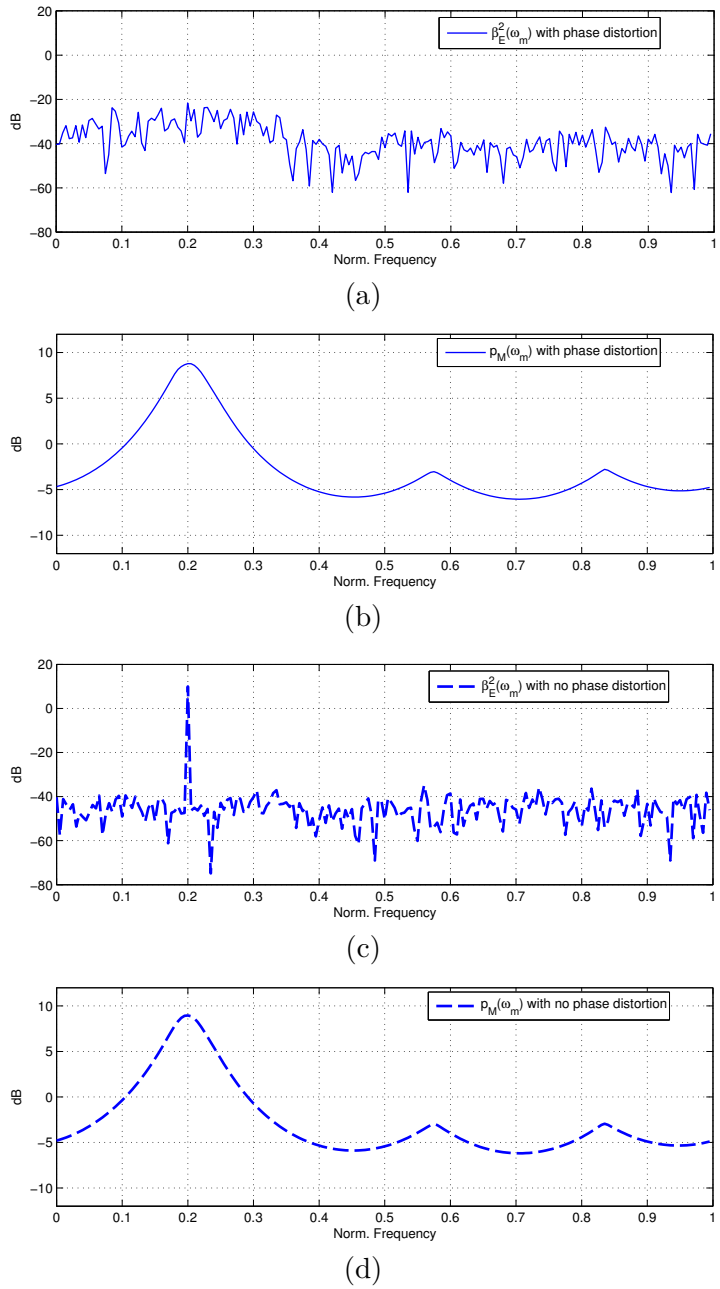

FIGURE 4.7: Comparison of the candidate detector applied in different domains. The scenario considers a single primary user with the following parameters: BPSK signal with rectangular pulse and 4 samples per symbol, SNR=10 dB at frequency $\omega = 0.2$. (a) $\beta_E^2(\omega_m)$ with phase distortion, (b) $p_M(\omega_m)$ with phase distortion, (c) $\beta_E^2(\omega_m)$ with no phase distortion, and (d) $p_M(\omega_m)$ with no phase distortion.

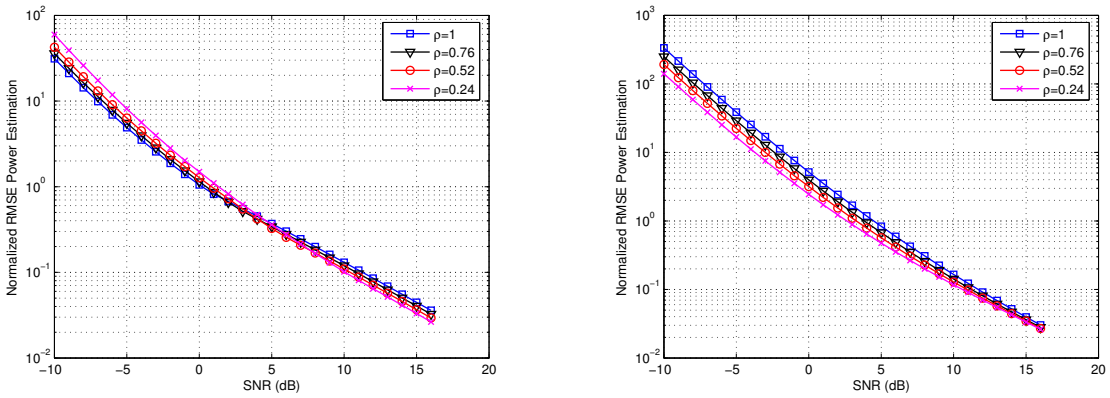

FIGURE 4.8: Performance of candidate detector solving direct correlation matching. Normalized RMSE of the estimated power level in a scenario with one desired user (BPSK with rectangular pulse shape and 4 samples per symbol located at $\omega = 0.2$) in the presence of noise. (a) $p_M(\omega_m)$, and (b) $p_G(\omega_m)$.

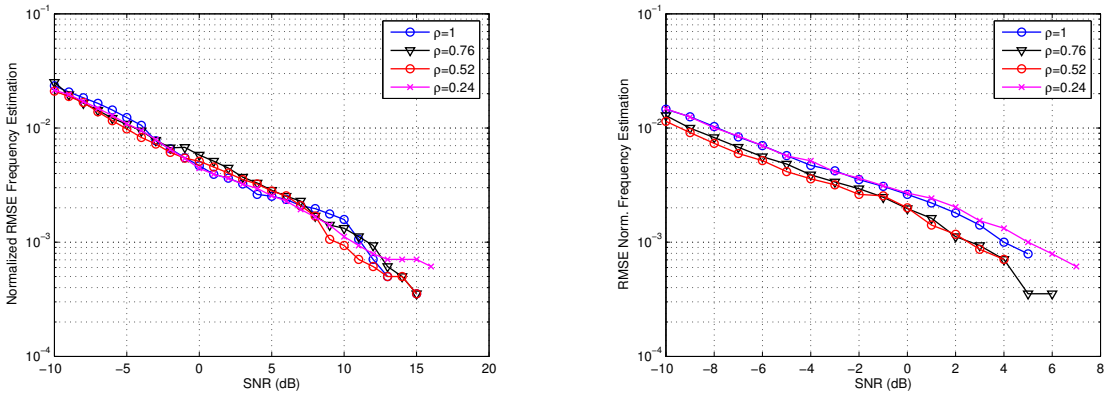

FIGURE 4.9: Performance of candidate detector solving direct correlation matching. RMSE of the estimated normalized frequency location in a scenario with one desired user (BPSK with rectangular pulse shape and 4 samples per symbol located at $\omega = 0.2$) in the presence of noise. (a) $p_M(\omega_m)$, and (b) $d^{-1}_{geo,min}(\omega_m)$.

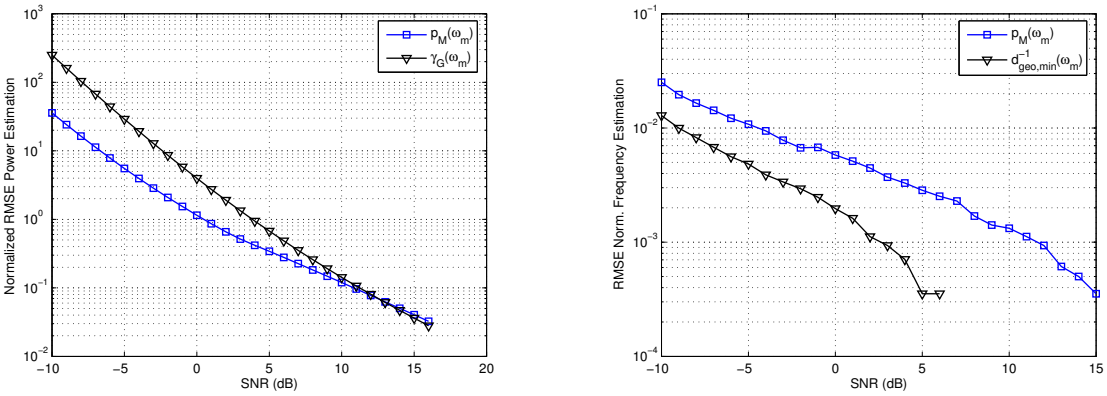

(a) (b)

FIGURE 4.10: Performance of candidate detector solving direct correlation matching. RMSE of the estimated parameters for $\rho = 0.76$ in a scenario with one desired user (BPSK with rectangular pulse shape and 4 samples per symbol located at $\omega = 0.2$) in the presence of noise. (a) Normalized RMSE of the estimated power level, and (b) RMSE of the estimated normalized frequency location.

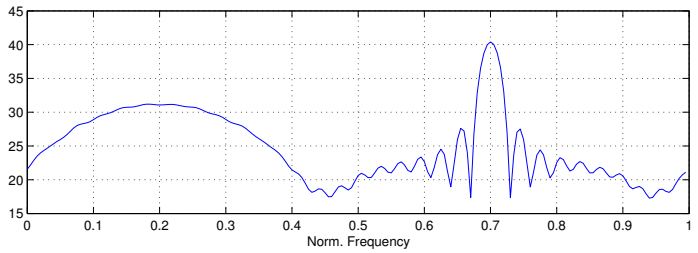

(a)

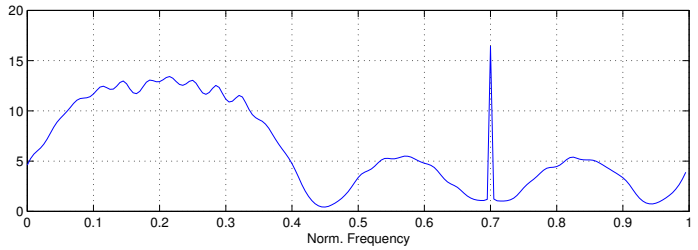

(b)

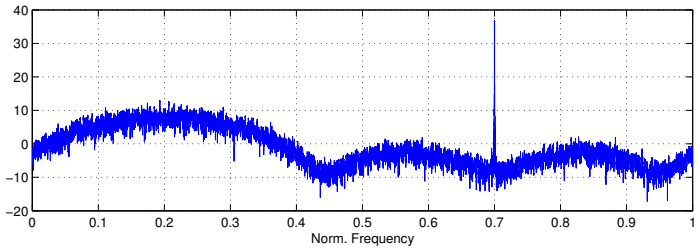

(c)

FIGURE 4.11: Performance of conventional spectral estimation procedures. The scenario considers a desired signal with the following parameters: BPSK signal, rectangular pulse shape with 4 samples per symbol, SNR=10 dB at frequency $\omega = 0.2$, plus an interference signal which is a pure tone located at frequency $\omega_I = 0.7$ and with SNR=10dB. Compression is not considered. The interference is a pure sinusoid located at frequency $\omega_I = 0.7$ and with SNR=10dB. (a) Periodogram, (b) Normalized Capon (NMLM), and (c) Thompson's multitaper method (MTM).

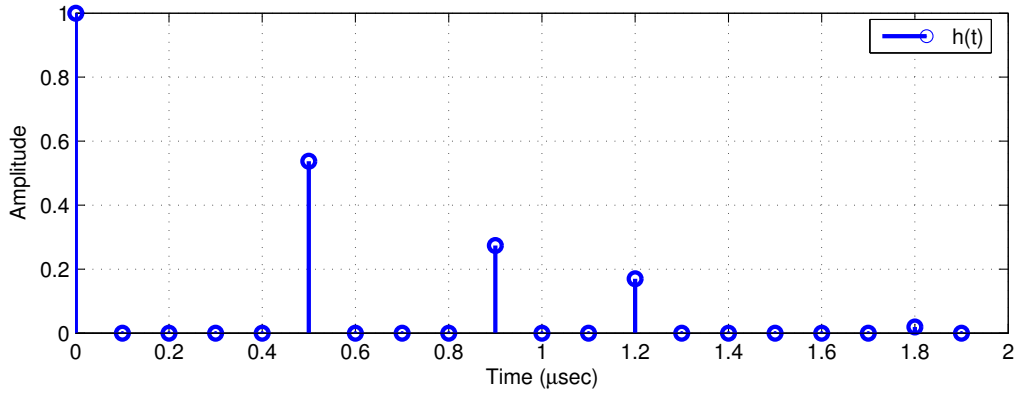

FIGURE 4.12: Example of 20-length Rice channel under consideration.

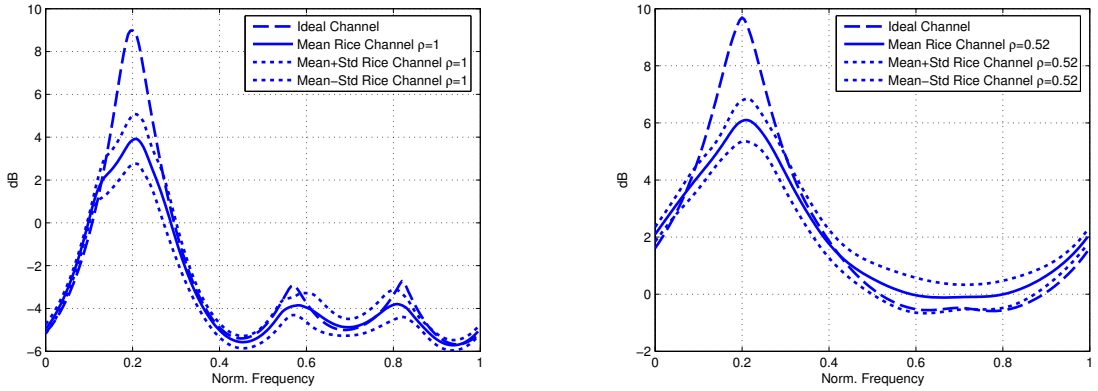

(a) (b)

FIGURE 4.13: Performance of candidate detector solving direct correlation matching in a Rice Channel. The scenario considers a desired signal with the following parameters: BPSK signal, rectangular pulse shape with 4 samples per symbol, SNR=10 dB at frequency $\omega = 0.2$, plus an interference signal which is a pure tone located at frequency $\omega_I = 0.7$ and with SNR=10dB. 20-length Rice channel is considered. The results are obtained averaging 100 different channel realizations. (a) $\rho = 1$, and (b) $\rho = 0.52$.

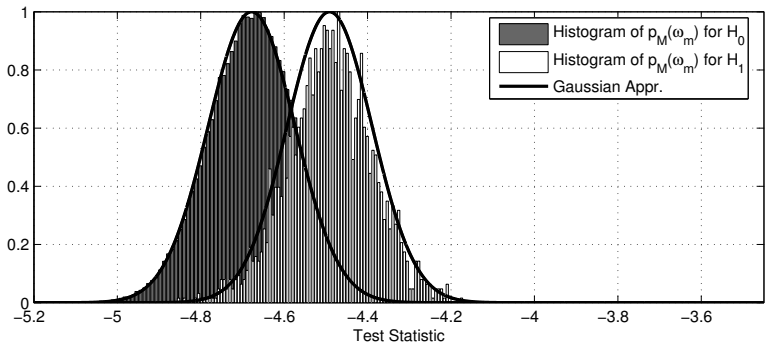

(a)

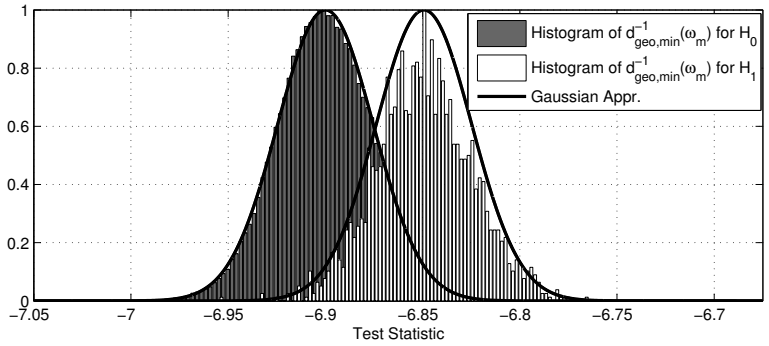

(b)

FIGURE 4.14: Performance of the candidate detector solving direct correlation matching. Theoretical and empirical distributions of (a) $p_M(\omega_m)$, and (b) $d^{-1}_{geo,min}(\omega_m)$, for H1 and H0 for SNR=-18 dB and $\rho = 0.52$. The scenario for H1 consists of a BPSK primary user (4 samples per symbol) located at frequency $\omega = 0.5$ plus noise, and the scenario for H0 consists of only noise.

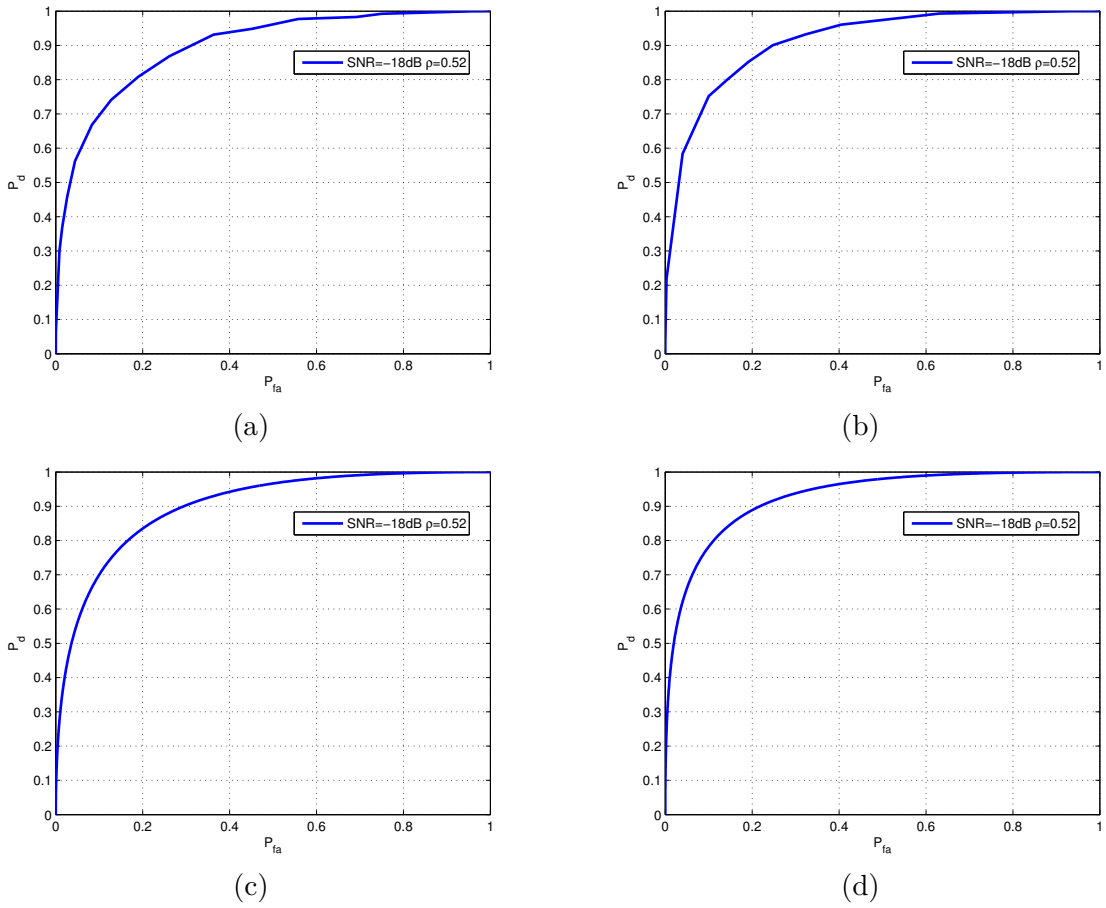

FIGURE 4.15: Agreement between ROC curves obtained with the Gaussian approximation and the ROC curves obtained with Monte Carlo runs for an scenario with a BPSK primary signal at $\omega = 0.5$ and SNR=−18dB. The compression rate is $\rho = 0.52$. (a) $p_M(\omega_m)$ with Monte Carlo runs, (b) $d^{-1}_{geo,min}(\omega_m)$ with Monte Carlo runs, (c) $p_M(\omega_m)$ with Gaussian approximation, and (d) $d^{-1}_{geo,min}(\omega_m)$ with Gaussian approximation.

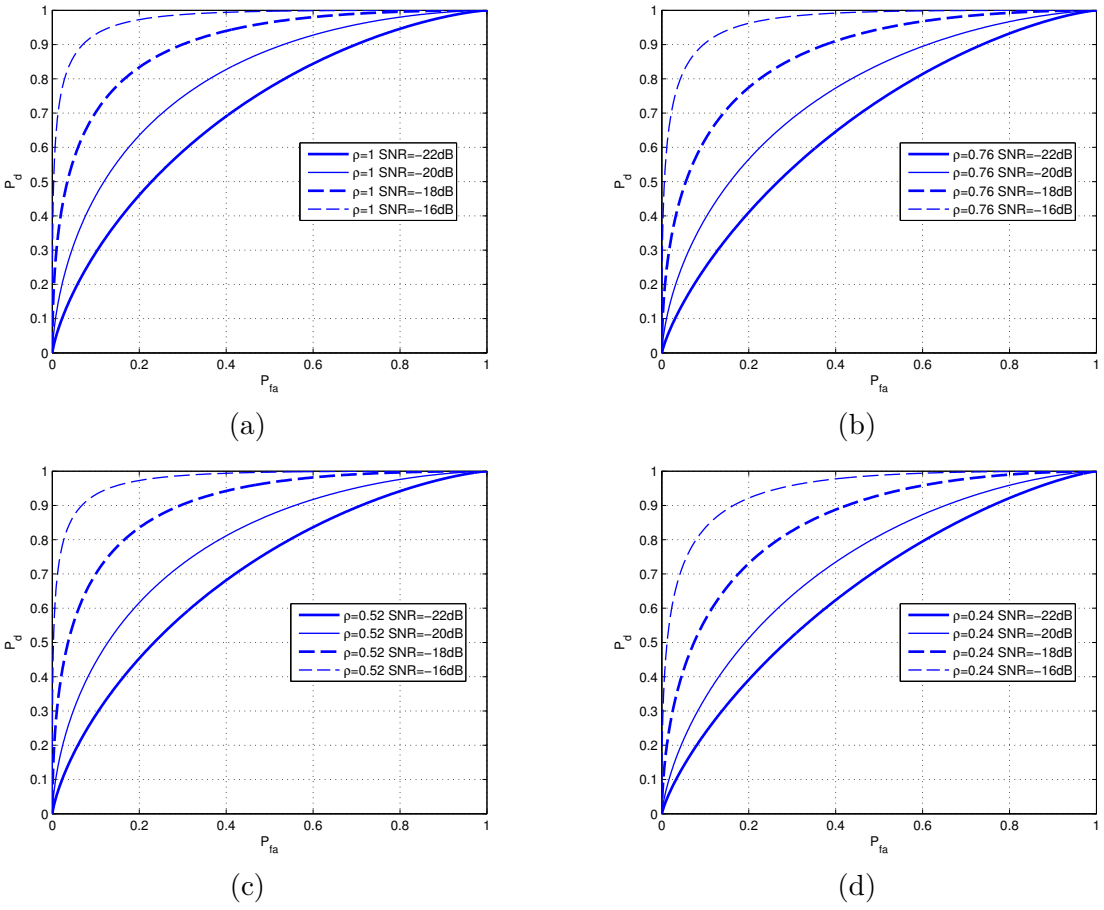

FIGURE 4.16: Performance of $p_M(\omega_m)$. ROC figures for different compression rates. The scenario considers a single desired signal which is a BPSK signal with rectangular pulse shape and 4 samples per symbol, located at frequency $\omega = 0.5$. (a) $\rho = 1$, (b) $\rho = 0.76$, (c) $\rho = 0.52$, and (d) $\rho = 0.24$.

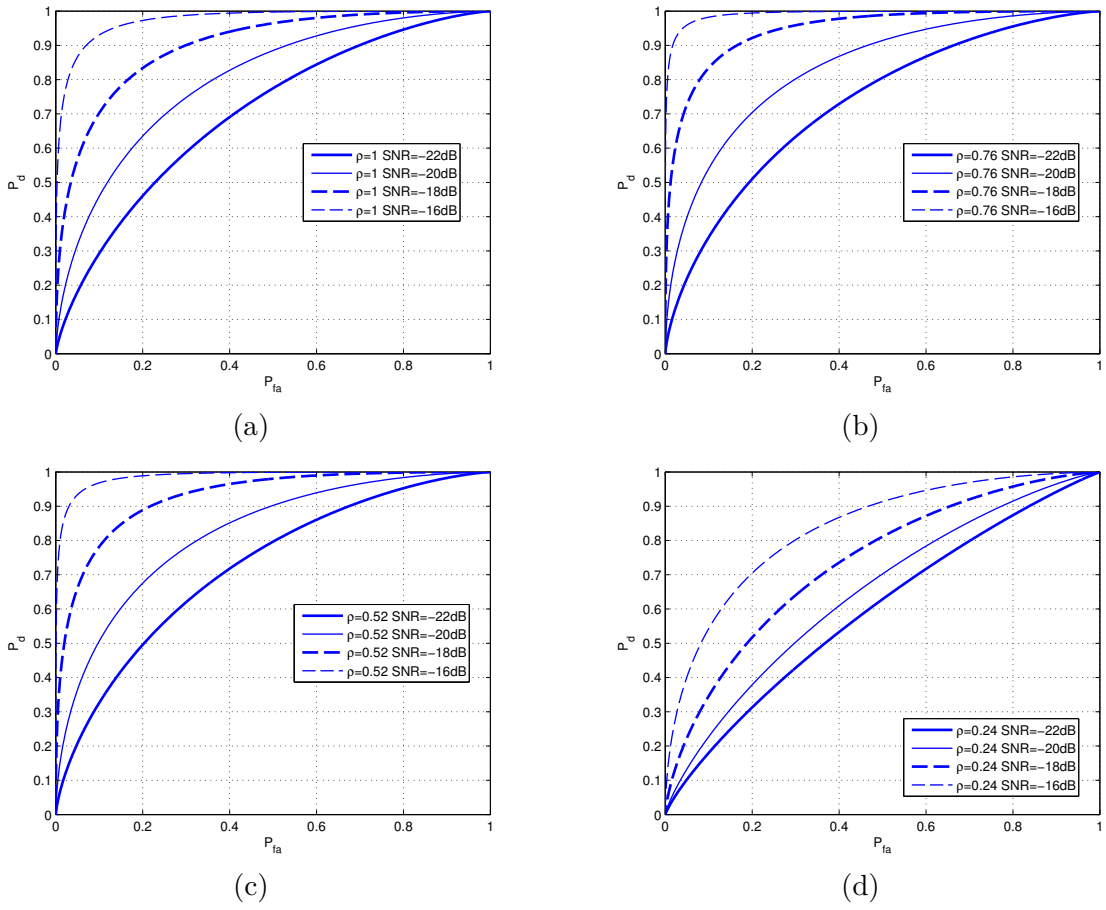

FIGURE 4.17: Performance of $d^{-1}_{geo,min}(\omega_m)$. ROC figures for different compression rates. The scenario considers a single desired signal which is a BPSK signal with rectangular pulse shape and 4 samples per symbol, located at frequency $\omega = 0.5$. (a) $\rho = 1$, (b) $\rho = 0.76$, (c) $\rho = 0.52$, and (d) $\rho = 0.24$.

Frequency and AoA scanning

Let us now evaluate the ability of the direct correlation matching based detector to accurately estimate, not only the frequency location of the primary user, but also its AoA. To do so, we first consider the same simple scenario than the previous section, which consists on a primary user with BPSK using rectangular pulse shape (4 samples per symbol) and a pure tone interference plus AWGN. The array is composed of $N = 6$ antennas with an antenna separation equal to $\lambda/2$. The scenario characteristics have been summarized in Table 4.2.

TABLE 4.2: Scenario Characteristics

	Primary User	**Interference**
Modulation	BPSK	Pure Tone
Normalized Frequency(*)	0.2	0.3
AoA (degrees)	30	60
SNR (dB)	10	10

(*) The bandwidth under scrutiny is 10MHz.

We consider the same parameters defined in Table 4.1. In this case, the constant ϵ is chosen to be 30 in order to take samples for a longer period of time and, thus, gave robustness to the correlation matrix estimate. The AoA predefined grid goes from $-90°$ to $+90°$ with an angle step of $\Delta_\omega = 10°$ and the frequency step is $\Delta_\omega = 500$ KHz. These resolution values correspond to a grid of $M = 20$ and $Q = 19$.

Fig. 4.18 shows the performance of the eigenvalue-based method, i.e. $p_M(\omega_m, \theta_i)$, for different compression rates. The resulting estimate provides a clear estimate of the frequency and angle location, and produces a power level close to 10 dB, which coincides with the SNR. The interfering tone has disappeared due to the feature-based nature of the estimate. Although the compression affects the resolution capabilities (the peak becomes wider in frequency axis), is interesting to note that the frequency, AoA and power level accuracy of the estimates do not suffer from the compression.

Fig. 4.19 and Fig. 4.20 shows the performance of the geodesic distance based detector. The independence of $p_G(\omega_m, \theta_i)$ with respect to the frequency ω_m can be observed in Fig. 4.20, where the value of $p_G(\omega_m, \theta_i)$ only depends on the angle of arrival. Thus, the angle dependence of $p_G(\omega_m, \theta_i)$ overcomes the problem encountered in the previous section because it helps in correctly estimating the transmitted power of multiple primary user. The inverse of the geodesic distance is shown in Fig. 4.19. It shows higher robustness against the compression compared with $p_M(\omega_m, \theta_i)$, while providing an accurate estimation of the frequency and angle location.

Both methods achieve similar performance when multiple primary users are present, however, the results are not shown here to avoid redundancy.

For the evaluation of the frequency, AoA and power estimation accuracy, an scenario with one active primary user with BPSK, using a rectangular pulse shape (with 4 samples per symbol) and AWGN is considered. The frequency and angle location are chosen randomly in each of the 200 iterations. Here ϵ is equal to 10 and the grid resolution is $\Delta_\theta = 1.4°$ and $\Delta_\omega = 78$ KHz. Fig. 4.21 shows the normalized RMSE of the estimated power level, the RMSE of the AoA estimation (in degrees), and the RMSE of the estimated normalized

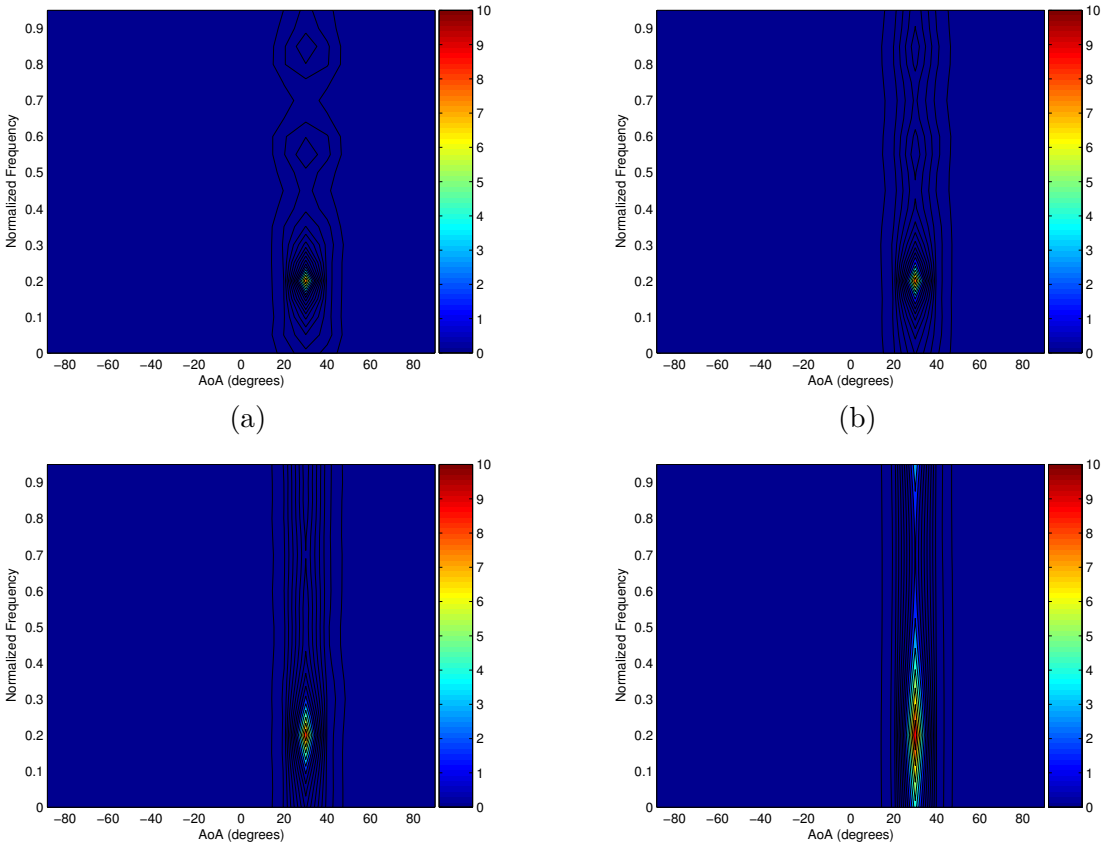

FIGURE 4.18: Performance of candidate detector solving direct correlation matching with eigenvalue-based technique: $p_M(\omega_m, \theta_i)$. The scenario is summarized in Table 4.2. for (a) ρ=1, (b) ρ=0.76, (c) ρ=0.52, and (d) ρ=0.24.

frequency location, respectively, using the geodesic-based detector (blue) and the eigenvalue-based detector (black) for $\rho = 0.24$. The results displayed in Fig. 4.21(a) show that the power level accuracy obtained with $p_M(\omega_m, \theta_i)$ is very similar to the one obtained with $p_G(\omega_m, \theta_i)$. Similarly, it is seen from Fig. 4.21(b) that the AoA estimation accuracy remains almost constant for both detectors. However, is clear form Fig. 4.21(c) that $d^{-1}_{geo,min}(\omega_m, \theta_i)$ provides better results than $p_M(\omega_m, \theta_i)$ whatever the SNR used. This loss in frequency accuracy together with the preservation of the AoA accuracy agrees with the fact that the peak provided by $p_M(\omega_m, \theta_i)$ becomes wider in the frequency axis as ρ decreases.

The performance in low SNR scenarios is evaluated by means of the ROC curves. To evaluate the probability of false alarm versus the probability of detection we did the same simulation as in the previous section. This is, we run 200 simulations considering the presence of the primary user (H1), and 200 records of the same length without the primary user (H0). In this case, the primary user is located at $\omega = 0.2$ and angle of arrival equal to $\theta = 30°$. Again, the primary user is a BPSK (4 samples per symbol). No interference is considered here. Fig. 4.22(a) shows the ROC of $d^{-1}_{geo,min}(\omega_m, \theta_i)$ for SNR=-14 dB and Fig. 4.22(b) the ROC of $d^{-1}_{geo,min}(\omega_m, \theta_i)$ for SNR=-16 dB for different compression rates. As it was expected, the general performance of the geodesic-based detector is deteriorated as the compression rate

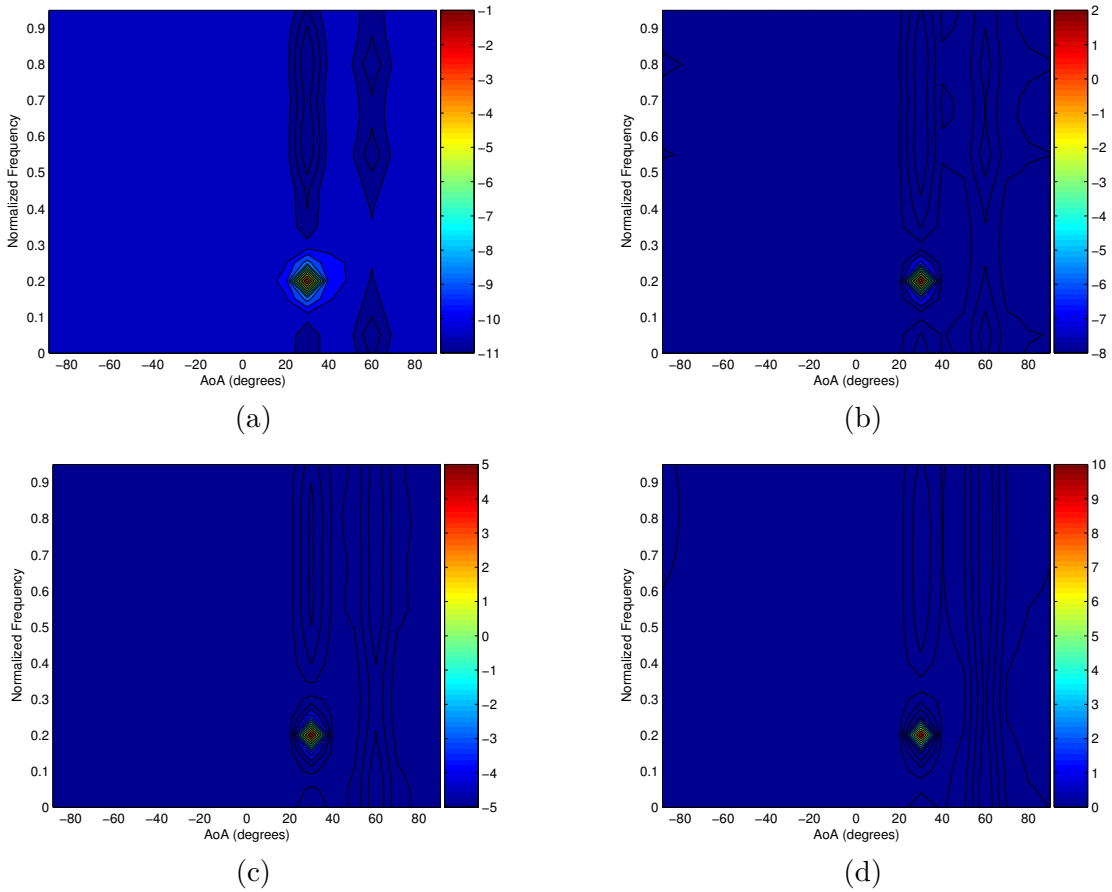

FIGURE 4.19: Performance of candidate detector solving direct correlation matching with geodesic-based technique: $d^{-1}_{geo,min}(\omega_m, \theta_i)$. The scenario is summarized in Table 4.2. (a) ρ=1, (b) ρ=0.76, (c) ρ=0.52, and (d) ρ=0.24.

decreases. Fig. 4.23 shows the ROCs for the eigenvalue-based detector for (a) SNR=-16dB and (b) SNR=-22dB. The superiority of $p_M(\omega_m, \theta_i)$ is clear from the comparison of Fig. 4.23 with Fig. 4.22, where the robustness of the $p_M(\omega_m, \theta_i)$ is observed as the resulting plots for the geodesic-based detector are worse with respect to those obtained by the eigenvalue-based detector.

Conclusion

The candidate detector was studied in this section using computer simulations. In particular, the detection of predetermined spectral shapes in sparse wideband regimes was addressed by means of a correlation-matching procedure. The main contribution of the new sub-Nyquist sampling approach is that it allows to alleviate the amount of data needed in the spectrum sensing process. Once the sampling bottleneck is solved, the data autocorrelation matrix is obtained from sub-Nyquist samples. Following the correlation matching concept, the method is able to provide an estimate of the frequency location, a power level estimation, and an estimate of the angle of arrival of the desired user. Three different methods were tested: The first one, which is based on the Frobenius distance, is discarded because of its low rejection to interference. The second one, which is based on the geodesic distance, works well in terms of

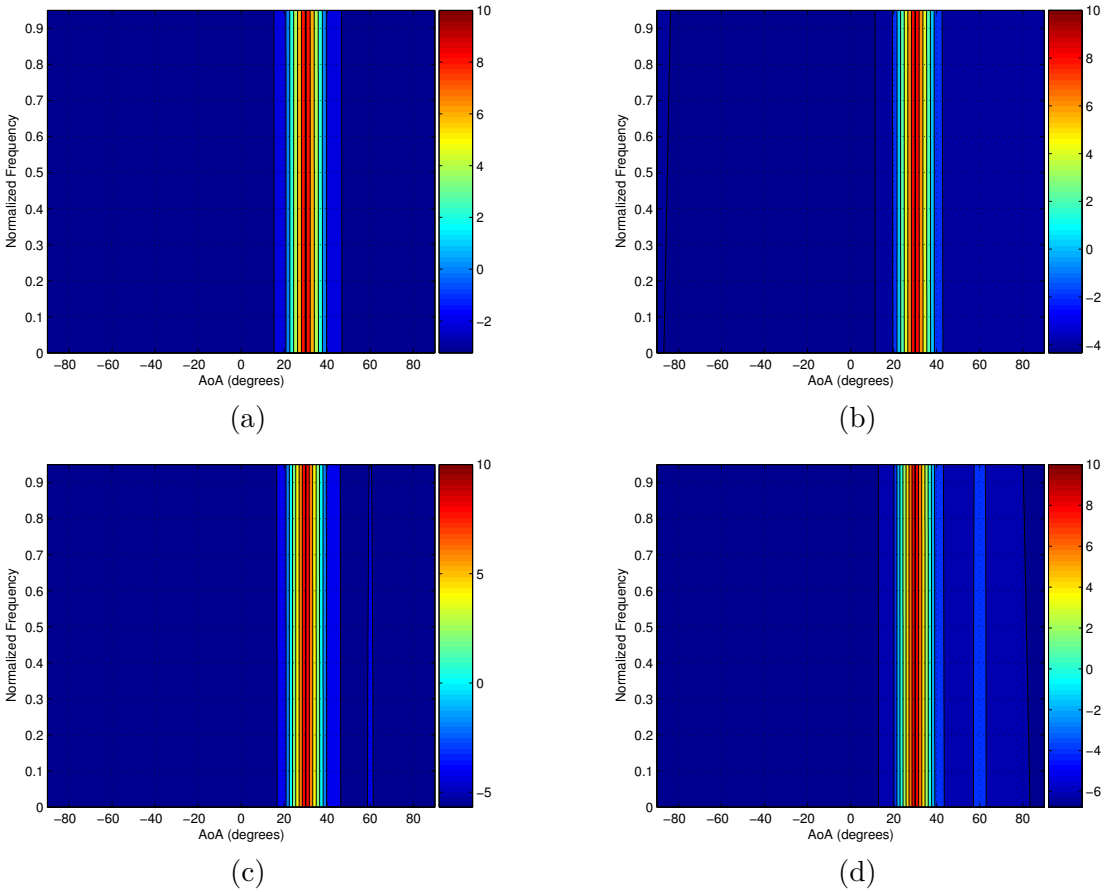

FIGURE 4.20: Performance of candidate detector solving direct correlation matching with geodesic-based technique: power level $p_G(\omega_m, \theta_i)$. The scenario is summarized in Table 4.2. (a) ρ=1, (b) ρ=0.76, (c) ρ=0.52, and (d) ρ=0.24.

interference rejection but the power level estimate that this method provides does not depend on the frequency parameter and therefore, it is not indicated when detecting more than one desired user. Moreover, its the robustness against noise is quite poor. The third method, which is based on the positive semidefinite difference between matrices, provides the most compliant performance, offering acceptable accuracy of the estimated parameters and good performance in terms of robustness against noise. As it was expected, simulation results have shown that the compression affects the detection capabilities of all the correlation-matching methods. However, we have also shown that the undersampling technique slightly affects the accuracy of the estimated parameters.

As observed in the results, the presence of few primary signals makes the response of the detector to be sparse. Section 3.5 presented the CS-based reconstruction techniques that take advantage of this fact. Next section provides Matlab-based simulation results to evaluate the performance of the latter scheme.

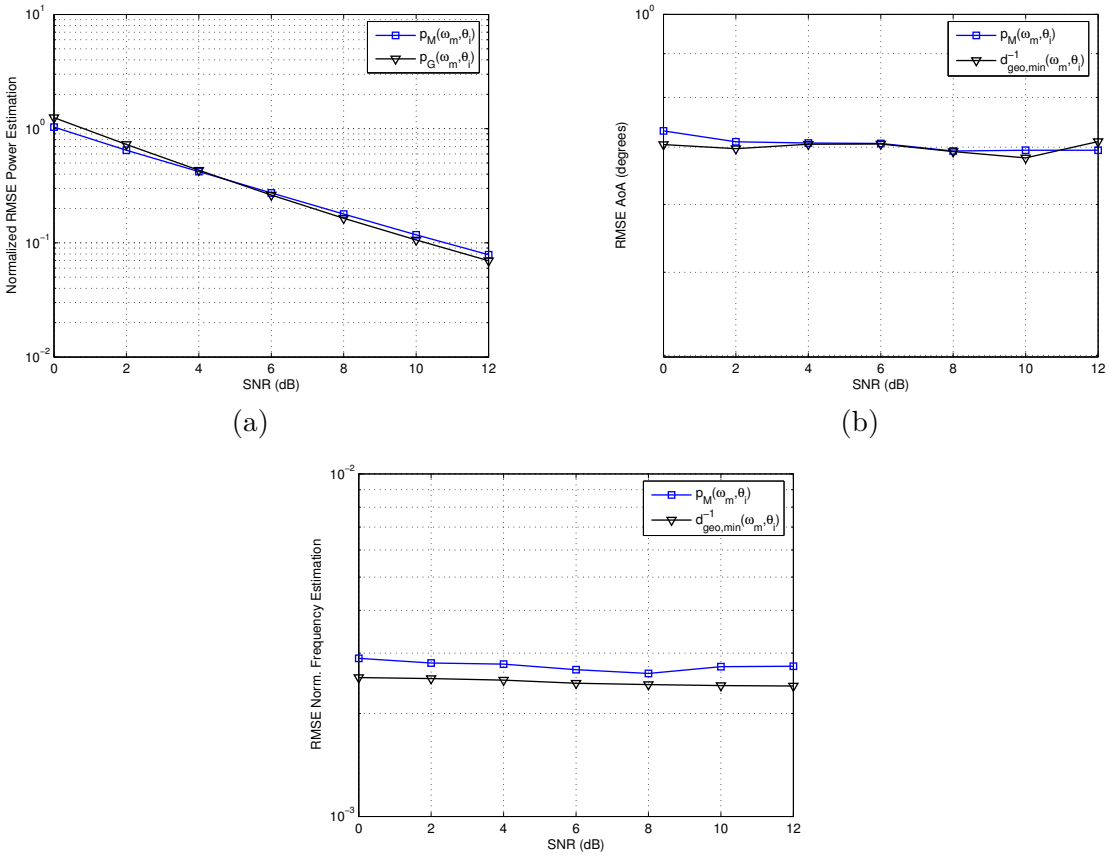

FIGURE 4.21: Performance of candidate detector solving direct correlation matching. RMSE of estimated parameters for $\rho = 0.24$ in a scenario with a single active primary user with BPSK, using a rectangular pulse shape (with 4 samples per symbol) plus noise. The frequency and angle location are chosen randomly in each of the 200 iterations. (a) Normalized RMSE of the estimated power level, (b) RMSE of the estimated AoA (degrees), and (c) RMSE of the estimated normalized frequency location.

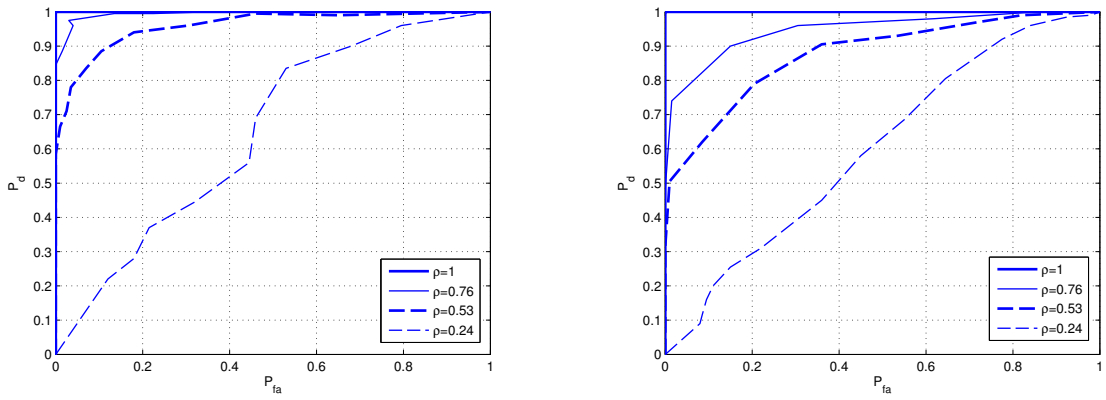

FIGURE 4.22: Performance of candidate detector solving direct correlation matching. ROC obtained with Monte Carlo runs for different compression rates for the geodesic distance based detector. The scenario considers a single desired signal which is a BPSK signal with rectangular pulse shape and 4 samples per symbol, located at frequency $\omega = 0.2$. (a) SNR=-14 dB, and (b) SNR=-16 dB.

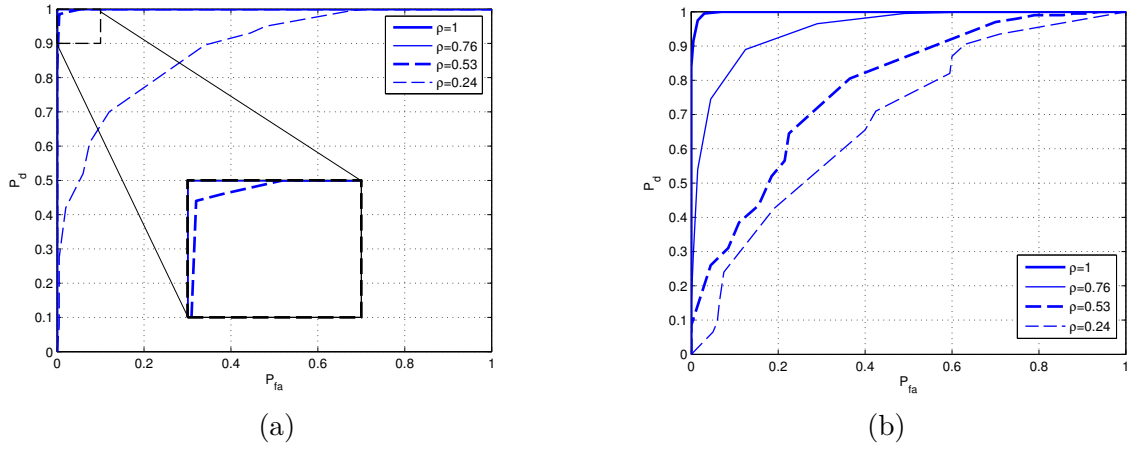

FIGURE 4.23: Performance of candidate detector solving direct correlation matching. ROC obtained with Monte Carlo runs for different compression rates for the eigenvalue-based detector. The scenario considers a single desired signal which is a BPSK signal with rectangular pulse shape and 4 samples per symbol, located at frequency $\omega = 0.2$. (a) SNR=-16 dB, and (b) SNR=-22 dB.

4.3.2 CS-reconstruction based matching

In this section, the candidate detector is solved with CS-based reconstruction techniques. The proposed scheme is evaluated for frequency scanning only, leaving the angular search for further extension of the present work in the future.

The spectral band under scrutiny has bandwidth equal to $f_{max} = 20$ MHz. The size of the observation Nyquist-sampled signal $\mathbf{z}_f$ is $L = 33$ samples. In this case, the constant ϵ is chosen to be 10. The simulation parameters are the same summarized in Table 4.1. Unless otherwise noted, the grid resolution for this section is $\Delta_\omega = 100$ KHz.

To test the ability of the proposed sparse spectral matching technique to properly label licensed users, we first consider a scenario with two primary user in the presence of noise and interference. The interference is included as a 10 dB pure tone at frequency $\omega_I = 0.375$. The primary user is assumed to be a BPSK signal with a rectangular pulse shape and 8 samples per symbol. The SNR of the desired users are 10 dB and 7 dB, respectively, and their carrier frequencies are $\omega_1 = 0.125$ and $\omega_2 = 0.625$, respectively. The spectral occupancy for this particular example is 0.5 (the primary users are using half of the available spectrum). The values of ξ for determining the stopping criterion of the WOMP are chosen $\xi_{up} = 2$ and $\xi_{down} = 0.5$.

Fig. 4.24 shows the result of the proposed detector for 1000 Monte Carlo runs for different compression rates. Blue points indicate the output of the detector, black crosses represent the true primary users location and the red solid line indicates the interference location. From Fig. 4.24 we observe that, in agreement with the Landau's lower bound [103], the proposed technique works well until the compression exceeds the limit given by the spectral occupancy. When the compression rate surpass $\rho = 0.5$, the acquisition procedure loses too much information, which translates into a degradation of the detector performance.

The results obtained in Fig. 4.24 can be compared with the performance of the conventional periodogram spectral estimation. To this end, Fig. 4.25 shows the periodogram for the scenario under consideration for different compression rates. Besides presenting low resolution (becoming worse as the compression rate decreases), note also that they are not robust to the strong interference. In contrast, the proposed method provides a clear frequency and power estimate and makes the interference disappear because of their feature-based nature.

The interference rejection characteristic is linked to the reliability of the weights, which must provide a coarse estimate of the inverse transmitted power of the primary users. Fig. 4.26 shows the inverse of the weights for the scenario under consideration for different compression rates. As expected, the maxima of the inverse weights are located at the frequencies where a primary user is present and its value coincides with the primary users' SNR. However, the dynamic range of the weights significantly decrease when the compression rate surpass the limit of $\rho = 0.5$.

For the evaluation of the frequency, power estimation accuracy and reconstruction accuracy, two types of scenario were considered. The first one with one active primary user with BPSK, using a rectangular pulse shape (with 8 samples per symbol) located at frequency $\omega = 0.5$ and with AWGN. The second one is the same as the first plus a pure tone interference with SNR=10 dB located close to the primary at frequency $\omega_I = 0.6$. The noise is randomly generated among 5000 Monte Carlo iterations. Fig. 4.27(a) and Fig. 4.27(b) show the normalized RMSE of the estimated power level and the RMSE of the reconstruction error, respectively. The reconstruction error is computed using the spike trains distance defined in [117]. The amplitudes are first fixed to 1 and the resulting spike trains are independently convolved with $e^{-|\omega|/\Delta_\omega}$, producing slight spike spreading. Finally, the l_2-norm between the

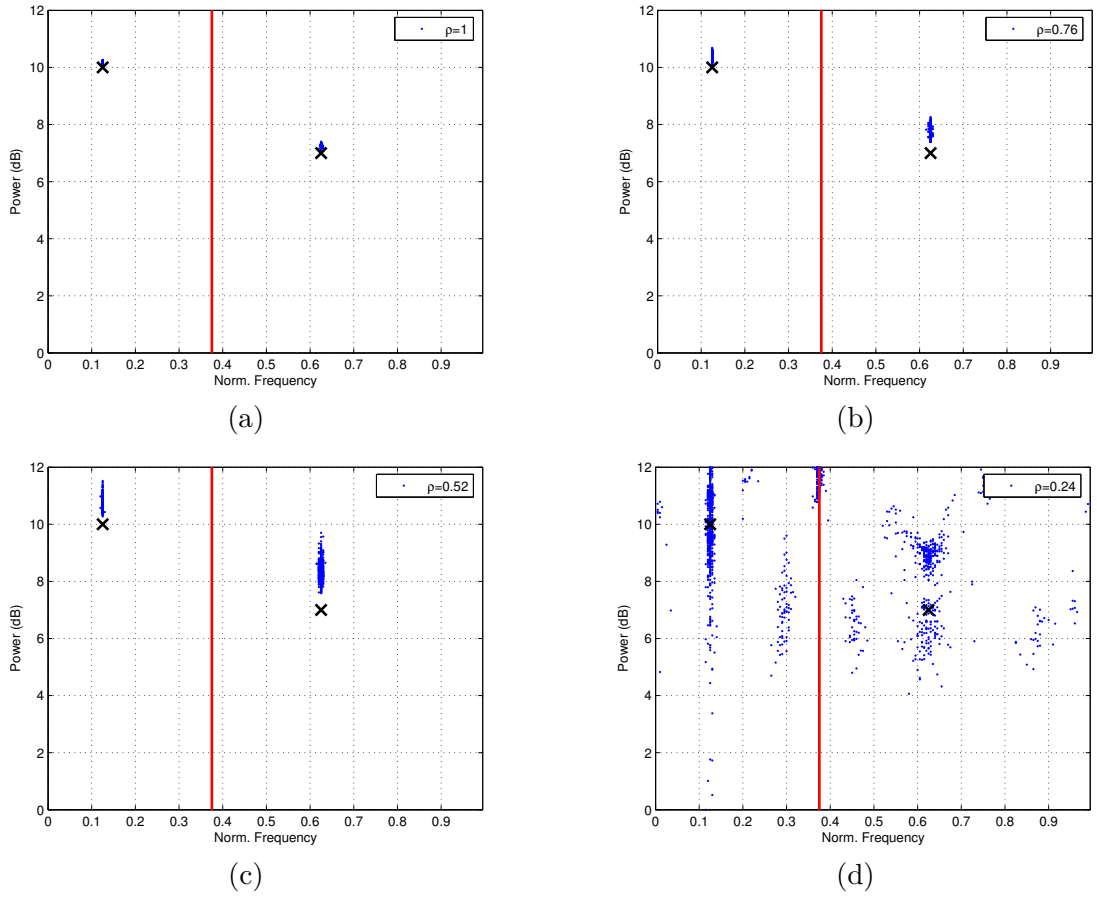

FIGURE 4.24: Performance of the candidate detector with CS-based reconstruction. The scenario considers two BPSK primary users (rectangular pulse and 8 samples per symbol) with SNR=10 dB and SNR=7 dB, respectively, and at frequencies $\omega_1 = 0.125$ and $\omega_2 = 0.625$, respectively. Black crosses represent the true primary users location. A pure tone interference signal with SNR=10 dB is located at $\omega_I = 0.375$ (indicated by red solid line). (a) $\rho = 1$, (b) $\rho = 0.76$, (c) $\rho = 0.52$, and (d) $\rho = 0.24$.

resulting convolved spike train and the convolved spike train corresponding to the real scenario is computed. The goal of this metric is to accurately represent perceptual differences between sparse signals. In general, the results displayed in Fig. 4.27 make evident that the presence of interference adversely affects the detector performance in terms of accuracy of the estimated parameters. As expected, the errors decrease as the sampling factor and the SNR increase.

High detection sensibility is a fundamental aspect in spectrum sensing for CR. In CS-based reconstruction, the stopping rule applied to halt the iterative reconstruction algorithm plays an important role in the detection performance. In particular, the interference rejection of the proposed detector is highly dependent on the value of ξ_{up} used in the stopping criterion defined in (3.55). To evaluate the probability of false alarm P_{fa} with respect to ξ_{up}, we have run 1000 Monte Carlo iterations of an scenario consisting of a BPSK primary user located at frequency $\omega = 0.25$ and with SNR=0 dB and an interferent signal with the same SNR located at frequency $\omega_I = 0.75$. A false alarm occurs when the WOMP reconstruction algorithm selects something that is not the desired BPSK signal. In the whole simulation

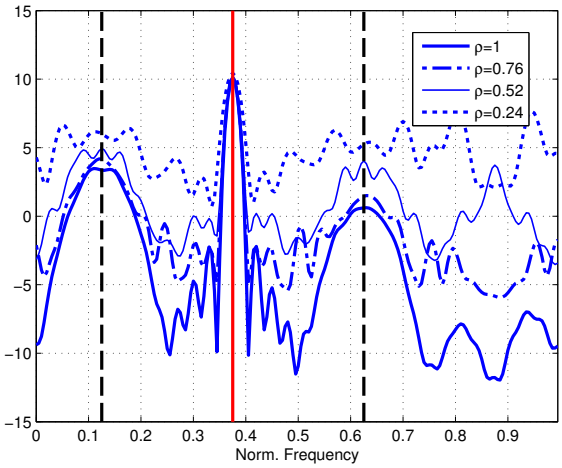

FIGURE 4.25: Periodogram performance. The scenario considers two BPSK primary users (rectangular pulse and 8 samples per symbol) with SNR=10 dB and SNR=7 dB, respectively, and at frequencies $\omega_1 = 0.125$ and $\omega_2 = 0.625$, respectively. A pure tone interference signal with SNR=10 dB is located at $\omega_I = 0.375$.

exercise we fixed $\xi_{down} = 0.5$ to focus only on the parameter ξ_{up}. Fig. 4.28(a) shows the P_{fa} versus ξ_{up} results for different compression rates when the interference is a pure tone. Note that values of ξ_{up} close to zero indicate very low interference rejection capabilities. As it can be appreciated from Fig. 4.28(a), the value of ξ_{up} that ensures low P_{fa} is far away from zero when dealing with BPSKs and very narrow band interference. Fig. 4.28(b) shows the P_{fa} versus $1 + \xi_{up}$ results when the interference is a QPSK modulated signal. The QPSK and the BPSK have similar spectral shape, which can lead to a high chance of miss-classification events. This fact is reflected in Fig. 4.28(b) with the values of ξ_{up} that provide acceptable values of P_{fa}, which are much lower than those shown in Fig. 4.28(a) for the pure tone interference.

Assuming that the stopping criterion is doing well in rejecting interference, let us now evaluate the probability of detection (P_d) versus SNR and versus P_{fa} for scenarios free from interference. To do so, we consider an scenario for H1 with a BPSK primary user (8 samples per symbol) located at frequency $\omega = 0.5$ plus noise, and an scenario with absence of primary user with only noise for H0. To evaluate when the desired signal is correctly selected by the first iteration of the WOMP, we shall understand how the selection step of the algorithm works. At each iteration, the greedy selection chooses the atom that is most strongly correlated with the residual part of the signal. In the first iteration, this is the atom that minimizes $\|\hat{\mathbf{r}}_y - \mathbf{A}\mathbf{p}\|_{l_2}$. Denoting the columns of $\mathbf{A}$ as $\mathbf{a}_m$, the aforementioned selection at the first iteration is done as follows,

$$\arg \max_{m=0,\ldots,M-1} |\langle \hat{\mathbf{r}}_y, \mathbf{a}_m \rangle| \cdot w_m^{-1} \tag{4.31}$$

Thus, the function defined by $f(\omega_m) = |\langle \hat{\mathbf{r}}_y, \mathbf{a}_m \rangle| \cdot w_m^{-1}$ determines the detection performance. Usually, a threshold for $f(\omega_m)$ is chosen based a given value of P_{fa}. Theoretical derivation of the threshold to meet the required P_{fa} requires the statistical distribution of $f(\omega_m)$ for H1 and H0, which is a difficult task, especially when eigenvalues appear on the function $f(\omega_m)$. To find an approximate distribution of $f(\omega_m)$, we recorded 10.000 Monte Carlo simulations for H1 and H0, keeping the value of $f(\omega_m)$ of the true primary user frequency. Fig. 4.29 shows

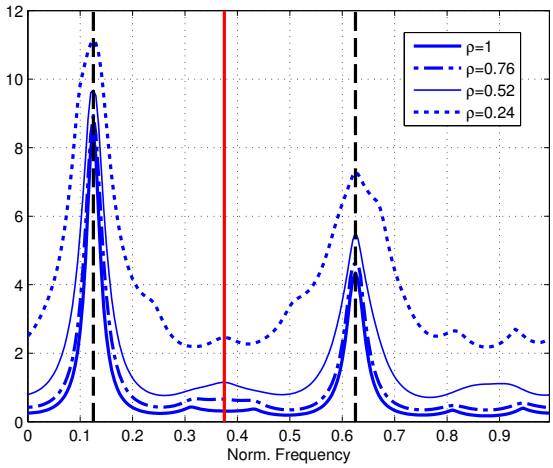

FIGURE 4.26: Inverse of weights performance. The scenario considers two BPSK primary users (rectangular pulse and 8 samples per symbol) with SNR=10 dB and SNR=7 dB, respectively, and at frequencies $\omega_1 = 0.125$ and $\omega_2 = 0.625$, respectively. A pure tone interference signal with SNR=10 dB is located at $\omega_I = 0.375$.

the obtained distributions of the function $f(\omega_m)$ for H0 and H1 for a particular example with SNR=-18 dB and $\rho = 0.76$. In Fig. 4.29 it is seen that both distributions closely match the Gaussian approximation (also shown in the figure with black solid line). In view of the results we have obtained, we decided to adopt Gaussian models for computing ROC figures. Therefore, from the 10.000 Monte Carlos runs we extract mean and variance of each hypothesis to build the corresponding probability density function (PDF) in the following way,

$$\text{pdf}(x) = \frac{1}{\sqrt{2\pi\sigma_x^2}} e^{-\frac{(x-\mu_x)^2}{2\sigma_x^2}} \tag{4.32}$$

where μ_x and σ_x^2 denote the mean and the variance, respectively.

In order to show the effect of the compression rate on the proposed detector, the ROC curves of the scenarios described above are compared in Fig. 4.30 for different compression rates and for SNR ranging from -16 dB to -20 dB. The curves corresponding to $\rho = 1$ and $\rho = 0.76$ are almost identical, while those corresponding to $\rho = 0.52$ and $\rho = 0.24$ progressively deteriorate as ρ decreases.

Fig. 4.31 shows the P_d versus SNR results for the same scenario (a BPSK primary user located at $\omega = 0.5$, free from interference) for a fixed probability of false alarm $P_{fa} = 10^{-3}$. It is clear that, even for low compression rates, the proposed sparsity-based primary user detection approach is able to reliably detect very low primary transmission. For comparison, we plot in the same figure the results for the energy detection without noise uncertainty and the performance of the coarse estimate given by the inverse of the weights for the same scenario and for $\rho = 1$. As shown in the figure, the energy detection and the estimates given by the weights are much worse than that of the proposed technique.

Let us now investigate the performance of the proposed detector with Ricean fading channel. We consider here that the data consists of the sum of noise, pure tone interference and BPSK primary user's signal with the same 100 different 20-tap Rice channel realizations used in Fig. 4.13. The performance is shown in Fig. 4.32 for different compression rates. The scenario consists of a BPSK primary user with 8 samples per symbol and SNR=10 dB at

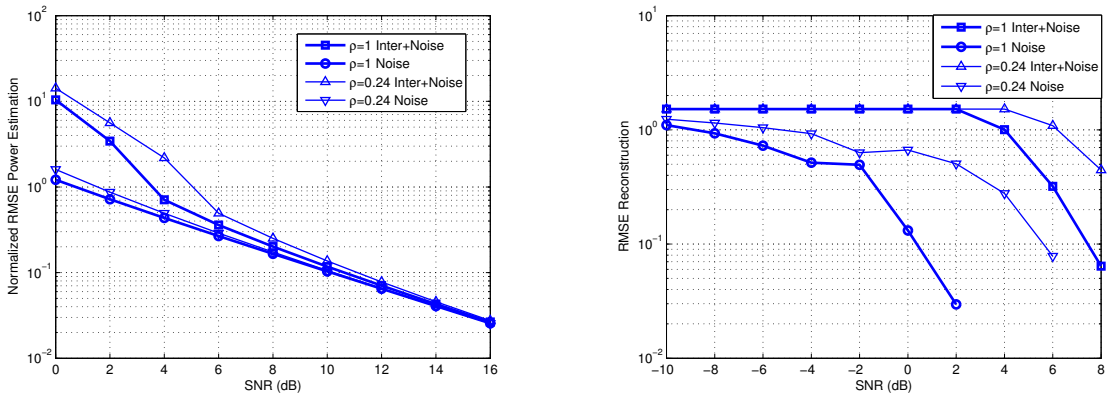

(a) (b)

FIGURE 4.27: Performance of the candidate detector with CS-based reconstruction. RMSE results. Two types of scenario were considered. The first one with one active primary user with BPSK, using a rectangular pulse shape (with 8 samples per symbol) located at frequency $\omega = 0.5$ and with AWGN. The second one is the same as the first plus a pure tone interference with SNR=10 dB located at frequency $\omega_I = 0.6$. (a) Normalized RMSE of the estimated power level, (b) RMSE of the reconstruction error.

frequency 0.25 and a pure tone interference signal located at 0.75 with SNR=10 dB. In Fig. 4.32, blue points indicate the output of the detector, black cross represents the true primary user location and the red solid line indicates the interference location. It is seen that the method is robust in front of a frequency selective channel in terms of detection capabilities since the majority of detection events took place in close vicinity of the true primary user location. However, is clear from Fig. 4.32 that the multipath causes quite small bias on the frequency and power estimation.

Conclusion

The performance of the candidate detector considering CS-based reconstruction strategies was evaluated in this section using synthesized data. In our previous work, the sparsity of the primary signals sent out over the spectrum was used to alleviate the sampling burden but not imposed on the primary user detection. In this part, we take advantage of the sparsity described by the low spectral occupancy of the licensed radios not only to alleviate the sampling bottleneck but also to increase the accuracy of the detections by using sparsity-based recovery methods. Results based on computer simulations were presented, which showed the effectiveness in primary user detection and proved the interference rejection capabilities of the proposed method.

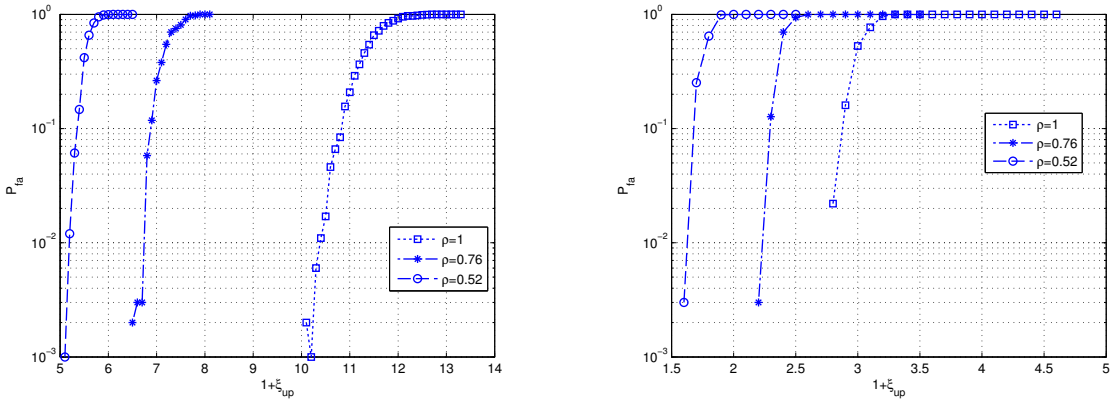

(a) (b)

FIGURE 4.28: Performance of the candidate detector with CS-based reconstruction. Probability of false alarm versus $1 + \xi_{up}$ for different compression rates. The scenario consists of a BPSK primary user located at frequency $\omega = 0.25$ with SNR=0 dB plus an interferent signal with the same SNR located at frequency $\omega_I = 0.75$. (a) Interference is pure tone, (b) Interference is QPSK.

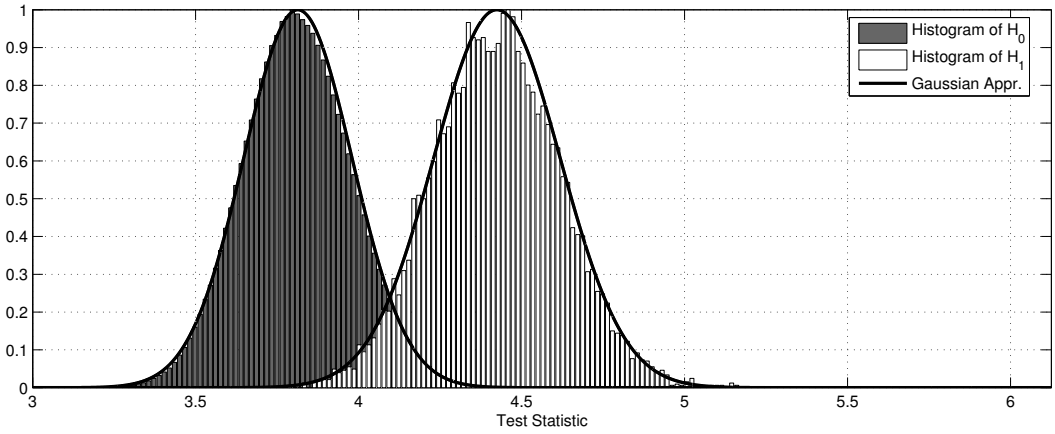

FIGURE 4.29: Performance of the candidate detector with CS-based reconstruction. Theoretical and empirical distributions of $f(\omega_m)$ for H1 and H0 for SNR=-18 dB and $\rho = 0.76$. The scenario for H1 consists of a BPSK primary user (8 samples per symbol) located at frequency $\omega = 0.5$ plus noise, and the scenario for H0 consists of only noise.

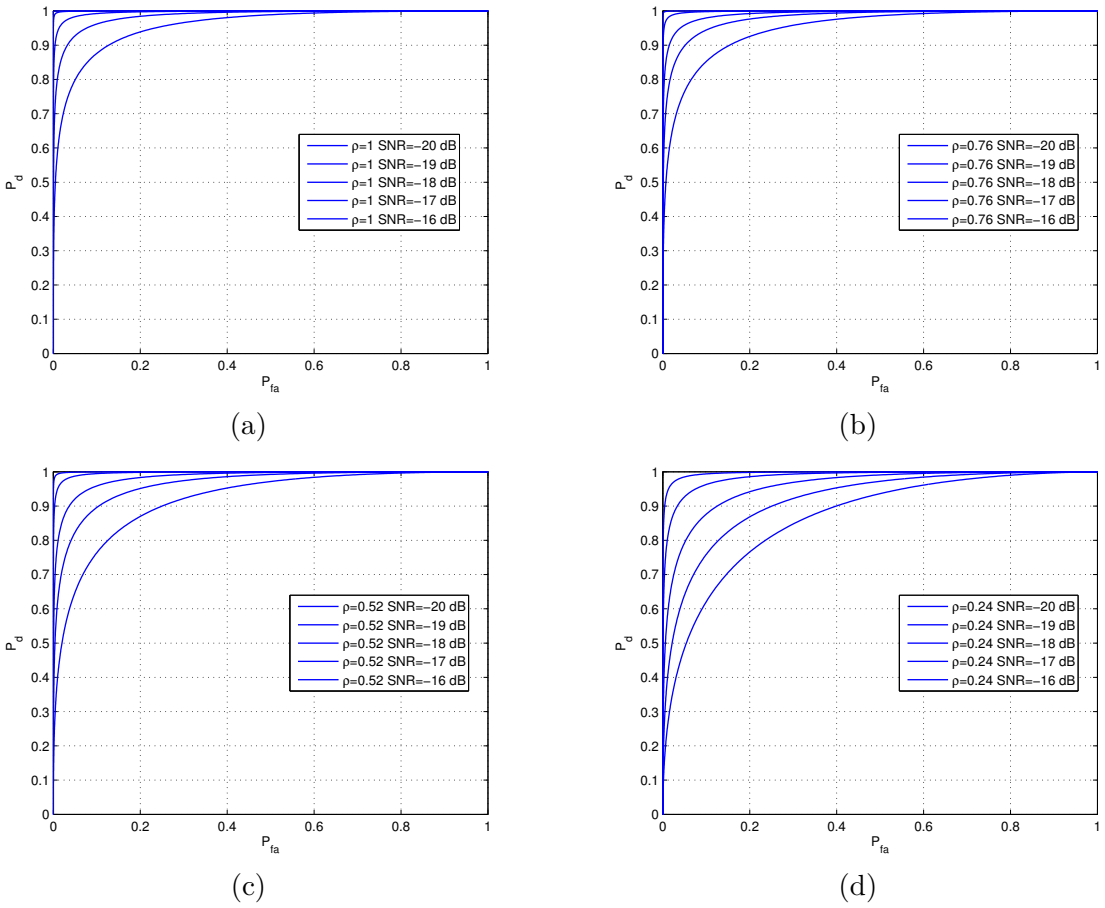

FIGURE 4.30: Performance of the candidate detector with CS-based reconstruction. ROC figures for different compression rates. The scenario considers a single desired signal which is a BPSK signal with rectangular pulse shape and 8 samples per symbol, located at frequency $\omega = 0.5$. (a) $\rho = 1$, (b) $\rho = 0.76$, (c) $\rho = 0.52$, and (d) $\rho = 0.24$.

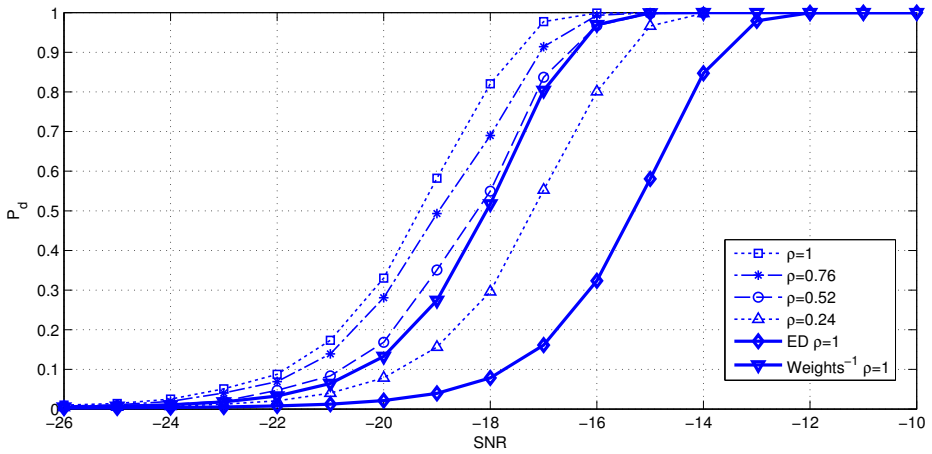

FIGURE 4.31: Performance of the candidate detector with CS-based reconstruction. Probability of detection versus SNR. The scenario considers a single desired signal which is a BPSK signal with rectangular pulse shape and 8 samples per symbol, located at frequency $\omega = 0.5$.

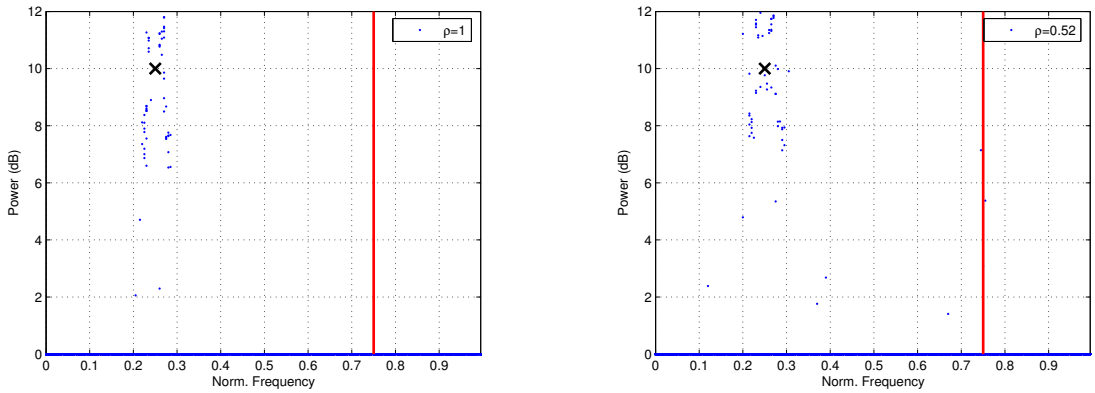

(a) (b)

FIGURE 4.32: Performance of the candidate detector with CS-based reconstruction in a Rice Channel. The primary user is a BPSK, with 8 samples per symbol, and SNR=10 dB at frequency 0.25. The interference is a pure tone located at 0.75 with SNR=10 dB. 20-length Rice channel is considered. The results are obtained averaging 100 different channel realizations. Here, $1 + \xi_{up} = 10$. (a) $\rho = 1$, and (b) $\rho = 0.52$.

Chapter 5

Application II: Through-the-Wall Radar Imaging

The material presented in this chapter was partially published by the author in [**III**], [**IV**], [**VI**], [**IX**], [**XI**], [**XIII**], [**XIV**] and [**XV**].

In this section, the candidate detector based on compressive sampling is applied to the TWRI.

5.1 Through-the-wall general notation

5.1.1 TWR signal model

Consider a homogeneous wall of thickness d and dielectric constant ϵ located along the x-axis, and the region to be imaged located beyond the wall along the positive z-axis. Consider a N-element line array of transceivers (SAR) in which a single antenna at one location transmits and receives the wideband radar signal, then moves to the next location, and repeats the same operation along a line-path parallel to the front wall at a standoff distance z_{off}, as shown in Fig. 5.1 and Fig. 5.2. Let the nth transceiver, located at $\mathbf{x}_n = (x_n, -z_{off})$, illuminate the scene with a stepped-frequency signal of M frequencies, which are equispaced over the desired bandwidth $B_\omega = \omega_{M-1} - \omega_0$,

$$\omega_m = \omega_0 + m\Delta_\omega \quad m = 0, \ldots, M-1 \tag{5.1}$$

where ω_0 and Δ_ω are the lowest frequency in the desired frequency band and the frequency step size, respectively. Note that, due to the specular nature of the wall reflections, only contributions from walls parallel to the antenna array will be received at the array. Thus, a SAR system located parallel to the front wall will only be able to detect walls which are parallel to the front wall. The detection of perpendicular walls is only possible if we have access to another side of the building. Assuming the scene contains P point targets, the output of the nth transceiver corresponding to the mth frequency is given by,

$$y(m,n) = \sigma_\omega \exp(-j\omega_m \tau_\omega) + \sum_{p=0}^{P-1} \sigma_p \exp(-j\omega_m \tau_{p,n}) \tag{5.2}$$

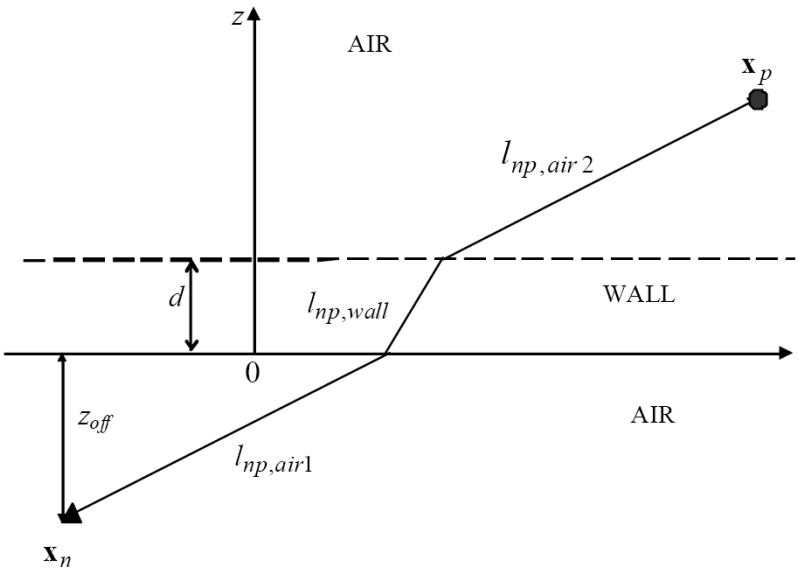

FIGURE 5.1: Geometry on transmit of the equivalent two-dimensional problem.

where σ_ω is the complex reflectivity of the wall, σ_p is the complex reflectivity of the pth target, τ_ω is the two-way traveling time of the signal from the nth antenna to the wall, and $\tau_{p,n}$ is the two-way traveling time between the nth antenna and the target. It is noted that both the wall and target reflectivities are assumed to be independent of frequency and aspect angle. The propagation delay τ_ω is given by

$$\tau_\omega = \frac{2z_{off}}{c} \tag{5.3}$$

where c is the speed of light in free-space. On the other hand, $\tau_{p,n}$ is given by [67]

$$\tau_{p,n} = \frac{2l_{np,air1}}{c} + \frac{2l_{np,wall}}{v} + \frac{2l_{np,air2}}{c} \tag{5.4}$$

where $v = c/\sqrt{\epsilon}$ is the speed through the wall, and the variables $l_{np,air1}$, $l_{np,wall}$, and $l_{np,air2}$ represent the traveling distances of the signal before, through, and beyond the wall, respectively, from the nth transceiver to the pth target.

5.1.2 Image formation

A radar image is generated from the MN observations, $y(m,n)$, $m = 0,\ldots,M-1$, $n = 0,\ldots,N-1$, using a wideband synthetic aperture beamformer as follows. The scene being imaged is partitioned into a finite number of pixels, $N_x \times N_z$, in crossrange and downrange. That is, the scene can be represented by the complex reflectivity function $r(k,l), k = 0,\ldots,N_x-1, l = 0,\ldots,N_z-1$. The complex composite signal, corresponding to the (k,l)th pixel, is obtained by applying a set of focusing delays, $\tau_{(k,l),n}$, to align all signal returns from the (k,l)th pixel, and then summing the results [67],

$$r(k,l) = \frac{1}{MN}\sum_{n=0}^{N-1}\sum_{m=0}^{M-1} y(m,n)e^{j\omega_m\tau_{(k,l),n}}. \tag{5.5}$$

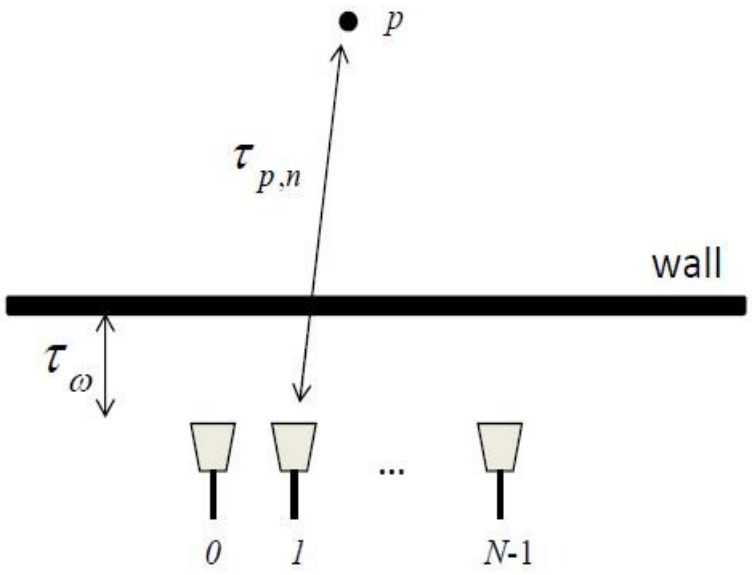

FIGURE 5.2: Data collection using a synthetic array in through-the-wall radar imaging.

Note that the focusing delay, $\tau_{(k,l),n}$ corresponds to the two-way signal propagation time between the nth antenna location and the (k,l)th pixel. The process described by eqn. (5.5) is performed for all $N_x \times N_z$ pixels to generate the image of the scene. The aforementioned image formation procedure is commonly known as frequency-domain backprojection. Note that expression (5.5) assumes the point target model.

5.2 Sparse representation of the image

An equivalent matrix-vector representation of the received signals in (5.2) can be obtained as follows. Assume that the region of interest is given by the pixels grid $N_x \times N_z$ defined by $r(k,l)$, and the point targets occupy no more than P ($<< N_x \times N_z$) pixels. Function $r(k,l)$ can be seen as a weighted indicator function, which takes the value σ_p if the pth point target exists at the (k,l)th pixel; otherwise, it is zero. With the values $r(k,l)$ lexicographically ordered into a column vector $\mathbf{r}$ of length N_xN_z, the received signal corresponding to the nth antenna can be expressed in matrix-vector form as,

$$\mathbf{y}_n = \mathbf{\Psi}_n \mathbf{r} \tag{5.6}$$

where $\mathbf{\Psi}_n$ is a matrix of dimensions $M \times N_xN_z$, and its mth row is given by,

$$[\mathbf{\Psi}_n]_m = \begin{bmatrix} e^{-jw_m\tau_{n,00}} & \dots & e^{-jw_m\tau_{n,N_xN_z}} \end{bmatrix} \tag{5.7}$$

Considering the measurement vector corresponding to all N antennas, defined as,

$$\mathbf{y} = \begin{bmatrix} \mathbf{y}_0^T & \mathbf{y}_1^T & \cdots & \mathbf{y}_{N-1}^T \end{bmatrix}^T \tag{5.8}$$

the relationship between $\mathbf{y}$ and $\mathbf{r}$ is given by

$$\mathbf{y} = \mathbf{\Psi}\mathbf{r} \tag{5.9}$$

where

$$\mathbf{\Psi} = \begin{bmatrix} \mathbf{\Psi}_0^T & \mathbf{\Psi}_1^T & \cdots & \mathbf{\Psi}_{N-1}^T \end{bmatrix}^T \tag{5.10}$$

Note that the expression given in (5.9) provides a linear relationship between the sparse image and the received data.

5.3 Sparsity-based data acquisition and scene reconstruction

The expression in (5.9) involves the full set of measurements made at the N array locations using the M frequencies. The prevalent assumptions in CS-based TWRI literature are that i) the scene being imaged itself is sparse, and ii) the targets satisfy the point target model. The approach based on these assumptions is presented next, and it will be called *conventional* approach henceforth.

For a sparse scene, it is possible to recover $\mathbf{r}$ from a reduced set of measurements. Consider $\breve{\mathbf{y}}$,which is a vector of length Q_1Q_2 ($<< MN$) consisting of elements chosen from $\mathbf{y}$ as follows,

$$\breve{\mathbf{y}} = \mathbf{\Phi}\mathbf{y} = \mathbf{\Phi}\mathbf{\Psi}\mathbf{r} \tag{5.11}$$

where $\mathbf{\Phi}$ is a $Q_1Q_2 \times MN$ matrix of the form,

$$\mathbf{\Phi} = \text{kron}\left(\boldsymbol{\vartheta}, \mathbf{I}_{Q_1}\right) \cdot \text{diag}\left\{\boldsymbol{\varphi}^{(0)}, \ldots, \boldsymbol{\varphi}^{(N-1)}\right\} \tag{5.12}$$

In (5.12), 'kron' denotes the Kronecker product, $\mathbf{I}_{Q_1}$ is a $Q_1 \times Q_1$ identity matrix, $\boldsymbol{\vartheta}$ is a $Q_2 \times N$ measurement matrix constructed by either uniformly or randomly selecting Q_2 rows of an $N \times N$ identity matrix, and $\boldsymbol{\varphi}^{(n)}, n = 0, 1, \ldots, N-1$, is a $Q_1 \times M$ measurement matrix constructed by uniformly or randomly selecting Q_1 rows of an $M \times M$ identity matrix. We note that $\boldsymbol{\vartheta}$ determines the reduced antenna locations, whereas $\boldsymbol{\varphi}^{(n)}$ determines the reduced set of frequencies corresponding to the nth antenna location. The number of measurements Q_1Q_2 required to achieve successful CS reconstruction highly depends on the coherence between $\mathbf{\Phi}$ and $\mathbf{\Psi}$. For the problem at hand, $\mathbf{\Phi}$ is the canonical basis and $\mathbf{\Psi}$ is similar to the Fourier basis, which have been shown to exhibit maximal incoherence [9]. Given $\breve{\mathbf{y}}$, we can recover $\mathbf{r}$ by solving the following equation,

$$\arg\min_{\mathbf{r}} \|\mathbf{r}\|_{l_1} \quad \text{subject to} \quad \breve{\mathbf{y}} \approx \mathbf{\Phi}\mathbf{\Psi}\mathbf{r} \tag{5.13}$$

In this thesis, we consider MP to solve (5.13). More specifically, we use the Orthogonal Matching Pursuit (OMP), which is known to provide a fast and easy to implement solution. Moreover, OMP is better suited when frequency measurements are used [17]. In this part of the thesis, we consider five different measurement strategies listed below. Reduced set of frequencies (antennas) means using a smaller number of frequencies (antennas) than those available.

1. **Case (a):** Measure all M frequencies at each of the N antenna locations. The corresponding space-frequency sampling pattern is shown in Fig. 5.3, where the vertical axis represents the antenna locations, and the horizontal axis represents the frequency. The gray filled boxes represent the sampled data.

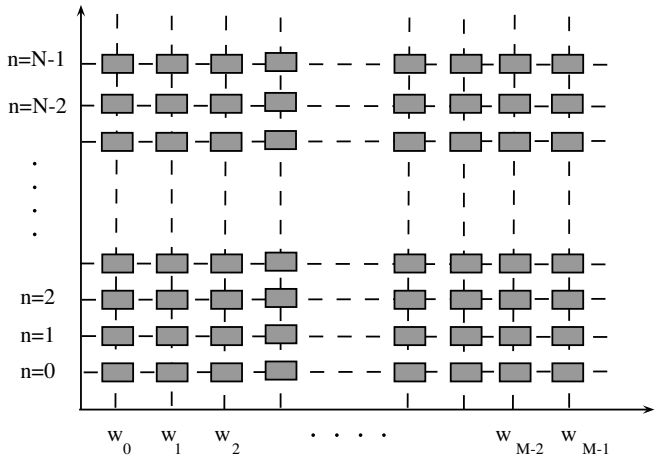

FIGURE 5.3: Case (a) - Illustration of an example of the pattern of the conventional configuration.

2. **Case (b):** Measure the same reduced set of frequencies for all N antenna locations. The corresponding space-frequency sampling pattern is illustrated in Fig. 5.4(a) for uniform sampling and in Fig. 5.4(b) for random sampling.

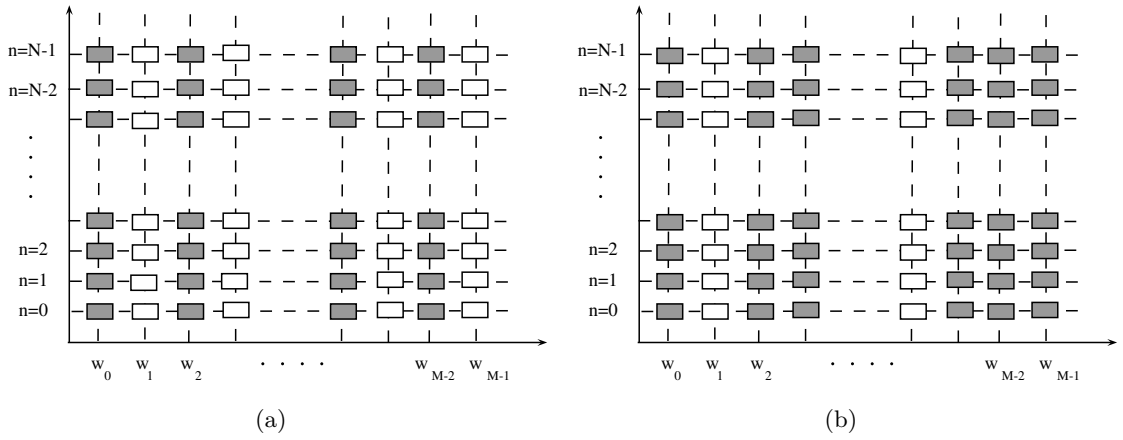

FIGURE 5.4: Case (b) - Illustration of an example of subsampling pattern of the conventional configuration: (a) uniform subsampling, (b) random subsampling

3. **Case (c):** Measure the same reduced set of frequencies for a reduced set of antenna locations. The corresponding space-frequency sampling pattern is illustrated in Fig. 5.5(a) for uniform sampling and in Fig. 5.5(b) for random sampling.

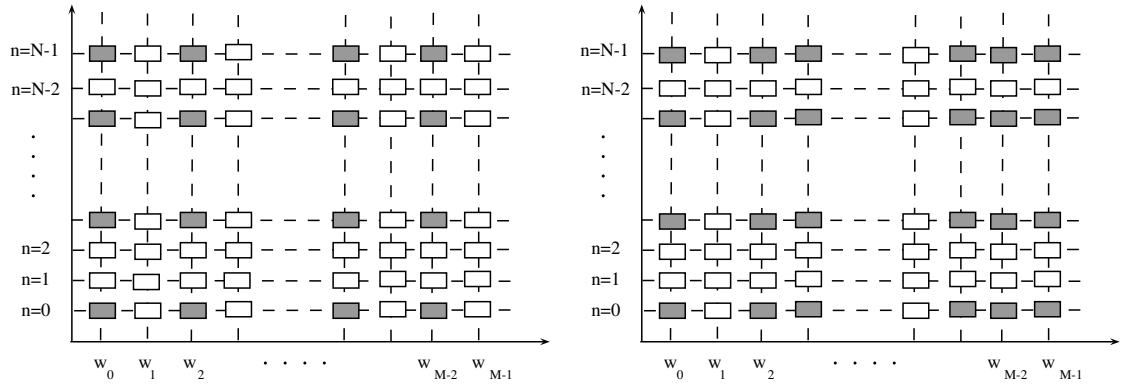

FIGURE 5.5: Case (c) - Illustration of an example of subsampling pattern of the conventional configuration: (a) uniform subsampling, (b) random subsampling

4. **Case (d):** Measure a different set of reduced frequencies for each of the N antenna locations. The corresponding space-frequency sampling pattern is shown in Fig. 5.6.

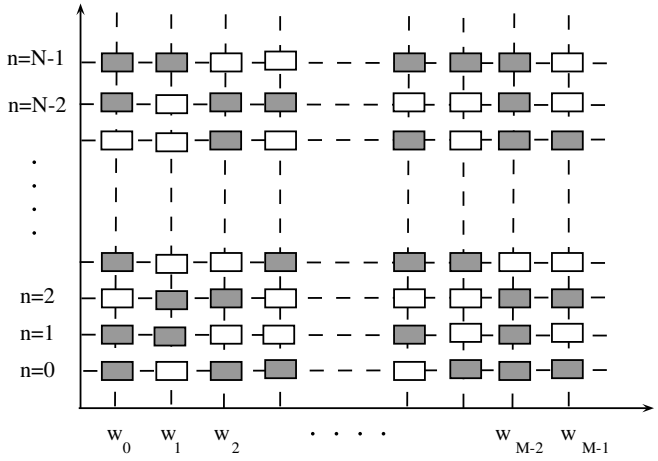

FIGURE 5.6: Case (d) - Illustration of an example of random subsampling pattern of the conventional configuration.

5. **Case (e):** Measure a different set of reduced frequencies for a reduced set of antenna locations. The corresponding space-frequency sampling pattern is shown in Fig. 5.7.

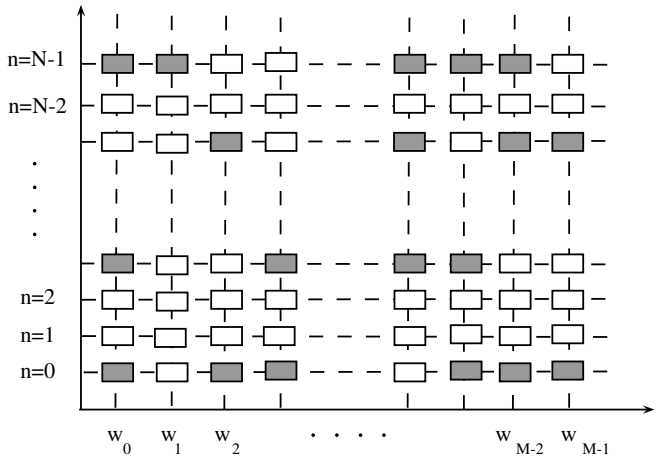

FIGURE 5.7: Case (e) - Illustration of an example of random subsampling pattern of the conventional configuration.

Each of the above strategies has a corresponding $\mathbf{\Phi}$ matrix associated with it. When the full set of measurements is available (case (a)), $\mathbf{\Phi}$ equals an identity matrix of dimensions $MN \times MN$. If the same reduced set of frequency measurements are used at each antenna location (case (b) and case (c)), then $\boldsymbol{\varphi}^{(0)} = \boldsymbol{\varphi}^{(1)} = \ldots = \boldsymbol{\varphi}$ and $\mathbf{\Phi}$ takes the form

$$\mathbf{\Phi} = \text{kron}\left(\mathbf{I}_N, \boldsymbol{\varphi}\right) \qquad \text{case(b)} \tag{5.14}$$

$$\mathbf{\Phi} = \text{kron}\left(\boldsymbol{\vartheta}, \boldsymbol{\varphi}\right) \qquad \text{case(c)} \tag{5.15}$$

where $\mathbf{I}_N$ is an identity matrix of dimensions $N \times N$. For case (d), in which all antenna positions are used but different reduced frequency sets are emitted by different antennas, the expression in (5.12) reduces to,

$$\mathbf{\Phi} = \text{diag}\left\{\boldsymbol{\varphi}^{(0)}, \ldots, \boldsymbol{\varphi}^{(N-1)}\right\} \tag{5.16}$$

The general expression presented in (5.12) corresponds to case (e).

5.3.1 Relation between compression and image resolution

As it was mentioned in the Introduction, radar imaging achieves its down-range and cross-range resolutions through the exploitation of, respectively, the bandwidth of the signals and the aperture of the array of sensors used in the operation. The down-range resolution of a radar system is approximately $2\pi c/2B_\omega$, where c is the speed of propagation and B_ω the transmitted signal bandwidth. Thus, to achieve sufficient down-range resolution, large bandwidth are required. The cross-range resolution is linked to the azimuth resolution and is approximately $\lambda R/D$, where λ is the wavelength, R is the range and D is the aperture size of the array.

SAR principles are similar to a conventional radar, where electromagnetic waves are sequentially transmitted and the backscattered echoes are collected by the radar antenna. In the case of SAR, however, the consecutive time of transmission/reception translates into different positions due to the platform movement. The introduction of SAR concept represented a significant advancement in radar technology since it can produce finer resolution without

requiring a large-size physical antenna. The azimuth resolution is provided by the construction of the synthetic aperture: A long synthetic aperture is favorable since it results in a narrow virtual beamwidth and a high azimuth resolution [118]. On the other hand, TWRI need to operate at low frequencies (typically below 3GHz) to be able to penetrate through the lossy wall materials. However, the lower the frequency, the larger the antenna. Because all these considerations, most researchers in the field consider the range about $1-4$ GHz being optimal for most type of TWRI scenarios [119].

Frequency reduction

CS requires many fewer samples to construct the target space image if the target space is sparse. In stepped-frequency TWRI, we can choose the reduced set of samples in two different ways: through uniform or random sub-sampling. One possible way to reduce frequency samples is uniform sampling over the bandwidth with larger frequency steps. As mentioned earlier in this thesis, the uniform sampling interval and the upper limit of the recoverable signal are inexorably linked. The phenomenon of aliasing manifested in TWRI is caused by the non proper choice of the measurement parameters. The maximum unambiguous down-range of the image is determined by the Nyquist limit, which in TWRI is related to the frequency step size. Let us focus on a particular antenna (see Fig. 5.8). In a general stepped-frequency signal, the M frequencies are equispaced over the desired bandwidth $2\pi/B_\omega$. The step size is indicated in Fig. 5.8 with the variable Δf. To convert these values to a range domain we can apply the Fast Fourier Transform (FFT) to the stepped-frequency signal. Clearly, the inverse of B_ω determines the inter-sample range while the inverse of Δf determines the maximum unambiguous range. Table 5.1 shows some examples of maximum unambiguous range for different step sizes. The maximum range in the Radar Imaging Lab, in Villanova University, is of the order of 7-8m. Thus, the limit in this case will be $\Delta f \approx 20$MHz. Uniform sampling is very straight forward to implement.

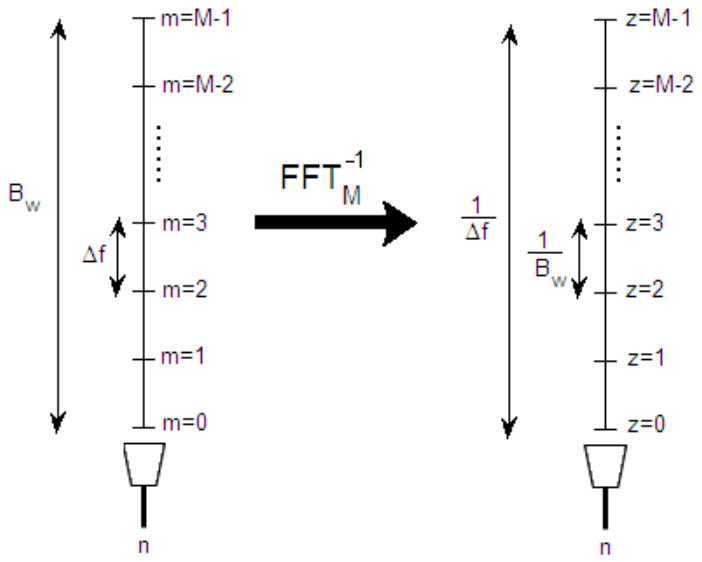

FIGURE 5.8: Scheme of a stepped-frequency signal and its FFT.

The potential problems of systematic sampling are avoided by suitable use of random sampling. The ambiguity with uniform sub-sampling is overcomed with the random selection

TABLE 5.1: Max. Unambiguous Range

Step Size	3MHz	6MHz	9MHz	12MHz	15MHz	18MHz	21MHz	24MHz	27MHz	30MHz
Max. Range	50m	25m	16.67m	12.5m	10m	8.33m	7.14m	6.25m	5.56m	5m

of samples. In this case, the intervals between successive samples are independent random variables with a common distribution (usually uniformly distributed). The only restriction imposed on the minimum number of random samples is given by the conventional CS theory.

Antenna reduction

The number of positions from which we illuminate the scene can also be reduced in the same way we did for frequency samples: uniformly or randomly selecting samples.

For a uniformly spaced line array with an inter-element spacing of d and operating at wavelength λ, the grating lobes (aliased copies of mainlobe) occur at $\sin(\theta) = k\frac{\lambda}{d}$, where θ is the angle from the y-axis if the array is positioned along the x-axis and k is the grating lobe index. That is, $k = 0$ corresponds to the mainlobe, $k = 1$ corresponds to the first grating lobe and so on. More details about antenna design can be found in [120,121]. The element spacing has a large influence on the radar performance: A larger spacing results in a higher directivity. However, the element spacing is generally kept smaller than $\lambda/2$ to avoid the occurrence of grating lobes, i.e., another unwanted peak value in the radiation pattern of the array. As d takes values beyond $\lambda/2$, the grating lobes locations for $k \geq 1$ occur within the visible region, -90° to $+90^\circ$. As the cross-range value will vary for the same θ with range, typically specifiying the maximum angular extent free of grating lobes should suffice. Table 5.2 shows some examples of maximum inter-element spacing d for different operating frequencies. The aforementioned formulas and limits are for general uniform line array case, where we assume multistatic operation, i.e., when an antenna element transmits and all others including itself can receive. In that case, the spacing needs to be $\lambda/2$ to satisfy Nyquist. For a monostatic line array, which typically is the case for SAR, the spacing has to be $\lambda/4$ to satisfy Nyquist, which is half of the distance defined by general physical line arrays.

One important parameter in through-wall radar is the radio wavelength: longer wavelengths are better able to pass through the wall. Fig. 5.9 shows the RF attenuation in different types of walls (figure extracted from [122]). From Fig. 5.9 is clear that electromagnetic waves with frequencies of few GHz are able to penetrate through almost all types of materials. Low frequencies, however, require larger inter-element spacing between antennas.

TABLE 5.2: Max. Inter-Element Spacing

Frequency	3GHz	2GHz	1.5GHz	1GHz	750MHz	500MHz	250MHz
d	5cm	7.5cm	10cm	15cm	20cm	30cm	60cm

To mitigate the grating lobes that are manifested with a uniformly subsampled array, it is desirable to study arrays with non-uniform inter-element spacing. Randomization of array element locations has been studied in [123–125] with the objective of reducing sidelobes in sparsely populated arrays. Both random arrays and CS main goal is high resolution via relatively small number of measurements. The connection between random sensor arrays and the random nature of CS is studied in [126]. In CS parlance, the $\lambda/2$-spaced array perform spatial sampling at Nyquist rate. A random array setup in which the spatial sampling is at sub-Nyquist rates is usually used for spatial compression. Again, the restriction of the

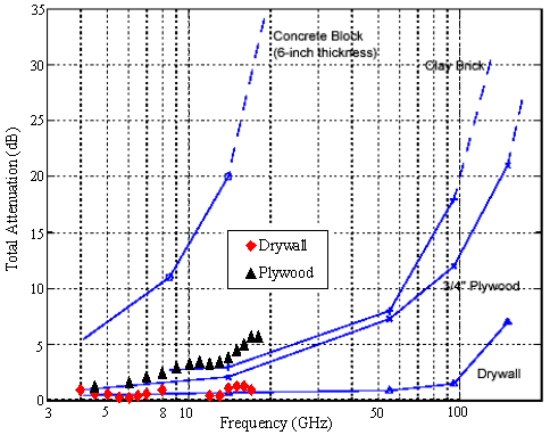

FIGURE 5.9: RF signal attenuation versus frequency

conventional CS theory will determine the minimum number of random scan positions. An explicit lower bound on the number of random array elements needed to achieve a prescribed probability of correct DOA estimation is derived in [127].

5.4 Joint wall mitigation and compressive sensing for indoor image reconstruction

In order to detect and localize targets behind the wall, the clutter, caused by the front wall EM backscatterings, must be suppressed, or significantly mitigated, and its effects on the imaged scene accuracy and fidelity must be limited. Behind-the-wall target returns are relatively weak compared to front wall reflections and, therefore, stationary targets cannot be generally detected without an effective removal of front wall clutter.

In TWRI, backprojection is typically employed for image formation. Recently, it has been shown that CS and l_1 norm reconstruction techniques can be applied, in lieu of backprojection, to reveal the target positions behind walls. In so doing, significant savings in acquisition time can be achieved. Further, as mentioned in section 2.3.4, producing an image of the indoor scene using few observations can be logistically important, as some of the data measurements in space and frequency can be difficult, or impossible to attain. In this part of the thesis, we apply joint CS and wall mitigation techniques using reduced data measurements. In essence, we address wall clutter mitigations in the context of CS.

The application of CS for TWRI was first reported in [95] and further developed in [96–98]. However, wall mitigation in conjunction with CS has never been considered in these references. That is, CS was applied to TWRI, already assuming prior and complete removal of the front wall EM returns. Without this assumption, strong wall clutter, which extends along the range dimension, reduces the sparsity of the scene and, as such, impedes the application of CS. If the reference scene is known, then background subtraction can be performed to remove wall clutter, thereby improve sparsity. Having access to the background scene or reference data, however, is not always possible in practical applications.

Several approaches which successfully mitigate the front wall contribution to the received signal were presented in section 2.3.2. They can be categorized into those based on estimating the wall parameters and others incorporating either wall backscattering strength or invariance with antenna location [77, 79, 80, 128, 129]. These approaches were originally introduced to

work on the full data volume and did not account for nor were they ever examined under reduced data measurements.

In this thesis, we examine the performance of the spatial filtering [79] and subspace projection wall mitigation techniques [80, 130] in conjunction with sparse image reconstruction. Only a small subset of measurements is employed for both wall clutter reduction and image formation. The wall parameter estimation and backscattering modeling technique [77, 78] is outside the scope of this paper. Unlike the two other techniques, strong antenna ringing hinders EM modeling and prevents performance validation experimentally in our Lab.

We consider two cases of frequency measurement distributions over antenna positions. In the first case, the same subset of frequencies is used for each antenna. The other case allows the frequencies to differ from one antenna to another. For the subspace projection and spatial filtering methods, we show that when the same subset of frequency measurements is used at each antenna, those two methods maintain their proper performance as their full-data set counterparts. CS techniques for image reconstruction can then be applied with the same reduced measurements but of much higher signal-to-clutter ratio. On the other hand, using different frequencies at different antenna positions would impede the application of either method. This is because the phase returns across the antenna elements would be different, which deprives the wall mitigation algorithms of the underlying assumption of spatial invariance of the wall clutter. This problem is overcome in this section by first reconstructing the range profile, which is based on l_1 norm minimization. This is performed at each antenna individually. Then, the data of the missing frequencies can be obtained by taking the FFT of the reconstructed range profile at each antenna. A similar approach was adapted in [97]; however, it required the fundamental assumption of prior removal of wall EM scattering. Once the phase returns corresponding to all original frequencies are estimated, wall mitigation can proceed using spatial filtering, subspace projection, or any other conventional wall mitigation method.

In this section, sparse data reconstruction is performed using Orthogonal Matching Pursuit (OMP) which provides fast l_1 solutions and is appropriate for stepped frequency radar imaging. Since the target is behind the wall, the OMP can be modified such that the iterations corresponding to the range up to the wall can be combined. This allows a quicker inclusion of the target into the reconstruction algorithm. We compare OMP with the modified OMP and show the abilities as well as the challenges of performing TWRI with arbitrary data measurements.

5.4.1 Wall mitigation techniques

In this section, we review the front wall clutter mitigation techniques of spatial filtering and subspace projection presented in [79] and [80, 130], respectively.

Spatial filtering approach

From (5.2), we note that τ_ω does not vary with the antenna location since the array is parallel to the wall. Furthermore, as the wall is homogeneous and assumed to be much larger than the beamwidth of the antenna, the first term in (5.2) assumes the same value across the array aperture. Unlike τ_ω, the time delay $\tau_{p,n}$ in (5.2) is different for each antenna location, since the signal path from the antenna to the target is different from one antenna to the other. For the mth frequency, the received signal is a function of n via the variable $\tau_{p,n}$. Therefore, we

can rewrite (5.2) as,

$$y_{\omega_m}(n) = v_{\omega_m} + \sum_{p=0}^{P-1} u_{p,\omega_m}(n) \tag{5.17}$$

where $v_{\omega_m} = \sigma_\omega e^{-j\omega_m \tau_\omega}$ and $u_{p,\omega_m}(n) = \sigma_p e^{-j\omega_m \tau_{p,n}}$. Thus, separating wall reflections from target reflections amounts to basically separating constant from non-constant valued signals across antennas, which can be performed by applying a proper spatial filter [79] across the antenna array.

In its simplest form, the spatial filter, which removes, or significantly attenuates, the zero spatial frequency component, can be implemented as the subtraction of the average of the radar return across the antennas. That is,

$$\tilde{y}_{\omega_m}(n) = y_{\omega_m}(n) - \bar{y}_{\omega_m} \tag{5.18}$$

where

$$\bar{y}_{\omega_m} = \frac{1}{N} \sum_{n=0}^{N-1} y_{\omega_m}(n) \tag{5.19}$$

It can be readily shown that the spatial frequency transform of $\tilde{y}_{\omega_m}(n)$ is given by,

$$\begin{aligned} \tilde{Y}_{\omega_m}(\kappa) &= \sum_{n=0}^{N-1} \tilde{y}_{\omega_m}(n) \exp(-j2\pi\kappa n/N) \\ &= \sum_{n=0}^{N-1} (y_{\omega_m}(n) - \bar{y}_{\omega_m}) \exp(-j2\pi\kappa n/N) \\ &= Y_{\omega_m}(\kappa) - N\bar{y}_{\omega_m}\delta[\kappa] \end{aligned} \tag{5.20}$$

where κ is the spatial frequency. As $Y_{\omega_m}(\kappa)|_{\kappa=0}$ equals $N\bar{y}_{\omega_m}$, the filtered spatial spectrum $\tilde{Y}_{\omega_m}(\kappa)$ is 0 for $\kappa = 0$; otherwise, $\tilde{Y}_{\omega_m}(\kappa) = Y_{\omega_m}(\kappa)$. Thus, the subtraction operation removes the single spatial frequency component ($\kappa = 0$) without changing other components. In practice, the spatial spectrum of the wall reflections may have a nonzero width due to unstable antenna path and/or local inhomogeneities, and a more sophisticated filter with a wider stopband could be applied. However, care should be exercised to not alter the target response. These issues are discussed in detail in [79]. The output spatial filter data will have little or no contribution from the wall reflections.

Subspace projection

The signals received by the N antennas at the M frequencies are arranged into an $M \times N$ matrix, $\mathbf{Y}$,

$$\mathbf{Y} = \begin{bmatrix} \mathbf{y}_0 & \cdots & \mathbf{y}_n & \cdots & \mathbf{y}_{N-1} \end{bmatrix} \tag{5.21}$$

where $\mathbf{y}_n$ is the $M \times 1$ vector containing the stepped-frequency signal received by the nth antenna,

$$\mathbf{y}_n = \begin{bmatrix} y(0,n) & \cdots & y(m,n) & \cdots & y(M,n) \end{bmatrix}^T \tag{5.22}$$

with $y(m,n)$ given by (5.2). The eigen-structure of the imaged scene is obtained by performing the SVD of $\mathbf{Y}$,

$$\mathbf{Y} = \mathbf{U}\mathbf{\Lambda}\mathbf{V}^H \tag{5.23}$$

where 'H' denotes the Hermitian transpose, $\mathbf{U}$ and $\mathbf{V}$ are unitary matrices containing the left and right singular vectors, respectively, and $\mathbf{\Lambda}$ is a diagonal matrix containing the singular values $\lambda_1, \lambda_2, \ldots, \lambda_N$ in decreasing order, i.e.,

$$\mathbf{\Lambda} = \begin{pmatrix} \lambda_1 \ldots 0 \\ \vdots \ddots \vdots \\ 0 \ldots \lambda_N \\ \vdots \ddots \vdots \\ 0 \ldots 0 \end{pmatrix} \tag{5.24}$$

and $\lambda_1 \geq \lambda_2 \geq \ldots \geq \lambda_N$. Without loss of generality, the number of frequencies are assumed to exceed the number of antenna locations, i.e., $M > N$.

The subspace projection method assumes that the wall returns and the target reflections lie in different subspaces. Therefore, the first K dominant singular vectors of the $\mathbf{Y}$ matrix are used to construct the wall subspace,

$$\mathbf{S}_{wall} = \sum_{i=1}^{K} \mathbf{u}_i \mathbf{v}_i^H \tag{5.25}$$

The subspace orthogonal to the wall subspace is,

$$\mathbf{S}_{wall}^{\perp} = \mathbf{I} - \mathbf{S}_{wall}\mathbf{S}_{wall}^H \tag{5.26}$$

where $\mathbf{I}$ is the identity matrix. To mitigate the wall returns, the data matrix $\mathbf{Y}$ is projected on the orthogonal subspace,

$$\tilde{\mathbf{Y}} = \mathbf{S}_{wall}^{\perp}\mathbf{Y} \tag{5.27}$$

5.4.2 Joint wall mitigation and CS for TWRI

In this section, we consider joint wall mitigation and sparsity-based scene reconstruction under the various measurement strategies enumerated in section 5.3.

Same set of reduced frequencies at each antenna location

Both spatial filtering and subspace projection methods for wall clutter reduction rely on the fact that the wall reflections are the same for all antenna locations. When the same set of frequencies is employed for all employed antennas, i.e. cases (a), (b) and (c), the condition of spatial invariance of the wall reflections is not violated. This permits direct application of the wall clutter mitigation methods as a preprocessing step to the l_1 norm based scene reconstruction of (5.13).

A different set of reduced frequencies at each antenna location

Cases (d) and (e) use different sets of reduced frequencies for the various antenna locations, resulting in different wall reflection phase returns across the antenna elements. This would deprive the wall mitigation algorithms of the underlying assumption of spatial invariance of the wall clutter, thereby rendering the direct application of the wall mitigation methods ineffective. Therefore, cases (d) and (e) require additional data processing before the wall clutter mitigation techniques could be applied. More specifically, the range profile at each antenna

location is first reconstructed through l_1 norm minimization using the reduced frequency set. Then, the Fourier transform of each reconstructed range profile is taken to recover the full frequency data measurements at each antenna location. Direct application of the wall mitigation techniques can then proceed, followed by the scene reconstruction. Mathematically, the problem can be formulated as follows. Assuming the range of interest is divided into M equally spaced gates (range resolution cells), the relationship between the nth received signal and the target locations can be expressed as,

$$\mathbf{y}_n = \mathbf{A}\mathbf{s}_n \tag{5.28}$$

where $\mathbf{s}_n$ is the discrete range profile corresponding to the nth antenna location, $\mathbf{y}_n$ is the measured data corresponding to all M frequencies at the nth antenna, and $\mathbf{A}$ is an $M \times M$ matrix whose lth column is given by,

$$\mathbf{A}_l = \begin{bmatrix} e^{-j\omega_0 \frac{2ld_r}{c}} & \dots & e^{-j\omega_{M-1} \frac{2ld_r}{c}} \end{bmatrix}^T \qquad l = 0, 1, \dots, M-1 \tag{5.29}$$

with $d_r = \frac{c}{2(\omega_{M-1} - \omega_0)}$ being the radar range resolution. Note that the dimension of $\mathbf{s}_n$ is equal to the number of range gates, whereas the dimension of $\mathbf{y}_n$ is equal to the number of frequencies.

Consider $\breve{\mathbf{y}}_n$, which is a vector of length Q ($<< M$) consisting of elements chosen from $\mathbf{y}_n$ as follows,

$$\breve{\mathbf{y}}_n = \boldsymbol{\varphi}^{(n)}\mathbf{y}_n = \boldsymbol{\varphi}^{(n)}\mathbf{A}\mathbf{s}_n \tag{5.30}$$

where the $Q \times M$ matrix $\boldsymbol{\varphi}^{(n)}$ is constructed in the same manner as in (5.12). Given $\breve{\mathbf{y}}_n$, we can recover $\mathbf{s}_n$ by solving the following equation,

$$\hat{\mathbf{s}}_n = \arg\min_{\mathbf{s}_n} \|\mathbf{s}_n\|_{l_1} \quad \text{subject to} \quad \breve{\mathbf{y}}_n \approx \boldsymbol{\varphi}^{(n)}\mathbf{A}\mathbf{s}_n \tag{5.31}$$

Once the range profile $\hat{\mathbf{s}}_n$ has been obtained, we can recover all M frequency measurements at the nth antenna location as $\hat{\mathbf{y}}_n = \mathbf{A}\hat{\mathbf{s}}_n$. Then, the wall mitigation methods can be readily applied. Finally, backprojection can be used to reconstruct the image of the scene [95]. However, since the wall clutter has been suppressed, the l_1 minimization based scene reconstruction can be applied, in lieu of backprojection, to improve the target-to-clutter ratio.

5.4.3 Modified OMP for TWRI applications

Conventional OMP can be modified to take into account the specificities of through-the-wall radar problems. Prior knowledge of the wall standoff distance in the reconstruction algorithm can allow the OMP to reconstruct the target pixels in fewer iterations, and thus speed up the convergence of the algorithm. More specifically, the classic OMP is modified to allow the algorithm to reconstruct all pixels in the image up to and including the wall, in a single iteration. The proposed modified OMP is described in detail in **Algorithm 1**, where the variables $\boldsymbol{\Gamma}$, $\bar{Q}$ and D are equivalent to $\boldsymbol{\Phi}\boldsymbol{\Psi}$, Q_1Q_2 and N_xN_z, defined in section 5.3, respectively. Let the set of columns of the matrix $\boldsymbol{\Gamma}$ corresponding to the pixels up to the wall maximum downrage distance be denoted by $\boldsymbol{\chi}_{\text{wall}}$ and the corresponding set of column indices be $\boldsymbol{\lambda}_{\text{wall}}$. The first iteration in **Algorithm 1** reconstructs all of the pixels corresponding to $\boldsymbol{\chi}_{\text{wall}}$. In each subsequent iteration, the algorithm proceeds as for classic OMP. In so doing, the modified OMP algorithm is forced to explore behind the wall scene in the subsequent iterations, thereby significantly reducing the number of iterations required to

detect behind the wall targets.

It is noted that when solving (5.31) using the modified OMP, the variables $\mathbf{\Gamma}$, $\check{\mathbf{y}}$, $\bar{Q}$ and D are equivalent to $\boldsymbol{\varphi}^{(n)}\mathbf{A}$, $\check{\mathbf{y}}_n$, Q and M, respectively.

A detailed description of the proposed modification of the OMP is given on next page.

Algorithm 1 Modified OMP for l_1 minimization in TWRI

Input

(·) A $\bar{Q} \times D$ ($\bar{Q} << D$) matrix $\mathbf{\Gamma}$ which columns are expressed as $\boldsymbol{\gamma}_j$

(·) The measurement data vector $\breve{\mathbf{y}}$ of dimension $\bar{Q}$

(·) The sparsity level P of the vector being reconstructed

(·) The wall maximum downrange distance

Procedure

(1) Initialize the index set $\mathbf{\Lambda}_0 = \{\boldsymbol{\lambda}_{\text{wall}}\}$, the matrix of chosen atoms $\boldsymbol{X}_0 = \{\boldsymbol{\chi}_{\text{wall}}\}$, the vector being reconstructed $\hat{\mathbf{r}} = \mathbf{0}$ and the iteration counter $t = 0$.

if $t \neq 0$ **then**

(2) Find the index $\boldsymbol{\lambda}_t$ that solves the following optimization problem,

$$\boldsymbol{\lambda}_t = \arg \max_{j=1,\ldots,\bar{Q}} \left| \left\langle \mathbf{g}_{t-1}, \boldsymbol{\gamma}_j \right\rangle \right|$$

(3) Augment the index set and the matrix of chosen atoms,

$$\mathbf{\Lambda}_t = \mathbf{\Lambda}_{t-1} \cup \{\boldsymbol{\lambda}_t\} \qquad \boldsymbol{X}_t = \begin{bmatrix} \boldsymbol{X}_{t-1} & \boldsymbol{\gamma}_{\boldsymbol{\lambda}_t} \end{bmatrix}$$

end if

(4) Solve the least square problem to obtain a new signal estimate,

$$\mathbf{z}_t = \arg \min_{\mathbf{z}} \|\breve{\mathbf{y}} - \boldsymbol{X}_t \mathbf{z}\|_2^2$$

(5) Calculate the new residual,

$$\mathbf{g}_t = \breve{\mathbf{y}} - \boldsymbol{X}_t \mathbf{z}_t$$

(7) Increment t, and return to Step 2 if $t < (P - 1)$.

(8) The final estimate $\hat{\mathbf{r}}$ is given by,

$$\hat{\mathbf{r}}(\mathbf{\Lambda}_t) = \mathbf{z}_t$$

5.4.4 Experimental results

Experimental setup

A through-the-wall wideband synthetic aperture radar system was set up in the Radar Imaging Lab at Villanova University. A 67-element line array with an inter-element spacing of 0.0187m, located along the x-axis, was synthesized parallel to a 0.14m thick solid concrete wall of length 3.05m and at a standoff distance equal to 1.24m. A stepped-frequency signal covering the 1-3 GHz frequency band with a step size of 2.75MHz was employed, providing a range resolution d_r of 0.075m. Thus, at each scan position, the radar collects 728 frequency measurements. A vertical metal dihedral was used as the target and was placed at (0,4.4)m on the other side of the front wall. The size of each face of the dihedral is 0.39m by 0.28m. The empty scene without the dihedral target present was also measured for comparison. The region to be imaged is chosen to be 4.9m $\times$ 5.4m centered at (0,2.7)m and divided into 33 $\times$ 73 pixels, respectively. The back and the side walls of the room were covered with RF absorbing material to reduce clutter. However, the effectiveness of the proposed techniques for the case where the back wall is not covered with absorbing material is given at the end of this section.

Effect of the wall clutter

Fig. 5.10(a) shows the image corresponding to the measured scene obtained with backprojection applied directly to the full raw dataset. In this figure and all subsequent figures in this section, we plot the image intensity with the maximum intensity value in each image normalized to 0dB. The target area is centered at the true target position and is indicated with a solid red rectangle. With the availability of the empty scene measurements, background subtraction generates an image where the target can be easily identified, as shown in Fig. 5.10(b). Fig. 5.11(a) shows the result obtained with l_1 norm reconstruction using the full raw dataset, while the l_1 norm reconstruction result after background subtraction is provided in Fig. 5.11(b). The classic OMP was used in both cases. The number of iterations of the OMP is usually associated with the level of sparsity of the scene. For this particular example, the number of OMP iterations was set to 100 for Fig. 5.11(a) and 5 for Fig. 5.11(b). Since access to the background scene is not available in practice, it is evident from Fig. 5.11(a) that the wall mitigation techniques must be applied, as a preprocessing step, prior to CS in order to detect the targets behind the wall. As a performance measure, we use the Target-to-Clutter Ratio (TCR) [79], which is commonly adopted in SAR image evaluations [131]. The TCR is defined as the ratio between the maximum pixel magnitude value of the target to the average pixel magnitude value in the clutter region,

$$TCR = 20\log_{10}\left(\frac{\max_{(k,l)\in A_t}|r(k,l)|}{\frac{1}{N_c}\sum_{(k,l)\in A_c}|r(k,l)|}\right) \tag{5.32}$$

where A_t is the target area, A_c is the clutter area and N_c is the number of pixels in the clutter area. The target area is manually selected in close vicinity to the target (9 pixels in all). We consider two types of clutter areas. Type I clutter area is made up of all pixels, excluding the target area and including the wall area, whereas Type II clutter area is the same as Type I, but without considering the wall as a clutter. Figs. 5.10 and 5.11 depict the target and wall clutter areas, indicated by solid and dashed rectangles, respectively. Table 5.3 shows the TCR values for the background subtracted images. As expected, the TCR is improved when using l_1 reconstruction over backprojection.

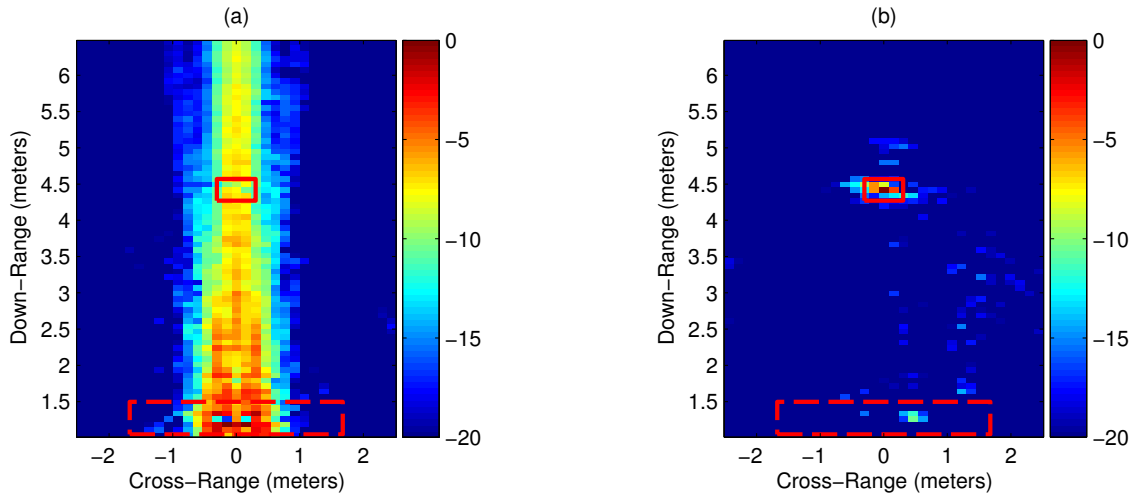

FIGURE 5.10: Backprojection images of the scene: (a) no preprocessing, (b) after background subtraction.

TABLE 5.3: TCR: Background Subtraction - Full data

Method / Clutter	Backprojection	CS with OMP
Type I	27.84	69.75
Type II	27.83	79.76

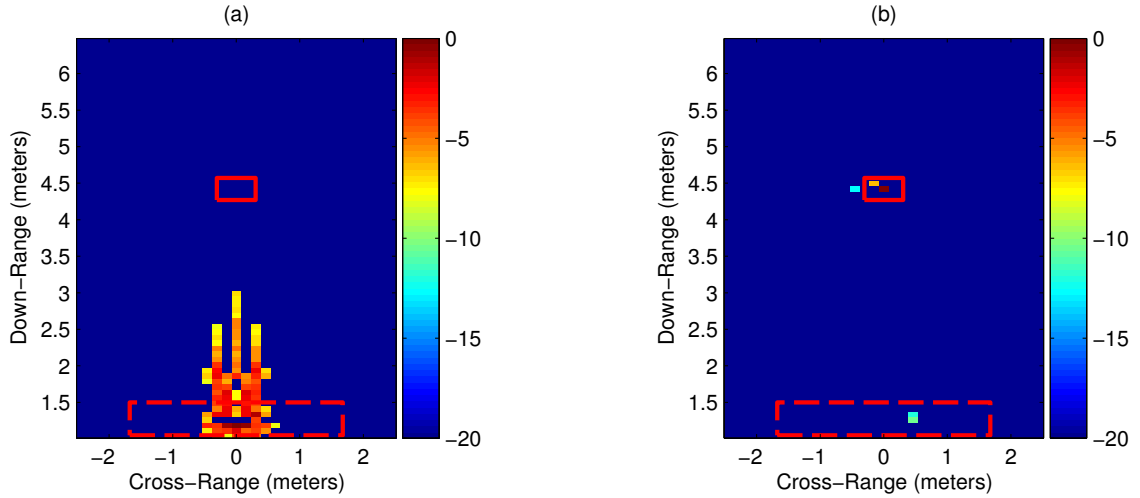

FIGURE 5.11: l_1-norm reconstruction obtained considering full data set. (a) No preprocessing, classic OMP. (b) After background subtraction, classic OMP.

Wall clutter mitigation

Case (a): Full sets of frequencies and antenna locations If the full data set of 728 frequencies and 67 antenna locations are available, the preprocessing based on the spatial filtering method defined in (5.18) and the subspace projection method defined in (5.27) results in the backprojection images shown in Fig. 5.12(a) and Fig. 5.12(b), respectively. In general, the dimension of the wall subspace depends on the wall-type and building material. However, [130] showed that, for a frequency-independent homogeneous wall, the wall subspace is one-dimensional. Thus, in all subspace projection-based method results presented in this section, the first dominant singular vector (K=1) of the data matrix $\mathbf{Y}$ is used to construct the wall subspace. Although the wall return has not been completely suppressed in both Fig. 5.12(a) and Fig. 5.12(b), its shadowing effect has been sufficiently reduced, allowing the detection of the target. Fig. 5.13(a) and Fig. 5.13(b) show the l_1 reconstructed images obtained with the classic OMP for the spatial filtering and the subspace projection-based methods, respectively. Finally, Fig. 5.13(c) and Fig. 5.13(d) depict the l_1 reconstructed images obtained using the modified OMP instead of the classic OMP. The classic OMP required 25 iterations to include the target in the reconstructions in Fig. 5.13(a) and Fig. 5.13(b), whereas the scene reconstructions using the modified OMP in Fig. 5.13(c) and Fig. 5.13(d) required only 5 iterations. Therefore, exploitation of the prior knowledge about the standoff distance from the wall resulted in an 80% reduction in the number of iterations required by the OMP.

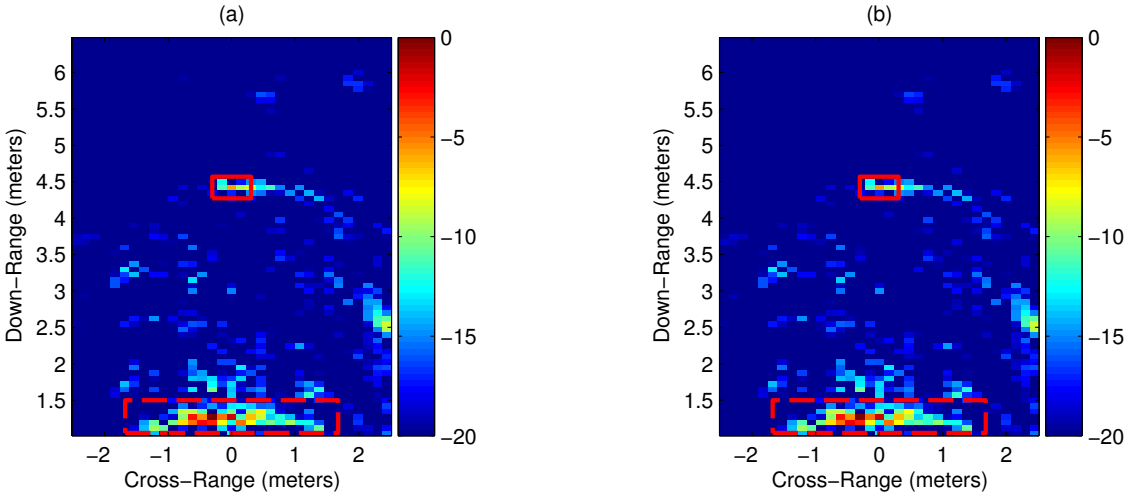

FIGURE 5.12: Case (a) backprojection images: (a) Spatial filtering, (b) Subspace projection.

The TCRs of the aforementioned figures are provided in Table 5.4. We observe from Table 5.4 that both classic and modified OMP based CS reconstructions provide an improvement over the corresponding backprojection results. However, in case of modified OMP, the reduction in the number of iterations is achieved at the expense of the TCR for Type I clutter, which is reduced due to an increase in the wall clutter residuals compared to classic OMP reconstruction. Further, comparing the TCR values in Tables 5.3 and 5.4, we observe that, as expected, background subtraction provides higher TCR compared with the wall mitigation results.

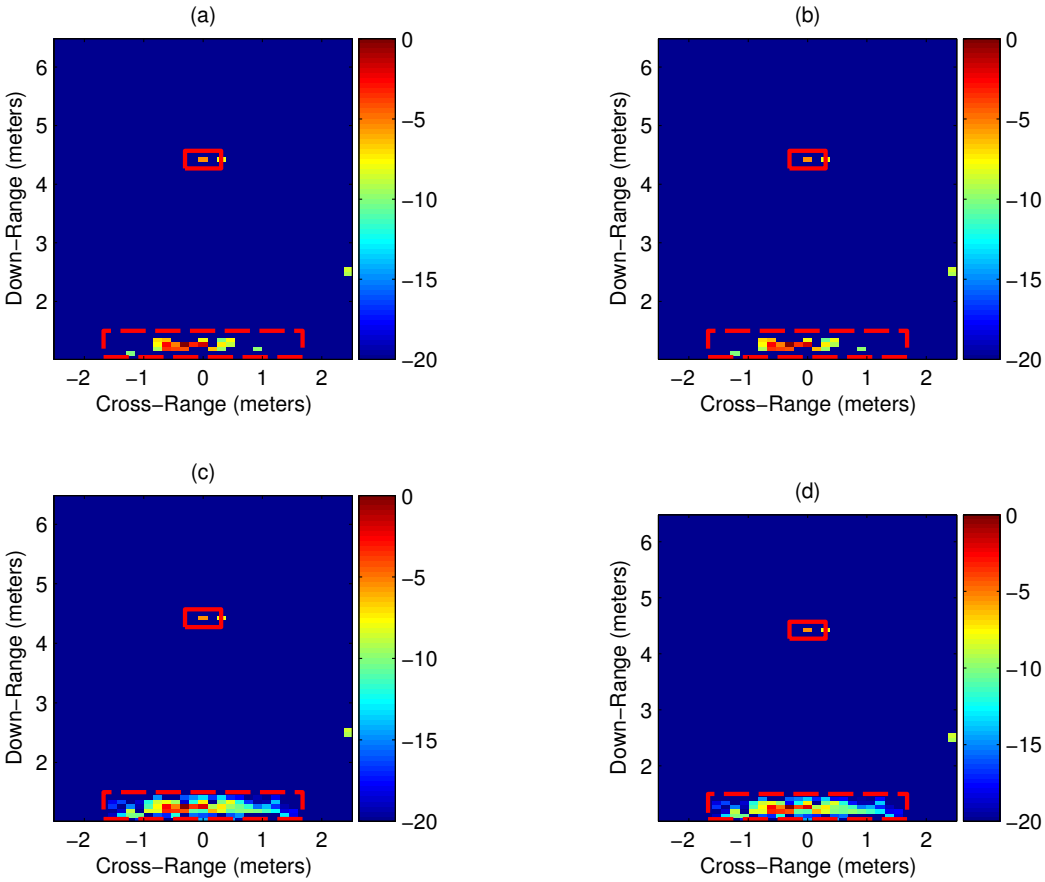

FIGURE 5.13: Case (a) l_1 reconstruction-based imaging results: (a) Spatial filtering - classic OMP, (b) Subspace projection - classic OMP, (c) Spatial filtering - modified OMP, (d) Subspace projection - modified OMP.

TABLE 5.4: TCR: case (a)

Wall mitigation	**Clutter**	**Backprojection**	**CS with OMP**	**CS with modified OMP**
Spatial Filtering	Type I	17.64	40.76	33.52
	Type II	18.60	60.81	60.82
Subspace projection	Type I	17.67	40.80	33.58
	Type II	18.63	60.80	60.82

Case (b): Same reduced frequency set for all antenna locations Instead of using full frequency data, we first use 146 uniformly selected frequencies at each of the 67 antenna locations, which represent 20% of the total data volume. The corresponding space-frequency sampling pattern is illustrated in Fig. 5.4(a). Applying the spatial filtering and the subspace projection methods to the reduced data set provides the backprojection images shown in Fig. 5.14(a) and Fig. 5.14(b), respectively, which are degraded compared to their CS counterparts, depicted in Fig. 5.15. Both classic OMP and modified OMP were used to recover the scene image using only 20% of the frequency measurements. The l_1 minimization based reconstructed images using classic OMP are plotted in Fig. 5.15(a) and Fig. 5.15(b) for the spatial filtering and the subspace projection methods, respectively, where the number of iterations was set to 25. The corresponding results using the modified OMP with the number of iterations set to 5 are depicted in Fig. 5.15(c) and Fig. 5.15(d). It is evident that the two wall mitigation techniques maintain their proper performance when the same subset of uniformly selected frequencies is considered at each antenna location. This statement is confirmed by the comparison of the TCR values for case (b), provided in Table 5.5, and the TCR values for case (a) in Table 5.4. Alternatively, the reduced set of frequencies can be

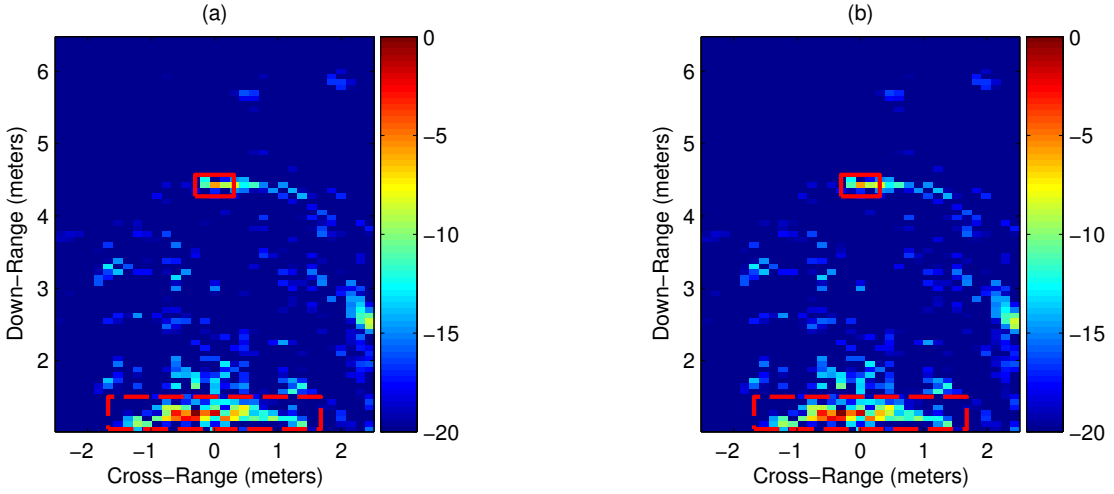

FIGURE 5.14: Case (b) backprojection images with uniformly selected frequencies: (a) Spatial filtering, (b) Subspace projection.

chosen randomly instead of a uniform selection, as illustrated in Fig. 5.4(b). Backprojection and CS methods are applied to the reduced data comprising 20% randomly selected spatial-frequency measurements, maintaining the same set of reduced frequencies at each antenna location. In this case, and for all subsequent random selection-based imaging, each imaged pixel is the result of averaging 100 runs, with a different random selection for each run. The results for the random selection are summarized in Table 5.5. The TCR values provided in Table 5.5 suggest that, compared to uniform selection, the random frequency selection reduces the quality of the backprojection images while preserving the CS reconstructed image quality. Similar to the uniform selection, the performance of the modified OMP is comparable to that of the classic OMP for Type II clutter, while it degrades for Type I clutter.

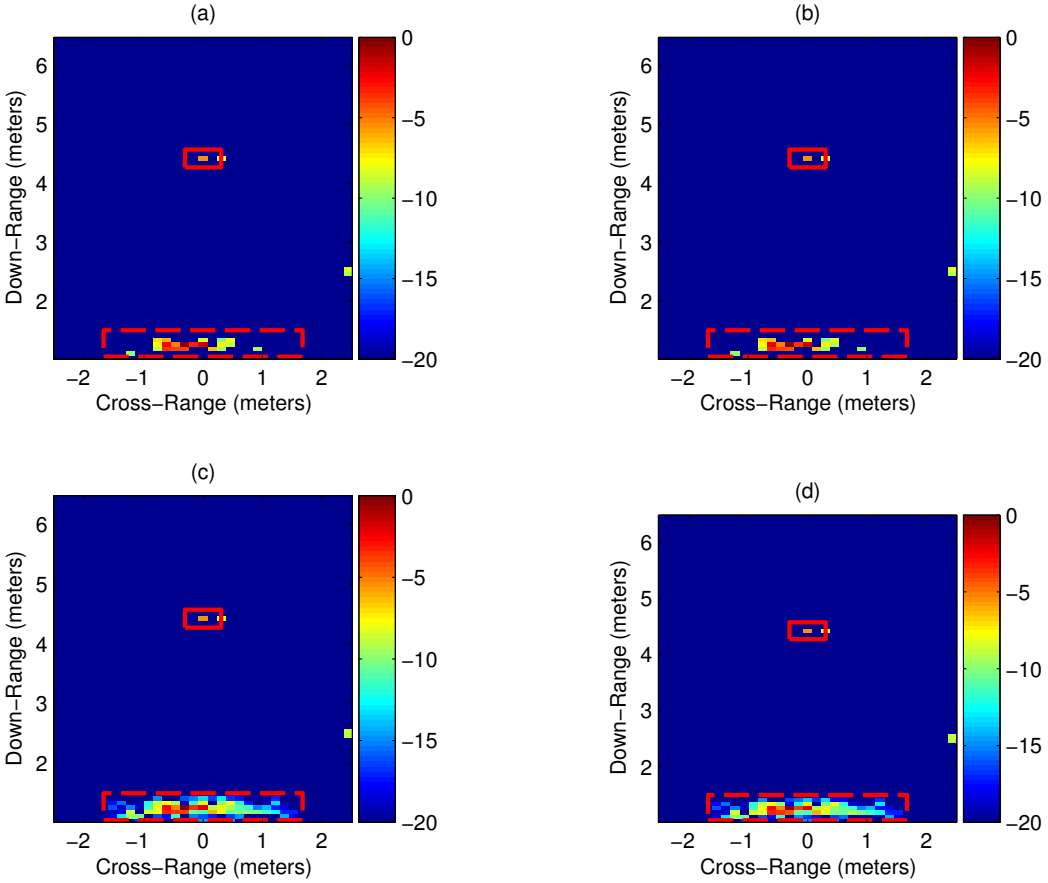

FIGURE 5.15: Case (b) l_1 reconstruction-based imaging results: (a) Spatial filtering - classic OMP, (b) Subspace projection - classic OMP, (c) Spatial filtering - modified OMP, (d) Subspace projection - modified OMP.

TABLE 5.5: TCR: case (b)

Frequency Selection	Wall mitigation	Clutter	Backprojection	CS with OMP	CS with modified OMP
Uniform	Spatial Filtering	Type I	17.54	40.71	33.45
		Type II	18.50	60.67	60.71
	Subspace projection	Type I	17.56	40.73	33.49
		Type II	18.51	60.66	60.71
Random	Spatial Filtering	Type I	13.99	41.32	32.73
		Type II	14.46	59.49	60.22
	Subspace projection	Type I	14.08	41.34	32.78
		Type II	14.55	59.50	60.14

Case (c): Same set of reduced frequencies for a reduced set of antenna locations The space-frequency sampling pattern for case (c) is illustrated in Fig. 5.5(a) for uniform sampling and in Fig. 5.5(b) for random sampling. We first consider 146 uniformly selected frequencies (20% of 728) and 34 uniformly selected array locations (51% of 67), which collectively represent 10.2% of the total data volume. As in case (b), spatial filtering is implemented by subtraction of the average value of (5.18) across the thinned array for each of the reduced number of frequencies. The subspace projection based method is applied, in this case, to a reduced dimension $\mathbf{Y}$ matrix, 146×34 instead of 146×67 for case (b) and 728×67 for case (a). The backprojection images corresponding to spatial filtering and subspace projection methods are shown in Fig. 5.16(a) and Fig. 5.16(b), respectively. The l_1 norm reconstructed images obtained with classic OMP are depicted in Fig. 5.17(a) and Fig. 5.17(b) for the spatial filter and subspace projection approaches, respectively, which have less wall clutter residuals compared to the corresponding modified OMP images, shown in Fig. 5.17(c) and Fig. 5.17(d). It is clear that, even when both spatial and frequency observations are reduced, the CS results for both classic and modifed OMP provide better and *cleaner* images than those using backprojection.

The advantage of CS over backprojection is evident in Table 5.6, where the TCR for the

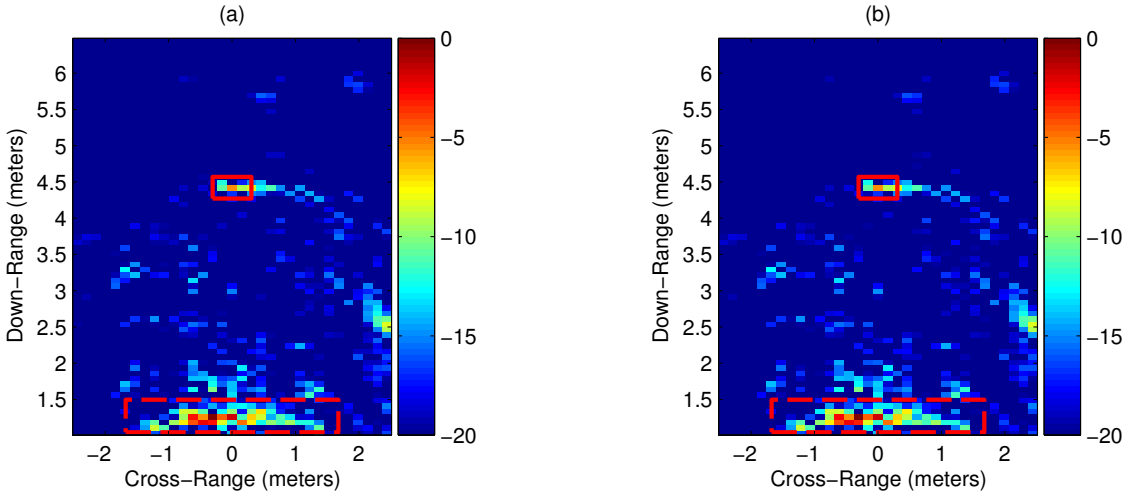

FIGURE 5.16: Case (c) backprojection images: (a) Spatial filtering, (b) Subspace projection.

uniform sampling are illustrated. As expected, the performance of the modified OMP is comparable to that of the classic OMP for Type II clutter, while it degrades for Type I clutter. The important point to note here is that the direct application of wall mitigation methods is robust to the reduction of the spatial domain samples. The random spatial-frequency measurements of Fig. 5.5(b) can alternatively be used for CS based imaging. The corresponding TCR values are listed in Table 5.6, which indicate that, similar to the uniform selection, the performance of the modified OMP is comparable to that of the classic OMP for Type II clutter, while it degrades for Type I clutter under random selection.

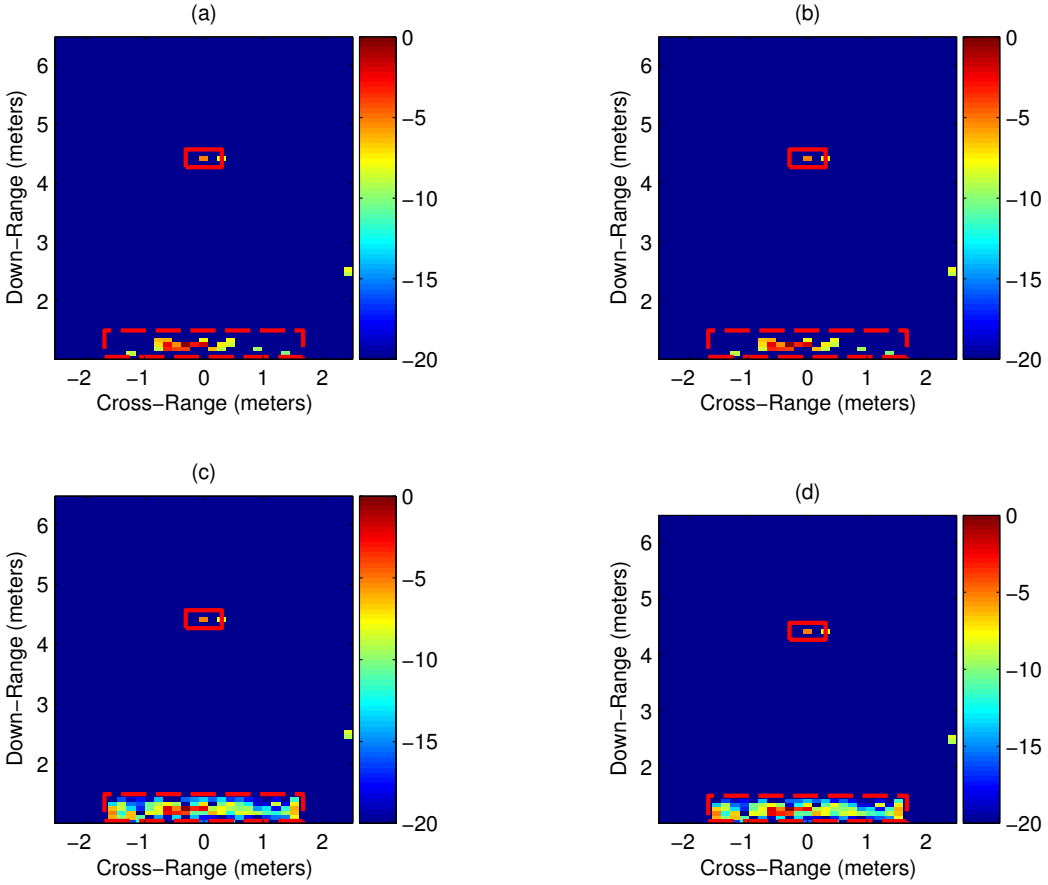

FIGURE 5.17: Case (c) l_1 reconstruction-based imaging results: (a) Spatial filtering - classic OMP, (b) Subspace projection - classic OMP, (c) Spatial filtering - modified OMP, (d) Subspace projection - modified OMP.

TABLE 5.6: TCR: case (c)

Frequency Selection	Wall mitigation	Clutter	Backprojection	CS with OMP	CS with modified OMP
Uniform	Spatial Filtering	Type I	17.67	40.80	31.82
		Type II	18.62	60.71	60.84
	Subspace projection	Type I	17.69	40.80	31.85
		Type II	18.64	60.71	60.84
Random	Spatial Filtering	Type I	12.33	39.50	29.44
		Type II	12.77	57.70	58.15
	Subspace projection	Type I	12.52	39.89	30.12
		Type II	13.01	58.60	58.86

Case (d): Different sets of reduced frequencies for all antenna locations As discussed at the beginning of this section, having the same frequency observations may not always be possible. Use of different sets of reduced frequencies at different antenna locations would lead to different wall reflection phase returns across the antennas, rendering the wall mitigation methods ineffective. The strategy proposed in Section (5.4.2) combats this shortcoming by recovering all the frequency measurements at each antenna location through l_1 norm range profile reconstruction. Both classic OMP and modified OMP were used to recover the range profiles using only 20% of the frequency measurements. The space-frequency sampling pattern for case (d) is illustrated in Fig. 5.6.

Fig. 5.18(a) and Fig. 5.18(c) show the backprojection images obtained after applying spatial filtering to the full data recovered from the reconstructed range profiles using classic OMP and modified OMP, respectively. Fig. 5.18(b) and Fig. 5.18(d) show the corresponding results when the subspace projection method was used for wall clutter mitigation. We observe that the target has not been localized in these images, which is in contrast to case (b), wherein target localization was successfully achieved with 20% data volume. This is because, in case (d), the various range profiles are reconstructed prior to the application of wall clutter mitigation techniques. As the sparsity in range is lower in the presence of wall clutter, the number of observed frequencies required for sparse reconstruction of the range profiles is expected to be higher compared with case (b). Next, the number of frequencies used for range profile reconstruction was increased to 40%. The corresponding backprojection images for classic OMP and modified OMP based range profile reconstructions are provided in Fig. 5.19(a) and Fig. 5.19(c), respectively, for the spatial filtering approach, and in Fig. 5.19(b) and Fig. 5.19(d), respectively, for the subspace projection. The classic OMP required 100 iterations for each range profile reconstruction. On the other hand, the modified OMP needed only 70 iterations as all range gates from 0m to 1.4m were reconstructed in the first iteration, thereby providing a 30% reduction in the number of iterations compared to classic OMP. The backprojection images for both classic and modied OMP based results appear very similar. This observation is confirmed by the corresponding TCRs provided in Table 5.7. Comparing the TCR values in Table 5.7 with the backprojection TCR values in Table 5.5 under random frequency selections for case (b), we note that the cost for not using the same set of reduced frequency measurements across all antennas manifests itself in terms of a reduced TCR. This loss in quality is due to the fact that the individual range profile reconstructions are not perfect. As a result, there are discrepancies in the recovered full-frequency data compared to the measured full-frequency data, as demonstrated in Fig. 5.20 and Fig. 5.21 for the first and the middle antenna positions, respectively. Finally, the l_1

TABLE 5.7: TCR: case (d) - Backprojection using l_1 reconstructed range profiles

Wall mitigation	**Clutter**	**classic OMP**	**modified OMP**
Spatial Filtering	Type I	7.12	7.06
	Type II	7.87	7.88
Subspace projection	Type I	7.19	7.13
	Type II	7.94	7.95

norm image reconstruction was performed, in lieu of backprojection, on the full frequency data recovered from the modified OMP based reconstructed range profiles. Fig. 5.22(a) and Fig. 5.22(b) show the images reconstructed using classic OMP corresponding to spatial filtering and subspace projection methods, respectively. Fig. 5.22(c) and Fig. 5.22(d) show

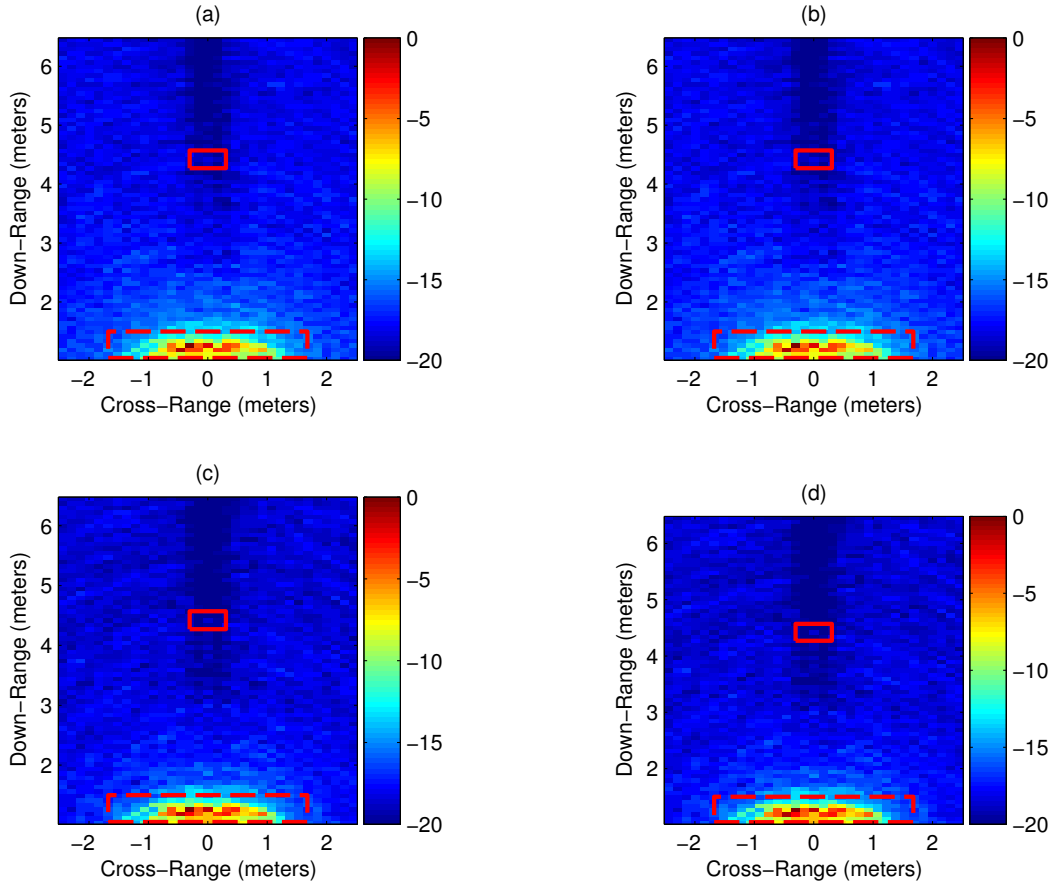

FIGURE 5.18: Case (d) backprojection images with 20% frequency measurements: (a) Spatial filtering - range profiles with classic OMP, (b) Subspace projection - range profiles with classic OMP, (c) Spatial filtering - range profiles with modified OMP, (b) Subspace projection - range profiles with modified OMP.

the l_1 reconstruction through modified OMP for spatial filtering and subspace reconstruction based preprocessing, respectively. In this case, the classic OMP required 100 iterations to ensure the inclusion of the target into the reconstructed image, while the modified OMP needed 70 iterations to achieve the same objective. We observe from Fig. 5.22 that both classic OMP and modified OMP are able to localize the target.

The image quality of the l_1 reconstructions are compared in Table 5.8 by means of the TCR, which approximately assumes the same values for classic and modified OMP. To re-iterate, the penalty for not using the same set of reduced frequency measurements across the antennas is two-fold. First, the reduction in data volume is lower compared to that of case (b) in which the same set of reduced frequencies is employed at each antenna location. Second, despite the use of a larger amount of data in case (d), the corresponding TCR is lower than that for case (b).

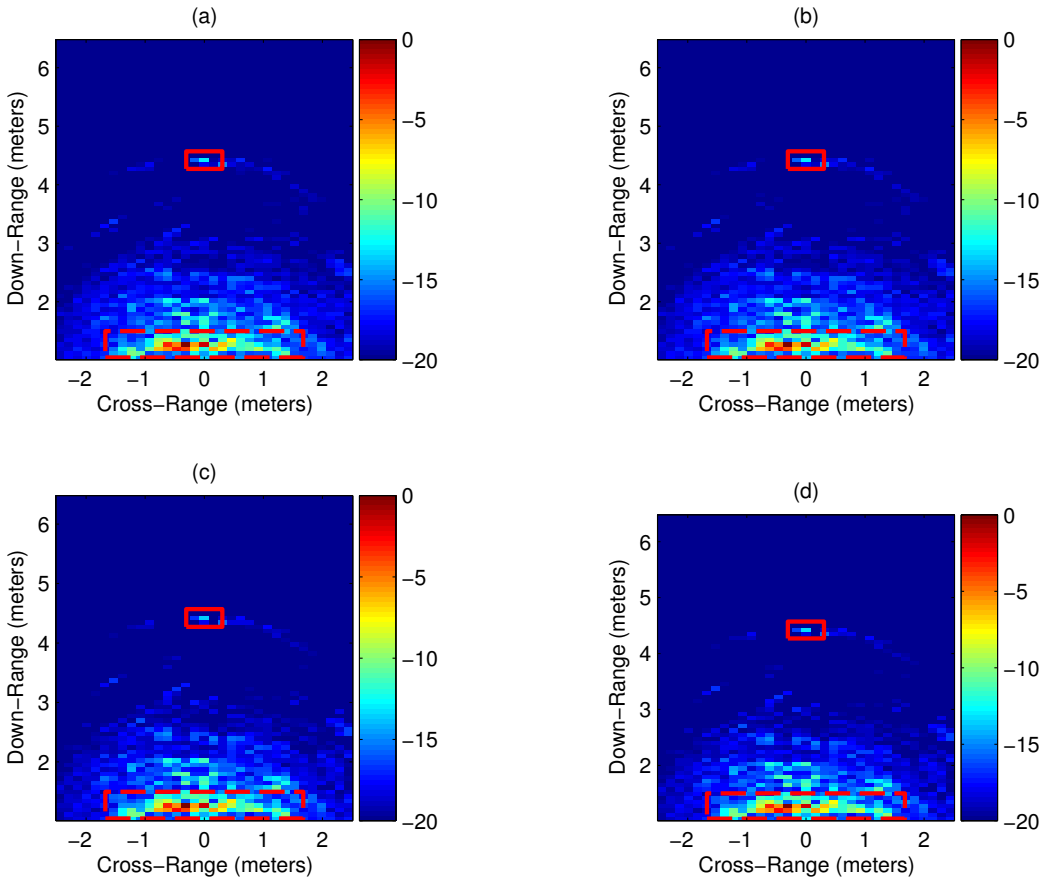

FIGURE 5.19: Case (d) backprojection images with 40% frequency measurements: (a) Spatial filtering - range profiles with classic OMP, (b) Subspace projection - range profiles with classic OMP, (c) Spatial filtering - range profiles with modified OMP, (b) Subspace projection - range profiles with modified OMP.

TABLE 5.8: TCR: case (d) - l_1 reconstructed images using the range profile obtained with modified OMP

Wall mitigation	**Clutter**	**classic OMP**	**modified OMP**
Spatial Filtering	Type I	15.51	12.00
	Type II	22.29	20.73
Subspace projection	Type I	15.80	12.84
	Type II	22.55	21.55

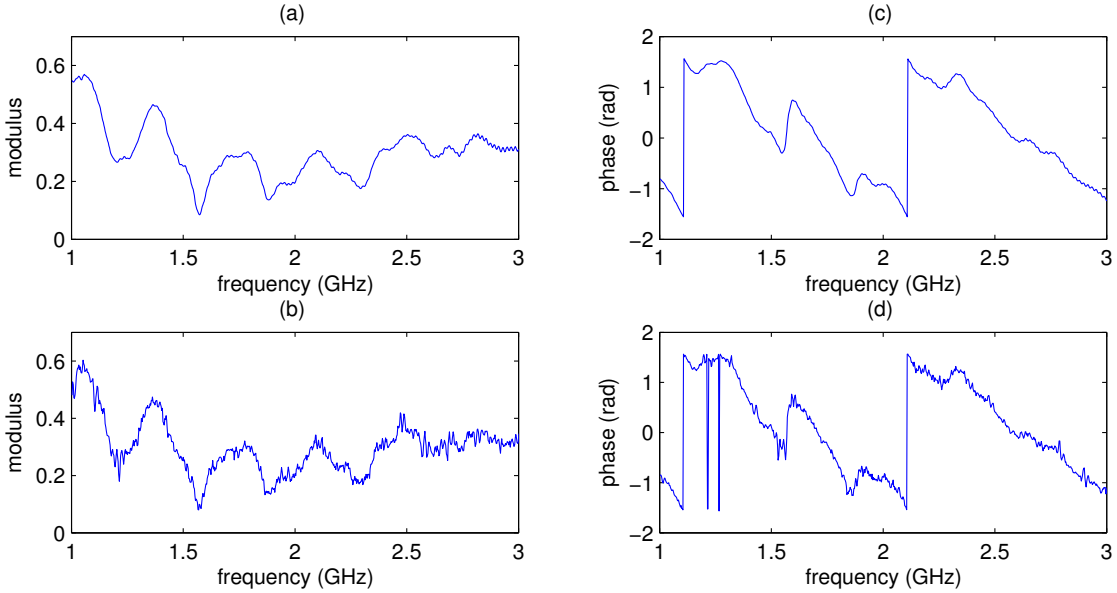

FIGURE 5.20: Comparison between the original data vector $\mathbf{y}_1$ and the recovered data vector from the range profile $\hat{\mathbf{y}}_1$: (a) Modulus of $\mathbf{y}_1$, (b) Modulus of $\hat{\mathbf{y}}_1$, (c) Phase of $\mathbf{y}_1$, (d) Phase of $\hat{\mathbf{y}}_1$.

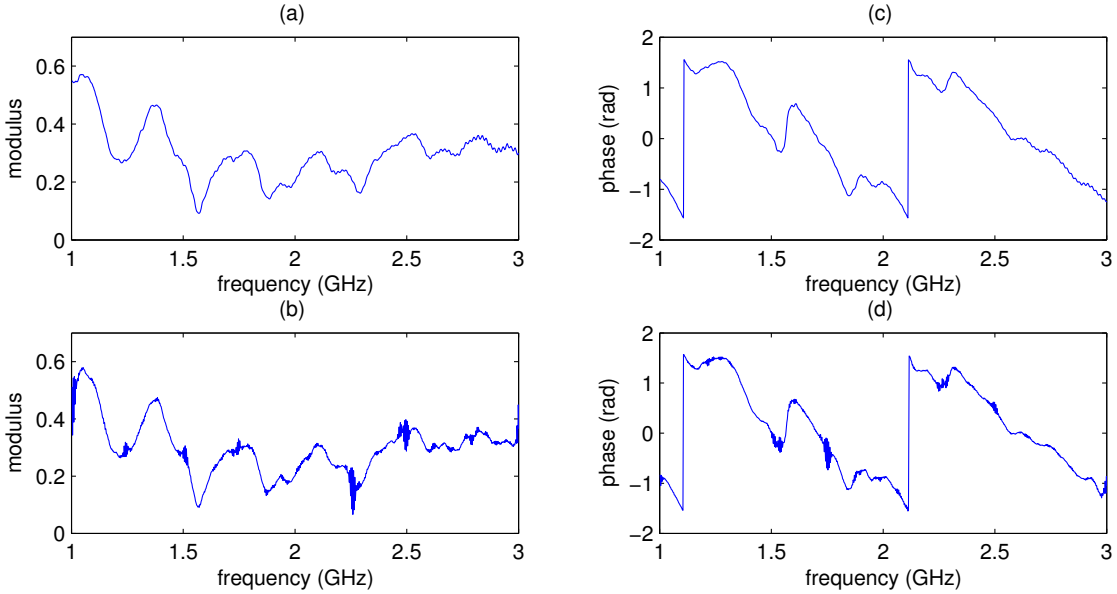

FIGURE 5.21: Comparison between the original data vector $\mathbf{y}_{34}$ and the recovered data vector from the range profile $\hat{\mathbf{y}}_{34}$: (a) Modulus of $\mathbf{y}_{34}$, (b) Modulus of $\hat{\mathbf{y}}_{34}$, (c) Phase of $\mathbf{y}_{34}$, (d) Phase of $\hat{\mathbf{y}}_{34}$.

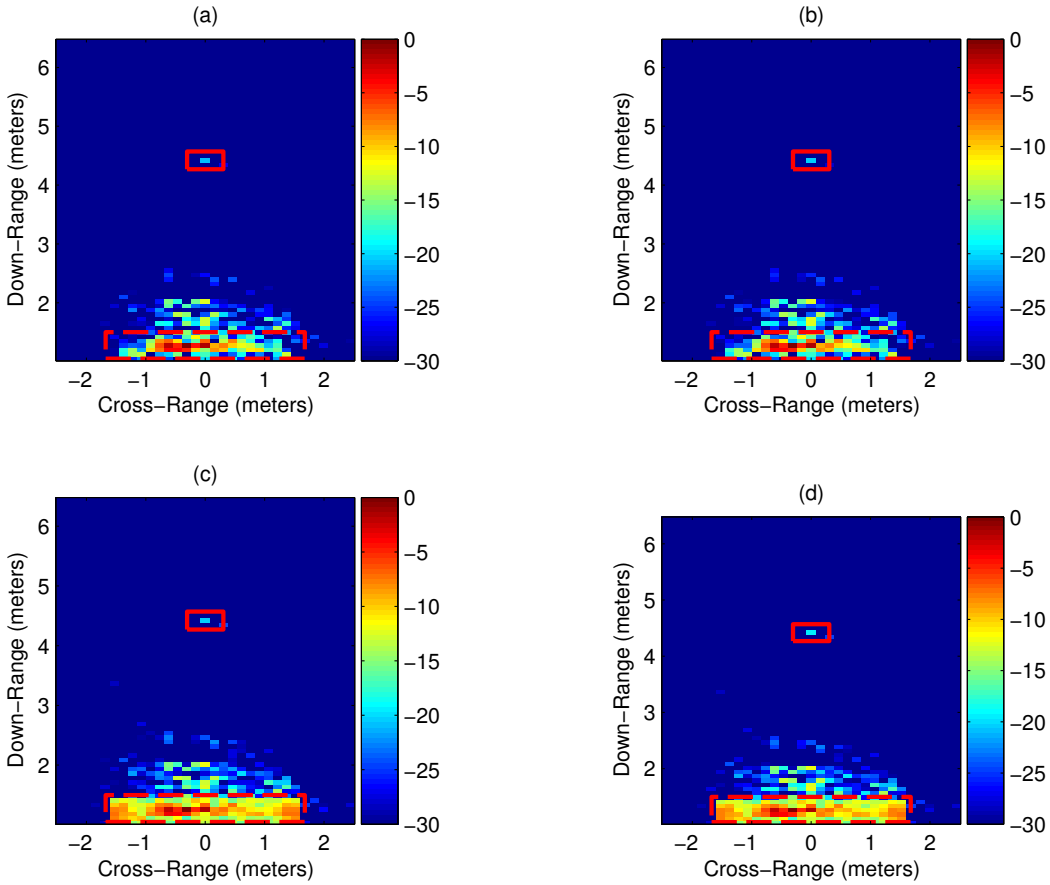

FIGURE 5.22: Case (d) l_1 reconstruction-based imaging results obtained using the range profiles with modified OMP: (a) Spatial filtering - classic OMP, (b) Subspace projection - classic OMP, (c) Spatial filtering - modified OMP, (d) Subspace projection - modified OMP.

Case (e): Different sets of reduced frequencies for a reduced set of antenna locations This is the most general case, where both spatial and frequency measurements are reduced and the employed frequency sets differ from one antenna location to the other. The corresponding space-frequency sampling pattern is illustrated in Fig. 5.7. We randomly selected 51% of the antenna locations and randomly chose 40% of the frequencies at each selected antenna location. Therefore, the reduced dataset considered in this case represents 20.3% of the total data volume. Full frequency data measurements were first recovered from both the classic OMP and modified OMP based reconstructed range profiles at each considered antenna location. Wall mitigation methods were then applied, followed by backprojection for image formation. The corresponding backprojection images for classic OMP and modified OMP are provided in Fig. 5.23(a) and Fig. 5.23(c), respectively, for the spatial filtering approach, and in Fig. 5.23(b) and Fig. 5.23(d), respectively, for the subspace projection approach. We observe that, despite the use of fewer antenna locations than case (d), the target has been successfully localized in all images. The TCRs of the backprojection images in Fig. 5.23, summarized in Table 5.9, indicate a slight deterioration in image quality compared to that under case (d).

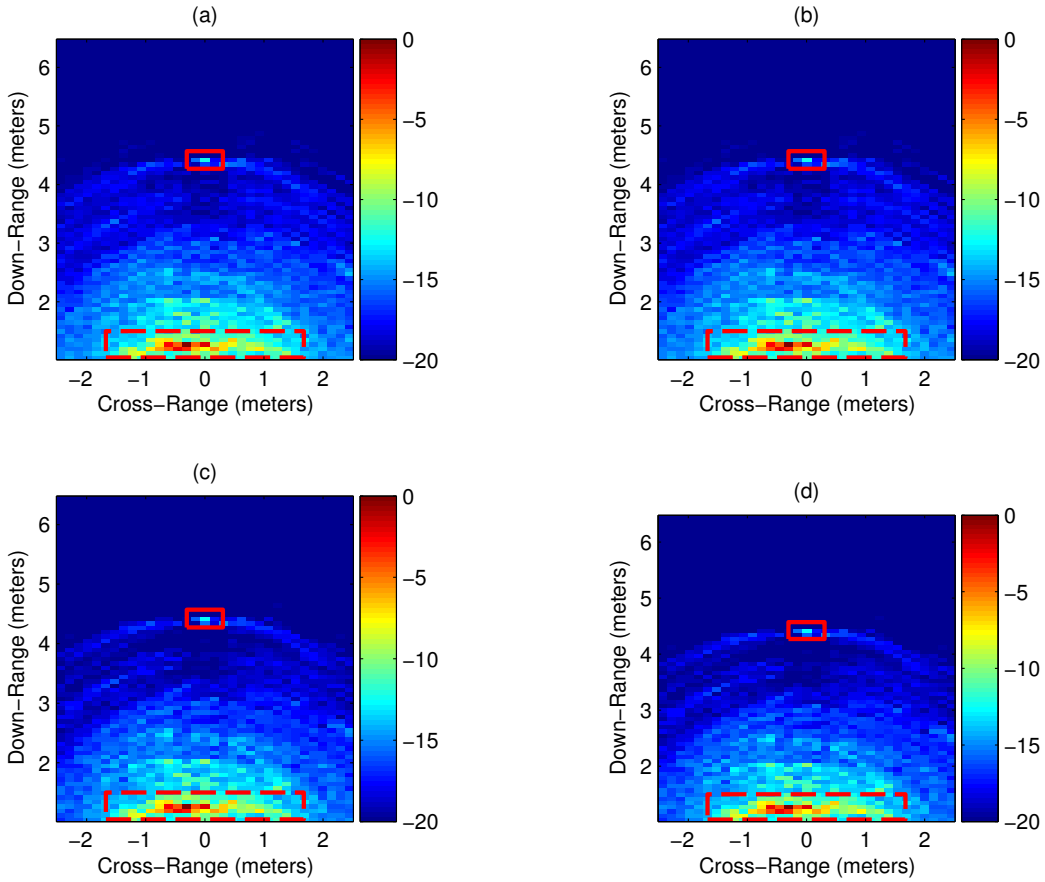

FIGURE 5.23: Case (e) backprojection images with 40% frequency measurements: (a) Spatial filtering - range profiles with classic OMP, (b) Subspace projection - range profiles with classic OMP, (c) Spatial filtering - range profiles with modified OMP, (b) Subspace projection - range profiles with modified OMP.

TABLE 5.9: TCR: case (e) - Backprojection using l_1 reconstructed range profiles

Wall mitigation	**Clutter**	**classic OMP**	**modified OMP**
Spatial Filtering	Type I	5.10	5.47
	Type II	5.77	6.21
Subspace projection	Type I	5.15	5.54
	Type II	5.83	6.28

Next, the l_1 norm reconstruction procedure was employed for image formation using the full frequency data measurements recovered through modified OMP at the selected antennas. Fig. 5.24(a) and Fig. 5.24(b) show the images reconstructed using classic OMP corresponding to spatial filtering and subspace projection methods, respectively, while Fig. 5.24(c) and Fig. 5.24(d) show the l_1 reconstruction through modified OMP for spatial filtering and subspace reconstruction based preprocessing, respectively. Similar to case (d), modified OMP provides a 30% reduction in the number of iterations required for image reconstruction. The target is visible in both classic and modified OMP based reconstructed images, albeit with relatively more residual wall clutter for the modified OMP recovered image. These observations are validated by the corresponding TCR values provided in Table 5.10.

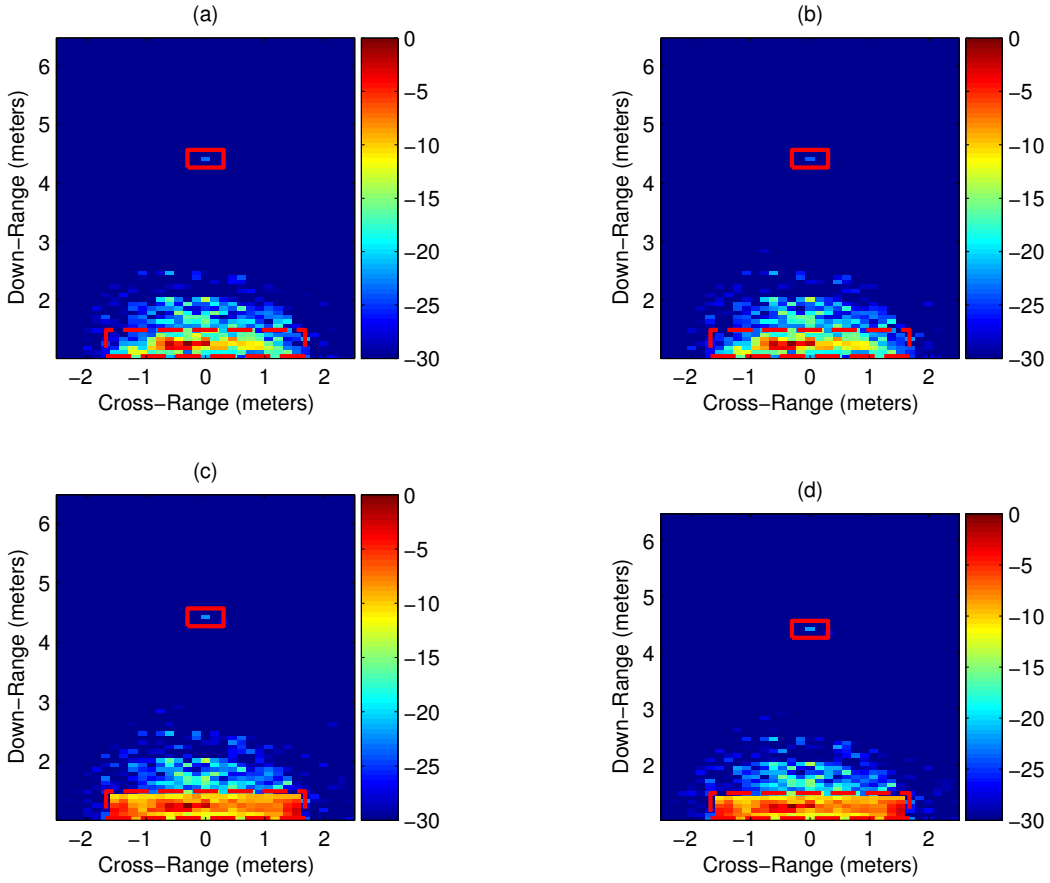

FIGURE 5.24: Case (e) l_1 reconstruction-based imaging results obtained using the range profiles with modified OMP: (a) Spatial filtering - classic OMP, (b) Subspace projection - classic OMP, (c) Spatial filtering - modified OMP, (d) Subspace projection - modified OMP.

TABLE 5.10: TCR: case (e) - l_1 reconstructed images using the range profile obtained with modified OMP

Wall mitigation	Clutter	classic OMP	modified OMP
Spatial Filtering	Type I	10.89	7.73
	Type II	16.68	16.58
Subspace projection	Type I	10.54	7.98
	Type II	16.32	16.81

Summary of the results

A recapitulation of the experimental results is provided in this section. The first part of the experimental results showed that the front wall, which is a highly reflective and attenuative medium, presents the main difficulty in revealing behind-the-wall stationary targets. Background subtraction achieves the best results in removing wall returns. It provides the highest TCR (27.8dB in backprojection image) compared with the spatial filtering and the subspace projection wall mitigation results, which for the non-compressive case, provide TCR of approximately 18dB in backprojection images. Access to the background scene is not typically available in practice. Thus, spatial filtering, subspace projection or any other wall mitigation technique must be applied. The second part of the experimental results dealt with the front wall clutter mitigation in conjunction with CS. The results for both spatial filtering and subspace projection methods demonstrated that target visibility and high TCR can be achieved when the same subset of frequencies is considered at each antenna location. This is due to the fact that the condition of spatial invariance of the wall reflections required by both spatial filtering and subspace projection methods is not violated when the same set of frequencies is employed at each antenna location. Occasionally, the same operating frequencies might not be available at each antenna position. In this case, the proposed preprocessing step permits the subset of frequencies to differ from one antenna location to another. However, this is accomplished at the expense of target visibility and TCR degradation; the latter being approximately 6dB in backprojection images.

Effect of the back wall reflections

In order to demonstrate the robustness of the proposed methods in a less controlled environment, a new through-the-wall experiment was set up in the Radar Imaging Lab at Villanova University. In this experiment, the side walls were covered with the absorbing material but the 0.31m thick reinforced concrete back wall was left uncovered. For imaging, a 93-element linear array with an interelement spacing of 0.02m was used, which was synthesized using a single horn antenna. The scene was illuminated with a stepped frequency signal of 2 GHz bandwidth centered at 2 GHz, using 641 frequencies with a step size of 3.125 MHz. A 0.2m thick solid concrete block wall was placed 3.13m in front of and parallel to the antenna baseline. The distance between the back face of the front wall and the front of the back wall is 3.76m. The same metal dihedral used for the previous experiments was used as a target, and was placed at (0.3,5.2)m. The region to be imaged is chosen to be 4.9m $\times$ 6.4m centered at (0,4.3)m and divided into 33 $\times$ 87 pixels, respectively. The backprojected images using the full data measurements are shown in Fig. 5.25. In Fig. 5.25(a), no preprocessing was applied to remove the front wall reflections, whereas in Fig. 5.25(b), background subtraction was applied. Fig. 5.25 confirms the need to reduce the front wall clutter in order to detect the presence of the target. Next, we applied the same space-frequency sampling pattern for

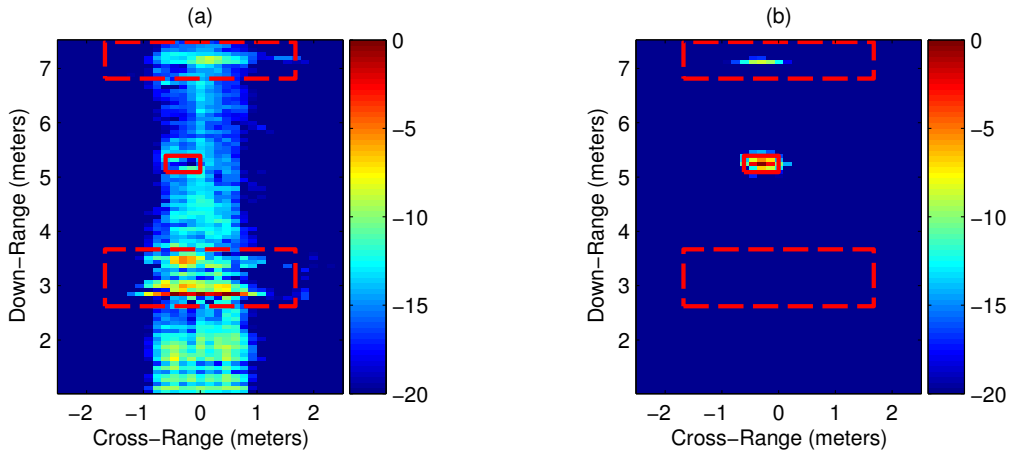

FIGURE 5.25: Backprojection images of the scene without absorbing material in the back wall of the room: (a) no preprocessing, (b) after background subtraction.

case (c), which is illustrated in Fig. 5.5(a). There are 65 uniformly selected frequencies (20% of 641) and 47 uniformly selected array locations (51% of 93). The backprojection images corresponding to spatial filtering and subspace projection methods are shown in Fig. 5.26(a) and Fig. 5.26(b), respectively. They demonstrate that both approaches are effective in reducing the wall reflections without significantly compromising the target image. The l_1 norm reconstructed images obtained with classic OMP are depicted in Fig. 5.27(a) and Fig. 5.27(b) for the spatial filter and subspace projection approaches, respectively, which have less wall clutter residuals compared to the corresponding backprojected images.

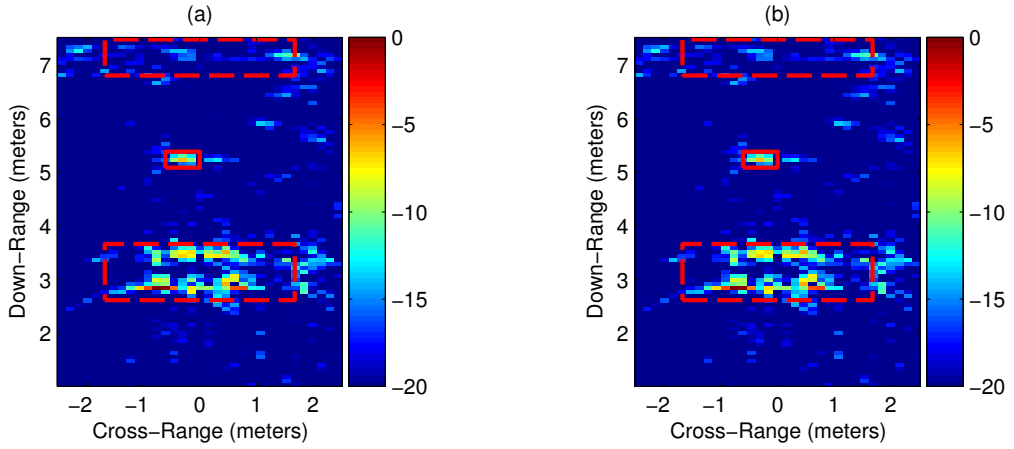

FIGURE 5.26: Case (c) backprojection images of the scene without absorbing material in the back wall of the room: (a) Spatial filtering, (b) Subspace projection.

5.4.5 Conclusion

In this section, we examined the performance of joint mitigation of the wall backscatterings and sparse scene reconstruction in TWRI applications. We focused on two leading methods for combating wall clutter, namely, spatial filtering and subspace projections. Using real data, collected in a laboratory environment with a stepped-frequency radar, we showed that these

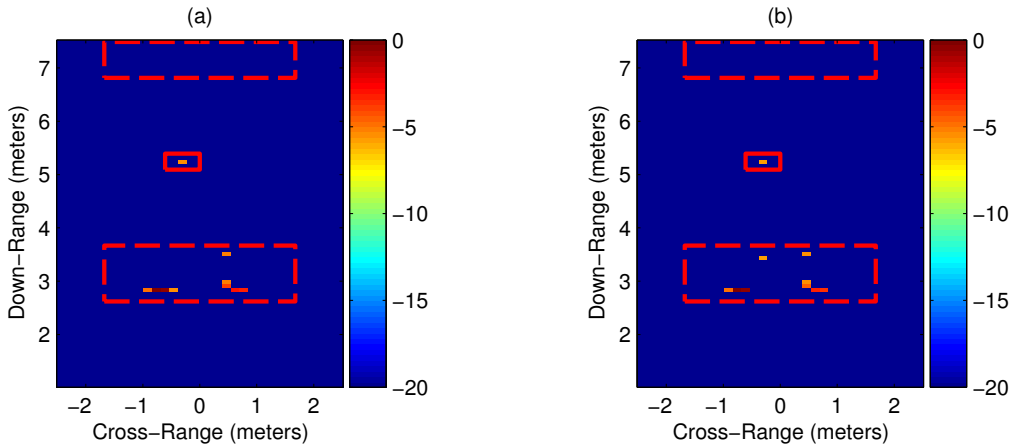

FIGURE 5.27: Case (c) l_1 reconstruction-based imaging results of the scene without absorbing material in the back wall of the room: (a) Spatial filtering - classic OMP, (b) Subspace projection - classic OMP.

two methods maintain proper performance when acting on reduced data measurements. We considered two cases of frequency measurement distributions over antennas. Direct application of wall clutter mitigation methods were effective when the same frequencies were used for each antenna. For the cases where different frequencies were used at different antennas, we reconstructed the sparse range profiles with a CS approach applied at each antenna. The signal responses of all frequencies were then generated using the Fourier transform. In so doing, signal processing techniques, such as spatial filtering and subspace projections, can be applied to capture and remove the wall EM returns. The proposed method is flexible in the sense that it permits the use of a different set of frequencies at each antenna location. Subsequent sparse reconstruction using the much reduced wall-clutter data successfully detected and accurately localized the targets. In applying CS, we used prior knowledge of the standoff distance from the wall to speed up the convergence of the Orthogonal Matching Pursuit for sparse data reconstruction.

5.5 Detection of building interior structures using overcomplete dictionaries

5.5.1 Detection of walls

In this section, we apply the compressive sensing based candidate detector to the problem of imaging building interior structures using a reduced number of measurements, acquired by a ground-based synthetic aperture radar system that is located parallel to the front wall. In particular, we consider interior walls as targets and attempt to reveal the building layout based on CS and sparse image reconstruction techniques. Construction practices suggest the exterior and interior walls to be parallel or perpendicular to each other. This enables sparse representations of the scene using an overcomplete dictionary of candidate wall orientations and locations. Conventional CS recovery algorithms can then be applied to a reduced number of observations to recover the positions of various walls, which is a primary goal in through-the-wall sensing. The proposed approach provides reliable determination of building interior layout while achieving substantial reduction in data volume. Using simulated data as well as

real data collected in a laboratory setting, we demonstrate the effectiveness of the proposed sparsifying dictionary for reconstruction of building structures. In particular, we show that the proposed approach outperforms the conventional point target based through-the-wall CS model, the wavelet sparsifying basis, and the block sparse model for imaging of building structures.

TWRI signal model for interior walls

For a scene consisting of P point targets and I_w interior walls parallel to the array axis, the signal received by the n-th transceiver at the m-th frequency can be expressed as,

$$y(m,n) = \sigma_w e^{-j\omega_m \tau_w} + \sum_{i=0}^{I_w-1} \sigma_{w_i} e^{-j\omega_m \tau_{w_i}} + \sum_{p=0}^{P-1} \sigma_p e^{-j\omega_m \tau_{p,n}}, \tag{5.33}$$

where σ_w, σ_{w_i} and σ_p are the complex reflectivity of the front wall, the i-th interior wall and the p-th target, respectively. It is noted that the wall and target reflectivities are assumed to be independent of frequency and aspect angle. In the above equation, τ_w, τ_{w_i} and $\tau_{p,n}$, respectively, represent the two-way traveling time of the signal from the n-th antenna to the wall, from the n-th antenna to the i-th interior wall and between the n-th antenna and the p-th target. As the wall is a specular reflector and the antennas are located parallel to the front wall, the delays τ_w and τ_{w_i} are independent of the variable n, as evident in the subscripts.

Improved sparse representation of the image

There are alternative ways for representing the image in a sparse basis. The conventional sparse representation presented in Section 5.2 was consistent with the fact that the targets satisfy the point target model. Recently, another CS-based approach has been proposed, which employs the 2D Discrete Wavelet Transform (2D-DWT) as a sparsifying transform for through-the-wall images [98]. The introduction of the 2D-DWT overcomes the point target limitation of the conventional approach and provides the capability to deal with extended targets. Alternatively, extended targets can also be handled by the exploiting the block-sparse structure of the scene, as proposed in [132] for general CS applications. The block-sparse approach, applied to TWRI, amounts to maintaining the conventional point-target based CS model and suitably extending the recovery algorithm by assuming blocks of contiguous target pixels. In this section, we review the wavelet-based and block-sparse approaches and present the proposed sparsifying basis for wall detection application.

2D Discrete wavelet transform In practical TWRI situations, medium sized targets populate more than a single pixel in the image, thus making the point target assumption no longer valid. Hence, a more appropriate basis other than just the columns of an identity matrix is desirable for dealing with extended targets. The wavelet basis is widely used for sparse representation in image compression [133], and is adequate for representing sharp variations of the image intensity. Thus, the conventional CS image formation was combined with the 2D-DWT in [98], yielding a more appropriate approach for extended target detection in CS-based TWRI.

An extensive study of the performance of different 2D-DWTs was carried out in [98], concluding that the Dual-Tree Complex Wavelet Transform (DT-CWT) is the most appropriate candidate for TWRI images. In this case, the sparsifying dictionary is given by $\mathbf{W}$, where

$\mathbf{W} \in \mathbb{C}^{N_x N_z \times W}$ is the matrix spanning the vector space of the DT-CWT basis, with W being the number of wavelet coefficients. The linear system of equations relating the observed data $\mathbf{y}$ and the wavelet coefficients is given by,

$$\mathbf{y} = \mathbf{\Psi r} = \mathbf{\Psi W x} \tag{5.34}$$

where $\mathbf{x}$ is the sparse image representation expressed in the wavelet basis. The optimization of the wavelet basis for the wall detection problem is out of the scope of this paper.

Proposed approach: Sparsifying dictionary for imaging of building structures In this section, we propose a new sparsifying approach for imaging building interior structures in TWRI. The typical geometrical signatures of building interior walls and prior information about common construction practices are exploited to design a sparsifying dictionary well-suited to the wall detection problem. This section is divided into two parts. The first part concentrates on the proper linear representation relating the observed data with the image, whereas the second part introduces the sparsifying basis for interior structure detection applications.

Linear model for interior wall detection Instead of the sensing matrix described in eqn. (5.10) where each antenna accumulates the contributions of all the pixels, we use an alternate sensing matrix, proposed in [134], to relate the scene vector, $\mathbf{r}$, and the observation vector, $\mathbf{y}$. This matrix underlines the specular reflections produced by the walls. Specular reflection is distinct from diffuse reflection produced by point-like targets, where incoming waves are reflected in a broad range of directions. Due to wall specular reflections, and since the array is assumed parallel to the front wall and, thus, parallel to interior walls, the rays collected at the n-th antenna will be produced by portions of the walls that are only in front of this antenna (see Fig. 5.28). The alternate matrix, therefore, only considers the

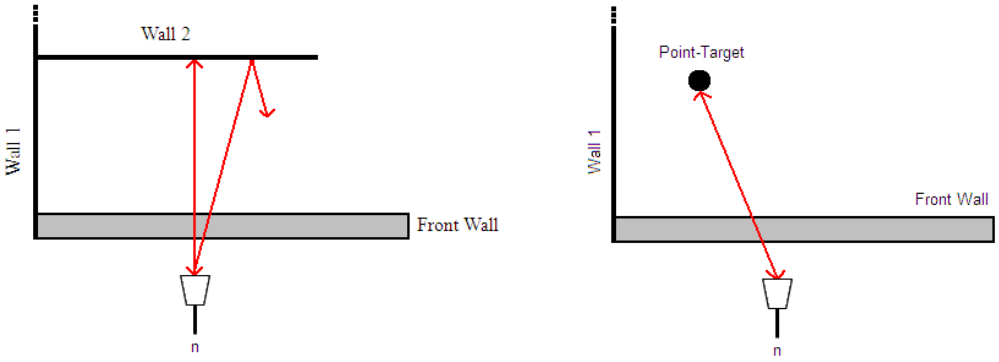

(a) (b)

FIGURE 5.28: Types of reflection in TWRI: (a) Specular reflection produced by walls, (b) Diffuse reflection produced by point-like targets.

contributions of the pixels that are located in front of each antenna. In so doing, the returns of the walls located parallel to the array axis are emphasized. As such, it is most suited to the specific building structure imaging problem, wherein the signal returns are mainly caused by EM reflections of exterior and interior walls. The alternate linear model can be expressed

as

$$\mathbf{y} = \hat{\mathbf{\Psi}}\mathbf{r} \tag{5.35}$$

where

$$\hat{\mathbf{\Psi}} = \begin{bmatrix} \hat{\mathbf{\Psi}}_0^T & \hat{\mathbf{\Psi}}_1^T & \cdots & \hat{\mathbf{\Psi}}_{N-1}^T \end{bmatrix}^T \tag{5.36}$$

with $\hat{\mathbf{\Psi}}_n$ defined as,

$$\left[\hat{\mathbf{\Psi}}_n\right]_m = \begin{bmatrix} \Im_{[(00),n]} e^{-j\omega_m \tau_{(0,0)}} & \cdots & \Im_{[(N_x-1,N_z-1),n]} e^{-j\omega_m \tau_{(N_x-1,N_z-1)}} \end{bmatrix} \tag{5.37}$$

In eqn. (5.37), $\tau_{(k,l)} = \frac{2\rho_l}{c}$ is the two-way signal propagation time associated with the downrange ρ_l of the (k,l)-th pixel, and the function $\Im_{[(k,l),n]}$ works as an indicator function in the following way,

$$\Im_{[(k,l),n]} = \begin{cases} 1 & \text{if the } (k,l)\text{-th pixel is in front of the } n\text{-th antenna} \\ 0 & \text{otherwise} \end{cases} \tag{5.38}$$

That is, if x_k, x_n and ∂x represent the crossrange coordinate of the (k,l)-th pixel, the crossrange coordinate of the n-th antenna location, and the crossrange sampling step, respectively, then $\Im_{[(k,l),n]} = 1$ provided that $x_k - \frac{\partial x}{2} \leq x_n \leq x_k + \frac{\partial x}{2}$ (see Fig. 5.29).

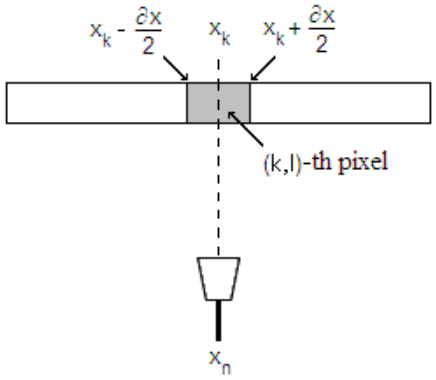

FIGURE 5.29: Indicator function $\Im_{[(k,l),n]}$: It takes value equal to 1 provided that $x_k - \frac{\partial x}{2} \leq x_n \leq x_k + \frac{\partial x}{2}$.

Sparsifying basis for interior wall detection With the synthetic array aperture parallel to the front wall, only interior walls parallel to the array will appear in the image. We, therefore, focus primarily on the detection of interior walls parallel to the front wall. It is noted that the walls perpendicular to the array could return the radiated wave through multipath via involvement of the parallel walls. This issue is discussed in Section 5.5.1. The number of parallel walls is typically much smaller compared to the downrange extent of the building, and thus, the decomposition of the image into horizontal walls can be considered as sparse. Note that although other indoor targets, such as furniture and humans, may be present in the scene, their projections onto the horizontal lines are expected to be negligible compared to those of the wall.

In order to obtain a linear matrix-vector relation between the scene and the horizontal projections, we define a sparsifying matrix $\mathbf{R}$ composed of possible wall locations. Specifically,

each column of the dictionary $\mathbf{R}$ represents an image containing a single wall of length l_x pixels, located at a specific crossrange and at a specific downrange in the image. Consider the crossrange to be divided into N_c non-overlapping blocks of l_x pixels each (see Fig. 5.30), and the downrange division defined by the pixel grid. The number of blocks N_c is determined by the value of l_x, which is the minimum expected wall length in the scene. Therefore, the dimension of $\mathbf{R}$ is $N_x N_z \times N_c N_z$, where the product $N_c N_z$ denotes the number of possible wall locations. Fig. 5.31 shows a simplified scheme of the sparsifying dictionary generation.

The projection associated with each wall location is given by,

$$g^{(b)}(l) = \frac{1}{l_x} \sum_{k \in B[b]} r(k, l) \tag{5.39}$$

where $B[b]$ indicates the b-th crossrange block and $b = 1, \ldots, N_c$. Defining

$$\mathbf{g} = \left[g^{(1)}(0) \quad \ldots \quad g^{(N_c)}(0) \quad g^{(1)}(1) \quad \cdots \quad g^{(N_c)}(1) \quad \cdots \quad g^{(1)}(N_z - 1) \quad \ldots \quad g^{(N_c)}(N_z - 1) \right]^T, \tag{5.40}$$

the linear system of equations relating the observed data $\mathbf{y}$ and the sparse vector $\mathbf{g}$ is given by,

$$\mathbf{y} = \hat{\mathbf{\Psi}} \mathbf{R} \mathbf{g} \tag{5.41}$$

In practice and by the virtue of collecting signal reflections corresponding to the zero aspect angle, any interior wall outside the synthetic array extent will not be visible to the system. Finally, the reconstructed CS image in this case is obtained by first recovering the projection vector $\mathbf{g}$ using OMP and then forming the product $\mathbf{Rg}$.

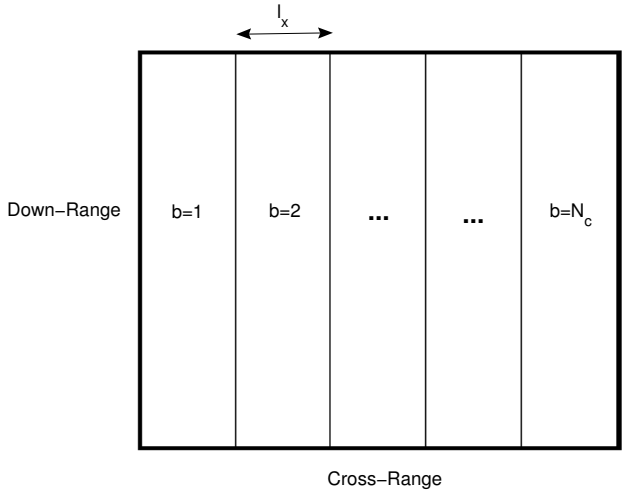

FIGURE 5.30: Crossrange division: the image is divided into N_c crossrange blocks of l_x pixels.

The projection defined in eqn. (5.39) clearly favors the detection of targets whose extent spreads in the crossrange image dimension. Thus, the contribution of horizontal walls will be much stronger than the contribution of point targets when using the proposed projection. This can be proven as follows. For simplicity, we assume that the crossrange pixel division

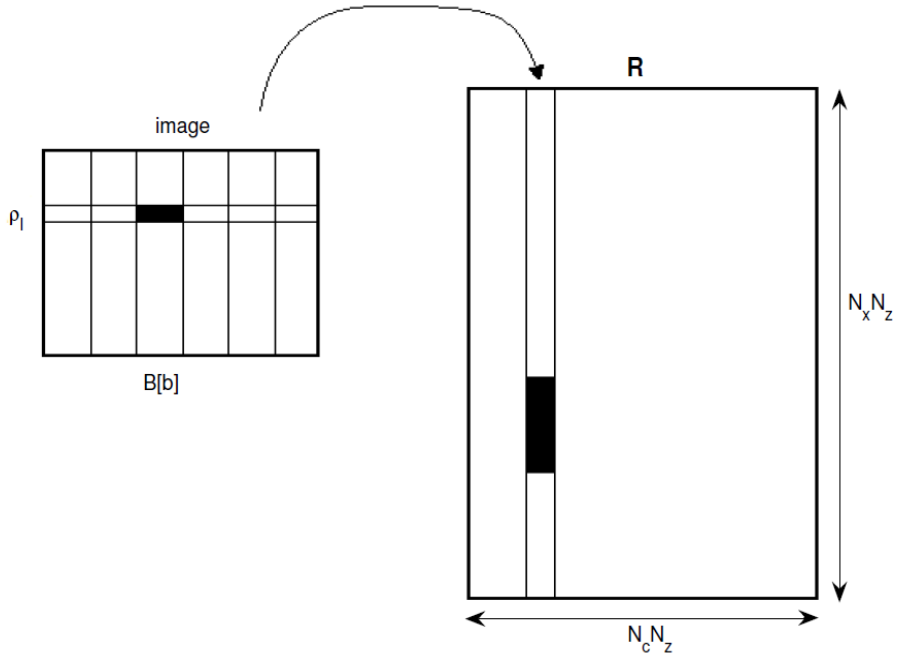

FIGURE 5.31: Sparsifying dictionary generation.

matches exactly the antenna array spacing ($x_k = x_n$ and ∂x=∂n, where ∂n represent the inter-element spacing of the array). Consider a single block $B[b]$ located at the l-th downrange, which contains a single point target with reflectivity σ_p. That is, out of the l_x pixels that form $B[b]$, all are equal to zero except one which assumes the value σ_p. Thus, the contribution of the point target under the proposed sparsifying basis is $g_p^{(b)}(l) = \frac{\sigma_p}{l_x}$. On the other hand, if the block $B[b]$ contains a wall instead of a point target, all the pixels that form $B[b]$ will be equal to the wall reflectivity σ_w and, thus, the contribution in this case will be $g_w^{(b)}(l) = \sigma_w$. Even considering the unusual case of $\sigma_p = \sigma_w$ (for the normal angle wall returns under consideration, $\sigma_p << \sigma_w$),

$$g_p^{(b)}(l) < g_w^{(b)}(l) \tag{5.42}$$

It is noted that we are implicitly assuming that the extents of the walls in the scene are integer multiples of the block of l_x pixels. In case this condition is not satisfied, the maximum error in determining the wall extent will be at the most equal to the chosen block size. In order to reduce this error, the chosen block size should be small. However, a smaller block size will cause the contributions from point-like targets to increase under the proposed sparsifying basis. In short, there exists a tradeoff between wall extent estimation error and the ability of the proposed basis to favor targets extended in crossrange.

Block-sparsity approach The sparsifying model proposed in (5.41) takes advantage of the additional structure in the form of the non-zero entries occurring in clusters exhibited by the scene image containing interior walls. Another possible approach that can take advantage of the clustering property is the block-sparsity approach [132]. Consider the sparse representation of the TWRI data defined in section 5.3, which operates under the point target model.

Similar to Section 5.5.1, in order to define block-sparsity, we view $\mathbf{r}$ as a concatenation of $N_c N_z$ blocks of length l_x, i.e. [132],

$$\mathbf{r} = \left[\underbrace{r_1 \quad \cdots \quad r_{l_x}}_{\mathbf{r}^T[1,0]} \quad \underbrace{r_{l_x+1} \quad \cdots \quad r_{2l_x}}_{\mathbf{r}^T[2,0]} \quad \cdots \quad \underbrace{r_{N_x N_z - l_x+1} \quad \cdots \quad r_{N_x N_z}}_{\mathbf{r}^T[N_c, N_z-1]} \right]^T \tag{5.43}$$

where $\mathbf{r}^T[b,l]$ denotes the b-th crossrange block located at the l-th downrange. For building layout detection, image $\mathbf{r}$ is block K-sparse, i.e., it has non-zero Euclidean norm for at most K blocks. Similarly, we can represent $\boldsymbol{\Psi}$ as a concatenation of column-blocks $\boldsymbol{\Psi}[b,l]$ of size $MN \times l_x$,

$$\boldsymbol{\Psi} = \left[\underbrace{\boldsymbol{\psi}_1 \quad \cdots \quad \boldsymbol{\psi}_{l_x}}_{\boldsymbol{\Psi}[1,0]} \quad \underbrace{\boldsymbol{\psi}_{l_x+1} \quad \cdots \quad \boldsymbol{\psi}_{2l_x}}_{\boldsymbol{\Psi}[2,0]} \quad \cdots \quad \underbrace{\boldsymbol{\psi}_{N_x N_z - l_x+1} \quad \cdots \quad \boldsymbol{\psi}_{N_x N_z}}_{\boldsymbol{\Psi}[N_c, N_z-1]} \right]^T \tag{5.44}$$

Once the formulation is expressed in a block form, the block extension of OMP (BOMP) can be applied to recover the sparse image $\mathbf{r}$ [132].

Multipath effects

EM propagation in highly scattering environment suffers from multipath effects. The multipath signals can cause ghost targets, which increase the number of false alarms reported by the system. The problem of multipath propagation in TWRI has been investigated in recent years in [135–137]. The image can be improved by correcting the ghosting problem while retaining the true targets, provided a good EM model of the propagation environment is available, which, in turn, requires knowledge of the building layout.

For the building layout detection problem considered in this paper, two types of multipath returns or reverberations are prevalent, namely, building reverberation and front wall reverberation. Building reverberation is a result of multiple reflections of the transmitted signal off interior walls within the building, whereas multiple reflections within the front wall constitute the front wall reverberation. In this section, we investigate the effects of the reverberations on the building layout detection problem. The walls are assumed to be smooth with specular reflection. Figure 5.32 shows the trajectory of one possible twice-bounced component of the building reverberation. Due to the specular nature of wall reflections, which requires the angle of incidence to be equal to the angle of reflection, it is clear from Fig. 5.32 that a twice-bounced reverberation component will never return to the transceiver location. There exist higher order multipath components with multiple bounces from other walls that may arrive at the transceiver location, but these paths are weaker due to the secondary reflections and the higher path loss. As such, their contribution is disregarded in this work. Based on the aforementioned observations, building reverberation will not pose a problem for the proposed method for interior layout detection.

On the other hand, front wall reverberation, depicted in Fig. 5.33-path(b), would cause replicas of the front wall to appear in the image at downranges behind the wall. We note that this issue will be less pronounced in wall materials, such as concrete, in which the radar signal undergoing multiple bounces within the wall suffers a higher degree of attenuation. We demonstrate this through simulation examples in Section 5.5.1.

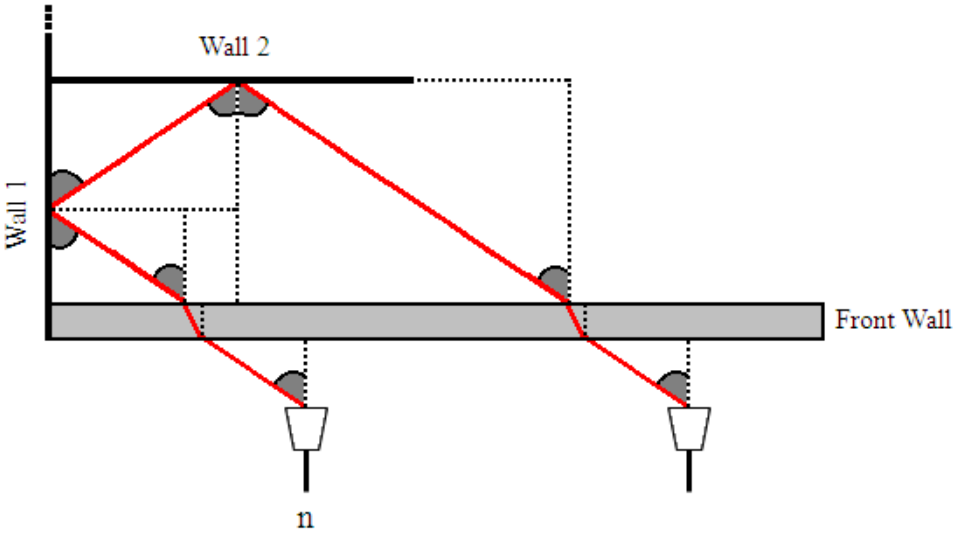

FIGURE 5.32: Geometry depicting Building Reverberation (two bounces).

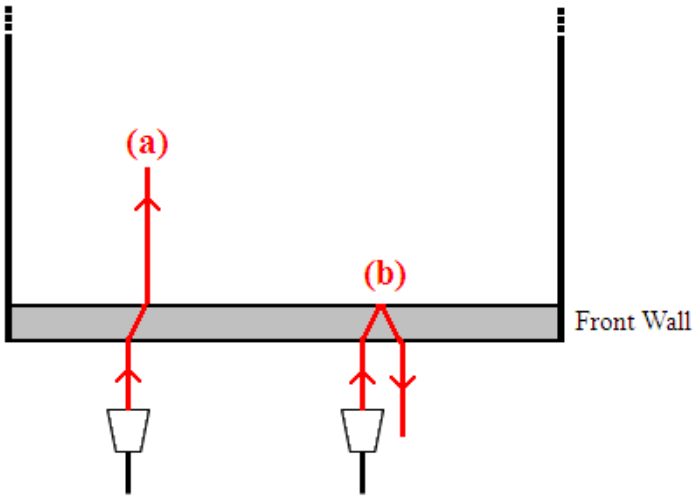

FIGURE 5.33: Geometry depicting wall reverberation: propagation through wall described by path (a) and first-order reverberation described by path (b).

Simulation and experimental results

Simulation results

In this section, we evaluate the performance of the proposed scheme using synthesized data. A stepped-frequency signal consisting of 335 frequencies covering the 1 to 2 GHz frequency band was used for interrogating the scene. A monostatic synthetic aperture array, consisting of 71-element locations with an inter-element spacing of 2.2cm, was employed. The array was located parallel to a 1.6m-wide front wall, and centered at 0m in crossrange at a standoff distance of 2.42m. The scene behind the front wall contained two interior walls, a back wall, and a single point target. The first interior wall extended from -0.78m to -0.29m in crossrange at a downrange of 3.37m, while the second wall was located at 5.12m downrange, extending from 0.29m to 0.78m in crossrange. The 1.6m wide back wall was located at 6.24m and was aligned with the front wall in crossrange. The point target was located at $(0.02, 4.24)$m. Fig. 5.34 depicts the geometry of the simulated scene. The attenuation caused by the front wall was set to 10dB. The region to be imaged is chosen to be 5.65m (crossrange) $\times$ 4.45m (downrange), centered at (0, 4.23)m, and is divided into 128×128 pixels.

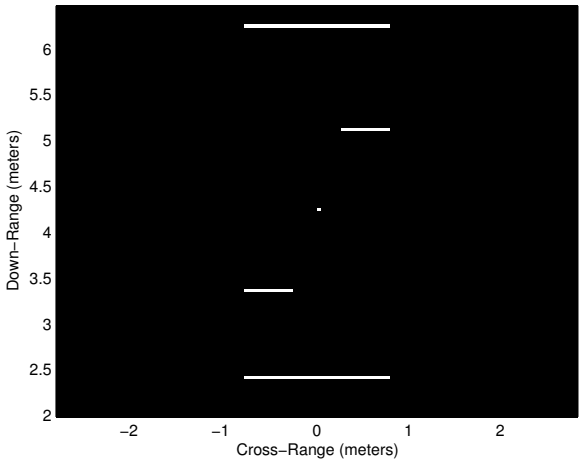

FIGURE 5.34: Geometry of the simulated scene

Figure 5.35 shows the through-the-wall radar image obtained with the backprojection algorithm, described in eqn. (3.55), using all MN observations. In this figure and all subsequent figures in this section, we plot the image intensity with the maximum intensity value in each image normalized to 0dB. The four walls and the point target are clearly visible in Fig. 5.35. For sparsity-based imaging, we consider only 6.4% of the full data volume (25% uniformly selected frequencies and 25% uniformly chosen sensor locations). Figure 5.36 depicts the CS image reconstruction obtained with the following three approaches: conventional CS approach, wavelet-based CS approach and the proposed approach. The number of wavelets coefficients, W, was set to 65536, which corresponds to a DT-CWT with depth of decomposition equal to 4. For the proposed approach, the number of blocks, N_c, was set equal to 3 and the size of each block was chosen to be 1 pixel in downrange and $l_x = 12$ pixels in crossrange, which corresponds to a minimum wall length of 0.53m. We forced the number of iterations of the OMP to be equal to 8 in all cases, which means that the output of the OMP will be a sparse vector of 8 non-zero components. Fig. 5.36(a) shows the image reconstructed with the conventional CS-based imaging with no sparsifying basis. Since the walls are extended targets and appear dense under the point target model, all the degrees of

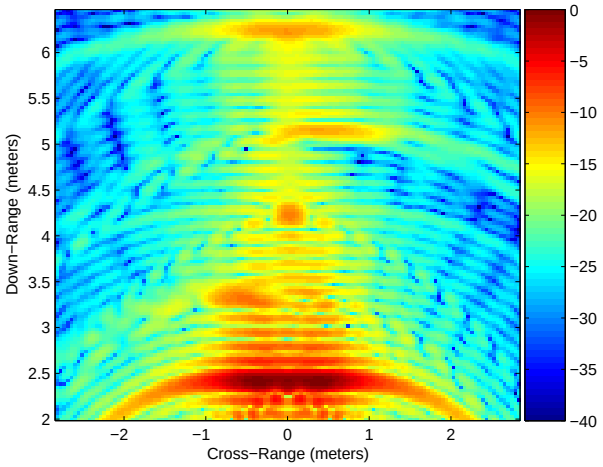

FIGURE 5.35: Through-the-wall radar image using conventional backprojection with 100% data.

freedom are used up in reconstructing the front wall. Thus, the conventional approach fails to recover the building structure. The corresponding reconstructed scene obtained with the wavelet approach is shown in Fig. 5.36(b). Although this approach is more suitable for representing extended targets than the point target model, it is clearly not enough to reconstruct the interior building structure with 8 non-zero wavelet coefficients. Finally, it is evident that the image produced by the proposed sparsifying model, which is shown in Fig. 5.36(c), has adequately reconstructed the structure of the building. Furthermore, the intensity values assigned to each reconstructed wall in Fig. 5.36(c) are related to the corresponding wall reflectivities and the attenuation produced by the front wall.

Considering the scene itself to be sparse and making use of the block-sparsity in the reconstruction algorithm with BOMP yields the image shown in Fig. 5.37(a). We observe that not only some portions of the back wall are missing from the image, but also a few false blocks have been reconstructed. These deficiencies can be attributed to the underlying point target model. Instead of using the point-target based sensing matrix of eqn. (5.10), we employed the alternate sensing matrix described in (5.37), which highlights the returns of the walls located parallel to the sensors, for the block-sparsity approach. Fig. 5.37(b) shows the resulting image. Although incorporation of the alternate sensing matrix leads to a reduction in the false reconstructions, the BOMP algorithm in this case reconstructs each wall with several gaps corresponding to the pixels located in front of the non-selected antennas. This shortcoming is due to the fact that the blocks are taken into account only in the reconstruction algorithm and not in the problem formulation. On the other hand, in the proposed sparsifying approach, the block structure of the image is introduced in the formulation through the matrix $\mathbf{R}$, and thus, the block information is also exploited in the conventional OMP. It is worth noting that the matrix size processed by BOMP is much larger than that of the proposed sparsifying model, as the number of pixels $N_x N_z$ is larger than the number of blocks $N_c N_z$.

Before we can evaluate the goodness of an estimation, some kind of measure is needed to assess the dissimilarity between the estimated image and the truth image. In order to provide a quantitative analysis of the performance of compressive reconstructed images, we use the

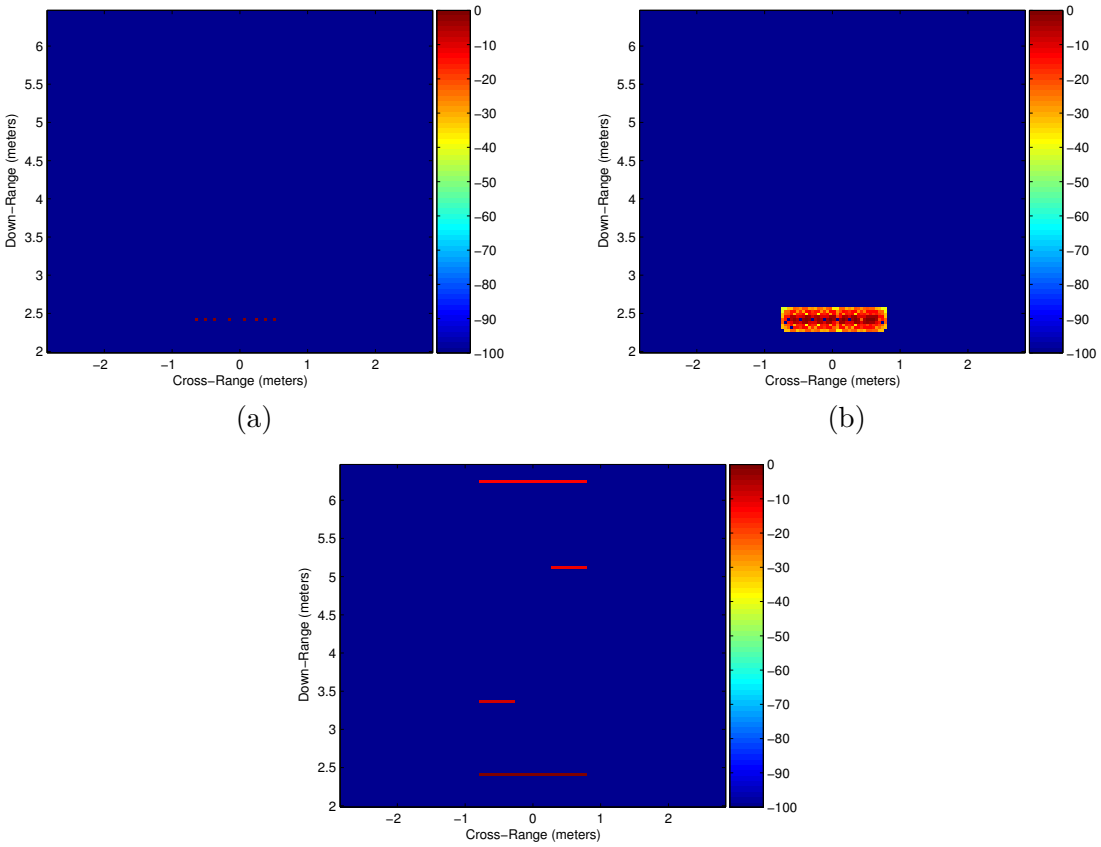

FIGURE 5.36: Reconstructed image from the recovered sparse vector using OMP and 6.4% data: (a) Conventional CS, (b) 2D-DWT based CS, (c) Proposed apprach.

Earth Mover's Distance (EMD) [138,139]. It was introduced as a histogram similarity metric for image retrieval and has become a popular metric in image processing community. Limiting the error of sparsely recovered images to l_p norms is quite inconvenient because they do not accurately represent perceptual differences between images [140,141]. For instance, in sparse images, the mean-squared error will equally penalize estimated target locations that are off by 1 cm and 100 cm. This problem is solved using EMD. Given two distributions, the EMD reflects the minimal amount of work that must be performed to transform one distribution into the other by moving *distribution mass* around. Basically, EMD naturally extends the notion of a distance between single elements to that of a distance between distributions of elements. EMD is a popular metric for comparing similarity between images, feature sets, etc. [140,142]. The MATLAB code implementing EMD was extracted from MATLAB Central File Exchange website[1]

A plot showing the EMD of the proposed approach versus signal-to-noise ratio (SNR) is provided in Fig. 5.38. In order to generate this plot, white Gaussian noise was added to the simulated data measurements (see Appendix 5.5.1 for more information about the noise generation). Fig. 5.38 makes evident the degradation of the proposed technique in terms of detection capability due to the reduction in the data volume. Fig. 5.38(a) corresponds

[1]http://www.mathworks.com/matlabcentral/fileexchange/

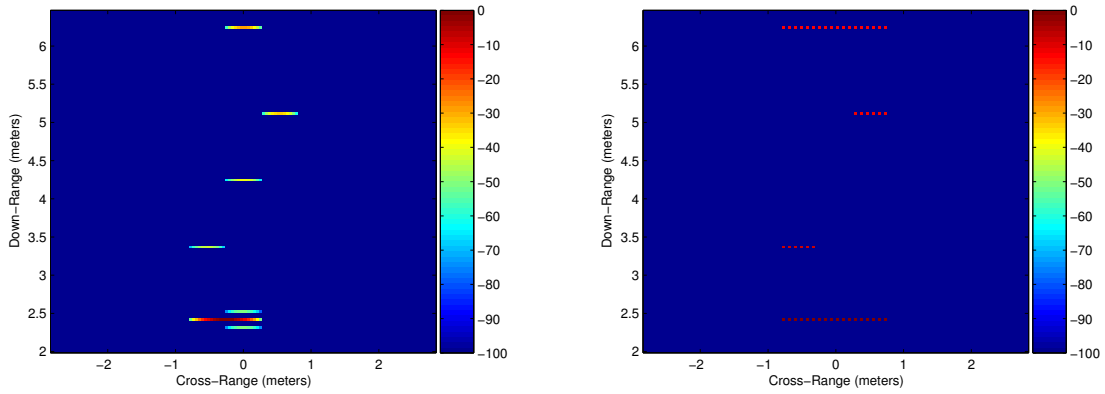

(a) (b)

FIGURE 5.37: Reconstructed image using BOMP and 6.4% data: (a) $\breve{\mathbf{y}} = \mathbf{\Phi\Psi r}$, (b) $\breve{\mathbf{y}} = \mathbf{\Phi\hat{\Psi}r}$.

to reduction of the frequency observations, while the number of sensors is reduced in Fig. 5.38(b). In both cases, the EMD increases as the SNR decreases. Furthermore, for a given SNR, the EMD increases with decreasing data volume.

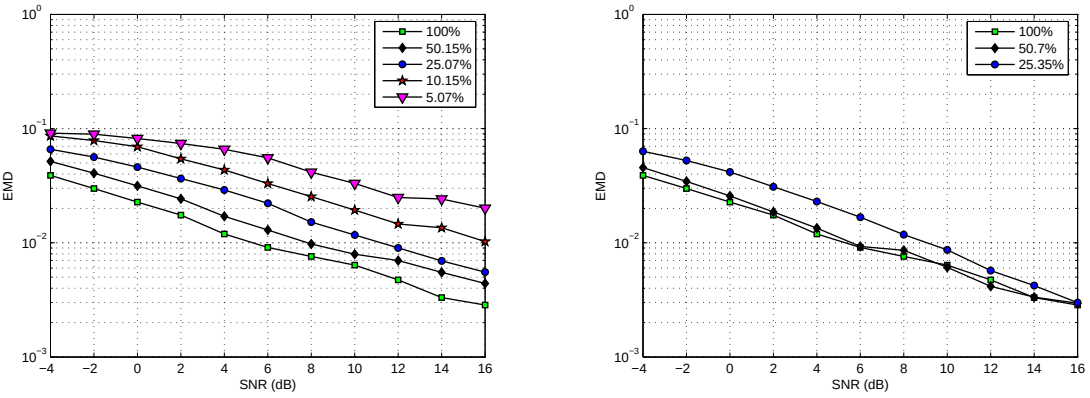

(a) (b)

FIGURE 5.38: EMD vs. SNR for the proposed approach: (a) frequency compression, (b) antenna compression.

Convergence of CS approaches In this section, the number of iterations required to converge to the desired result is studied for each of the three approaches.

Fig. 5.39 shows the reconstructed images obtained with the conventional CS approach and with different running times. It is a pixel-based method and that is why when we increase the number of iterations (or running time) of the reconstruction algorithm, it populates more pixels in the less-sparse part of the image. By simulation we have seen that the conventional CS methods requires around 100 iterations to detect all the interior structures present in the scene.

The convergence is faster when using the wavelet approach, as it can be observed in Fig. 5.40, where the reconstructed image obtained with different running times is shown for the

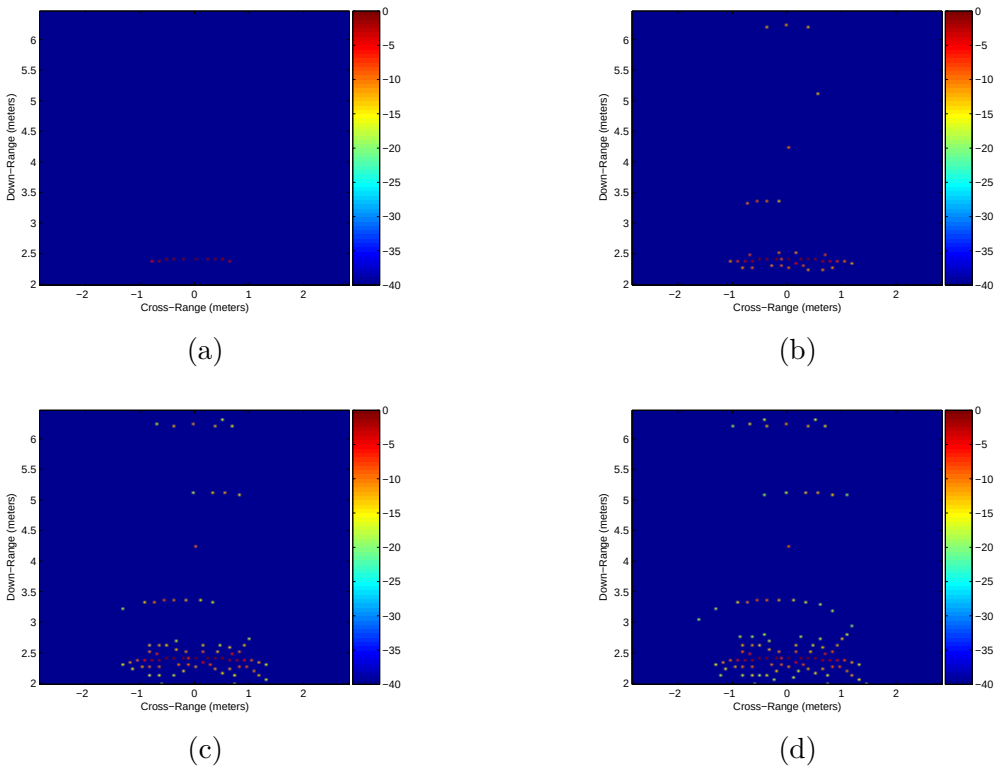

FIGURE 5.39: Reconstructed image with the conventional approach: (a) 10 iteration, (b) 40 iterations, (c) 80 iterations and (d) 100 iterations

case of 2D-DWT based CS approach. By simulations we have observed that all walls present in the scene are detected when the number of iterations is close to 60.

Finally, Fig. 5.41 shows the reconstructed image obtained with different running times for the proposed approach. Clearly, the convergence of the proposed method is faster compared with the other two alternative methods: all building interior and exterior structures have been detected with 8 iterations.

To complete the convergence study we will use the EMD parameter to compare the convergence of the conventional CS approach, the wavelet based approach and the proposed method. The EMD results for the three approaches with respect to the number of iterations are depicted in Fig. 5.42, where the convergence of the three techniques is shown in terms of EMD. Clearly, the proposed method achieves the lowest error in the fastest time. Note that, although the conventional CS was shown to provide acceptable image reconstruction quality with 100 iterations, the perceptual difference between the true building layout is quite high, and therefore, the EMD is high.

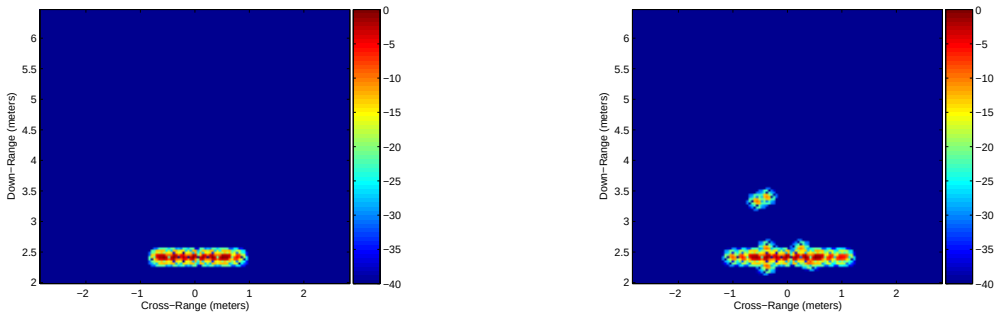

FIGURE 5.40: Reconstructed image with the 2D-DWT based CS approach: (a) 10 iteration, (b) 20 iterations, (c) 30 iterations and (d) 60 iterations

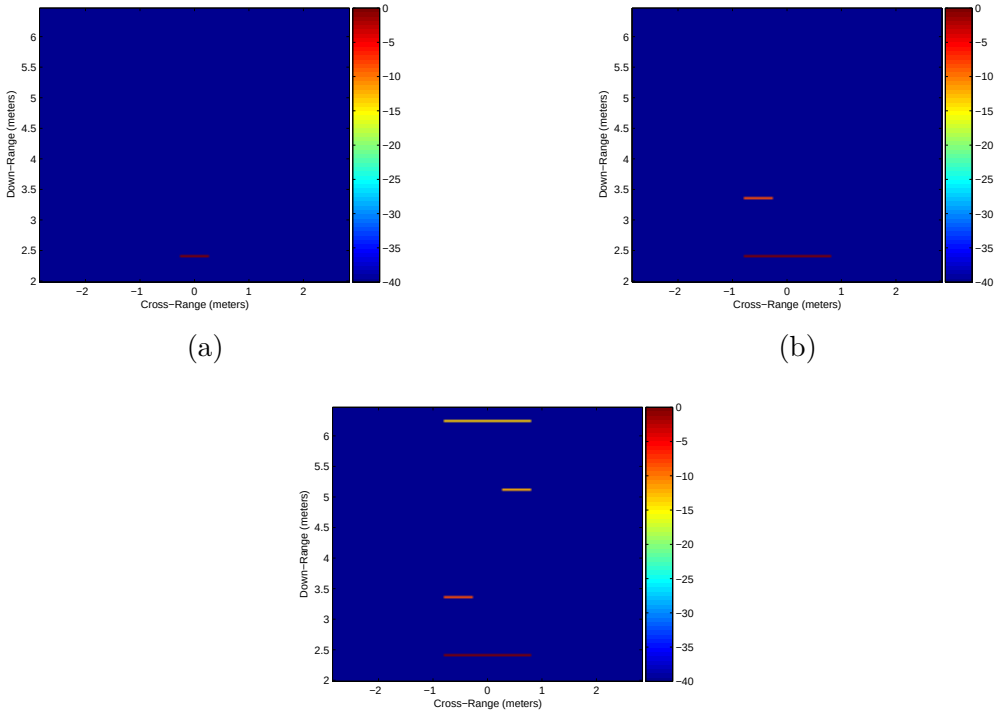

FIGURE 5.41: Reconstructed image with the proposed approach: (a) 1 iteration, (b) 4 iterations, (c) 8 iterations.

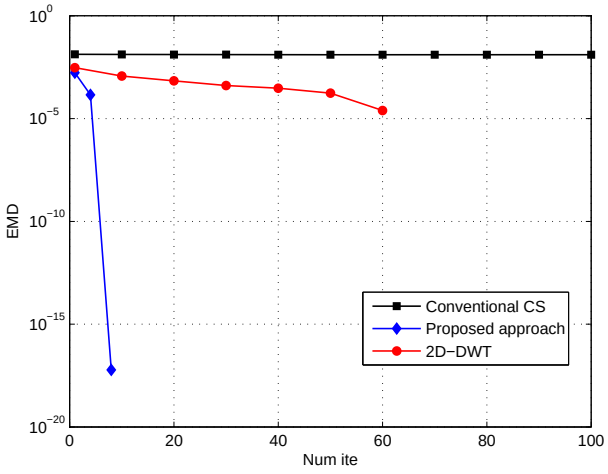

FIGURE 5.42: EMD vs number of iterations using OMP and 100% data.

Low SNR Scenarios: ROC Curves In this section, we evaluate the probability of false alarm P_{fa} versus the probability of detection P_d (i.e., the ROC curve). Each point on the ROC plot is obtained by averaging 50 simulation runs in the presence of one wall (Hypothesis H1) and 50 simulation runs without the presence of the wall (Hypothesis H0).

$$y(m,n) = \begin{cases} n(m,n) & H_0 \\ A_{tt}\sigma_w e^{-j\omega_m \tau_w} + n(m,n) & H_1 \end{cases} \tag{5.45}$$

The wall extends from -0.78m to -0.29m in crossrange at a downrange of 3.37m, and its contribution is attenuated $A_{tt} = 10$dB as if the front wall was present. Fig. 5.43 shows the ROC from Monte Carlo runs for SNR=-18.7dB. As it was expected, the general performance of the proposed building structure detector is deteriorated as the compression rate decreases.

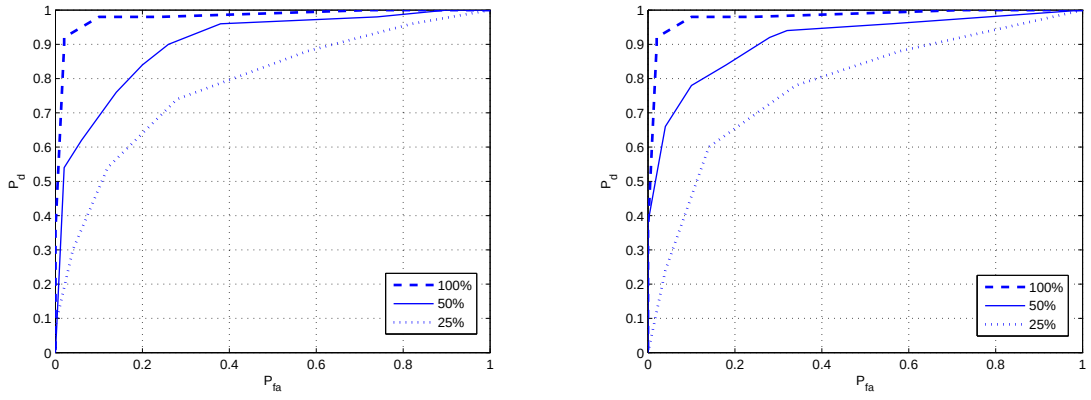

FIGURE 5.43: ROCs for SNR=-18.7dB obtained with Monte Carlo runs for different compression rates: (a) frequency compression (b) antenna compression.

Wall reberveration Finally, we investigate the effect of the echoes produced by front wall reverberation. In the simulation, we consider the first-order reverberation plotted in Fig. 5.33-path(b). Higher-order reverberation are, in general, weaker compared to the first-order one due to secondary reflections and high attenuation in the wall material. Therefore, these paths are not taken into account in our simulation. The simulated scene is the same described at the beginning of this section. We use 6.4% of the data and the number of iterations is set to 8, as before. Fig. 5.44 shows the performance of the proposed approach for two types of front wall. Fig. 5.44(a) considers solid concrete wall, whose first-order reverberation attenuation is set equal to 30dB. With this type of wall, the reverberation of the front wall is weak and thus, the proposed approach does not produce replicated images of the front wall. On the other hand, Fig. 5.44(b) considers a less attenuative wall (e.g. an adobe brick front wall), whose reverberation attenuation is equal to 15dB. In this case, the algorithm reconstructs the replica of the front wall and misses the back wall because the reverberation causes a ghost whose contribution is higher than the back wall of the room.

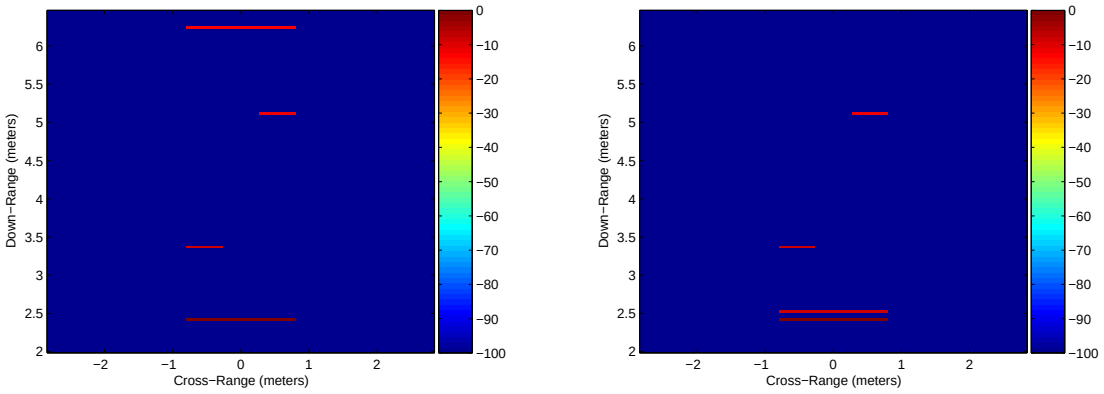

FIGURE 5.44: Performance of the proposed approach considering the reverberation effect of the front wall: (a) Solid concrete wall (attenuation of 30dB), (b) Adobe brick wall (attenuation of 15dB).

Experimental results A through-the-wall SAR system was set up in the Radar Imaging Lab, Villanova University. The system and signal parameters are the same as those for the simulated data. The scene consisted of two parallel plywood walls, each 2.25cm thick, 1.83m wide, and 2.43m high. Both walls were centered at 0m in crossrange. The first and the second walls were located at respective distances of 3.25m and 5.1m from the antenna baseline. Fig. 5.45 depicts the geometry of the experimental scene. The region to be imaged is chosen to be the same as in Section 5.5.1. Fig. 5.46 shows the conventional backprojection imaging

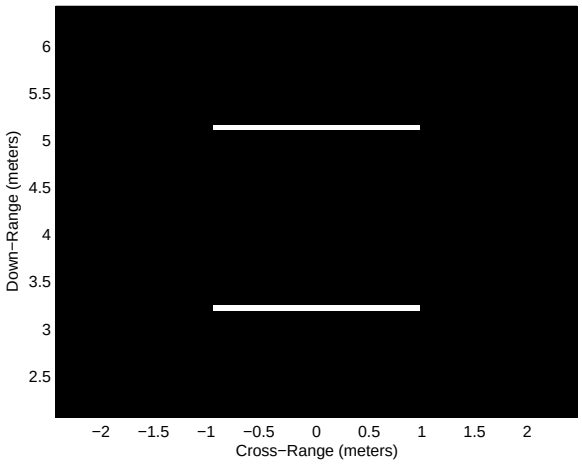

FIGURE 5.45: Geometry of the lab scene

result using the full dataset, wherein the two walls can be clearly seen. For the CS approach, instead of measuring all 335 frequencies at all 71 antenna locations, we use a uniform subset of only 84 frequencies at each of the 18 uniformly spaced antenna locations, which represents 6.4% of the full data volume. The CS reconstructed image is shown in Fig. 5.47. We note in Fig. 5.47 that the proposed algorithm was able to reconstruct the back side of both walls. This is because the attenuation of the plywood walls is not sufficiently high go unnoticed by

the reconstruction process and, thus, the first-order reverberation is being captured.

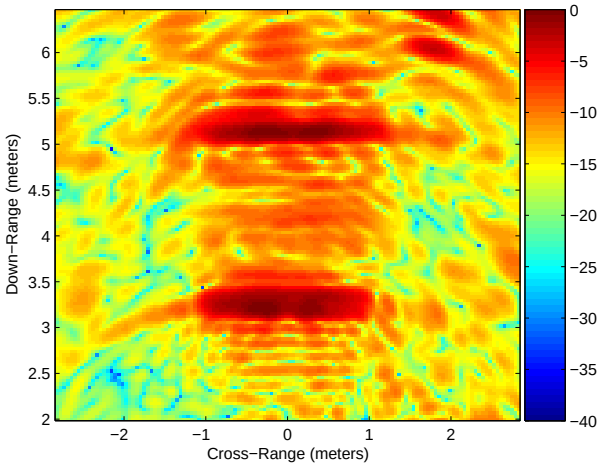

FIGURE 5.46: Through-the-wall radar image using conventional backprojection with 100% of the data volume.

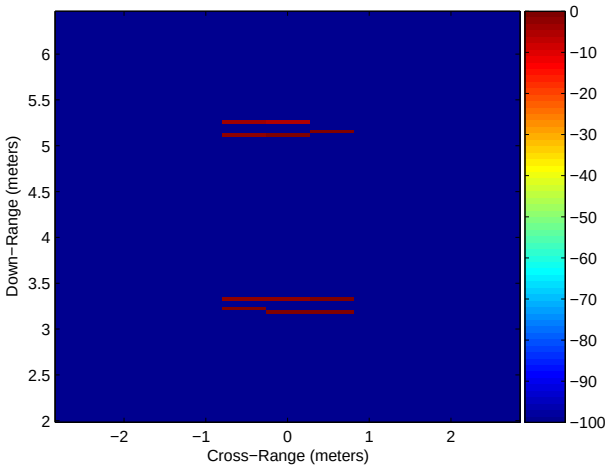

FIGURE 5.47: Reconstructed image from the recovered sparse vector with the proposed approach using OMP and 6.4% data.

Conclusion

A sparsity-based approach for imaging of interior building structure was presented. The proposed technique makes use of the prior information about building construction practices of interior walls to both devise an appropriate linear model and design a sparsifying dictionary based on the expected wall alignment relative to the radar's scan direction. The proposed method provides reliable determination of building layouts, while achieving substantial reduction in data volume. Results based on laboratory experiments were presented, which depicted the improved performance of the proposed method when compared to backprojection, conventional point-target based CS, and CS employing wavelet sparsifying basis.

Moreover, the proposed approach has been shown to overcome the limitations of the recently proposed block-sparsity model when applied to building interior layout detection.

Appendix: Noise generation

Consider the following noisy radar measurements,

$$\tilde{\mathbf{y}} = \mathbf{y} + \mathbf{n} \tag{5.46}$$

where $\mathbf{n}$ is i.i.d. complex Gaussian noise with variance σ_n^2. A compressed vector consisting of elements chosen from the noisy observations $\tilde{\mathbf{y}}$ is obtained using the sensing matrix $\mathbf{\Phi}$ as follows,

$$\breve{\tilde{\mathbf{y}}} = \mathbf{\Phi}\tilde{\mathbf{y}} = \mathbf{\Phi}\left[\mathbf{\Psi}\mathbf{r} + \mathbf{n}\right] \tag{5.47}$$

The expression in (5.47) is quite different from the conventional noise assumption in CS. The standard CS setup assumes that the compressive measurements are corrupted by additive noise, which is either assumed deterministic and bounded [143] or white typically Gaussian [28, 144]. This model is adequate when the noise is introduced in the measurement stage and there are some recovery algorithms, such as Lasso [26], designed according to this noise. However, in radar applications, noise is added to the signal to be measured before the acquisition stage. Many publications have focused its efforts on the following model,

$$\breve{\tilde{\mathbf{y}}} = \mathbf{\Phi}\left[\mathbf{\Psi}\left(\mathbf{r} + \mathbf{w}\right)\right] \tag{5.48}$$

where $\mathbf{w}$ is assumed zero-mean white additive noise. This model neither fits our scenario. From eqn. (5.47) it can be extracted that $\mathbf{n} = \mathbf{\Psi}\mathbf{w}$ and thus, $\mathbf{w}$ is not white Gaussian noise.

Although the noise is added in the data domain, this thesis evaluates the SNR of images according the definitions of Gonzalez [145]. The SNR definition, shown in (5.49), compares a reference image $r(k,l)$ with a test image $t(k,l)$. The two images should have the same size $[N_x, N_z]$.

$$SNR = 10\log_{10}\frac{\sum_{N_x-1}^{k=0}\sum_{N_z-1}^{l=0}[r(k,l)]^2}{\sum_{N_x-1}^{k=0}\sum_{N_z-1}^{l=0}[r(k,l)-t(k,l)]^2} \tag{5.49}$$

To show how the additive gaussian noise $\mathbf{n}$ affects the image, Fig. 5.48 depicts three different scenarios with SNR=10dB, SNR=0dB and SNR=-10dB.

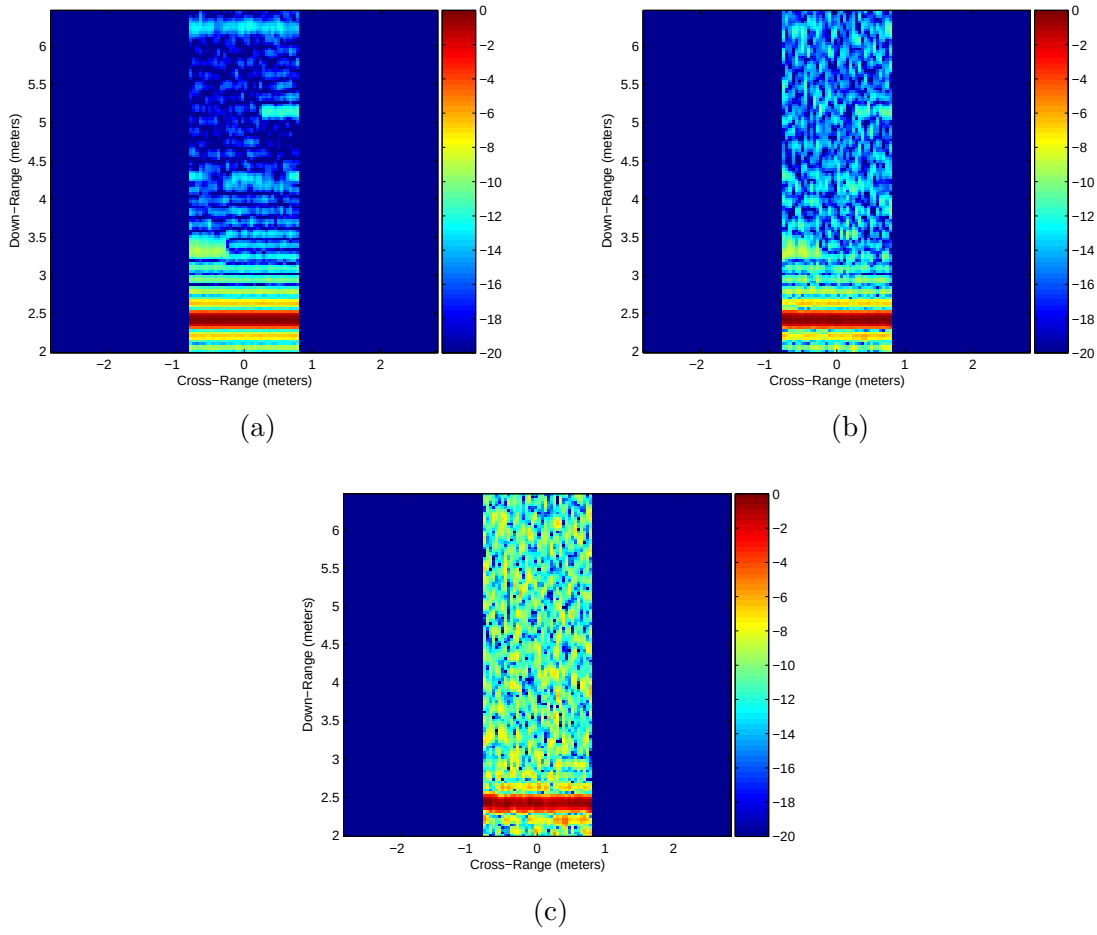

FIGURE 5.48: Noise effect on image domain: (a) SNR=10dB, (b) SNR=0dB, (c) SNR=-10dB.

5.5.2 Improved interior wall detection: Detection of corners

In the previous section, we addressed the problem of imaging building interior structures using a reduced number of measurements. In particular, we devised an overcomplete dictionary of candidate wall locations for sparse representation, which is consistent with the fact that interior walls are typically parallel or perpendicular to the front wall. CS was applied to a reduced set of observations to recover the true positions of the walls. While the proposed method was successful in detecting interior walls that were parallel to the front wall, it could not determine the exact extents of the detected walls. Moreover, the proposed scheme could not locate walls that were perpendicular to the front wall, without access from another side of the building. In this section, we extend the method to overcome its aforementioned shortcomings by exploiting the EM scatterings from corners created by the junction of parallel and perpendicular walls. As a follow-on step to the parallel wall detection scheme, we propose to use a sparsifying overcomplete dictionary of candidate corner reflectors, representing the reflection caused by the wall-wall junctions. CS techniques are applied to the reduced set of observations to recover the positions of the corners along the previously detected parallel walls. Determining corner reflectors along the wall segments indicates the extents of the detected parallel walls and locates perpendicular walls. The proposed enhancement provides

reliable determination of building interior layout while achieving substantial reduction in data volume.

Proposed extension based on corner detection

Once the wall locations have been determined, more information about the walls and their extent can be inferred by detecting the corners (dihedral) formed by the intersection of a parallel wall and a perpendicular wall. Thus, the following corner detection approach should be considered as a follow-on step after the wall detection approach described in section 5.5.1.

We first modify eqn. (5.33) to take into account the wall-wall junctions present in the scene [146]. Considering the presence of C corner reflectors, the signal received by the nth transceiver at the mth frequency can be expressed as,

$$y(m,n) = \sigma_w e^{-j\omega_m \tau_w} + \sum_{i=0}^{I_w-1} \sigma_{w_i} e^{-j\omega_m \tau_{w_i}} + \sum_{p=0}^{P-1} \sigma_p e^{-j\omega_m \tau_{p,n}} + \sum_{q=0}^{C-1} \Upsilon_{[q,n]} S_q(n,m,\bar{\phi}_q) e^{-j\omega_m \tau_{q,n}}, \tag{5.50}$$

with

$$S_q(n,m,\bar{\phi}_q) = \sigma_q \text{sinc}(\omega_m \frac{L_q}{c} \sin(\phi_{q,n} - \bar{\phi}_q)) \tag{5.51}$$

The function $\Upsilon_{[q,n]}$ works as an indicator function in the following way,

$$\Upsilon_{[q,n]} = \begin{cases} 1 & \text{if } n\text{-th antenna illuminates the concave side of the } q\text{th corner} \\ 0 & \text{otherwise} \end{cases} \tag{5.52}$$

In eqn. (5.50), σ_q contains the amplitude of each corner reflector, which includes the attenuation caused by the distance between the corner and the receiver, the attenuation caused by the propagation through the front wall, and the complex reflectivity of the corner reflector. The variables L_q and $\bar{\phi}_q$, respectively, define the length and the orientation angle of the qth corner reflector, whereas $\phi_{q,n}$ is the aspect angle associated with the qth corner reflector and the nth antenna. In the above equation, $\tau_{q,n}$ represents the two-way traveling time of the signal between the nth antenna and the qth corner.

Assuming that N_w parallel walls have been previously detected, the sparsifying dictionary based on possible dihedral locations, named $\mathbf{\Lambda}$, can be introduced with $2N_xN_w$ columns, each corresponding to a corner response, located at a different position with either 45° or 135° orientation angle. The corner response is modeled following eqn. (5.51). The linear relationship between the possible dihedral locations, represented by the column vector $\boldsymbol{\nu}$, and the reduced data measurements, $\breve{\mathbf{y}}$, is given by,

$$\breve{\mathbf{y}} = \mathbf{\Phi}\mathbf{\Lambda}\boldsymbol{\nu} \tag{5.53}$$

Therefore, the initial step in the proposed algorithm is to detect wall positions from the compressed data measurements using the sparse model defined in eqn. (5.41). Using the downranges of the detected walls, a dictionary of dihedral positions (eqn. (5.53)) is then used to determine the extent of the walls.

Simulation results

In this section, we evaluate the performance of the proposed scheme using synthesized data. A stepped-frequency signal consisting of 335 frequencies covering the 1 to 2 GHz frequency

band was used for interrogating the scene. A monostatic synthetic aperture array, consisting of 71-element locations with an inter-element spacing of 2.2cm, was employed. The array was located parallel to a 1.6m-wide front wall, and centered at 0m in crossrange at a standoff distance of 2.42m. The scene behind the front wall contained two interior walls, a back wall, and a single point target. The first interior wall extended from -0.78m to -0.56m in crossrange at a downrange of 3.37m, while the second wall was located at 5.12m downrange, extending from 0.02m to 0.78m in crossrange. The 1.6m wide back wall was located at 6.24m and was aligned with the front wall in crossrange. The two interior walls and the back wall have corner reflectors on their extremities to emulate the junctions between parallel and perpendicular walls. The point target was located at $(0.02, 4.24)$m. Fig. 5.49 depicts the geometry of the simulated scene. The attenuation caused by the front wall was set to 10dB.

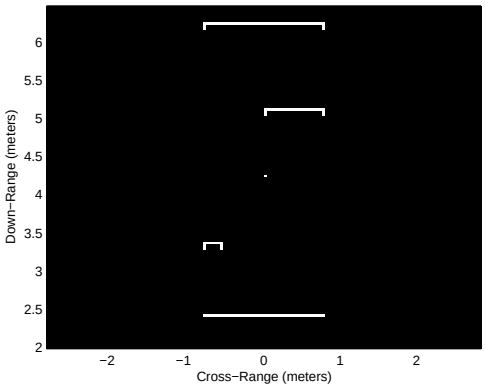

FIGURE 5.49: Geometry of the simulated scene

The region to be imaged is chosen to be 5.65m (crossrange) $\times$ 4.45m (downrange), centered at (0, 4.23)m, and is divided into 128 $\times$ 128 pixels. The sparsifying matrix $\mathbf{R}$ contains predefined walls of size 1 pixel in downrange and 12 pixels in crossrange, which corresponds to a minimum wall length of 0.53m. We enforced the first interior wall to be half of the predefined wall block length in the dictionary $\mathbf{R}$, whereas the second interior wall occupies one and a half of the predefined wall blocks. For sparsity-based imaging, we consider only 6.4% of the full data volume (25% uniformly selected frequencies and 25% uniformly chosen sensor locations). Fig. 5.50(a) and Fig. 5.50(b) show the recovered CS images from the wall detection step and the corner detection step, respectively. In these figures, we plot the image intensity with the maximum intensity value in each image normalized to 0dB. Fig. 5.50(a) shows how the wall that is occupying one and a half block is now recovered as a two block wall, and the half block wall is recovered as a complete block wall. Therefore, although the wall detection approach presented in [147] has adequately detected the downrange position of the walls, it fails to correctly determine the corresponding wall extents. These initial wall estimates in Fig. 5.50(a) can be refined with the proposed corner detection approach, which accurately estimates the extent of each wall, as shown in Fig. 5.50(b).

Conclusion

A sparsity-based approach for imaging of building interior structures was presented. The proposed two-step approach makes use of prior information about building construction practices to form an appropriate sparse representation of the building interior layout. In the first step,

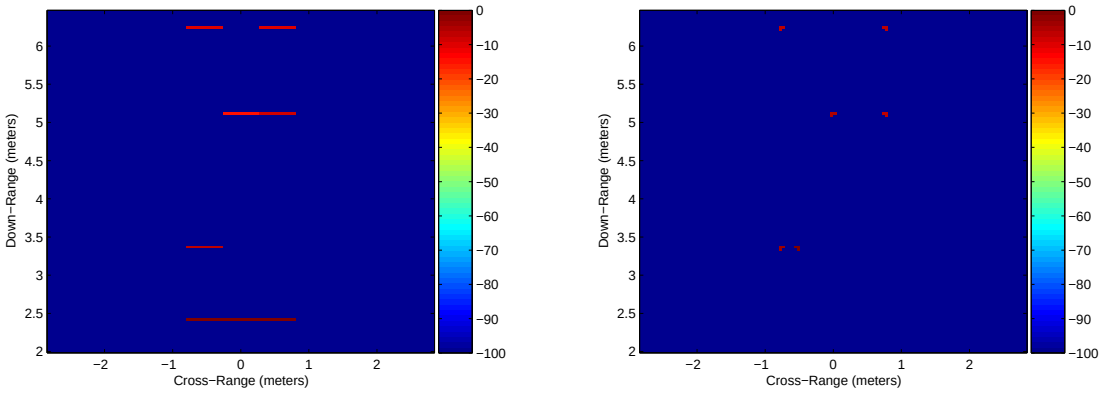

(a) (b)

FIGURE 5.50: Reconstructed image from the recovered sparse vector using OMP and 6.4% data: (a) Proposed approach for wall detection, (b) Proposed approach for corner detection.

a sparsifying dictionary based on the expected wall alignment relative to the radar's scan direction was designed and used to detect interior walls parallel to the front wall. In the second step, a sparsifying dictionary based on the possible corner reflector locations was employed to detect the wall-wall junctions along the detected parallel walls, in order to determine the wall extents and detect walls perpendicular to the front wall. The proposed method provides reliable determination of building layouts, while achieving substantial reduction in data volume. Results based on computer simulations were presented, which depicted the improved performance of the proposed method when compared to the wall-only detection approach of Ref. [147].

5.6 Pattern matching for building feature extraction

Dihedral-like reflectors have similar radar response than point-like scatterers. In the work presented in the previous section, we first detect horizontal walls and then use these estimated wall locations to limitate the corner search. In other words, we only look for corners in the places where we detected walls. This two-step procedure prevent classification confusion since we do not expect point-like reflectors to be placed in the same location than the walls.

Next, we assume flexibility in radar operation which allows proper angular radar illuminations, thereby avoiding the front wall returns and preserving the corner features created by the junction of walls. This can be achieved using squint beamforming or broadside beams with tilted aperture [91]. Estimating locations of dominant scatterers, such as corners, allows the inference of building interior structure without the need to detect walls. In this case, the problem of detecting building interior structures using a reduced number of measurements requires a different perspective.

This section proposes an image pattern matching strategy, which is based on a novel type of image descriptor, namely, the correlogram. Recently, several approaches have attempted to incorporate spatial information with color [148,149]. The correlogram proposed in this thesis encodes information about spatial correlation of the complex amplitudes. The basic detection strategy adopted here is to compare the known correlogram of the scattering response of an isolated canonical corner reflector with the correlogram of the received radar signal. The

correlation matching procedure can be applied using compressed observations. As such, it avoids the tedious l_1-norm constrained optimization problem encountered in conventional compressive sensing (CS). The feature-based nature of the proposed detector enables corner separation from other indoor scatterers, such as furniture or humans. Simulation results show that the use of spatial correlation of complex amplitudes makes the detection performance superior to that of either using raw signal matching [100, 147] or image matching [150].

5.6.1 TWR Signal model

We consider a monostatic N-element synthetic line array. It is noted that the concept can easily be extended to 2D and/or bistatic arrays. We assume that the data acquisition is carried out in an oblique position, as shown in Fig. 5.51(a), which significantly attenuates the wall returns and enhances corner scatterers. Let the nth transceiver illuminate the scene with a stepped frequency signal consisting of M frequencies. The response of the scene can be modeled as the sum of responses from individual scatterers, assuming that the scatterers do not interact. Thus, the signal received by the nth transceiver at the mth frequency can be represented as,

$$y(m,n) = \sum_{p=1}^{P} S_p(m,n,\bar{\phi}_p) e^{-j\omega_m \tau_{p,n}} + w(m,n) \tag{5.54}$$

where P is the number of corner scatterers present in the illuminated scene, $\tau_{p,n}$ is the two-way traveling time of the signal from the nth antenna to the pth corner scatterer, and the term $w(m,n)$ models the contributions of scatterers other than corners, including the walls, humans, and possible multipath propagation effects. The canonical scattering response $S_p(m,n,\bar{\phi}_p)$ of the pth corner (dihedral) reflector with orientation angle $\bar{\phi}_p$ is given in (5.51).

5.6.2 Corner detection strategies

This section describes different matching techniques for estimation of the locations of the corner scatterer. Corners appear in building structures as a result of the right angle intersection between two walls. Recently, overcomplete dictionaries for sparse representation of corners from compressed observations have been proposed [100, 147], whose atom coefficients directly indicate the presence of building features at specific positions. Alternatively, image-based complex matched filters were proposed for image feature extraction under full data volume [150]. In this section, we review these two approaches and present the proposed correlogram matching procedure, where the prior knowledge of the corner scattering model is used as a correlogram template or reference for corner recognition.

Overcomplete dictionary for sparse scene representation

We assume that the corners can be located at any pixel of the image and all corners have the same orientation angle, which is determined by the oblique illumination under consideration. A sparsifying dictionary $\mathbf{\Lambda}$ based on possible dihedral locations can be then introduced with $N_x N_z$ columns. Each column is based on the response of a corner located at the corresponding pixel position. The corner response is modeled following eqn. (5.51). The linear relationship between the possible dihedral locations, represented by the column vector $\boldsymbol{\nu}$, and the reduced data measurements, $\check{\mathbf{y}}$, is given by,

$$\check{\mathbf{y}} = \mathbf{\Phi}\mathbf{\Lambda}\boldsymbol{\nu} \tag{5.55}$$

where $\mathbf{\Phi}$ is the measurement matrix that defines the compressed measurement strategy. CS recovers the sparse vector $\boldsymbol{\nu}$ from $\breve{\mathbf{y}}$ by solving the following optimization problem,

$$\min_{\boldsymbol{\nu}} \|\boldsymbol{\nu}\|_{l_1} \quad \text{subject to} \quad \|\breve{\mathbf{y}} - \mathbf{\Phi}\mathbf{\Lambda}\boldsymbol{\nu}\|_{l_2} \leq \epsilon \tag{5.56}$$

where $\|\boldsymbol{\nu}\|_{l_1} = \sum_i |\nu_i|$ and ϵ is the regularization parameter which bounds the allowed error in the resconstuction. Several methods are available in the literature to solve the optimization problem in (5.56), such as Basis Pursuit techniques [8, 10, 13] and greedy iterative methods [15, 16].

Image-based matched filter

Another possible approach is to directly match the reference image, obtained from the canonical corner data model, to the backprojection image obtained with the observations [150].

Let the complex amplitude values of the illuminated scene image obtained from the compressed measurements be denoted by $\breve{\mathbf{r}}$, and the values of the image corresponding to the compressed measurements of a canonical corner at position (k, l) be represented by $\breve{\mathbf{r}}^{\text{ref}}_{(k,l)}$. Then, the corner detection problem can be expressed as,

$$\min_{\beta(k,l)} \left\| \breve{\mathbf{r}}, \beta(k,l)\breve{\mathbf{r}}^{\text{ref}}_{(k,l)} \right\|^2_{l_2}. \tag{5.57}$$

The solution to (5.57) is given by,

$$\beta(k,l) = \frac{\left(\breve{\mathbf{r}}^{\text{ref}}_{(k,l)}\right)^H \breve{\mathbf{r}}}{\left(\breve{\mathbf{r}}^{\text{ref}}_{(k,l)}\right)^H \breve{\mathbf{r}}^{\text{ref}}_{(k,l)}}. \tag{5.58}$$

which is exactly the same solution provided in eqn. (3.26) by the candidate matching approach but applied in the image domain.

Correlogram matching

We propose the use of the correlogram for corner scatterer detection. For convenience, we use L_∞-norm to measure the distance between pixels, i.e., we define the distance between the pixels (k_1, l_1) and (k_2, l_2) as $\max\{|k_1 - k_2|, |l_1 - l_2|\}$. For a reference pixel, each distance defines a set of pixels equidistant from that pixel. Let the complex amplitudes corresponding to the set of N_p pixels located at distance d from the (k, l)th pixel be denoted as $\breve{r}^{(d)}(k_i, l_i)$, $i = 1, \ldots, N_p$. Then, the correlogram of the (k, l)th pixel is defined as,

$$\gamma^{(d)}_{(k,l)} \triangleq \frac{1}{N_p} \sum_{i=1}^{N_p} \breve{r}(k,l)\text{conj}(\breve{r}^{(d)}(k_i, l_i)) \tag{5.59}$$

where $\mathbf{conj}(\cdot)$ is the complex conjugate function. From (5.59), we can build the correlogram matrix as,

$$\hat{\mathbf{R}}_{(k,l)} \triangleq \begin{bmatrix} \gamma^{(d=0)}_{(k,l)} & \gamma^{(d=1)}_{(k,l)} & \cdots & \gamma^{(d=D-1)}_{(k,l)} \\ \mathbf{conj}(\gamma^{(d=1)}_{(k,l)}) & \gamma^{(d=0)}_{(k,l)} & \cdots & \gamma^{(d=D-2)}_{(k,l)} \\ \vdots & \vdots & \ddots & \vdots \\ \mathbf{conj}(\gamma^{(d=D-1)}_{(k,l)}) & \mathbf{conj}(\gamma^{(d=D-2)}_{(k,l)}) & \cdots & \gamma^{(d=0)}_{(k,l)} \end{bmatrix} \tag{5.60}$$

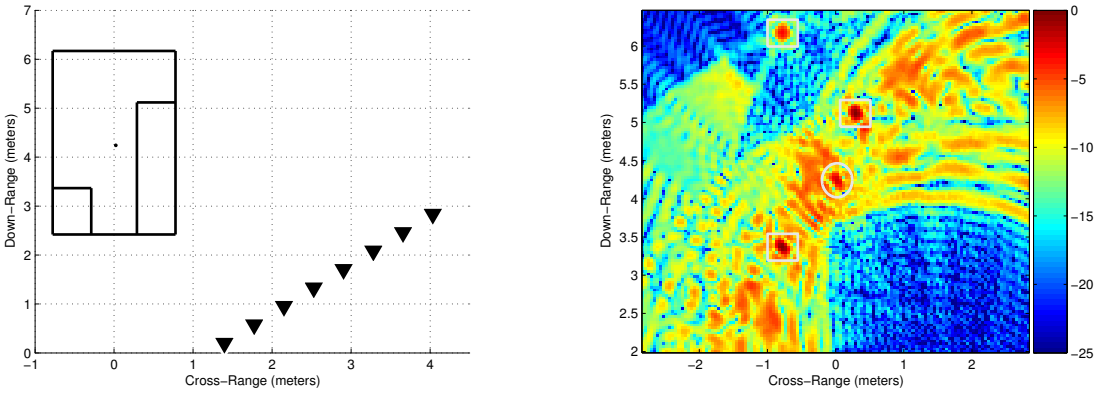

(a) (b)

FIGURE 5.51: (a) Geometry of the simulated scene, (b) Backprojection image of the scene considering the full data volume.

where D determines the dimension of the matrix. Note that $\hat{R}_{(k,l)}$ is positive semidefinite by definition.

The isolated presence of a canonical corner in the (k,l)th pixel will generate a particular reference correlogram matrix, which is denoted as $\mathbf{R}^{\text{ref}}_{(k,l)}$. The proposed procedure is based on a scan which reacts only when the reference scatterer is present. Based on this assumption, a similarity function is required to measure the reference corner contribution contained in the given sample correlogram matrix of each pixel. An estimate of the corner intensity level $\kappa(k,l)$ can be formulated as,

$$\max_{\kappa(k,l)\geq 0} \Psi\left(\hat{\mathbf{R}}_{(k,l)}, \kappa(k,l)\mathbf{R}^{\text{ref}}_{(k,l)}\right) \tag{5.61}$$

where $\Psi(\cdot,\cdot)$ is a similarity function between the two matrices. One choice for $\Psi(\cdot,\cdot)$ is the Frobenius norm of the error, which provided results similar to that obtained with (5.58).

As discussed earlier in this thesis, an alternative is a detector that best suits the space generated by hermitian matrices, and is derived by forcing a positive definite residual correlogram matrix $(\hat{\mathbf{R}}_{(k,l)} - \kappa(k,l)\mathbf{R}^{\text{ref}}_{(k,l)})$. That is,

$$\begin{aligned} \max_{\kappa(k,l)\geq 0} \quad & \kappa(k,l) \\ \text{s.t.} \quad & \hat{\mathbf{R}}_{(k,l)} - \kappa(k,l)\mathbf{R}^{\text{ref}}_{(k,l)} \succeq 0 \end{aligned} \tag{5.62}$$

As shown previously on section 3.5.2, the solution to (5.62) is given by the inverse of the maximum eigenvalue of $\hat{\mathbf{R}}^{-1}_{(k,l)}\mathbf{R}^{\text{ref}}_{(k,l)}$, that is,

$$\kappa_M(k,l) = \lambda^{-1}_{max}(\hat{\mathbf{R}}^{-1}_{(k,l)}\mathbf{R}^{\text{ref}}_{(k,l)}) \tag{5.63}$$

5.6.3 Simulation results

A stepped-frequency signal consisting of 335 frequencies covering the 1 to 2 GHz frequency band was used for interrogating the scene. The simulation employed a monostatic synthetic aperture radar (SAR) consisting of 8-element locations with an inter-element spacing of 53 cm

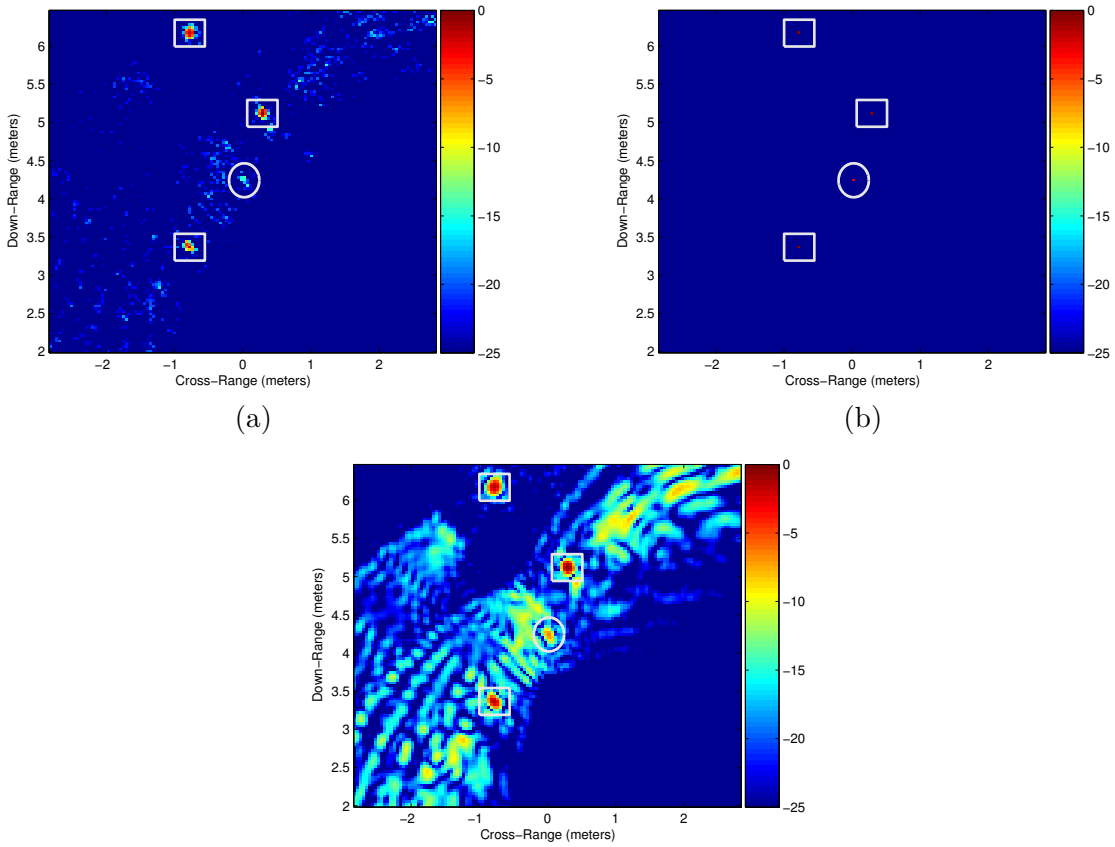

FIGURE 5.52: Resulting image for $\rho_f = 0.10$: (a) Correlogram matching - $\kappa_M(k,l)$, (b) CS-based reconstruction using overcomplete dictionary, (c) Image-based matched filter

(1.77λ where λ is the wavelength at 1 GHz). Conventional monostatic SAR theory assumes an antenna spacing smaller than 0.25λ in order to avoid grating lobes within the visible region -90° to +90°. For the simulated scene geometry of Fig. 5.51(a), the region of interest extends from -23° to +23°, which translates into a maximum antenna spacing equal to 0.36λ. Therefore, the antenna compression rate is $\rho_n = \frac{0.36\lambda}{1.77\lambda} = 0.2$. An oblique illumination of the scene is used to avoid wall returns while preserving the important corner features. The angular tilt of the SAR system is chosen to be 45° so that the corner response of (5.51) is maximized.

The system illuminates a building consisting of three rooms, as shown in Fig. 5.51(a). In the middle of the building, there is a point target located at (0.02,4.24)m, which emulates the presence of a human. The region to be scanned by the detector is the same as the region to be imaged and is chosen to be 5.64 (cross-range) × 4.45 (down-range) m^2, centered at (0, 4.23) m, and is divided into 128 × 128 pixels.

Fig. 5.51(b) shows the backprojection image corresponding to the measured scene, using all 335 frequencies. In this figure and all subsequent images in this section, we plot the image intensity with the maximum intensity value in each image normalized to 0dB. Although the corners are present in the images (indicated by white rectangles), it is difficult to discriminate the corners from the point target (indicated by white circle) and clutter contributions even when the full data set is considered.

For sparsity-based corner detection, we consider only 34 uniformly selected frequencies. Therefore, the frequency compression rate is $\rho_f = \frac{34}{335} = 0.10$. Fig. 5.52(a) shows the image obtained with the proposed correlogram matching approach. In particular, Fig. 5.52(a) gathers the values of $\kappa_M(k,l)$ for $D = 30$. Both true corner locations and the true point-like scatterer locations are indicated by white rectangles and white circle, respectively. Clearly, the image shown in Fig. 5.52(a) has less clutter compared to the corresponding backprojection image shown in Fig. 5.51(b). Moreover, the point target has been significantly diminished in Fig. 5.52(a) due to the positive semi-definite residual correlogram matrix restriction of the detector.

For comparison, Fig. 5.52(b) and Fig. 5.52(c) show the resulting image obtained with the CS-based reconstruction described in section 5.6.2 and the resulting image obtained with the image-based matching approach described in section 5.6.2, respectively. The iterative greedy algorithm known as Orthogonal Matching Pursuit (OMP) [17] was used for CS-based reconstruction, with $\epsilon = 10^{-6}$ used as the stopping criterion. We observe that the resulting image of the image-based matched filter approach, shown in Fig. 5.52(c), is much more cluttered than the image shown in Fig. 5.52(a), which underscores the importance of the positive semidefinite correlogram residual matrix condition. The sparsity-based reconstruction using overcomplete dictionary of possible corner locations, shown in Fig. 5.52(b), provides a very clean image with four dominant pixels, three of which correspond to the true corner locations (indicated by white rectangles), whereas the fourth represents a false corner at the human location (indicated by white circle).

The advantage of the proposed technique in terms of scatterer discrimination is confirmed by a comparison of the target-to-clutter-ratio (TCR), provided in Table 5.11. The TCR of an image $I(k,l)$ is defined as the ratio between the lowest pixel magnitude value of the true corner location area to the maximum pixel magnitude value of the clutter area,

$$TCR(I(k,l)) = 20\log_{10}\left(\frac{\min_{(k,l)\in A_t}|I(k,l)|}{\max_{(k,l)\in A_c}|I(k,l)|}\right). \tag{5.64}$$

where A_t and A_c are the corner and the clutter area, respectively. The corner area A_t contains the highest pixel values of the different detected corner areas, which are manually selected in close vicinity to the true corner positions (11×11 pixel rectangular box centered at the real corner position). The clutter area consists of the remaining pixels that are not included in the detected corner areas. Smaller values of TCR would increase the chance of misclassifications in subsequent thresholding-based detection schemes [84, 151]. From Table 5.11, we observe that the proposed method significantly surpasses the TCR values of its competitors, especially for large values of D, leading to an enhanced detection performance. The performance of the proposed method is clearly linked to the dimensionality of the correlogram matrix, which should be large enough to capture the image-domain response of a corner reflector. Increasing D adds more information to the correlogram matrix, resulting in higher TCR values as seen in Table 5.11. However, a higher D also increases the computational complexity and may infringe over neighboring corners.

5.6.4 Conclusion

In this section, we developed a correlogram matching corner detector for TWRI applications under reduced data volume. The correlogram of the scattering response of an isolated canonical corner reflector, which is known a priori, was compared with the correlogram of the

TABLE 5.11: TCR for $\rho_f = 0.10$

Method	**D=5**	**D=10**	**D=15**	**D=30**
Backprojection	-2.14 dB			
CS-based reconst.	5.58 dB			
Image-based match.	9.95 dB			
$\kappa_M(k,l)$	10.82 dB	14.42 dB	17.96 dB	23.65 dB

received radar image within a correlation matching framework. Simulation results demonstrated that the proposed method effectively detects the corner reflectors and outperforms its backprojection imaging, l_1-based reconstruction using overcomplete dictionaries, and image-based matched filter detector counterparts.

Chapter 6

Conclusion and Further Work

A summary and the main conclusions of the work performed in this thesis are provided in section 6.1. Finally, section 6.2 provides an outlook for possible future work.

6.1 Main conclusions

Based on the concept of matched filtering, this thesis proposed a generalized CS-based candidate detector for detecting predetermined candidate signals. The motivation of this work was the lack of solid and reliable detection strategies when dealing with signals contaminated with noise and interference signals. We showed that the interference immunity is achieve, in some cases, directly applying the candidate detector in the raw data domain either considering independent candidate matchings or jointly evaluating all possible hypothesis in a global unified optimization framework with CS-based reconstruction techniques. We examined both approaches for building interior structure detection in TWRI. The performance of the candidate detector was evaluated using real and synthetic data to demonstrate the effectiveness in wall and corner detection, while achieving substantial reduction in data volume.

One important drawback of the raw data domain is the difficulty on rejecting interference when the candidate signal is similar to the interference. The candidate detector formulated in correlation domain brings more tools to face the interference problem. In particular, the interference rejection capabilities can be strengthened with an appropriate choice of the matching error function in the matched filtering approach and through proper weighted sparsity constraint when solving the CS optimization problem. We examined both approaches for building interior structure detection in TWRI and for primary user detection in a cognitive radio framework. Supporting results based on MATLAB simulation were provided, which prove its feasibility in distinguishing between candidates and non-desired signals or scatterers.

6.2 Future work

Although the results presented in this thesis have demonstrated the effectiveness of the proposed CS-based candidate detector, many opportunities for extending the scope of this thesis remain. This section discusses some of the topics that we consider particularly interesting for extension.

- **Non-ideal channel propagation:** The impact of fading channels on the detector performance could be more extensively analyzed. Thus far, the performance of the detector has been analyzed through computer simulation for Ricean channel realizations. Evaluate the detector performance over more realistic channels (with fast fading or shadowing phenomenon) or considering the availability of imperfect channel estimation would be of great interest.

- **Close expressions for detection performance:** Another point to be further studied is the theoretical derivation of the threshold to be applied at the detector. For a good detection algorithm, the probability of detection should be high and the probability of false alarm should be low, which usually depends on the choice of the threshold. Throughout this thesis, computer simulations were used for evaluating the detection capabilities of the proposed detector. In the future, it would be interesting to spend more time to find close expressions of the probability distributions of each detection hypothesis.

- **The use of other CS-based reconstruction algorithms:** The work presented in this thesis have only focused on iterative CS-based reconstruction algorithms. The use of different reconstruction strategies which may improve the performance of the detector could be subject of further studies.

- **Stopping rule for iterative algorithms:** Regarding the stopping criteria proposed for the candidate detector using CS-based reconstruction, it is worth mentioning that the stopping criteria has an important impact on the final performance. Thus, focusing attention on the definition of a proper stopping criterion should be subject of further research.

- **Quantify the similarity of the interference signal:** It is clear that the performance of the proposed detector is significantly degraded when the interference signal show a high similarity with the candidate. In the future, it would be interesting to quantify this similarity with a metric.

- **Design of the sensing matrix:** An interesting problem in CS consist of designing a convenient measurement matrix $\mathbf{\Phi}$ such that salient information in any compressible signal is not damaged by the dimensionality reduction. The work presented in this thesis thus far assumed that $\mathbf{\Phi}$ is drawn at random. The CS reconstruction performance can be substantially improved by optimizing the choice of $\mathbf{\Phi}$ [18].

Bibliography

[1] S. Kirolos, J. Laska, M. Wakin, M. Duarte, D. Baron, T. Ragheb, Y. Massoud, and R. Baraniuk, "Analog-to-Information Conversion via Random Demodulation," *IEEE Dallas Circuits and Systems Workshop (DCAS)*, pp. 71–74, Oct, 2006.

[2] M. Mishali and Y. C. Eldar, "From Theory to Practice: Sub-Nyquist sampling of Sparse Wideband Analog Signals," *IEEE Journal of Selected Topics on Signal Processing*, vol. 4, no. 2, pp. 375–391, Apr, 2010.

[3] T. Yucek and H. Arslan, "A Survey of Spectrum Sensing Algorithms for Cognitive Radio Applications," *IEEE Communications Surveys and Tutorials*, vol. 11, no. 1, pp. 116–130, 2009.

[4] C. E. Shannon, "Communication in the presence of noise," *Proc. Institute of Radio Engineers*, vol. 37, no. 1, pp. 10–21, Jan, 1949.

[5] M. Unser, "Sampling: 50 Years After Shannon," *Procedings of the IEEE*, vol. 88, no. 4, pp. 569–587, 2000.

[6] J. A. Tropp, J. N. Laska, M. F. Duarte, J. K. Romberg, and R. G. Baraniuk, "Beyond Nyquist: Efficient Sampling of Sparse Bandlimited Signals," *IEEE Transactions on Information Theory*, vol. 56, no. 1, pp. 520–544, Jan, 2010.

[7] D. Donoho, "Compressed Sensing," *IEEE Trans. Inf. Theory*, vol. 52, no. 4, pp. 1289–1306, Apr, 2006.

[8] E. J. Candes, J. Romberg, and T. Tao, "Robust Uncertainty Principles: Exact Signal Reconstruction From Highly Incomplete Frequency Information," *IEEE Trans. Inf. Theory*, vol. 52, no. 2, pp. 489–509, 2006.

[9] E. J. Candes and M. B. Wakin, "An Introduction to Compressed Sampling," *IEEE Signal Processing Magazine*, vol. 25, no. 2, pp. 21–30, March, 2008.

[10] E. J. Candes and T. Tao, "Near Optimal Signal Recovery from Random Projections: Universal Encoding Strategies," *IEEE Transactions on Information Theory*, vol. 52, no. 12, pp. 5406–5425, Dec, 2006.

[11] Y. C. Eldar, *Compressed Sensing: Theory and Applications.* Cambridge University Press, 2012.

[12] M. Aharon, M. Elad, and A. Bruckstein, "K-SVD: An Algorithm for Designing Overcomplete Dictionaries for Sparse Representation," *IEEE Trans. Signal Process.*, vol. 54, no. 11, pp. 4311–4322, Nov, 2006.

[13] S. S. Chen, D. L. Donoho, and M. A. Saunders, "Atomic Decomposition by Basis Pursuit," *SIAM Journal on Scientific Computing*, vol. 20, no. 1, pp. 33–61, 1999.

[14] S. Boyd and L. Vandenberghe, *Convex Optimization.* Cambridge University Press, 2004.

[15] S. G. Mallat and Z. Zhang, "Matching Pursuits with Time-Frequency Dictionaries," *IEEE Trans. Signal Process.*, vol. 41, no. 12, pp. 3397–3415, Dec, 1993.

[16] J. A. Tropp, "Greed is Good: Algorithmic Results for Sparse Approximation," *IEEE Transactions on Information Theory*, vol. 50, no. 10, pp. 2231–2242, Oct, 2004.

[17] J. A. Tropp and A. C. Gilbert, "Signal Recovery From Random Measurements Via Orthogonal Matching Pursuit," *IEEE Transactions on Information Theory*, vol. 53, no. 12, pp. 4655–4666, Dec, 2007.

[18] M. Elad, "Optimized Projections for Compressed Sensing," *IEEE Trans. Signal Process.*, vol. 55, no. 12, pp. 5695–5702, Dec, 2007.

[19] ——, *Sparse and Redundant Representations: From Theory to Applications in Signal and Image Processing.* Springer, 2010.

[20] M. Aharon, "Overcomplete Dictionaries for Sparse Representation of Signals," *Ph.D. thesis, Technion, Israel*, Nov, 2006.

[21] E. Candes, Y. Eldar, D. Needell, and P. Randall, "Compressed Sensing with Coherent and Redundant Dictionaries," *Applied and Computational Harmonic Analysis*, vol. 31, no. 1, pp. 59–73, 2010.

[22] Y. C. Pati, R. Rezaiifar, and P. S. Krishnaprasad, "Orthogonal Matching Pursuit: Recursive Function Approximation with Applications to Wavelet Decomposition," 27^{th} *Asilomar Conference on Signals, Systems and Computers*, vol. 1, pp. 40–44, Nov, 1993.

[23] D. Donoho, Y. Tsaig, I. Drori, and J. Starck, "Sparse Solution of Under-Determined Linear Equations of Stagewise Orthogonal Matching Pursuit," *Technical Report, Department of Statistics, Stanford University*, 2006.

[24] T. Blumensath and M. Davies, "Gradient Pursuits," *IEEE Trans. Signal Process.*, vol. 56, no. 6, pp. 2370–2382, Jun, 2008.

[25] J. Tropp and D. Needell, "CoSaMP: Iterative Signal Recovery from Incomplete and Inaccurate Samples," *Applied and Computational Harmonic Analysis*, vol. 26, no. 3, pp. 301–321, Apr, 2008.

[26] R. Tibshirani, "Regression Shrinkage and Selection via the Lasso," *Journal of the Royal Statistical Society*, vol. 58, no. 1, pp. 267–288, 1996.

[27] D. Donoho, M. Elad, and V. Temlyakov, "Stable Recovery of Sparse Overcomplete Representations in the Presence of Noise," *IEEE Trans. Inf. Theory*, vol. 52, no. 1, pp. 6–18, Jan, 2006.

[28] E. J. Candes and T. Tao, "The Dantzig Selector: Statistical Estimation when p is much larger than n," *Annals of Statistics*, vol. 35, no. 6, pp. 2313–2351, Dec, 2007.

[29] P. Boufounos, M. Duarte, and G. Baraniuk, "Sparse Signal Reconstruction from Noisy Compressive Measurements using Cross Validation," *IEEE Workshop on Statistical Signal Processing (SSP), Madison, WI, USA*, pp. 299–303, Aug, 2007.

[30] M. Lopes, "Estimating Unknown Sparsity in Compressed Sensing," *Int. Conf. Machine Learning, Atlanta, Georgia, USA*, 2013.

[31] E. J. Candes, J. Romberg, and T. Tao, "Stable Signal Recovery from Incomplete and Inaccurate Measurements," *Comm. on Pure and Applied Mathematics*, vol. 59, no. 8, pp. 1207–1223, Aug, 2006.

[32] M. Davenport, P. Boufounos, and R. Baraniuk, "Compressive Domain Interference Cancellation," *Signal Processing with Adaptive Sparse Structured Representations (SARS)*, Mar, 2009.

[33] Z. Wang, G. Arce, B. Sadler, J. Paredes, S. Hoyos, and Z. Yu, "Compressed UWB Signal Detection with Narrowband Interference Mitigation," *IEEE Int. Conf. UWB (ICUWB)*, Sep, 2008.

[34] J. Laska, M. Davenport, and R. Baraniuk, "Exact Signal Recovery from Sparsely Corrupted Measurements Through the Pursuit of Justice," *Asilomar Conf.*, Nov, 2009.

[35] E. Candes, M. Wakin, and S. Boyd, "Enhancing Sparsity by Reweighted l_1 Minimization," *Journal Fourier Analysis and Applications*, vol. 14, no. 5–6, pp. 877–905, Oct, 2008.

[36] M. Asif and J. Romberg, "Fast and Accurate Algorithms for Re-Weighted l_1 Norm Minimization," *under review at IEEE Trans. Signal Process.*, Jul, 2012.

[37] P. Feng, "Universal Minimum-Rate Sampling and Spectrum-Blind Reconstruction for Multiband Signals," *PhD, University of Illinois at Urbana-Champaign, USA*, 1997.

[38] R. Venkataramani and Y. Bresler, "Optimal Sub-Nyquist Nonuniform Sampling and Reconstruction for Multiband Signals," *IEEE Signal Processing Letters*, vol. 18, no. 8, pp. 443Ű–446, Aug, 2011.

[39] M. Mishali, Y. Eldar, O. Dounaevsky, and E. Shoshan, "Xampling: Analog to Digital at sub-Nyquist Rates," *IET Cir. Dev. and Systems*, vol. 5, no. 1, pp. 8–20, Jan, 2011.

[40] M. Herman and T. Strohmer, "High-resolution radar via compressed sensing," *IEEE Trans. Signal Process.*, vol. 57, no. 6, pp. 2275–2284, Jun,2009.

[41] M. Lustig, D. Donoho, and J. Pauly, "Sparse MRI: The Application of Compressed Sensing for Rapid MR Imaging," *Magnetic Resonance in Medicine*, vol. 58, no. 6, pp. 1182–1195, Dec, 2007.

[42] W. Tang, J. Ma, and F. Herrmann, "Optimized Compressed Sensing for Curvelet-based Seismic Data Reconstruction," *Preprint*, 2009.

[43] F. C. Commission, "Tech. Report," *TR 02-155*, Nov, 2002.

[44] J. I. Mitola and G. J. Maguire, "Cognitive radio: making software radios more personal," *IEEE Personal Communications*, vol. 6, no. 4, pp. 13–18, Aug, 1999.

[45] J. Mitola, "An integrated agent architecture for software defined radio," Ph.D. dissertation, Royal Institute of Technology (KTH), May, 2000.

[46] I. Akyildiz, B. F. Lo, and R. Balakrishnan, "Cooperative spectrum sensing in cognitive radio networks: A survey," *ELSEVIER Physical Communication*, vol. 4, pp. 40–Ű62, 2011.

[47] Z. Tian and G. B. Giannakis, "Compressed Sensing for Wideband Cognitive Radios," *International Conference on Acoustics, Speech and Signal Processing (ICASSP), Las Vegas, NV*, pp. 1357–1360, May, 2008.

[48] A. Sahai and D. Cabric, "Spectrum Sensing: Fundamental Limits and Practical Challenges," *IEEE Int. Symp. New Frontiers Dynamic Spectrum Access Networks (DySPAN), Baltimore, MD, USA*, Nov, 2005.

[49] R. Tandra and A. Sahai, "Fundamental Limits on Detection in Low SNR under Noise Uncertainty," *Int. Conf. Wireless Net., Comm. and Mobile Comp., Maui, HI, USA*, Jun, 2005.

[50] D. Cabric, S. M. Mishra, and R. W. Brodersen, "Implementation issues in Spectrum Sensing for Cognitive Radios," *Asilomar Conference on Signals, Systems and Computers*, vol. 1, pp. 772–776, Nov, 2004.

[51] H. Urkowitz, "Energy Detection of Unknown Deterministic Signals," *Proceedings of the IEEE*, vol. 55, pp. 523–531, Apr, 1967.

[52] W. Gardner, "Signal Interception: A Unifying Theoretical Framework for Feature Detection," *IEEE Transactions on Communications*, vol. 36, pp. 897–906, Aug, 1988.

[53] W. Gardner, A. Napolitano, and L. Paura, "Cyclostationarity: Half a century of Research," *Elsevier Signal Processing*, vol. 86, pp. 639–697, Apr, 2006.

[54] M. Haddad, A. Hayar, H. Fetoui, and M. Debbah, "Cognitive Radio Sensing Information Theoretic Criteria Based," *Cognitive Radio Oriented Wireless Net. and Com. (CrownCom), Orlando, USA*, 2007.

[55] B. Zayen, A. Hayar, and K. Kansanen, "Blind Spectrum Sensing for Cognitive Radio based on Signal Space Dimension Estimation," *IEEE Int. Conf. on Communications (ICC), Dresden, Germany*, 2009.

[56] B. Zayen and A. Hayar, "A Performance Study of Kullback-Leibler Distance-Based Spectrum Sensing Algorithm," *EURASIP Journal on Wireless Communications and Networking, 2012:64*, Feb, 2012.

[57] H. Akaike, "Information Theory and Extension of the Maximum Likelihood Principle," *Int. Symp. Information Theory, Budapest, Hungary*, 1973.

[58] Y. Zeng and Y. C. Liang, "Eigenvalue-Based Spectrum Sensing Algorithms for Cognitive Radio ," *IEEE Trans. Communications*, vol. 57, no. 6, pp. 1784–1793, Jun, 2009.

[59] R. Schmidt, "Multiple Emitter Location and Parameter Estimation," *IEEE Trans. Antennas and Propagation*, vol. 34, no. 3, pp. 276–280, Mar, 1986.

[60] I. Ziskind and M. Wax, "Maximum Likelihood Localization of Multiple Sources by Alternating Projection," *IEEE Trans. Acoustics, Speech and Signal Processing*, vol. 36, no. 10, pp. 1553–1560, Oct, 1988.

[61] X. Wang, G. Arce, B. Sadler, J. Paredes, and X. Ma, "Compressed Detection for Pilot Assisted Ultra-Wideband Impulse Radio," *IEEE International Conference on UWB*, pp. 393–398, Sept, 2007.

[62] D. Sundman, S. Chatterjee, and M. Skoglund, "On the use of Compressive Sampling for Wide-Band Spectrum Sensing," *IEEE Int. Sym. on Sig. Proc. and Inf. Tech., Luxor, Egypt*, Dec, 2010.

[63] Y. L. Polo, Y. Wang, A. Pandharipande, and G. Leus, "Compressive Wide-Band Spectrum Sensing," *International Conference on Acoustics, Speech and Signal Processing (ICASSP), Taipei*, pp. 2337–Ű2340, Apr, 2009.

[64] Y. Wang, Z. Tian, and C. Feng, "A Two-Step Compressed Spectrum Sensing Scheme for Wideband Cognitive Radios," *IEEE Global Telecommunications Conference (GLOBECOM)*, pp. 1–5, Jan, 2010.

[65] M. Rashidi, K. Haghighi, A. Owrang, and M. Viberg, "A Wideband Spectrum Sensing Method for Cognitive Radio using Sub-Nyquist Sampling," *IEEE Signal Processing Society 14th DSP Workshop, 6th SPE Workshop, Arizona, USA*, 2010.

[66] M. A. Lexa, M. E. Davies, J. S. Thompson, and J. Nikolic, "Compressive Power Spectral Density Estimation," *International Conference on Acoustics, Speech and Signal Processing (ICASSP)*, pp. 3884–3887, May, 2011.

[67] M. G. Amin and F. Ahmad, "Wideband Synthetic Aperture Beamforming for Through-the-Wall Imaging," *IEEE Signal Process. Mag.*, vol. 25, no. 4, pp. 110–113, Jul, 2008.

[68] M. G. Amin, "Through-the-Wall Radar Imaging," *CRC Press*, 2010.

[69] M. G. Amin, K. Sarabandi, and (Eds), "Remote Sensing of Building Interior," *IEEE Trans. Geoscience and Remote Sensing*, vol. 47, no. 5, pp. 1270–1420, May, 2009.

[70] F. Soldovieri and R. Solimene, "Through-Wall Imaging Via a Linear Inverse Scattering Algorithm," *IEEE Geosci. Remote Sens. Letters*, vol. 4, no. 4, pp. 513–517, Oct, 2007.

[71] H. Burchett, "Advances in Through Wall Radar for Search, Rescue and Security Applications," *Inst. of Eng. and Tech. Conf. Crime and Security, London, UK*, pp. 511–525, Jun, 2006.

[72] M. G. Amin, "Advances in Indoor Radar Imaging," *Journal of Franklin Institute*, vol. 345, no. 6, pp. 556–722, Sep, 2008.

[73] E. Ertin and R. Moses, "Through-the-Wall SAR Attributed Scattering Center Feature Estimation," *IEEE Trans. Geosci. Remote Sens.*, vol. 47, no. 5, pp. 1338–1348, May, 2009.

[74] A. Martone, K. Ranney, and R. Innocenti, "Automatic Through the Wall Fetection of Moving Targets Using Low-Frequency UWB Radar," *IEEE Int. Radar Conference, Washington D.C., USA*, May, 2010.

[75] F. Soldovieri, R. Solimene, and R. Pierri, "A simple strategy to detect changes in through the wall imaging," *Progress in Electromagnetics Research M*, vol. 7, pp. 1–13, 2009.

[76] F. Ahmad and M. G. Amin, "Matched-Illumination Waveform Design for a Multistatic Through-the-Wall Radar System," *IEEE Journal on Selected Topics in Signal Processing*, vol. 4, no. 1, pp. 177–186, Dec, 2009.

[77] C. Thajudee, W. Zhang, and A. Hoorfar, "Time-Domain Wall Parameter Estimation and Mitigation for Through-the-Wall Radar Image Enhancement," *Progress In Electromagnetics Research Symposium, Cambridge, USA*, Jul, 2010.

[78] C. Thajudee, A. Hoorfar, and W. Zhang, "Estimation of Frequency-Dependent Parameters of Unknown Walls for Enhanced Through-the-Wall Imaging," *IEEE Int. Symp. Antennas and Propagation AP-S/URSI*, Jul, 2011.

[79] Y. S. Yoon and M. Amin, "Spatial Filtering for Wall-Clutter Mitigation in Through-the-Wall Radar Imaging," *IEEE Trans. Geoscience and Remote Sensing*, vol. 47, no. 9, pp. 3192–3208, Sep, 2009.

[80] F. Tivive, A. Bouzerdoum, and M. Amin, "An SVD-Based Approach for Mitigating Wall Reflections in Through-the-Wall Radar Imaging," *IEEE Int. Radar Conference, Kansas City, USA*, pp. 519–524, May, 2011.

[81] P. Setlur, F. Ahmad, M. Amin, and P. Zemany, "Experiments on Through-the-Wall Motion Detection and Ranging," *SPIE Command, Control, Comm. and Intelligence (C3I) Tech. Homeland Security and Defense, Orlando, FL*, vol. 6538, Apr, 2007.

[82] P. Setlur, M. Amin, and T. Thayaparan, "Micro-Doppler Signal Estimation for Vibrating and Rotating Targets," *Int. Symp. Signal Processing and Its Applications, Sydney, Australia*, Aug, 2005.

[83] P. Setlur, M. Amin, and F. Ahmad, "Analysis of Micro-Doppler Signals Using Linear FM Basis Decomposition," *SPIE Symp. Defense and Security, Orlando, FL, USA*, 2006.

[84] C. Debes, M. G. Amin, and A. M. Zoubir, "Target Detection in Single-and Multiple-View Through-The-Wall Radar Imaging," *IEEE Trans. Geosci. Remote Sens.*, vol. 47, no. 5, pp. 1349–1361, May, 2009.

[85] E. Lavely, Y. Zhang, E. Hill III, Y. Lai, P. Weichman, and A. Chapman, "Theoretical and experimental study of through-wall microwave tomography inverse problems," *J. Franklin Inst.*, vol. 345, no. 6, pp. 592–617, 2008.

[86] M. Nikolic, M. Ortner, A. Nehorai, and A. Djordjevic, "An Approach to Estimating Building Layouts Using Radar and Jump-Diffusion Algorithm," *IEEE Trans. Antennas and Propag.*, vol. 57, no. 3, pp. 768–776, Mar, 2009.

[87] G. Hickman and J. Krolik, "A Graph-Theoretic Approach to Constrained Floor Plan Estimation From Radar Measurements," *IEEE Trans. Signal Process.*, vol. 57, no. 5, pp. 1877–1888, May, 2009.

[88] C. Le, T. Dogaru, L. Nguyen, and M. Ressler, "Ultrawideband (uwb) radar imaging of building interior: Measurements and predictions," *IEEE Trans. Geosci. Remote Sens.*, vol. 47, no. 5, pp. 1409–1420, May, 2009.

[89] N. Subotic, E. Keydel, J. Burns, A. Morgan, K. Cooper, B. Thelen, B. Wilson, W. Williams, S. McCarty, B. Lampe, B. Mosher, and D. Setterdahl, "Parametric reconstruction of internal building structures via canonical scattering mechanisms," *IEEE Int. Conf. Acoustics, Speech and Signal Processing (ICASSP), Las Vegas, USA*, 2008.

[90] M. Aftanas and M. Drutarovsky, "Imaging of the Building Contours with Through the Wall UWB Radar System," *Radioengineering Journal*, vol. 18, no. 3, pp. 258–264, 2009.

[91] P. Sevigny and D. DiFilippo, "A Multi-Look Fusion Approach to Through-Wall Radar Imaging," *IEEE Radar Conference, Ottawa, Canada*, Apr, 2013.

[92] A. Hunt, "Use of a Frequency-Hopping Radar for Imaging and Motion Detection Through Walls," *IEEE Trans. Geoscience and Remote Sensing*, vol. 47, pp. 1402–1408, May, 2009.

[93] F. Ahmad and M. G. Amin, "Multi-location Wideband Synthetic Aperture Imaging for Urban Sensing Applications," *Journal of the Franklin Institute*, vol. 345, no. 6, pp. 618–639, 2008.

[94] M. Amin and F. Ahmad, "Compressive Sensing for Through-the-Wall Radar Imaging," *SPIE Journal of Electronic Imaging*, vol. 22, no. 3, Jul, 2013.

[95] Y. Yoon and M. G. Amin, "Compressed Sensing Technique for High-Resolution Radar Imaging," *Proc. SPIE*, vol. 6968, pp. 69 681A–1–69 681A–10, 2008.

[96] Q. Huang, L. Qu, B. Wu, and G. Fang, "UWB Through-Wall Imaging based on Compressive Sensing," *IEEE Trans. Geosci. Remote Sens.*, vol. 48, no. 3, pp. 1408–1415, 2010.

[97] Y. Yoon and M. G. Amin, "Through-the-Wall Radar Imaging Using Compressive Sensing Along Temporal Frequency Domain," *IEEE Int. Conf. Acoustics, Speech and Signal Processing (ICASSP), Dallas, USA*, Mar, 2010.

[98] M. Leigsnering, C. Debes, and A. Zoubir, "Compressive Sensing in Through-the-Wall Radar Imaging," *IEEE Int. Conf. Acoustics, Speech and Signal Processing (ICASSP), Prague, Czech Republic*, pp. 4008–4011, 2011.

[99] A. C. Gurbuz, J. McClellan, and W. Scott, "Compressive Sensing of underground structures using GPR," *Digital Signal Processing*, vol. 22, no. 1, pp. 66–73, Jan, 2012.

[100] W. van Rossum, J. de Wit, and R. Tan, "Radar Imaging of Building Interiors using Sparse Reconstruction," *European Radar Conference (EuRAD), Amsterdam, Netherlands*, Nov,2012.

[101] R. Tan, J. de Wit, and W. van Rossum, "Radar mapping of building structures applying sparse reconstruction," *1st Int. Workshop on Compressed Sensing applied to Radar, Bonn, Germany*, May, 2012.

[102] A. Gurbuz, J. McClellan, and W. Scott, "A Compressive Sensing Data Acquisition and Imaging Method for Stepped Frequency GPRs," *IEEE Trans. Signal Process.*, vol. 57, no. 7, pp. 2640–2650, Jul, 2009.

[103] H. Landau, "Necessary density conditions for sampling and interpolation of certain entire functions," *Acta Math.*, vol. 117, no. 81, pp. 37Ű–52, 1967.

[104] J. Duarte-Carvajalino and G. Sapiro, "Learning to sense sparse signals: Simultaneous sensing matrix and sparsifying dictionary optimization," *Image Processing, IEEE Transactions on*, vol. 18, no. 7, pp. 1395–1408, 2009.

[105] P. Feng and Y. Bresler, "Spectrum-blind Minimum-rate Sampling and Reconstruction of Multiband Signals," *Inter. Conf. on Acoustics, Speech, and Signal Processing*, vol. 3, pp. 1688Ű–1691, 1996.

[106] M. Davenport, P. Boufounos, M. Wakin, and R. Baraniuk, "Signal Processing With Compressive Measurements," *IEEE J. Sel. Topics Signal Process.*, vol. 4, no. 2, pp. 445–460, Apr, 2010.

[107] F. Back, R. Jenatton, J. Mairal, and G. Obozinski, "Optimization with Sparsity-Inducing Penalties," *Foundations and Trends in Machine Learning*, vol. 4, no. 1, pp. 1–106, 2012.

[108] J. Haupt and R. Nowak, "Signal Reconstruction from Noisy Random Projections," *IEEE Trans. on Inf. Theory*, vol. 52, no. 9, pp. 4036–4048, 2006.

[109] J. Boutros, F. Hharrat, and H. Randriambololona, "A Classification of Multiple Antenna Channels," *Int. Zurich Seminar Communications (IZS)*, pp. 14–17, Feb, 2006.

[110] O. Escoda, L. Granai, and P. Vandergheynst, "On the Use of a Priori Information for Sparse Signal Approximations," *IEEE Trans. Sig. Process.*, vol. 54, no. 9, pp. 3468–3482, Sep, 2006.

[111] M. Rojas, A. Pérez-Neira, and M. Lagunas, "DVB-T Candidate Power Detector for Cognitive Radio," *European Signal Processing Conference (EUSIPCO), Glasgow, Scotland*, Aug, 2009.

[112] M. Lagunas, A. Pérez-Neira, P. Stoica, and M. Rojas, "Spectrum Labeling for Cognitive Radio Systems: Candidate Spectral Estimation," *IAPR Workshop on Cognitive Information Processing (CIP), Santorini, Greece*, Jun, 2008.

[113] M. Lagunas, M. Rojas, and P. Stoica, "New Spectral Estimation Based on Filterbank for Spectrum Sensing," *IEEE Int. Conf. Acoustics, Speech and Signal Processing (ICASSP), Las Vegas, USA*, Apr, 2008.

[114] A. Pérez-Neira, M. Lagunas, M. Rojas, and P. Stoica, "Correlation Matching Approach for Spectrum Sensing in Open Spectrum Communications," *IEEE Trans. Signal Process.*, vol. 57, no. 12, pp. 4823–4836, Dec, 2009.

[115] W. Stutzman and G. Thiele, *Antenna Theory and Design.* John Wiley and Sons, New York, USA, 1981.

[116] P. D. Welch, "The use of FFT for the estimation of power spectra: A method based on time averaging over short modified periodograms," *IEEE Trans. Audio Electroacustic*, vol. AU-15, no. 2, pp. 70–73, Jun, 1967.

[117] M. van Rossum, "A novel spike distance," *Neural Computation*, vol. 13, no. 4, pp. 751–763, Apr, 2001.

[118] A. Moreira, P. Prats-Iraola, M. Younis, G. Krieger, I. Hajnsek, and K. Papathanassiou, "A tutorial on synthetic aperture radar," *IEEE Geoscience and Remote Sensing Magazine*, vol. 1, no. 1, pp. 6–43, 2013.

[119] M. Amin, *Through-the-Wall Radar Imaging.* CRC Press, 2010.

[120] C. Balanis, *Antenna Theory: Analysis and Design.* John Wiley and Sons, New York, USA, 2005.

[121] M. Martone, *Multiantenna Digital Radio Transmission.* Artech House, Boston, USA, 2002.

[122] Y. Yang, "See-Through-Wall Imaging using Ultra Wideband Short-Pulse Radar System," *IEEE Antennas and Propagation Society International Symposium, Washington D.C., USA*, Jul, 2005.

[123] Y. Lo, "A Mathematical Theory of Antenna Arrays with Randomly Spaced Elements," *IEEE Trans. Antenna Propag.*, vol. AP-12, pp. 257–268, 1964.

[124] H. Unz, "Linear Arrays with Arbitrarily Distributed Elements," *IEEE Trans. Signal Process.*, vol. AP-8, pp. 222–223, Mar, 1960.

[125] R. Harington, "Sidelobe Reduction by Nonuniform Element Spacing," *IEEE Trans. Signal Process.*, vol. AP-9, pp. 187–192, Mar, 1961.

[126] L. Carin, "On the Relationship Between Compressive Sensing and Random Sensor Arrays," *IEEE Antennas Propag. Mag.*, vol. 51, no. 5, pp. 72–81, Oct, 2009.

[127] M. Rossi, A. Haimovich, and Y. Eldar, "Global Methods for Compressive Sensing in MIMO Radar with Distributed Sensors," *Asilomar Conf. Signals, Systems and Computers, Pacific Grove, California*, Nov, 2011.

[128] M. Dehmollaian and K. Sarabandi, "Through-The-Wall Imaging: Measurement and Modeling Techniques," *IEEE International Geoscience and Remote Sensing Symposium*, Jul, 2008.

[129] A. Chandra, D. Gaikwad, D. Singh, and M. Nigam, "An Approach to Remove the Clutter and Detect the Target for Ultra-Wideband Through-Wall Imaging," *Journal of Geophysics and Engineering*, vol. 5, no. 4, pp. 412–419, 2008.

[130] F. Tivive, M. Amin, and A. Bouzerdoum, "Wall Clutter Mitigation Based on Eigen-Analysis in Through-The-Wall Radar Imaging," *Int Conf. Digital Signal Process., Corfu, Greece*, pp. 1–8, Jul, 2011.

[131] M. Dehmollaian and K. Sarabandi, "Analytical, Numerical, and Experimental Methods for Through-the-Wall Radar Imaging," *IEEE Int. Conf. Acoustics, Speech and Signal Processing (ICASSP), Las Vegas, USA*, Apr, 2008.

[132] Y. C. Eldar, "Analog Compressed Sensing," *IEEE International Conference on Acoustics, Speech and Signal Processing*, pp. 2949–2952, Apr, 2009.

[133] S. Mallat, "A Wavelet Tour of Signal Processing," *Academic Press, 3rd edition*, Dec, 2008.

[134] F. Ahmad and M. G. Amin, "Partially Sparse Reconstruction of Behind-the-Wall Scenes," *Proc. SPIE Symp. Defense, Security, and Sensing, Compressive Sensing Conference, Baltimore, MD*, vol. 8365, Apr, 2012.

[135] P. Setlur, M. Amin, and F. Ahmad, "Multipath Model and Exploitation in Through-the-Wall and Urban Radar Sensing," *IEEE Trans. Geosci. Remote Sens.*, vol. 49, no. 10, pp. 4021–4034, Oct, 2011.

[136] T. Dogaru and C. Le, "SAR Images of Rooms and Buildings based on FDTD Computer Models," *IEEE Trans. Geosci. Remote Sens.*, vol. 47, no. 5, pp. 1388–1401, May, 2009.

[137] R. Burkholder, "Electromagnetic Models for Exploiting Multi-Path Propagation in Through-Wall Radar Imaging," *Int. Conf. Electromagnetics in Advanced Applications (ICEAA), Torino, Italy*, Sep, 2009.

[138] Y. Rubner, C. Tomasi, and L. Guibas, "A Metric for Distributions with Applications to Image Databases," *IEEE Int. Conf. Computer Vision, Bombay, India*, Jan, 1998.

[139] Y. Rubner, "Perceptual Metrics for Image Database Navigation," *Ph.D. thesis, Stanford University, USA*, May, 1999.

[140] R. Gupta, P. Indyk, and E. Price, "Sparse Recovery for Earth Mover Distance," *Conf. Communication, Control, and Computing (Allerton)*, Sep, 2010.

[141] K. Krueger, J. McClellan, and W. Scott, Jr., "3-D imaging for groung penetrating radar using compressive sensing with block-toeplitz structures," *IEEE 7th Sensor Array and Multichannel Signal Process. Workshop, Hoboken, NJ*, Jun, 2012.

[142] Y. Rubner and C. Tomasi, "Texture Metrics," *IEEE Int. Conf. Systems, Man. and Cybernetics, San Diego, CA, USA*, Oct, 1998.

[143] E. J. Candes, J. Romberg, and T. Tao, "Stable Signal Recovery from Incomplete and Inaccurate Measurements," *Communications on Pure and Applied Mathematics*, vol. 59, no. 8, pp. 1207–1223, 2006.

[144] Z. Ben-Haim and Y. Eldar, "Coherence-Based Performance for Estimating a Sparse Vector under Random Noise," *IEEE Trans. Signal Process.*, vol. 58, pp. 5030–5043, Oct, 2010.

[145] R. Gonzalez and R. Woods, *Digital Image Processing.* Third Edition, Prentice Hall, 2008.

[146] M. Gerry, L. Potter, I. Gupta, and A. van der Merwe, "A Parametric Model for Synthetic Aperture Radar Measurements," *IEEE Trans. Antennas and Propagation*, vol. 47, no. 7, pp. 1179–1188, jul, 1999.

[147] E. Lagunas, M. Amin, F. Ahmad, and M. Najar, "Determining Building Interior Structures Using Compressive Sensing," *SPIE Journal of Electronic Imaging*, vol. 22, no. 2, p. 021003, 2013.

[148] J. Huang, S. Kumar, M. Mitra, W. Zhu, and R. Zabih, "Image Indexing Using Color Correlograms," *IEEE Conf. Computer Vision and Pattern Recognition, San Juan, Puerto Rico*, pp. 762–768, Jun, 1997.

[149] J. Smith and S. Chang, "Tools and Techniques for Color Image Retrieval," *SPIE Proceedings*, vol. 2670, pp. 1630–1639, 1996.

[150] M. Greitans, M. Pudzs, and R. Fuksis, "Object Analysis in Images using Complex 2D Matched Filters," *IEEE Region 8 Conf. EUROCON, Saint-Petersburg, Russia*, May,2009.

[151] C. Seng, M. Amin, F. Ahmad, and A. Bouzerdoum, "Image Segmentations for Through-the-Wall Radar Target Detection," *IEEE Trans. Aerosp. Electronic Syst.*, vol. 49, no. 3, pp. 1869–1896, Jul. 2013.